University of Trento

Department of Physics

PH.D. IN PHYSICS
XXXVII° CYCLE

SSD FIS/06

Academic Year 2023–2024

Electromagnetic characterization of the ionosphere in the framework of the magnetosphere-ionosphere-lithosphere coupling

Supervisor
Prof. Roberto Battiston
Prof. Mirko Piersanti

Ph.D. Candidate
Dario Recchiuti
226756

Final examination date: 04/11/2024

"If you haven't found something strange during the day, it hasn't been much of a day."
John Wheeler

A Greta,
che mi è stata vicina anche a oceani di distanza

Abstract

The ionospheric environment has become a focal point in the study of earthquake-related anomalies. In particular, both electromagnetic anomalies and particle bursts have been detected in the ionosphere and proposed as potential seismo-related phenomena. This thesis addresses the challenges in distinguishing earthquake-induced electromagnetic anomalies from the complex and variable background of ionospheric signals. Utilizing data from the CSES-01 satellite, this work introduces a robust methodology for characterizing both medium-long and short-duration electromagnetic signals in the ionosphere. A new approach to defining ionospheric EM background is proposed, considering temporal and geographical variations, and a statistically rigorous definition of anomalies is introduced. Additionally, a novel algorithm is developed for the efficient detection of short-duration whistler waves, revealing significant insights into their spatiotemporal distributions. To explore the coupling mechanisms between electromagnetic anomalies and particle bursts, numerical simulations using a hybrid particle-in-cell code were conducted, simulating ionospheric plasma interactions with small amplitude Alfvén waves. The results demonstrate modifications in ion velocity distributions and the emergence of fast ion beams, providing the first estimates of time delays between the impact of the electromagnetic waves and plasma disturbances. This research advances the understanding of seismo-ionospheric coupling, offering valuable tools for the identification of earthquake-related anomalies.

Keywords: Ionosphere, Electromagnetic anomalies, Earthquakes, CSES-01 satellite, Electromagnetic waves, Hybrid particle-in-cell simulations

Contents

Glossary of Abbreviations and Acronyms

AGW: Acoustic Gravity Waves
CAMELIA: Current Advance Method Et cycLIc leApfrog
CIR: Corotating Interaction Region
CME: Coronal Mass Ejections
CSES: China Seismo-Electromagnetic Satellite
EE: earthquake epicenter
EFD: Elecgric Field Detector
ELF: Etreme-low frequency
EMD: Empirical Mode Decomposition
EME: Electromagnetic Emission
FAC: Field Aligned Current
FIF: Fast Iterative Filtering
GEC: Global ELectric Circuit
GOR: GNSS Occultation Receiver
HCS: Heliospheric Current Sheet
HEPD: High-Energy Particle Detector
HEPP: High-Energy Particle Package
HF: High-frequency
HPIC: Hybrid Particle In Cell
HPM: High-Precision Magnetometer
HSA: Hilbert Spectral Analysis
HTT: Hilbert–Huang Transform
IAR: Ionospheric Alfvén Resonator
IF: Iterative Filtering
IMC: Intrinsic Mode Component
IMF: Interplanetary Magnetic Field
IPSD: Integrated Power Spectral Density
IRI: International Reference Ionosphere
LAP: Langmuir Probe
LEO: Low-Earth Orbit

LT: Local Time
MHD: Magnetohydrodynamics
MILC: Mangetosphere-Ionosphere-Lithosphere Coupling
PAP: Plasma Analyzer Package
PB: Particle Burst
PC: Polar cap
PCA: Principal Component Analysis
PDE: Partial Differential Equation
PIC: Particle-In-Cell
PSD: Power spectral density
SCM: Search Coil Magnetometer
SI: Sudden Impulse
Sq: Solar quiet
SR: Schumann Resonance
SW: Solar Wind
TBB: Tri-Band Beacon
TEC: Total Electron Content
ULF: Ultra-low frequency
UT: Universal Time
VDF: velocity distribution function
VLF: Very-low frequency
WPI: Wave-particle interactions
WWI: Wave-wave interactions

Introduction

Earthquakes (EQs) are one of the most severe natural disasters impacting human society. Consequently, the scientific community has always been focused on mitigating their effects to preserve lives and enhance economic and social resilience (see Basile et al. [19]). Over the past decades, the scientific pursuit of earthquake-related signals has directed its attention towards the ionosphere. Indeed, many anomalies, such as electromagnetic (EM) signatures and enhancements in the particle fluxes, often referred as particle bursts (PBs), temporally correlated with large-magnitude earthquakes, have been found in the ionosphere rather than in the lithosphere (see e.g. Picozza, Conti, and Sotgiu [213] for a review of observations in space of signals reconciled with earthquakes).

The spectrum of electromagnetic variations surrounding the Earth extends across an enormous frequency range (see Sabaka, Hulot, and Olsen [234] and figure 1, representing the amplitude spectrum of geomagnetic variation from 10^{-15} to 10^{5} Hz.) The characteristic scales of these signatures exhibits significant overlaps, making it challenging to differentiate between the various sources of ionospheric variations (Constable [65]). Consequently, the intricate nature of Earth's EM environment presents a significant challenge to an accurate identification of earthquake-related ionospheric EM anomalies.

In recent years, significant progress has been made in this field. In 2004, the DEMETER mission (Lagoutte et al. [158]) has been the first one dedicated to the detection of EM emissions transmitted from seismic regions. At present, the most advanced Low-Earth Orbit (LEO) mission for the investigation of seismo-induced phenomena in the near-Earth electromagnetic environment is the CSES mission (Shen et al. [241]), whose first satellite of the constellation (CSES-01) has been launched in 2018. This satellite has already furnished systematic evidence of EM anomalies correlated with seismic activity (Piersanti et al. [217], Zong, Tao, and Shen [306]). In 2020, the first analytical lithospheric–atmospheric–ionospheric–magnetospheric coupling model has been proposed (Piersanti et al. [217], Carbone et al. [43]). This model is capable of providing quantitative indicators to interpret the observations in the proximity of the earthquake. However, the topic of ionospheric disturbances in connection to intense seismic events remains one of the most debated in literature, as it still presents three major challenges. First, the absence of a well-defined characterization of the background ionospheric EM environment devoid of seismic activity and other external influences. Second, the current methods for identification of EQ-related signatures lack a statistically rigorous definition of an anomaly. Third, the absence of a well-defined causal mechanism underlying the concurrent occurrence of PBs and EM anomalies.

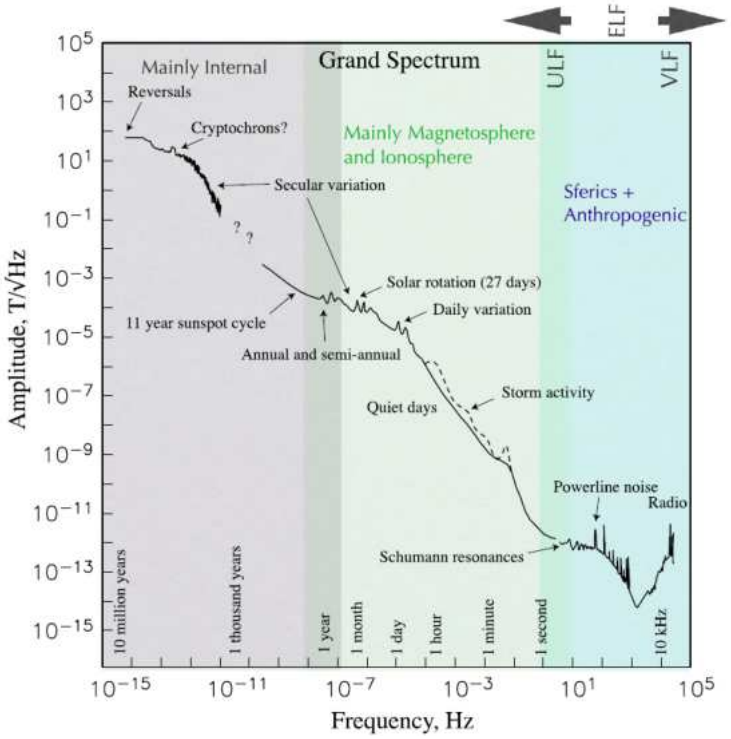

Figure 1: Amplitude spectrum of geomagnetic variation. (From Constable and Constable [66].)

In the present thesis, we have addressed all these critical issues. Indeed, we propose a new procedure for the characterization of the ionospheric EM environment. The proposed method uses data acquired by the CSES-01 satellite and employs two different approaches for characterizing ionospheric EM signatures with varying durations: medium-long duration (>1 second) and short duration (<1 second). In the first case, the procedure leads to the first robust definition and calculation of the ionospheric EM background, which takes into account the varying ionospheric conditions. In the second case, we have introduced a new algorithm for identifying short signals in the ionosphere. This algorithm is extremely fast in terms of computational time and is solely based on physical observables. Furthermore, we present a statistically robust definition of an anomaly, applicable to any signal emerging from the background. This definition involves analysing the statistical distribution of EM wave energy over the entire time window of CSES-01 data availability, allowing to discriminate between rare and anomalous event. Finally, we present the findings from our investigation into the effects of EM waves impact on a low-beta plasma (as the real ionospheric plasma). These results were obtained through numerical simulations employing a hybrid particle-in-cell (HPIC) code. To the best of our knowledge, this represents the first instance in the literature where a plasma with characteristics resembling real ionosphere has been successfully simulated using an HPIC code. These results provide the first estimation of the time delay between the observed EM wave and the expected modification of the plasma distribution.

The thesis is structured into four chapters followed by a discussion of the achieved results and future research directions. In chapter 1 we provide a concise yet comprehensive overview

of the ionospheric environment. We summarize the current understanding of ionospheric disturbances, both from above (solar wind-magnetosphere-ionosphere coupling) and from below (lithosphere-atmosphere-ionosphere coupling). Chapter 2 details the data and methods employed in this study. In chapter 3 we present the ionospheric EM characterization results, categorized into medium-long duration and short duration signatures. Finally, chapter 4 presents the results of numerical simulations investigating the perturbation of a low-beta plasma by EM waves.

Chapter 1

The Earth's ionosphere

In this chapter we provide a concise overview of the Earth's ionospheric environment. Since the ionosphere is significantly influenced by processes originating in the neutral atmosphere and the magnetosphere, a fundamental understanding of these regions is essential for accurate ionospheric characterization. Consequently, we provide a description of the key drivers and mechanisms governing the solar wind-magnetosphere-ionosphere coupling (section 1.2) and the lithosphere-atmosphere-ionosphere coupling (section 1.3). We focus on the relevant aspects and open problems related to this study. For a more comprehensive description of Earth's ionosphere, interested readers can refer to Kelley [148].

1.1 The ionosphere: an overview

The Earth's ionosphere is a partially ionized layer between the totally ionized magnetosphere and the neutral atmosphere, extending from about 50 km to 1000 km above sea level (Kelley [148]). It is composed by a mixture of ionized and neutral particles, with the number density of the neutral gas exceeding that of the ionospheric plasma.

The influence of gravity causes the horizontal stratification of both the atmosphere and ionosphere, at first approximation. Usually, in the literature, atmospheric layers are represented by the neutral temperature profile, while the ionospheric environment is organized by the plasma density. Figures 1.1a and 1.1b show respectively the typical neutral gas temperature and plasma density variations with respect to the altitude above sea level.

In the lower atmospheric layer, the troposphere, the neutral temperature decreases with a rate of $\approx$ 6.5 K/km (Wallace and Hobbs [278]). Then at $\approx$ 10 km, there is an inversion point, where the temperature starts to increase: the tropopause. The inversion of the trend is essentially due to the absorption of part of the ultraviolet portion of the solar radiation by the ozone. This effect has a maximum at about 50 km, where the stratosphere ends with the stratopause, the mesosphere begins and the temperature trend reverses again. The temperature decrease (due to radiative cooling) ends at $\approx$ 90 km, which is the minimum point for neutral temperature (the mesopause). Above this minimum, the absorption of higher energy solar photons leads to an enormous increase in the temperature (termosphere).

As mentioned, the huge increase in the temperature in the termosphere is caused by solar

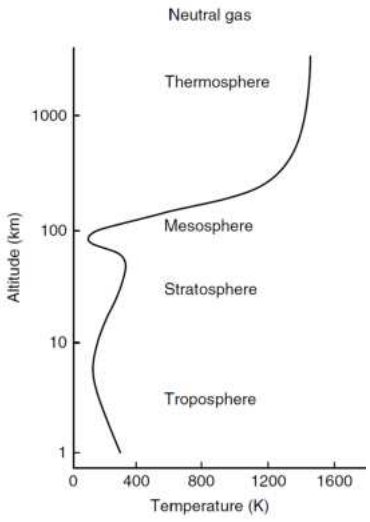

(a) Atmospheric layers with typical mid-latitude profile of neutral gas temperature.

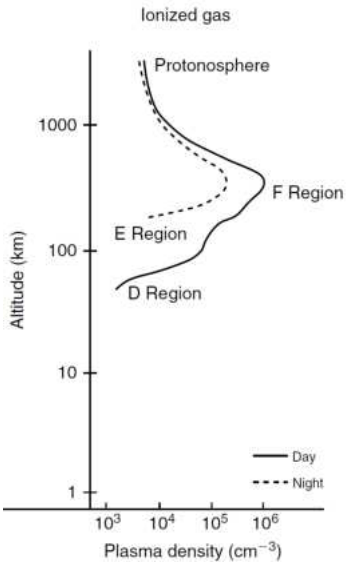

(b) Ionospheric regions with typical mid-latitude profile of number density of the plasma.

Figure 1.1: Atmospheric layers and ionospheric regions as a function of altitude (adapted from Kelley [148].

radiation, in particular in the ultraviolet (UV) and extreme ultraviolet (XUV) spectral range (wavelength $< 10^{-7}$ m). The presence of these radiations also produces the plasma in the sunlit hemisphere. In fact, they have an energetic content high enough to generate charged particles through the photoionization and photodissociation of atmospheric neutral particles, like N_2, O_2 and O (Kelley [148]).

For this reason, two different plasma density profiles are reported in figure 1.1b, one regarding typical diurnal condition (solid line) and one regarding nighttime (dashed line). Since the photoionization rate is dependent on solar flux, the ionosphere depends on time of the day, season, altitude, geographical latitude and longitude (Baumjohann and Treumann [21]). Specifically, the population of charged particles grows during the day with the Sun elevation and, through recombination, decreases during the night when the solar radiation disappears.

At higher altitude, the concentration of ionisable gases decreases. On the contrary, the intensity of the solar radiation increases, since the beam itself is reduced in intensity as it penetrates. The combination of this factors must generate a maximum at some given altitude, which is called F layer ($\approx 10^6$ cm^{-3} in correspondence of the local noon, Kelley [148]).

Actually, there are other two elements to take into account. The first one is the presence of another ionization mechanism, the so called impact ionization (Kamiyama [143]). It is caused by solar or magnetospheric particles that precipitates into the ionosphere and it is the most important ionization mechanism at high latitudes, since it maintains the ionosphere during the polar night. The other one is that the atmospheric profiles of the various atomic species

are different (see figure 1.2), as well as the response to solar radiation.

Below $\approx$ 100 km the atmospheric composition is quite uniform, due to the presence of various turbolent mixing phenomena. On the contrary, above this level (the turbopause), the various ionospheric population starts to split according to their masses (Kelley [148]). Near that altitude, N_2 and O_2 are the most abundant populations (in a ratio $\approx$ 4:1). Above this level, the abundance of atomic oxygen O_+ begins to increase; at $\approx$ 120 km, it equals that of O_2 and at $\approx$ 250 km it exceeds that of N_2, becoming the dominant species. This trend is explained by the photodissociation of O_2 by UV radiation coupled with molecular diffusion; all of this in an environment without turbolent mixing above the turbopause.

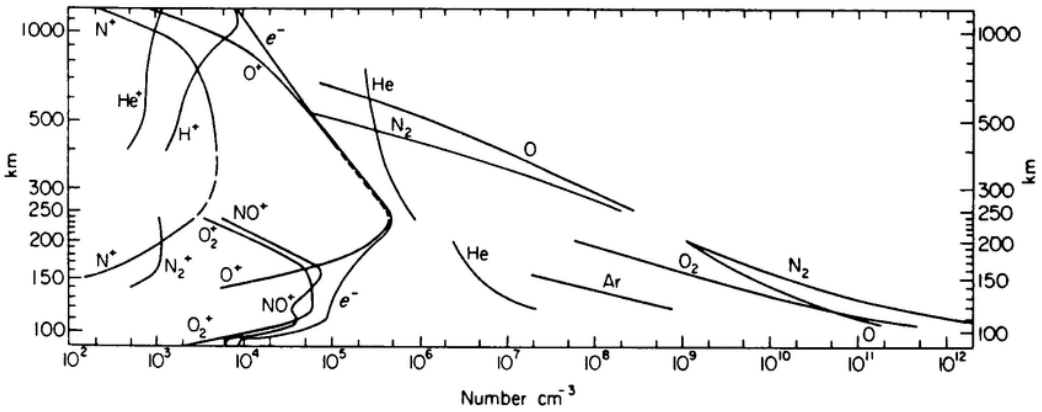

Figure 1.2: Daytime atmospheric composition above New Mexico. Taken from Kelley [148]. Copyright 1969 by MIT.

All these effects and the complex environment lead to an electron density exhibiting relative maxima and minima (line labeled e^- in figure 1.2). Due to the role of molecular ions, during daytime, the F region is split into F1 and F2, so that four different regions are identified: D, E, F1, F2 (Hunsucker and Hargreaves [131]). We summarized their main characteristics in table 1.1. The typical mid-latitude electron density and the four layers are show in figure 1.3, which illustrates also the impact of the solar activity, by highlighting the difference in the density profile between solar minimum and solar maximum.

name	**altitude**(km)	**electron density** (m^{-3})
D	60-90	10^8-10^{10}
E	100-160	10^{11}
F1	160-180	10^{11}-10^{12}
F2	$\approx$ 300 (variable)	10^{12}

Table 1.1: Characteristics of the ionospheric layers.

As shown in figure 1.3, all of these regions are strongly dependent on both solar activity and solar radiation. In particular, the differences are remarkable between a diurnal and a nocturnal ionosphere. In fact, F1 and D regions disappear at night, while F2 and D regions remain but

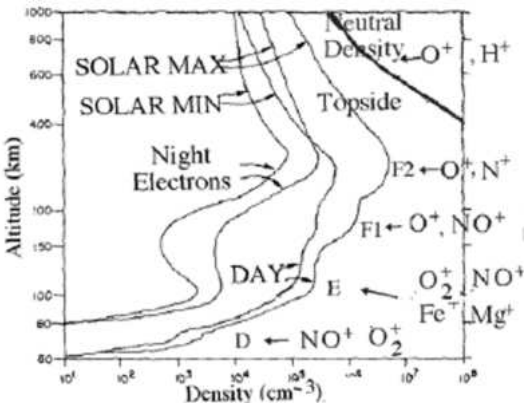

Figure 1.3: Typical mid-latitude electron density profiles for solar activity at maximum and minimum during daytime and nighttime, adapted from Jursa et al. [140].

with a much lower density value. Each region has its critical frequency, defined as the upper limit for wave reflection and corresponding to the maximum plasma frequency (Hargreaves [112]). The electron plasma frequency is given by $f_p = 8980\sqrt{n_e}$ Hz, where n_e is the electron density in cm^{-3} (Gurnett and Bhattacharjee [111]).

1.1.1 The ionosphere: a dynamic layer between Earth and space

The ionosphere serves as a dynamic interface between Earth's atmosphere and the magnetosphere. Consequently, it is significantly influenced by processes originating in both these environments, receiving substantial energy and momentum fluxes from both directions (Kelley [148]). These fluxes are transported by particles, electromagnetic fields, and atmospheric waves.

Both the neutral atmosphere and the magnetosphere are very dynamic media, but they exhibits very different characteristics. A comprehensive understanding of the ionospheric environment and its interactions from both above and below necessitates a fundamental comprehension of these regions, encompassing both space plasma physics and atmospheric dynamics. To provide a foundational framework, the following sections offer a concise description of the key drivers and mechanisms governing the coupling between the ionosphere and the overlying solar wind-magnetosphere system (section 1.2) and the underlying lithosphere-atmosphere system (section 1.3). While this descriptive approach serves as a valuable starting point, its limitations will be addressed by delving deeper into specific processes, such as wave-particle interactions, when their detailed treatment becomes relevant in subsequent sections.

1.2 Solar wind-magnetosphere-ionosphere coupling

The impact of solar activity on Earth's ionosphere has been extensively investigated, and its effects have been quantified through numerous studies (Lyon [172], Fedder and Lyon [81], Horton et al. [127], Milan et al. [187], Borovsky [33].) In the following sections, we provide a synthetic overview of the key drivers and mechanisms governing the coupling between these regions.

1.2.1 The solar wind

Most of the energy produced by the Sun arrives on Earth in the forms of photons (Akasofu and Chapman [3]), but there is also a flow of ionized plasma that escapes from the corona with a supersonic velocity (Parker [210]). This plasma, composed mostly of protons and electrons, with a small percentage of alpha particles (from 1 to 5 $\%$ depending on the solar cycle, see e. g. Kasper et al. [146]) and heavy ions, is known as the solar wind (SW). It originates because of the difference in the gas pressure between the solar corona and interplanetary space (Kivelson and Russell [151]). The first model of an expanding corona was suggested by Parker [210]. In his hydrodynamic stationary model, he considered an isothermal plasma, since the high temperature of the corona ($T \approx 10^6$) slowly decreases away from the Sun. The Parker model solutions for different corona temperature are shown in figure 1.4a, representing different velocity profile versus the distance from the Sun.

Moving with the magnetic field of the Sun, the coronal plasma can be approximated as a magnetohydrodynamic (MHD) fluid with infinite conductivity (Schunk and Nagy [237]). It drags the solar magnetic field in the interplanetary space, forming the Interplanetary Magnetic Field (IMF), which is about 3-4 nT at 1 Astronomical Unit, (AU, corresponding to Sun-Earth distance). Due to the radial propagation of the SW plasma and the rotation of the Sun, the IMF lines assume a configuration called *Parker spiral* (figure 1.4b). The SW speed V_{SW} at the Earth's orbit is between ≈400 and ≈800 km/s, the particle number density varies between ≈ 1 and ≈ 10 cm^{-3}, the temperature is ≈ 10^5 K, the magnetic field has strength around ≈ 5 nT and, in the ecliptic plane, it is tilted by ≈ $45°$ with respect to Earth-Sun direction (Kivelson and Russell [151], Parks [211]).

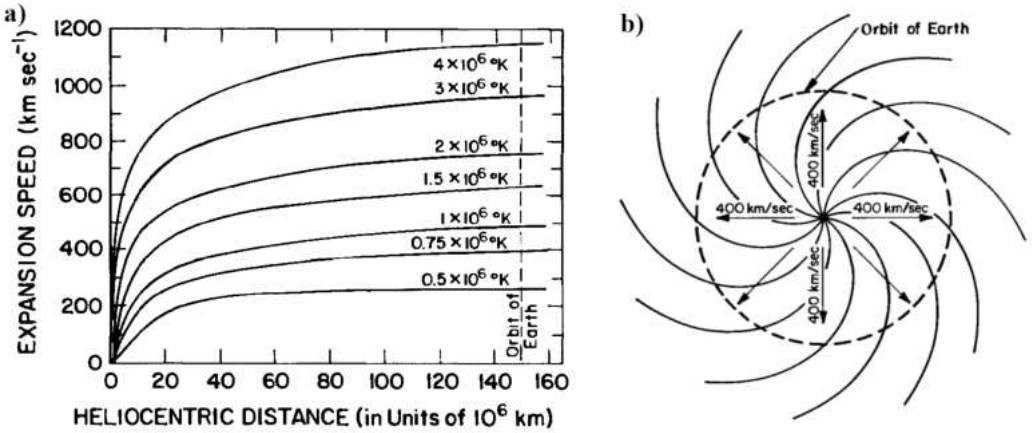

Figure 1.4: a) Solutions of the Parker model for different corona temperatures expressed in terms of the V_{SW} vs the heliocentric distance. b) Representation of the SW flow (black arrow) dragging tha magnetic field lines of the Sun, resulting in the Parker spiral. At Earth's orbit (dashed circle) the IMF is tilted by ≈ $45°$ with respect to Sun-Earth direction (Adapted from Kivelson and Russell [151]).

1.2.2 The magnetosphere

The SW confines the Earth's magnetic field in a cavity called magnetosphere (Ratcliffe and Holzer [224]). In the absence of the SW's influence, the Earth's magnetic field can be approximated, to a first order, by a dipole field with its axis currently forming an angle of $\approx$9.7° with the Earth's rotation axis (Finlay et al. [84]). The dynamic pressure of the solar wind compresses it on the dayside and stretches it out on the nightside into a long magnetotail (Hones [123]).

According to Alfvén theorem (also known as the frozen-in flux theorem, Alfvén [6]) magnetic fields embedded within electrically conducting fluids are constrained to move together. This theorem, valid for electrically conducting fluids in the limit of very high electrical conductivity (very low magnetic diffusivity), implies that plasma coming from the Sun cannot leave the IMF. Consequently, the Earth's magnetic field deflects the solar wind around itself. The boundary between the Earth's magnetic field lines and the IMF is the magnetopause (Kivelson and Russell [151]).

As the magnetopause represents a discontinuity for the magnetic field, forming a dynamic boundary between the SW and the geomagnetic field, it is associated with a current system: the magnetopause or Chapman-Ferraro current (Chapman [48]). This current layer flows from dawn to dusk in the dayside and it plays a crucial role in sustaining the magnetosphere (Ganushkina, Liemohn, and Dubyagin [98]). Going towards the downwind region, this current circles around the polar cusps. Moving to the the nightside, the magnetopause current flows from dusk to dawn connecting at the equator to the tail current which flows in the opposite direction. The magnetopause and the tail current systems together sustain the magnetotail, a cylindrical shaped night side region extending for hundreds of Earth radii (R_E, Hones Jr et al. [124]). In addition to these current systems, a crucial role in sustaining the magnetosphere is played by the ring current and the field-aligned currents (FACs). The ring current flows azimuthally around the Earth from east to west between $\approx$ 4 R_E and $\approx$6 R_E (Hargreaves [112]). At this altitude, nearly all atmospheric particles become fully ionized, subjecting them to the influence of electric and magnetic fields. Consequently, these particles exhibit three distinct types of motion: gyration around magnetic field lines, bouncing along field lines, and azimuthal drift forming rings around the Earth (Baumjohann and Treumann [21]). The FACs follow the magnetic field direction and are responsible for the transfer of energy derived from the interaction between the solar wind and the magnetosphere to the ionosphere. In addition, they allow the transfer of convection electric fields and particle precipitation (see e.g Kamide and Chian [141]). Therefore, they allow the electromagnetic interaction between hot magnetospheric plasma and cold ionospheric plasma (Baumjohann and Treumann [21]). Figure 1.5 illustrate the main ionospheric current systems. Here, ticker arrows indicate the current systems and thinner arrows the magnetospheric field lines.

1.2.3 Solar wind-magnetosphere-ionosphere interactions

When the IMF has on opposite direction with respect to the Earth's magnetic field, magnetic reconnection can occur, allowing plasma from the solar wind to penetrate into the magnetopause (Frey et al. [92]). Magnetic reconnection, which is a topological rearrangement of magnetic field that occurs on time scales much faster than the global magnetic diffusion time

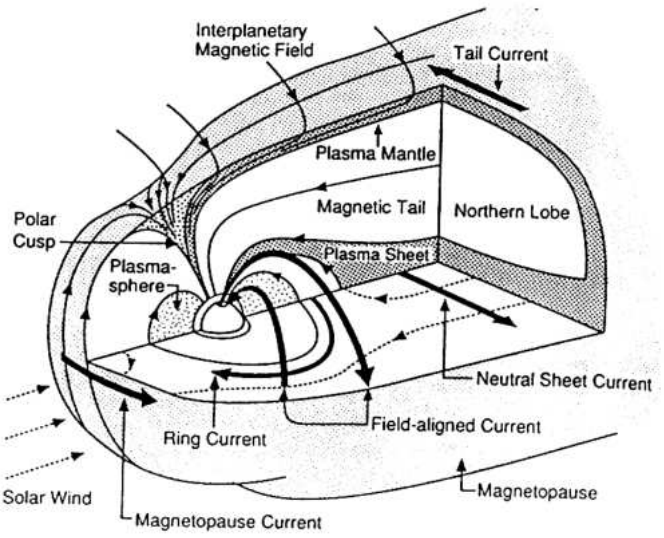

Figure 1.5: The magnetosphere and the magnetospheric current systems. Credits: Russell [232].

(Zweibel and Yamada [307]), is a naturally occurring process leading to the release of energy stored in magnetic fields (resulting in particle acceleration, Hesse and Cassak [118]). For a full treatment of the topic, which is beyond the scope of this work, the reader may refer to: Biskamp [30], Loureiro and Uzdensky [171], Hesse and Cassak [118], Pontin and Priest [218].

Since the Earth's magnetic field at the nose of the magnetosphere is essentially directed along the south-north direction (Lanza and Meloni [161]), the vertical component of the IMF ($B_{Z,IMF}$) play the main role in the reconnection process. In particular, if $B_{Z,IMF}$ is positive or negative, two different situations can be observed, as schematically shown in figure 1.6.

- $B_{Z,IMF} < 0$ (**open magnetosphere**): reconnection occur on the dayside, equatorward of the polar cusp (Lepping, Berdichevsky, and Wu [164]). There are two reconnection points on the equatorial plane (indicated by the "N" in figure 1.6a) where magnetic field lines of different origins merge and allow exchanges of magnetic flux and plasma. This configuration is generated by a southward oriented IMF line that reaches the magnetopause and connects to the Earth's field line, leading to two different lines (one for each hemisphere) with a fixed point on the ground and the other extreme on the Sun (open lines). These open lines are pushed by the SW in an anti-solar direction towards the nocturnal magnetosphere, where they reconnect. This night side reconnection point is characterized by a closed and stretched configuration. The relaxation of this newly closed line carries the plasma flow towards the Earth. In addition, after the reconnection point, an open line is dragged away by the solar wind.
- $B_{Z,IMF} > 0$ (**closed magnetosphere**): a tailward polar cusp reconnection can occur (Crooker [69], Chisham et al. [53]) and a reconnection point for each hemisphere appears ("N" in figure 1.6b) on the magnetospheric lobes. In this configuration, particles of solar origin can penetrate at high latitudes even in the so-called closed magnetosphere.

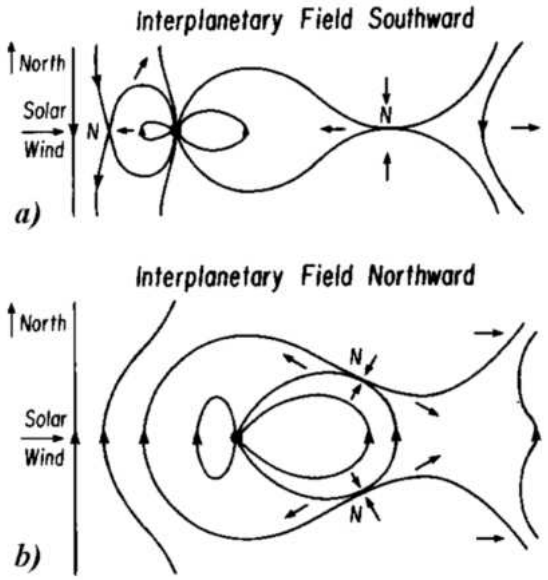

Figure 1.6: Schematic representation of the field lines in the noon-midnight meridian when a) the IMF is antiparallel to the Earth's magnetic field near the nose of the magnetosphere. b) when it is parallel (Achilli [2]).

Solar wind-magnetosphere interactions trigger several events, including geomagnetic storms (Gonzalez et al. [108]), the creation of large fluxes of accelerated particles (Bingham et al. [28] and reference therein) and chorus wave activity (Li et al. [165] and reference therein). All of them are influenced by the dynamic conditions in the Earth's space environment and driven by processes originating on the Sun (Pulkkinen [222]). The strength of these effects depends significantly on the interplay between the impacting solar wind and Earth's magnetic field and plasma environment. Under typical solar wind conditions, the kinetic energy flux of the solar wind impinging the diurnal magnetopause is of the order of $\approx 10^4$ GW (considering a 30 R_E cross section, Kamide and Baumjohann [142]). A portion of this energy flux penetrates into the magnetosphere (through the mechanisms described) where it is immediately stored, then distributed and eventually dissipated.

A fraction of the energy entering in the dayside magnetosphere is transferred to the ionosphere via various mechanisms (Kamide and Baumjohann [142]):

- a fraction of the energy is directly transferred to the high-latitude ionosphere through the FAC;
- the remainder is transferred to the magnetotail where it is temporarily stored in kinetic, thermal plasma and magnetic field energy;
  - a portion of the energy stored in the magnetotail is then transferred to the ring current via particle injection;
  - a part is transferred to the auroral ionosphere by the means of particle precipitation and via the FAC;
  - the remainder re-enters the downstream solar wind and therefore is not dissipated inside the magnetosphere.

In the last decades, thanks to the increasing number of spacecraft missions exploring the solar wind, the magnetosphere and the ionosphere, the coupling between these three regions has been confirmed by several observations (see e.g. Lyon [173], Milan et al. [186], Walsh et al. [279], Tenfjord and Østgaard [257] and reference therein).

1.3 Lithosphere-atmosphere-ionosphere coupling

The atmosphere and ionosphere are interconnected by a complex network of electrical currents. The concept of a global electric circuit (GEC) was first proposed by Wilson (Wilson [292], Wilson [291]) to account for the presence of a vertical atmospheric electric field. However, while the study of ionospheric disturbances caused by the solar wind-magnetosphere-ionosphere coupling is a topic to which scientists have devoted entire careers over the last century, the study of ionospheric disturbances from below has become of great interest only in recent decades. In fact, despite it was well known that the ionospheric medium can be influenced from below by atmospheric waves generated in the neutral atmosphere (Hines [119]), the interest of the scientific community has only grown in recent years, mainly due to the hypothesis of a possible causal link between ionospheric disturbances and seismic activity.

The ionosphere can be perturbed by a variety of natural phenomena, ranging from seismic events to atmospheric electrical discharges, such as lightning and transient luminous events.

1.3.1 Lightning

Lightning arises from thunderstorm electrification processes that separate electrical charges within the clouds (Rakov and Uman [223]). These discharges manifest primarily as intracloud/intercloud (most frequent), cloud-to-ground, and, less commonly, ground-to-cloud events (Chen et al. [50]). Each discharge involves the transfer of positive or negative charge through a conductive channel (Nicora et al. [203]). Typically, negative cloud-to-ground discharges transfer a total charge of approximately 25 C, with a peak current reaching $\approx$ 30 kA, and releasing around 500 MJ of energy (Singh, Singh, and Kamra [245] and reference therein).

Experiments described by Kelley et al. [147] and Holzworth et al. [122] provided definitive evidence for the penetration of a quasi-static electric field "pulse" from the troposphere into the ionosphere. Their high-altitude rocket probes detected whistler waves, a phenomenon associated with lightning-generated sferics, within the ionosphere.

Beyond its role as a source of electromagnetic waves, lightning significantly impacts wave propagation by inducing localized ionization within the medium. This ionization alters the electrical conductivity of the atmosphere, affecting the propagation of electromagnetic waves across different frequency bands (with a frequency spectrum peaked at a few to 10 kHz, see Simões et al. [244]). The extent of this impact depends on various factors, including the lightning discharge parameters, the ambient atmospheric conditions, and the specific wave propagation characteristics (Rakov and Uman [223] and reference therein).

1.3.2 Transient Luminous Events

Wilson's conceptualization of the GEC ((Wilson [292], Wilson [291]) also predicted the existence of transient luminous events (TLEs) above large thunderstorms. The advent of space shuttle video imagery and satellite-based optical detectors has revealed the astonishing beauty and diverse forms of these phenomena (see figure 1.7). These events, encompassing sprites, elves, blue jets, and other less common forms, are manifestations of high-altitude electrical breakdown phenomena triggered by large thunderstorms and mesoscale convective systems.

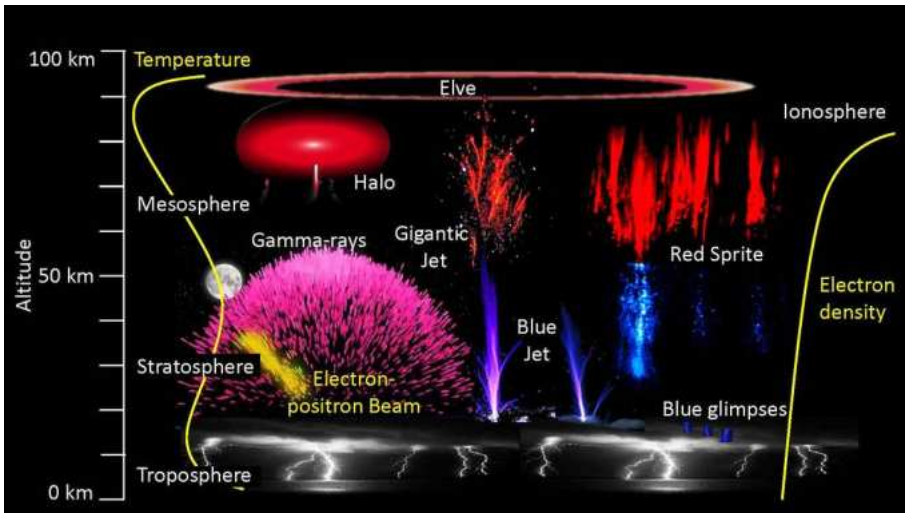

Figure 1.7: The variety of upper atmospheric phenomena powered by thunderstorms. Taken from https://www.nasa.gov/image-article/upper-atmosphere-phenomena-caused-by-thunderstorms/

Among these events, red sprites and blue jets are particularly noteworthy. Red sprites extend from altitudes of 80 to 55 km and have a visible lifetime of a few milliseconds (Rowland [231]). Blue jets originate from cloud tops (15 km) and ascend to altitudes of 40 km, traveling at a velocity of 100 km/s, resulting in a lifetime of approximately 300 milliseconds (Rowland [231]). Füllekrug and Rycroft [95] evaluated the contribution of sprites to the GEC, estimating their individual impact to be lower than 44 mV/m. Cummer et al. [71] reported a significant charge transfer of -144 C to the lower ionosphere during a gigantic jet event. Krehbiel et al. [157] proposed that positive blue jets contribute to the charging of the global electric circuit, while negative gigantic jets act to discharge the circuit. As a consequence of the variation in the GEC, the ionosphere can be affected by irregularities. In particular, TLEs can exert a range of influences on ionospheric dynamics, including modification of electron density and the production of new chemical species than can affect ionospheric dynamics (Siingh et al. [243], Williams [290], Rycroft and Harrison [233]).

1.3.3 Seismic activity

Seismic events characterized by vertical displacements of the ground or ocean floor can trigger co-seismic perturbations in the overlying atmosphere and ionosphere (see e.g Astafyeva [16]). The first documented observations of co-seismic perturbations in the atmosphere and ionosphere were made following the 28 March 1964 M_W 9.2 Alaska earthquake, USA (Davies and Baker [73]). Subsequently, the growing number of space missions facilitated numerous observations of earthquake-related ionospheric disturbances. For a review of seismo-associated ionospheric phenomena the reader may refer e.g. to Picozza, Conti, and Sotgiu [213], Astafyeva [16], Heki [115]. This has spurred numerous recent studies investigating the mechanisms responsible for the generation of ionospheric irregularities near large EQs. In this section, we present a concise review of the most prominent theories and models proposing a lithosphere-atmosphere-ionosphere coupling mechanism during the co-seismic phase (for more details see e.g. Tanimoto and Heki [254] and reference therein).

Ground motions induced by an earthquake in the ambient geomagnetic field, due to the conductivity of the Earth's crust, can cause an electromotive force, which in turn leads to the rise of EM fields. This mechanism is well explained in the paper by Koshevaya et al. [156]. This study investigates the spectrum of seismo-electromagnetic and acoustic waves generated by seismic and volcanic activity. The spectrum encompasses both electromagnetic emissions (EME) and acoustic emissions. The authors model EME by considering a piezoelectric crystal subjected to mechanical stresses, which induce uniform crack propagation. This, in turn, generates non-stationary polarization currents in the vicinity of the moving crack. The study estimates the potential spectrum of EME arising from piezoelectric fracturing in rocks, alongside the spectrum of acoustic emissions, originating from the excitation and non-linear propagation of acoustic waves through the Earth's crust, atmosphere, and ionosphere.

In the last decades, this mechano-electric mechanism has been referred as the motional induction effect (Gershenzon, Gokhberg, and Yunga [103], Yamazaki [295]) or seismic dynamo effect (Matsushima et al. [181]), and it has been proposed as a possible explanation for the EM disturbances observed during large seismic events (Gershenzon and Bambakidis [102], Matsushima et al. [180], Ujihara, Honkura, and Ogawa [264], Honkura, Satoh, and Ujihara [125]) mainly in the ionosphere (Pulinets and Boyarchuk [220]).

The MILC model

The increasing number of observations of ionospheric anomalies associated with seismic activity in recent years (Picozza, Conti, and Sotgiu [213]) has led to the development of few models trying to explain these observations. However, the first analytical-quantitative model able to reproduce, with a high statistical significance, the observed temperature fluctuations induced by strong earthquakes was only introduced in 2020 (MILC model, Piersanti et al. [217], Carbone et al. [43]). This model assumes the generation of an acoustic gravity wave (AGW), which propagates through the atmosphere, and interacts with the ionosphere. This interaction can also lead to an EM wave injection into the Van Allen Belts. The core of the model can be summarized in three causal steps:

1. An AGW is generated in the vicinity of the earthquake epicenter (EE) and subsequently

propagates upward through the atmosphere;

2. the propagating AGW interacts mechanically with the ionosphere, generating a localized plasma density perturbation via a pressure gradient. This perturbation disrupts the equilibrium state of the ionosphere, inducing a non-stationary electric current within the E-layer. Consequently, this current generates an EM wave;

3. the EM wave interacts with the magnetospheric field, inducing a perturbation in the eigenfrequency of the relative field lines. The ionospheric footprint of these perturbed field lines coincides with the radial projection of the EE.

1.4 Ionospheric EM signatures

Within the complex framework of phenomena described in the preceding paragraphs, it is necessary to discriminate among the various signatures originating from different sources of potential ionospheric disturbances (for a review of ionospheric signatures, interested readers may refer to Simões et al. [244]). To avoid misinterpretation, this is a fundamental prerequisite to the eventual detection of anomalies possibly correlated to seismic activity.

Schumann resonances

Schumann resonances (SR) are extremely low-frequency (ELF) electromagnetic waves that resonate in the Earth's cavity between the ionosphere and the Earth's surface. They are excited by lightning discharges and have a fundamental frequency of around 7.83 Hz, with higher harmonics occurring at approximately 14.1 Hz, 20.3 Hz, 26.2 Hz, and so on (Sentman [238]). When a lightning bolt strikes, it creates a sudden pulse of electromagnetic energy. This energy propagates upwards into the ionosphere, where it is reflected back to the Earth's surface. The Earth's surface then acts as a mirror, reflecting the energy back up into the ionosphere. This process of reflection and re-reflection sets up a standing wave, which is what is named a SR (Galejs [96], Füllekrug [94]).

As many other ionospheric waves, SRs can propagate around the globe due to the waveguide effect of the Earth's ionosphere. In fact, the Earth can be approximated as a near-perfectly conducting sphere enveloped by a thin dielectric atmosphere extending upwards to the lower boundary of the ionosphere; consequently, the Earth-ionosphere system forms a cavity analogous to a waveguide (Wait [276]).

Sferics and tweeks

Lightning discharges produce broadband EM impulses that propagate in the Earth-ionosphere cavity and are referred as sferics (Helliwell [116]). They occur across a wide frequency spectrum, ranging from a few hertz to tens of megahertz, and can be detected at distances of thousands of kilometers from the source (Hayakawa et al. [113]). The generation of sferics is a complex process that involves several stages (Rakov and Uman [223]). When a lightning bolt strikes, it rapidly ionizes the air along its path, creating a conductive channel. This channel

acts as an antenna, radiating EM energy into the surrounding environment. The EM radiation is produced by the sudden acceleration and deceleration of electrons in the lightning channel. The specific characteristics of sferics depend on a number of factors, including the type of lightning discharge, the altitude of the lightning channel, and the electrical properties of the atmosphere. In general, they are typically characterized by their short duration, broad bandwidth, and complex waveform (Hayakawa et al. [113], Rakov and Uman [223]).

Multiple reflections between the Earth's surface and the ionosphere lead to constructive interference, filtering the broadband signal and favoring specific resonant frequencies related to the upper boundary height. Upon escaping the cavity and propagating within the ionosphere, potentially along wave guiding ducts, the signal undergoes slight dispersion, resulting in a "tweek" (essentially a sferic experiencing minimal frequency spreading during ionospheric traversal). Conversely, waves traveling further along geomagnetic field lines through the plasmasphere, in the right-handed mode (Storey [250]), encounter significant frequency dispersion, manifesting as whistlers in the conjugate hemisphere due to their characteristic descending frequency tones.

Whistlers

Whistlers are a class of naturally occurring very low frequency (VLF) electromagnetic waves that propagate along the Earth's magnetic field lines, producing distinctive, descending tones. They are generated by lightning sferics that penetrate into the Earth's lower ionosphere (Hayakawa et al. [113]). As whistler waves travel along magnetic field lines, they encounter regions of varying electron density. The interaction between the waves and the plasma causes the whistler frequency to decrease as the wave propagates deeper into the magnetosphere. This frequency dispersion gives rise to whistlers' characteristic descending tones (Storey [250]). A typical spectrogram of a whistler (from Lichtenberger et al. [167]) wave is shown in figure 1.8, where the typical chirped structure with a falling tone frequency can be easily seen.

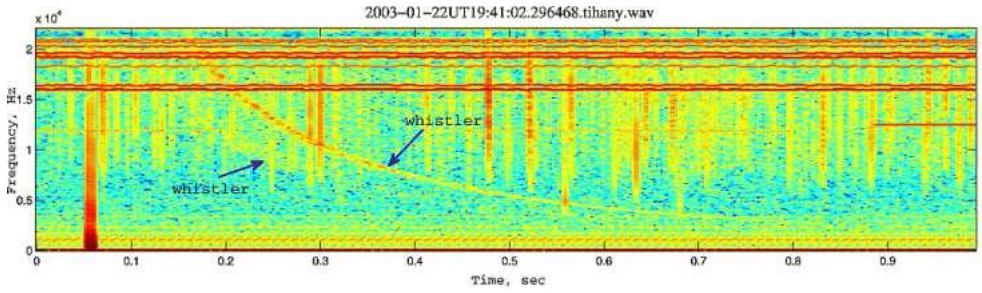

Figure 1.8: Typical spectrogram of a whistler wave in the time-frequency domain (adapted from Lichtenberger et al. [167]). The arrows indicate the whistlers.

Whistler research has provided valuable insights into the Earth's magnetosphere, offering a natural probe of its structure and dynamics. Eckersley [79] and Storey [250] have shown that the time travel t of a frequency f is given by the equation:

$$t = Df^{-1/2}, \tag{1.1}$$

where D is termed dispersion of the whistler and it is usually constant over a frequency range of several octave (Crouchley [70]). It is defined as:

$$D = \frac{1}{2c} \int \frac{f_p}{\sqrt{f_g}} \mathrm{d}s \tag{1.2}$$

where f_p is the plasma frequency, f_g is the local electron gyrofrequency, c is the speed of light and the integration is with respect to a length element $\mathrm{d}s$ along the whistler path. Therefore, if the propagation path and gyrofrequency variation are known and a form for the electron distribution is assumed, the electron density can be determined (KImpara [150]). Indeed, the dispersion characteristics of whistlers have been used to derive the electron density in the plasmasphere (see e.g. Park, Carpenter, and Wiggin [208]). Due to the importance of whistlers to map and monitor the ionosphere and the magnetosphere, several monographs has been dedicated to cover whistler theory, measurements, and applications (e.g. Helliwell [116], Sazhin [236], Ferencz [82]).

Whistler mode chorus waves

Whistler mode chorus (WMC) are electromagnetic waves characterized by their distinctive "whistling" sound, exhibiting a chorus-like structure. They are predominantly observed in the auroral region, closely associated with the precipitation of energetic electrons from the magnetosphere. WMC waves are composed of numerous wave packets with closely spaced frequencies in the range from few kilohertz to tens of kilohertz (Helliwell [116]). Despite extensive research, the precise generation mechanisms and propagation characteristics of WMC waves remain an active area of investigation. A recent paper (Bortnik, Thorne, and Meredith [34]) suggested that WMC waves can propagate into the plasmasphere from tens of thousands of kilometres away and evolve into hiss (see next paragraph).

Plasmaspheric hiss

Hiss is a type of naturally occurring, high-frequency electromagnetic (EM) noise that permeates the inner region of the magnetosphere and contributes crucially to the dynamic behaviour of the radiation belts. This pervasive hiss, spanning a frequency range of a few kHz to tens of kHz, is a ubiquitous feature, detectable by ground-based receivers and satellite instruments (Falkowski et al. [80], Ni et al. [202] and reference therein). The generation of plasmaspheric hiss is attributed to several mechanisms, such as plasma instabilities and wave-particle interactions (WPI, Gendrin [101]), in particular the interaction between EM waves and electrons gyrating around magnetic field lines at their cyclotron frequency. Each of these mechanisms contribute to the overall hiss intensity and spectral characteristics. The effects of the plasmaspheric hiss span from the modification of the plasma distribution to the impact on the particle precipitation and propagation of radio waves (see Bortnik, Thorne, and Meredith [34] and reference therein).

1.5 Open problems and research aims

The study of the ionosphere has been driven by the fundamental need to comprehend the influence of this layer on radio wave propagation. Consequently, most ionospheric research has focused on explaining the various layers and their variability (in terms of latitude, local time, season, etc.). As a consequence, one of the primary tools for ionospheric studies is the ionosonde, which is a remote sensing device providing the electron density profile (Kelley [148]).

In recent years, with the increase in space missions, ionospheric research has made significant advancements (see e.g. Yasyukevich et al. [300], Wood et al. [294]). However, a robust definition of the ionospheric EM background is still missing. Establishing the EM background is an essential prerequisite for accurately defining an electromagnetic anomaly in the ionosphere. Therefore, the ionospheric characterisation that is the subject of this study pursues a twofold objective: to compute the EM background and to provide the first robust definition of EM anomalies in the ionosphere. In addition to its potential for identifying correlations with seismic activity, this definition can be extended to a broader range of applications, including anomaly detection associated with severe atmospheric or space weather events.

Chapter 2

Data and methods

In the present study, we used data from the first satellite of the China Seismo-Electromagnetic Satellite (CSES) constellation. In the following, after a brief description of the CSES mission and its main purposes, we discuss the data and methods used in this thesis.

2.1 CSES mission

The CSES mission is a collaboration between the China National Space Administration (CNSA) and the Italian Space Agency (ASI), which aims to obtain global data of the electromagnetic field, plasma and energetic particles in the top-side ionosphere and inner Van Allen radiation belts (Picozza et al. [212]). Furthermore, it aims at investigating ionospheric perturbations originated by electromagnetic sources external and internal to the geomagnetic cavity, cosmic rays, and solar events (Shen et al. [241]). In particular, the main objective of this space mission is to study lithosphere–atmosphere–ionosphere coupling mechanisms that induce ionospheric perturbations during active seismic conditions and to determine the features of such perturbations (Shen et al. [241]).

The first satellite of the constellation, CSES-01, was launched on February 2, 2018. It will be followed by CSES-02 (approved in 2018 and whose launch was initially planned within 2022, De Santis et al. [75], then postponed to the end of 2024) and by CSES-03 (around 2030, Zhima et al. [304]). According to the scientific objectives, CSES-01 payload includes the 9 following instruments:

- **Electric Field Detector (EFD)**, see Diego et al. [76];
- **Search-Coil Magnetometer (SCM)**, see Cao et al. [42];
- **High Precision Magnetometer (HPM)**, see Bingjun et al. [29] and Yang et al. [298];
- **Plasma Analyzer Package (PAP)**, see Liu et al. [170];
- **Langmuir Probe (LAP)**, see Liu et al. [170];
- **High-Energy Particle Detector (HEPD)**, see Picozza et al. [212];

- **High-Energy Particle Package (HEPP)**, see Li et al. [166];
- **GNSS Occultation Receiver (GOR)**, see Wang et al. [284];
- **Tri-Band Beacon (TBB)**, see Hengxin et al. [117];

Such instruments can measure the electric and magnetic field and various plasma parameters, such as electrons and ions temperatures and densities (for a complete description of CSES-01 payloads and measured physical parameters see Shen et al. [241]). All payloads are planned to work continuously in the region between -65° and 65° of latitude (Shen et al. [241]). Figure 2.1 shows the disposition of instruments on the satellite.

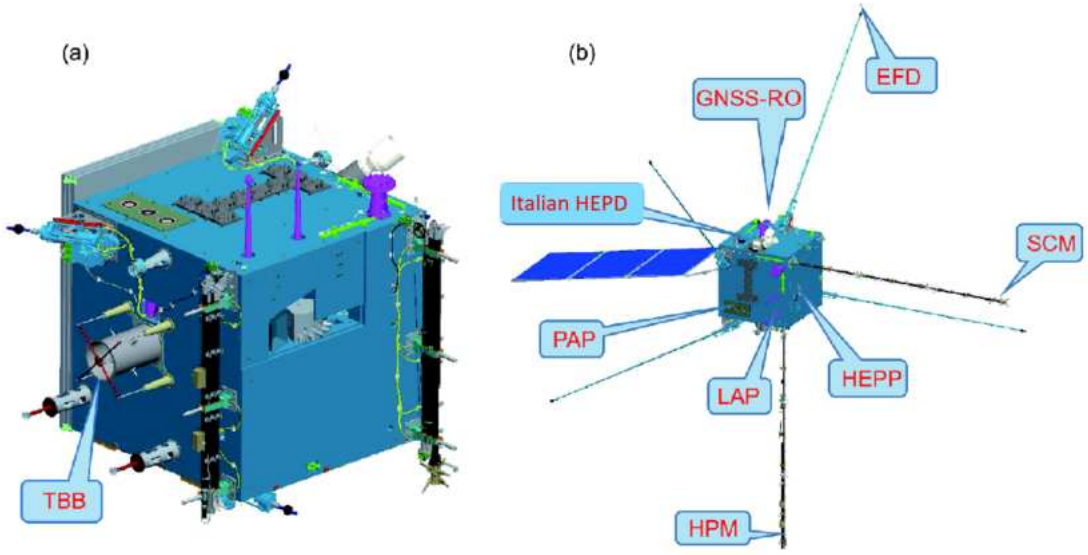

Figure 2.1: Launch a) and in-flight b) status of CSES-01 satellite (adapted from Shen et al. [241]).

The satellite is on a circular sun synchronous orbit (see Mortari, Wilkins, and Bruccoleri [192] for more details) at an altitude of $\approx$ 507 km and high orbital inclination of 97.4°. The distance between neighboring tracks is $\approx$ 2650 km in one day, and it is reduced to $\approx$ 530 km in the revisiting period of five days (Shen et al. [241]). CSES-01 flies 15.2 orbits around the Earth per day at $\approx$ 02:00 am (nightside) and 02:00 pm (dayside) in local time (LT) for descending (orbit path from north polar to south polar) and ascending (from south to north) half orbits data files, respectively (Zhima et al. [304]).

To date, one of the most important achievements of the mission is the CSES Global Geomagnetic Field Model (CGGM 2020.0, Yang et al. [298]), describing the Earth's magnetic main field and its linear temporal evolution. Such model has been validated by the International Association of Geomagnetism and Aeronomy (IAGA) and has been selected as one of 15 international candidate models for calculation of the 13th generation International Geomagnetic Reference Field (IGRF-13l, see Alken et al. [8] and Zhima et al. [304]). In addition, the mission accomplished remarkable results in identifying features of the ionospheric environment (e.g. Yan et al. [296]) and in the investigation of space weather processes (e.g. Piersanti et al. [215]).

2.1.1 CSES data

Analyses carried out for this thesis are based on EFD and SCM vector data within the geographical coordinate system. Since recent investigations (e.g. Zong, Tao, and Shen [306]) revealed that EM emissions associated with seismic activity are mainly found in the range from ≈50 to ≈300 Hz, the analysis has focused on the ELF band (≈1 Hz to 2.2 kHz; sampling rate: 5 kHz) for the electric field, and on the ULF band (≈1 Hz–200 Hz; sampling rate: 1024 Hz) for the magnetic field.

2.1.2 Electric Field Detector

Electric Field Detector (EFD) measures the electric potentials of four spherical sensors with reference to spacecraft (S/C) potential (Diego et al. [76]). The spheres are located at the end of four 4.5 meter long booms, and derives the electric field in the frequency range between about DC and 3.5 MHz (Huang et al. [129]). Its working principle is the active double-probe technique, in which the electric field components are obtained by the voltage difference between two probes divided by the distance d between the various probes pairs. Figures 2.2a and 2.2b shows the structure of EFD's spherical sensor probe and the scheme of its working principle respectively.

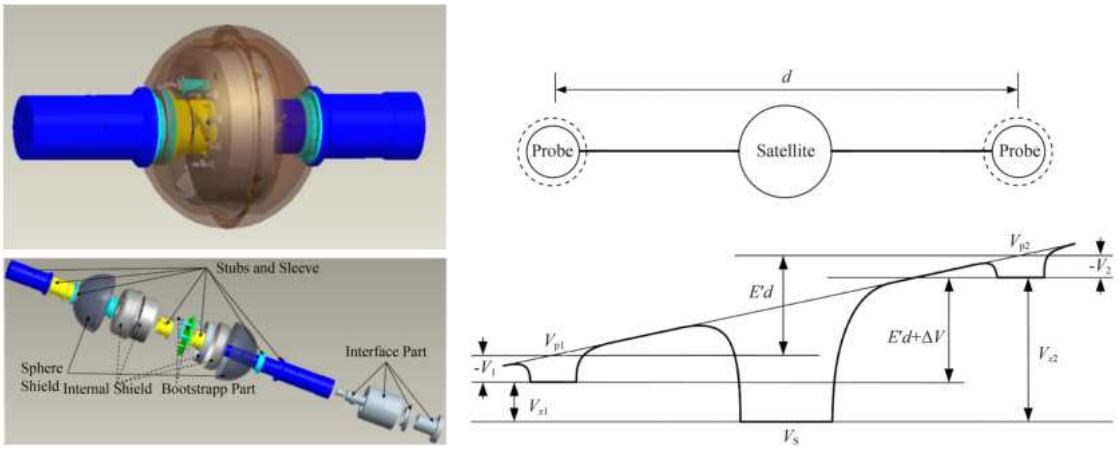

(a) (b)

Figure 2.2: Structure of the EFD's spherical sensor probe (a) and the scheme of its working principle (b). Credits: Huang et al. [129].

Figure 2.3 shows the EFD sensors position in the satellite orbit system X_S (flight direction), Y_S (orthogonal to the other two) and Z_S (directed from satellite to Earth), indicated by the red arrows. As can be seen, probe A lays in the X_S-Y_S plane (directed opposite to Y_S), probe B in the Z_S-X_S plane (directed at 45° between X_S and Z_S axis, probe C in X_S-Z_S plane and probe D in Z_S-Y_S plane.

Defining V_a, V_b, V_c and V_d as the probe potentials, the electric field components in the spacecraft reference frame are evaluated along the directions defined by the various sensors

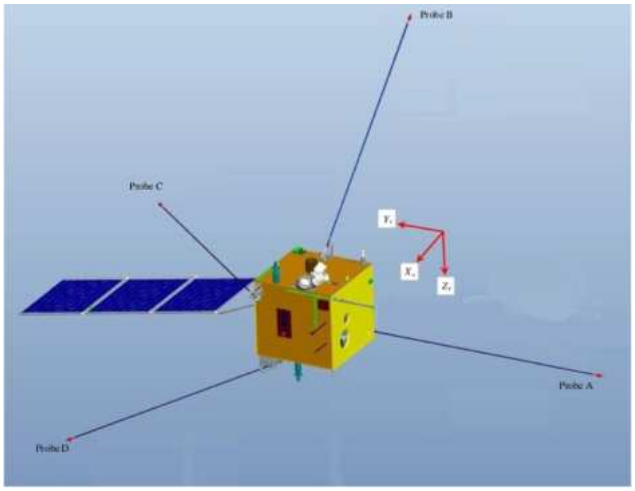

Figure 2.3: EFD probes orientation with respect to the satellite reference frame X_S, Y_S and Z_S (adapted from Huang et al. [129]).

pairs, from the voltage differences: $V_1 = V_a - V_b$, $V_2 = V_c - V_d$ and $V_3 = V_a - V_d$. Then, they are rotated into the geographical reference frame (X, Y and Z, see Huang et al. [129]).

The EFD purpose is to measure the three components of the ionospheric electric field over a broad frequency band (from DC to 3.5 MHz, Shen et al. [241]) with high sampling rates. The frequency range of EFD is divided into four sub-bands: Ultra Low Frequency (ULF), Extreme Low Frequency (ELF), Very Low Frequency (VLF) and High Frequency (HF), whose main characteristics are reported in table 2.1.

band	**sampling frequency (Hz)**	**frequency range (Hz)**
ULF	125	$DC - 16$
ELF	$5 \cdot 10^3$	$6 - 2200$
VLF	$5 \cdot 10^4$	$1.8 \cdot 10^3 - 2 \cdot 10^4$
HF	10^7	$1.8 \cdot 10^4 - 3.5 \cdot 10^6$

Table 2.1: Characteristics of EFD frequency bands.

EFD operates in two observation modes: survey and burst. The latter is activated for about 2 hours per day over seismic regions to increase data collection (see Shen et al. [241]). Specifically, in ULF and ELF bands, EFD collects waveform electric field data throughout the entire orbit in survey mode. In VLF band, survey mode provides only (Power Spectral Density) PSD, while waveform data are acquired exclusively in burst mode. Finally, in HF band, EFD operates exclusively in survey mode, providing PSD.

2.1.3 Search Coil Magnetometer

Search Coil Magnetometer (SCM) is a three axis search coil magnetometer that measures varying magnetic fluxes in the range 10 Hz - 20 kHz (Cao et al. [42]). Since the satellite generates

magnetic field disturbances, search coil sensors are mounted at the end of a boom that extends outside of the satellite (see Cao et al. [41]). The sensor of SCM is made of three orthogonal cores in permalloy, which is an high permeability material. All cores are wound by a main coil with 12000 turns of copper wire and a secondary coil with tens of turns providing a flux feedback (Cao et al. [42]). In this way, when a time-varying magnetic field passes through the coil, a time-varying voltage V is induced due to Faraday's law of magnetic induction. Specifically:

$$V_i = \mu_e N S \frac{dB}{dt} \tag{2.1}$$

where μ_e is the effective permeability of the core, N is the number of turns of the main coil, S is the cross-sectional area of the core, $\frac{dB}{dt}$ is the time variation of the magnetic field component parallel to the coil axis and i represents the three possible direction x, y, z.

The frequency range of 10 Hz–20 kHz is divided into the three sub-bands shown in table 2.2.

band	sampling frequency (Hz)	frequency range (Hz)
ULF	1024	$10 - 200$
ELF	$10.24 \cdot 10^3$	$200 - 2200$
VLF	$5.12 \cdot 10^4$	$2.2 \cdot 10^3 - 2 \cdot 10^4$

Table 2.2: Characteristics of SCM frequency bands.

SCM has two operation modes too: survey and detailed survey. The latter is switched on over main seismic regions on Earth, where SCM will output the waveform data over the whole frequency range. Elsewhere, SCM operates in survey mode, emitting data of the waveforms only in ULF and ELF bands and the PSD data in VLF band.

2.2 Geomagnetic data

One of the purposes of this study is to assess the impact of solar activity on the detection of anomalies. In order to give a measure to the signature of the response of the Earth's magnetosphere and ionosphere to solar forcing, space and Earth scientists usually refer to geomagnetic indices, which are proxies of geomagnetic disturbances observed on the ground. They are a measure of geomagnetic activity, which is a signature of the response of the Earth magnetosphere and ionosphere to solar forcing Menvielle et al. [184].

Geomagnetic conditions at mid/low latitudes are usually measured by the Disturbance storm time (Dst) and $\mathrm{SYM-H}$ indices (see, for example Lakhina and Tsurutani [159]). They both are a measure of the symmetric ring-current intensity (Iyemori [136]), but $\mathrm{SYM-H}$ is computed at higher time resolution (1 min) than Dst (1 h). In this work, $\mathrm{SYM-H}$ is employed to label days monitored for background calculation as quiet, disturbed, or storm. $\mathrm{SYM-H}$ data rely on the use of several magnetometer stations to calculate the symmetric portion of the horizontal component of the magnetic field near the equator (see Wanliss and Showalter [289] for details). Data utilized in this thesis were obtained from the OMNI

database, a comprehensive resource widely employed by the space weather research community (https://cdaweb.gsfc.nasa.gov/index.html). OMNI is a multi-source compilation of solar wind data, interplanetary magnetic-field data, solar and geomagnetic indices, energetic particle fluxes (Papitashvili and King [205]).

In this study, an average $\mathrm{SYM-H}$ value ($\overline{\mathrm{SYM-H}}$) and the standard deviation ($\mathrm{SYM-H_{SD}}$) are calculated for each day. The days are classified as follows:

$$I_Q : \overline{\mathrm{SYM-H}} \pm \mathrm{SYM-H}_{SD} \in [-10\ \mathrm{nT}, 10\ \mathrm{nT}]$$

$$I_D : \overline{\mathrm{SYM-H}} \pm \mathrm{SYM-H}_{SD} \in [-40\ \mathrm{nT}, -10\ \mathrm{nT}]$$

$$I_S : \mathrm{otherwise}$$

where I_Q, I_D and I_S mark quiet, disturbed and stormy days, respectively.

Compared to what is commonly found in the literature (e.g., Bertello et al. [25]), the selected intervals are much more stringent, which ensures that quiet days are effectively clear from any solar perturbation, and that disturbed days only include low-intensity solar disturbances. It is important to stress that slight variations in the bounds of any interval ($\pm$ 10 nT) do not significantly impact background evaluation, due to the effect of averaging over the entire cluster of days included in each interval.

2.3 Non-stationary signal analysis

A critical problem in data analysis of geophysical measurements is how to extract the main components and useful characteristics from them. In fact, a geophysical signal is often characterized by dynamic changes in time-frequency contents and therefore appears as a complex time-varying process. Thus, a technique that combines the time and frequency analysis and shows the signal evolution in both time and frequency is required to extract the signal components and capture the useful characteristics associated with them.

Over the last decades many techniques and approaches for time-frequency analysis and signals decomposition have been developed. Complex signals are usually decomposed in a superposition of simpler ones in order to be analyzed. The common approaches are based on Fourier analysis (Stein and Shakarchi [248]) or wavelets (Mallat [178]), which are well known to be not suitable for non-stationary signals (Cicone and Zhou [60], Piersanti et al. [216]). However, geophysical signals are, in general, strongly non-stationary. For this reason, alternative methods have been proposed recently, such as the Hilbert–Huang transform (HHT) technique (Huang et al. [130]), which comprises two primary steps. The first one is the signal decomposition via the empirical mode decomposition (EMD) method, which decompose the signal into components called "Intrinsic Mode Components" (IMCs). Such components are oscillatory function fulfilling two properties: the number of the extrema and the one of the zero crossings of an IMC must be equal or differ at most by one; at any point of an IMC, the mean value of the envelopes defined by the local extrema is zero (Cicone [56]). The second step is the

determination of the instantaneous frequency via the Hilbert Spectral Analysis (HSA, Huang et al. [130], Huang et al. [130], Lin, Wang, and Zhou [169] and Bendat and Piersol [24]).

The application of EMD and HSA led to the determination of hidden features of non-stationary signal in many fields, such as biology, medicine, geology, astronomy, engineering, geophysics, economics (for a partial list of successful applications of these techniques see references of Cicone and Zhou [61]). However, building a mathematical foundation remains a big challenge in the study of EMD and HSA. Indeed, the sifting algorithm, which is the basis of the EMD process and connects the local maxima and minima using cubic spline to form the upper and lower envelops, is unstable and there is no mathematical proof for its convergence (Lin, Wang, and Zhou [169]).

2.3.1 Fast Iterative Filtering

To address the mathematical issues, the so-called Iterative Filtering (IF) has been proposed in 2009 by Lin, Wang, and Zhou [169]. Such a technique establishes rigorous mathematical criteria for convergence under certain conditions (the mathematical analysis of IF has been addressed by several authors in recent years, see e.g. Cicone [55], Cicone and Dell'Acqua [57], Cicone, Liu, and Zhou [58], Huang, Yang, and Wang [128], Wang, Wei, and Yang [285], Wang and Zhou [286]). Instead of using the envelopes generated by splines, it involves a moving average to replace the mean of the envelops. The complete numerical analysis of the IF has been proposed by Cicone and Zhou [61] in 2021. The authors demonstrated that the IF algorithm convergence is guaranteed *a priori*. Furthermore, assuming a periodical boundary extension of a signal, the IF can be implemented on a computer using the Fast Fourier Transform (FFT). The derived method, known as Fast Iterative Filtering (FIF), is faster than EMD (Cicone [55]) and has been successfully used to extract features from many kind of signals in several fields (e.g. Ghobadi et al. [104], Chen et al. [49], Piersanti et al. [214], Reddy et al. [226], Myat et al. [194], Wang et al. [287], Sharma, Shedsale, and Sharma [240]). For its strengths, we used the FIF algorithm to decompose signals (in this case the three components of electric and magnetic field) and extract significant features from it.

Briefly, given a multidimensional signal $f(t)$, IF decomposes it into N IMCs so that:

$$f(t) = \sum_{l=1}^{N} IMC_l(t) + r(t) \tag{2.2}$$

where N is the number of the obtained IMCs, $IMC_l(t)$ is the l-th IMC and $r(t)$ is the residue of the decomposition. Each IMC_l is given by an iterative application of a low-pass filter which extract the moving average of the signal at a temporal scale τ_l, with the aim of isolating a fluctuating component with average spatial frequency $\omega_l \simeq 2\pi/\tau_l$. Value of τ_l is different for any IMC and it's increasing with l: so as l increases, IMCs will contain smaller frequencies.

Figure 2.4 shows an example of FIF decomposition applied to electric field data. The blue line represents the original signal, the red dashed line represents the baseline, and fluctuations (obtained by subtraction of the baseline from the original signal) are reported in black.

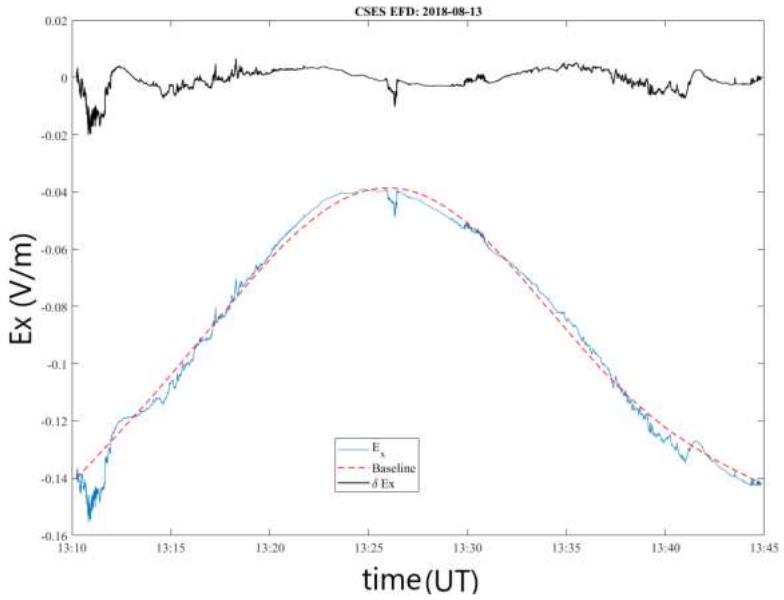

Figure 2.4: Application of the FIF technique to electric field data (expressed in V/m) from the CSES-01 satellite along an example orbit on Aug 13, 2018. The blue line represents the real signal, the red dashed line is the baseline, while fluctuations are shown in black.

The relation between each IMC and the l scale of variability for the $f(t)$ signal is analyzed using the technique proposed in Flandrin [85]. Precisely, a signal marked by robust scale separation can be expressed as the sum of a baseline $f_0(t)$ and the variation $\delta f(t)$ from the baseline:

$$f(t) = f_0(t) + \delta f(t). \tag{2.3}$$

Here, $\delta f(t)$ is identified by application of the method described by Alberti et al. [4]:

$$\delta f(t) = \sum_{l=1}^{k} IMC_l(t), \tag{2.4}$$

where k is a subset of the N modes, and l is the scale of variability. In this way, it is possible to obtain a reconstruction of a subset of modes characterized by fluctuations at higher frequency and standardized mean SM ≈ 0 (SM being the mean divided by the standard deviation).

In our analysis, l represents the frequency of any IMC for either the electric or magnetic field components.

2.3.2 Multiscale statistical analysis

Measured data from complex and multivariate processes (such as many geophysical processes) inherently exhibit multiscale characteristics due to the contributions of events occurring across various temporal and spatial scales (Bakshi [17]). In fact, effects such as spikes, drifts and variance shifts may occur in such processes at different times and frequencies, making the resulting process data multiscale (Ganesan, Das, and Venkataraman [97]). Consequently, data analysis and modeling methods that represent the measured variables at multiple scales are better suited for extracting information from measured data than methods that represent the variables at a single scale.

For this reason, we have performed multiscale statistical analysis on the IMCs. Specifically, at each frequency scale l we have calculated and studied the relative energy ϵ_{rel}:

$$\epsilon_{rel}(l,t) = \frac{\int_l |IMC_l(t)|^2 dt}{\int_l |f(t)|^2 dl} \tag{2.5}$$

which represents the ratio of the energy corresponding to a specific time to the total energy over the whole time interval. The relative energy is then investigated as a function of the frequency and satellite latitude, through the study of ϵ_{rel}-latitude-frequency spectra for the three components of the electric and magnetic field.

As showed in chapter 3, the analysis of the ϵ_{rel} is the milestone of the ionospheric electromagnetic characterization and the anomaly detection.

2.3.3 Cross-covariance

Since the electric and magnetic field signals are not synchronized due to the different hardware and software implementation between EFD and SCM (Zhima et al. [305], Yang et al. [297]), for a joint electric and magnetic field analysis it is necessary to realign the EFD and SMC measurements. To this purpose, we relied on the cross-covariance, which is a measure of similarity of two signals (see e.g. Park, Park, and James [209]).

The cross-covariance sequence of two signals x_n and y_n is given by (see e.g. Chen, Genton, and Sun [52], Larsen [162]):

$$\phi_{xy}(m) = \mathrm{E}(x_{n+m} - \mu_x)(y_n - \mu_y)* \tag{2.6}$$

where μ_x and μ_y are the mean values of the two stationary signals, the asterisk denotes complex conjugation, and E is the expected value operator.

2.3.4 Principal Component Analysis

To identify the direction of main oscillations of the electric and magnetic field, we performed a principal component analysis (PCA). PCA is a technique used for reducing the dimensionality of large datasets, enhancing interpretability while preserving as much information as possible (see e.g. Jolliffe [138]). It is defined as an orthogonal linear transformation on a real inner product space. Such transformation leads to the definition of a new coordinate system whose basis are the new variables, called principal components, that are linear combinations of the

original variables and uncorrelated with each other. The new coordinate system is obtained in a way that the maximum variance by some scalar projection of the data lies on the first coordinate (first principal component), the second greatest variance on the second coordinate, and so on (Jolliffe [138]).

In the standard case, finding such new variables is equivalent to solving an eigenvalue/eigenvector problem (Jolliffe and Cadima [139]). Consider a $p \times n$ data matrix $\mathbf{X}$, whose j_{th} column corresponds to the n observations on the j_{th} variable ($\mathbf{x_1}, \mathbf{x_2}, \ldots, \mathbf{x_n}$). The goal is to find the linear combination of the $\mathbf{X}$ columns that maximizes the variance. Being $\mathbf{a}$ a vector of constants $a_1, a_2, \ldots, a_n$, the linear combination is given by:

$$\mathbf{Xa} = \sum_{j=1}^{n} a_j \mathbf{x_j} \tag{2.7}$$

The variance of such linear combination is given by $var[\mathbf{Xa}] = \mathbf{a'Sa}$, where $\mathbf{S}$ is the covariance matrix associated with the dataset. Therefore, we seek the dimensional vector $\mathbf{a}$ which maximizes the quadratic form $\mathbf{a'Sa}$. The problem is equivalent to maximizing $\mathbf{a'Sa} - \lambda(\mathbf{a'a} - \mathbf{1})$, where λ is a Lagrange multiplier (Jolliffe and Cadima [139]). Differentiating with respect to $\mathbf{a}$, and equating to the null vector, we obtain:

$$\mathbf{Sa} = \lambda \mathbf{a} \tag{2.8}$$

It follows that $\mathbf{a}$ must be an eigenvector, and λ the corresponding eigenvalue, of the covariance matrix $\mathbf{S}$. In particular, we are interested in the largest eigenvalues, $\lambda_1, \lambda_1, \ldots, \lambda_m$ and the corresponding eigenvectors, with $m < n$. In this way, it is possible to summarize most of the "variation" contained in the original set of n variables using a subset m of principal components.

For a complete description of the PCA, the reader may refer to Greenacre et al. [110], Naik [195], Kong, Hu, and Duan [155], Gray [109].

Chapter 3

The characterization of the ionosphere

The identification of ionospheric disturbances in connection to strong earthquakes requires a preliminary robust characterization of the ionospheric background, where the background embeds all the ionospheric features in the absence of any possible external (e.g., transient changes in solar activity, interplanetary plasma and magnetic field conditions...) and internal (atmosphere and lithosphere) inputs. In this frame, a proper characterization of the ionosphere must take into account all temporal scales on which the ionosphere usually varies: medium-long term trends (from seconds to years) and short-time trends (less than one second).

3.1 Medium-long term signals: the ionospheric background

The calculation of the ionospheric EM background is based on the analysis of the ϵ_{rel}-latitude-frequency spectra obtained as described in section 2.3.1. Such a spectrum is generated for all the CSES-01 orbits crossing a square cell centered on a region on the Earth's surface. In this way, the cell encloses the portion of the ionosphere under analysis, which is the projection of the geographical region of the surface embedded by the cell.

3.1.1 Ionospheric background: calculation

In order to compute the background, all the orbits flying over the considered cell are taken into account for the multiscale analysis described in chapter 2. For each orbit satisfying such condition, a latitude-frequency vs. ϵ_{rel} spectrum is computed. Then, the ionospheric background is defined as the average of all the spectra.

It is important to underline that, in order to take into account the spectral differences between the orbits (generally both frequencies and latitudes change from orbit to orbit), we remapped all the dataset in a proper grid, constructed according to the following steps:

1. defining as lat_C and lon_C the geographical coordinates of the center of the cell and as L_G the length of the side of the cell;

2. adopting a linear spacing for latitudes. Specifically from $lat_C - L_G/2$ to $lat_C + L_G/2$ with 0.1 spacing. This spacing represents a good compromise between dense (implying an high number of null values) or sparse (leading to a shoddy interpolation) grid.

3. adopting a logarithmic spacing for frequencies. Since the frequency values span several orders of magnitude and the lowest frequencies retain most of the energy, the logarithmic spacing allows the best resolution of the spectra.

4. The number of frequencies for the final grid is chosen as the average of the number of IMCs in each orbit. This guarantees, on average, a single value for each point of the grid.

This procedure allows to obtain a $m \times n$ (latitudes $\times$ frequencies) grid on which to interpolate the ϵ_{rel} from each orbit on every grid point. The remapping process requires a minimum number of existing values on the original grid (i.e. a minimum value of IMCs and a minimum number of latitudes). Through a deep investigation based on the analysis of tens of thousands of orbits, we fixed this number to 18. This implies that orbits having existing values on the original grid < 18 were excluded from the background computation, because of the impossibility of a proper comparison with the other orbits. Even if such threshold implies the discharge of $\approx 10\%$ of the data-set, the analysis is not affected since the number of orbits included in the final procedure is of the order of hundreds.

Since the ionosphere exhibits different characteristics depending on latitude, time of the day, solar activity... (as described in chapter 1), it is necessary to define various background spectra. The latitudinal variation is included in the procedure through the selection of a specific geographical region on which the background calculation is performed. In order to take into account differences between a diurnal and a nocturnal ionosphere, we performed the background calculation distinguishing between diurnal and nocturnal orbits. Furthermore, the ionospheric variability induced by the variation in the solar activity is considered by the discrimination between orbits occurring during quiet, disturbed and stormy days. Such discrimination is carried out using the SYM-H index, as detailed in section 2.2.

This results in the nine ionospheric backgrounds, including all the ionospheric conditions, summarized in table 3.1. Downstream of these selections and calculations, the obtained background will include only EM observations whose origins are geographically close to the region of interest.

3.1.2 The effect of the cell size

The background calculation is influenced by the choice of cell size, which is not trivial. Indeed, it is the result of the balance between two conflicting objectives: from on side, the aim of calculating a local background that is free from effects due to ionospheric geographical variations, on the other side, the need for a large number of good observations. In principle, a smaller cell provide a more accurate background on the specific region we are interested in; however, it involves two problems. First, the number of orbits crossing the cell decreases with the square of the side, leading to a poorer statistics in the average background computation. Secondly, it leads to border effects, since with a smaller cell a large fraction of the orbits cross the cell only for a small portion of their trajectory.

	Background	Orbits considered
1	ALL	All orbits flying over the geographical cell
2	QUIET	Orbits relative to quiet days
3	DISTURBED	Orbits relative to disturbed days
4	DIURNAL	Diurnal orbits
5	NOCTURNAL	Nocturnal orbits
6	QUIET DIURNAL	Diurnal orbits relative to quiet days
7	QUIET NOCTURNAL	Nocturnal orbits relative to quiet days
8	DISTURBED DIURNAL	Diurnal orbits relative to disturbed days
9	DISTURBED NOCTURNAL	Nocturnal orbits relative to disturbed days

Table 3.1: Summary of the various generated backgrounds. All types of ionospheric conditions are considered.

To better clarify these two problems, we will show how the effect of the geometry of the satellite's trajectory can lead to a poor statistics and how the border effects can affect the background spectra.

As an example, we reported in figure 3.1 the CSES-01 orbits in and close to a $3^\circ \times 3^\circ$ geographical cell centered on the coordinates 18 °N, 73 °W. As can be seen in figure 3.1a, due to the not uniform satellite coverage, the number of orbits crossing the cell is low, which implies a poor statistics in the background calculation. In addition, in figure 3.1b, it is possible to appreciate how a considerable number of these orbits cross the cell only for a small fraction of their trajectory. Hereafter, we will refer to these orbits as *border orbits*.

The border orbits produce a spectrum such as the one showed in figure 3.2a. Since (as described in details in section 3.1.1), the ionospheric background is the average value of all the observations on a cell, a large number of border orbits may lead to undesired border effects in the background calculation. An example of these effects are shown in figure 3.2, which illustrates the background for a cell containing a large number of border orbits.

As can be seen, the inclusion of border orbits generates artefacts that mimic the presence of a specific signal only in a portion of the cell.

In order to overcome these problems and to automatize the procedure, we included a weight function in the average calculation of the ionospheric background. This weight function is based on the number of points of the satellite's trajectory enclosed by the cell; it exponentially goes from 0 for an orbit with a single point in the cell, to 1 for the full orbit. In this way, border orbits have negligible effects in the average calculation.

In addition, we tested different choices of cell size, from $1^\circ \times 1^\circ$ to $6^\circ \times 6^\circ$. As summarized in table 3.2, the optimum choices are $3^\circ \times 3^\circ$ to $6^\circ \times 6^\circ$ depending on the satellite's coverage.

3.1.3 Ionospheric background: investigation of the seismic activity

The procedure described in the previous sections ensures a proper characterization of the ionospheric environment in the desired conditions. If a detected signal differs in a statistically significant manner from the background is worthy of consideration for further analysis regarding

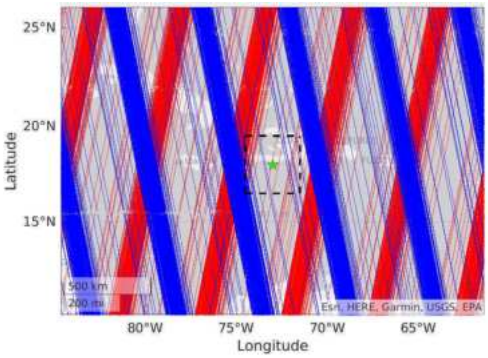

(a) All the satellite's orbits in the region of interest.

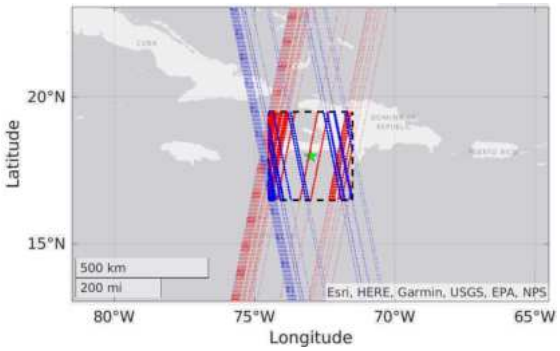

(b) Orbits selected. The portion of the orbit crossing the cell is represented with a ticker line.

Figure 3.1: Two different representations of the satellite's orbits around the geographical cell centered on the coordinates 18 °N, 73 °W (green star). Diurnal orbits are represented in red, nocturnal orbits in blue. The black dashed line indicates a 3 ° (in latitude-longitude) square cell surrounding the selected point.

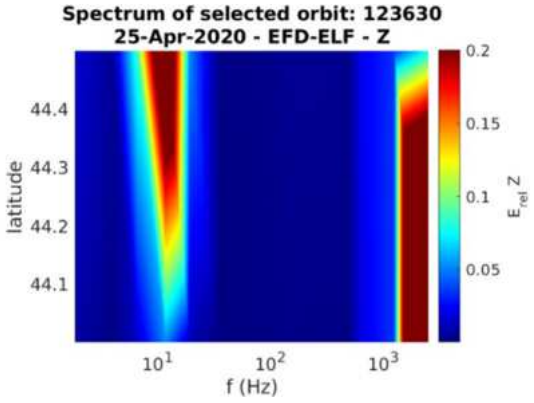

(a) Spectrum for the X component of the electric field regarding a single border orbit.

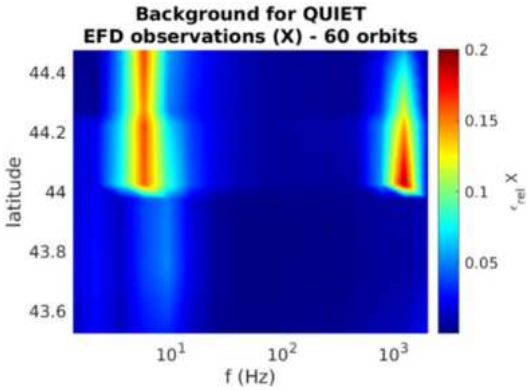

(b) Background spectrum for the X component of the electric field for a cell containing a large number number of border orbits.

Figure 3.2: Border effects in the background calculation.

Size	Results
$1^\circ \times 1^\circ$	This is not an optimal choice. Too few orbits selected and a large fraction of them are border orbits.
$3^\circ \times 3^\circ$	This could be a good compromise between geographical precision and orbits selection. However, if the center of the cell is on a region without a good coverage, border effects can still be present.
$6^\circ \times 6^\circ$	This is a safe choice: always a large number of selected orbits and no border effects. The disadvantage is the poor geographic precision.

Table 3.2: Cell's size and relative effects.

possible correlations to anomalous events. In particular, the background calculation can be used to detect possible signals connected to seismic activity.

A set of maps depicting ionospheric EM background over seismic regions has been generated using CSES-01 electric and magnetic field observations from 2019 to 2023. Every background map has been compared 1 to 1 with ionospheric conditions occurring in the closest (in time and space) observation to the earthquake. This comparison allows us to detect signals which could differ from the typical ionospheric features.

For our analysis, we chose earthquakes that occurred recently, thus matching CSES-01 data availability and events occurred under very different geomagnetic conditions, which enables an assessment of the role of solar forcing in this type of analysis.

In the following paragraphs, we will describe the ionospheric backgrounds obtained for different cells, analyzing also signals that could eventually emerge from the background in the proximity of the earthquake. For the reader's convenience, all the figures regarding the Cretan, Vanuata and Marche region are reported in appendix A.

Case event: 14 August 2021 - Haiti

On 14 August 2021, at 12:29:08 UTC, an earthquake struck the Tiburon Peninsula of Haiti, 150 km west of the capital Port-au-Prince. The magnitude of the event was 7.2 MW at EE geographical LAT-LON coordinates 18.417°N, 73.480°W (for further details on this seismic event, see D'Angelo et al. [72] and reference therein).

Following the procedure described in Recchiuti et al. [225], we have computed the ionospheric backgrounds for a geographical $6^\circ \times 6^\circ$ cell centered on the EE. The backgrounds for quiet and disturbed geomagnetic conditions are shown in figure 3.3 and 3.4, respectively. In each of these figures, the ϵ_{rel} spectrum (color scale: ϵ_{rel} intensity) is reported as a function of frequency and geographic latitude. Panel a) shows the E_x (geographic north-south) component, panel b) the E_y (east-west) component, and panel c) the E_z (vertical) component.

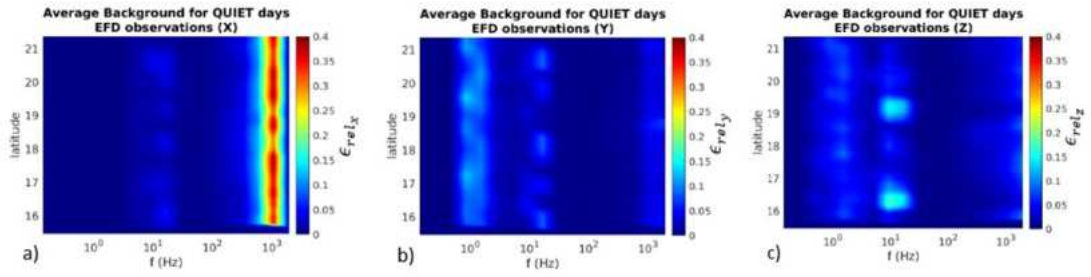

Figure 3.3: Ionospheric background for quiet conditions for a $6^\circ \times 6^\circ$ cell over Haiti, in terms of ϵ_{rel} intensity as a function of latitude and frequency for the three components of the electric field (E_x, E_y, E_z from left to right).

By comparing figures 3.3 and 3.4 it can be easily seen that "quiet" and "disturbed" spectra reveal activity in the same frequency bands, but with different energetic content (lower in the former case). In particular, the following frequencies emerge from both spectra:

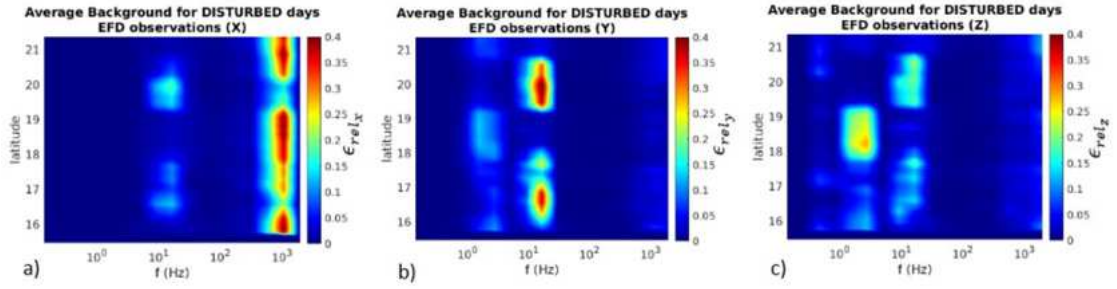

Figure 3.4: Ionospheric background for disturbed conditions expressed as ϵ_{rel} intensity vs. latitude (depending on time) and frequency for the three components of the electric field. ϵ_{rel} values are generally larger than in the quiet case, but EM activity covers the same frequency bands.

- $\approx$ 2 Hz (E_y, E_z): due to the $\mathbf{v} \times \mathbf{B}$ electric field present in the ELF band, caused by satellite motion into the geomagnetic field (see e.g. Diego et al. [76]);
- $\approx$ 8 and $\approx$ 15 Hz (E_x, E_y, E_z): first and second Schumann ionospheric resonances at CSES-01 orbit (see Rodríguez-Camacho et al. [229]);
- $\approx$ 1 kHz (E_x): signature of the plasmaspheric hiss (Tsurutani et al. [263], Malaspina et al. [177]).

Background spectra in figures 3.3 and 3.4 have been compared with the one closest to the earthquake (occurring on Aug 14, 2021, 6 hours before the earthquake), which is shown in figure 3.5.

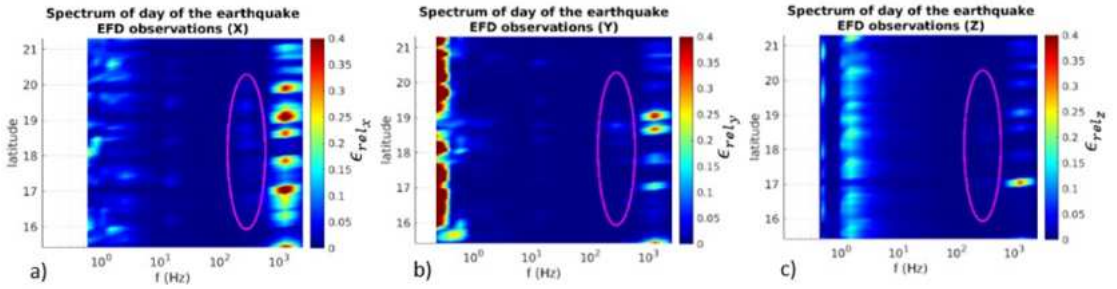

Figure 3.5: Spectra of Aug 14, 2021, six hours before the earthquake, on the same 6° $\times$ 6° LAT-LON cell considered for background spectra. In addition to the $\approx$2 Hz and $\approx$1 kHz peaks present in background spectra, another signal can be detected at 250 $\pm$ 70 Hz (especially in the x and y components).

As it can be seen from figure 3.7, showing the SYM-H values for August 14, 2021 and referring to the SYM-H thresholds defined in chapter 2, the day when the EQ occurred was a disturbed one.

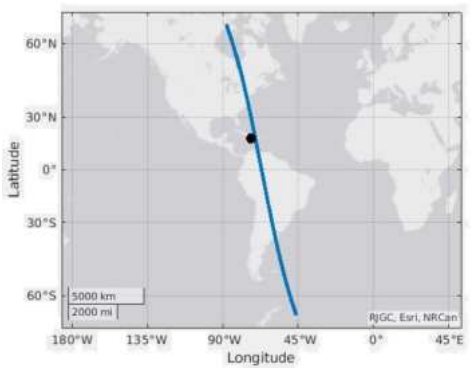

Figure 3.6: CSES-01 orbit (blue line) flying over the EE on Aug 14, 2021, 6 hours before the earthquake. The black point represents the EE.

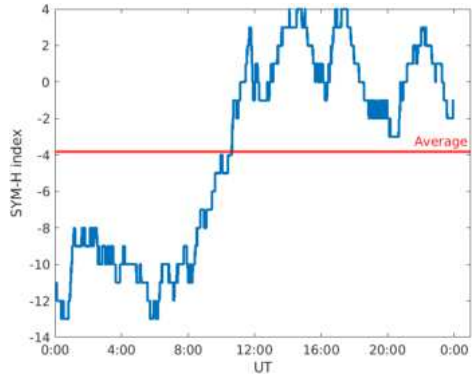

Figure 3.7: SYM-H index for Aug 14, 2021. Following the procedure described in section 2.2, this day can be classified as disturbed, in spite of SYM-H going slightly below 10 nT for a few hours.

Comparing figure 3.5 to figure 3.4, signals at 2 Hz, 8 Hz, 15 Hz and 1 kHz appear in both sets. An additional signal at ≈250 ± 70 Hz (enclosed in magenta ellipses) appears in figure 3.5 along the three components (more clearly in the x and y components).

The homologous analysis (figure 3.8) has been repeated for the local magnetic field along the geographic North-South (B_x), East-West (B_y) and vertical (B_z) components. In this case, the $\overline{\epsilon_{rel,SCM}}$ background spectra clearly show the signature of the second Schumann resonance at ≈16 Hz.

Figure 3.9 shows the relative energy of SCM observations on Aug 14, 2021, six hours before the earthquake, where the second Schumann resonance clearly appears in all components. An additional peak is detected in the same frequency band as already observed in EFD data ($\approx 190 \pm 60$ Hz, enclosed in magenta ellipses), especially for the z component.

Case event: Sept 27, 2021 - Crete (Greece)

A 6.0 M_W earthquake struck Crete (Greece) on September 27, 2021, at 06:17:22 UTC. As described in Recchiuti et al. [225], the EE was located at (35.252°N, 25.260°E) and the day is classified as disturbed (referring to figure A.3, showing the SYM-H for that day, and the thresholds defined in chapter 2). The same analysis as the one reported in the preceding paragraph has been performed. The environmental background obtained under disturbed conditions is shown in figure A.1. CSES-01/EFD observations for Sept 27, 2021 appear in figure A.2. The satellite flew in the proximity of the EE about 17 hours before the earthquake (figure A.3). As it is

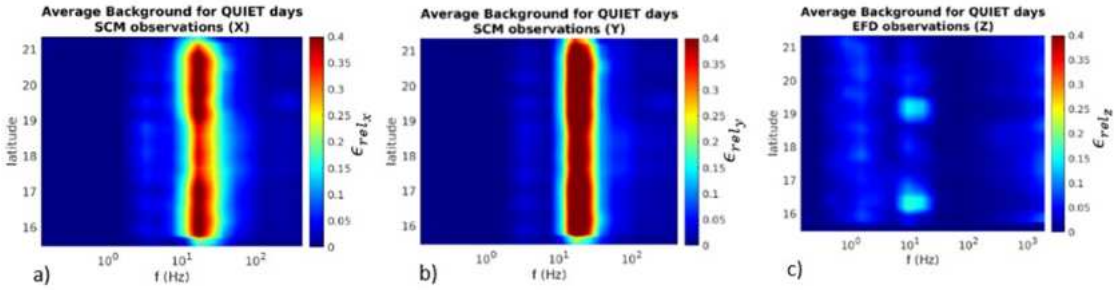

Figure 3.8: CSES-01/SCM observations. Environmental background evaluated in a 6° × 6° cell centered over the EE, in terms of $\overline{\epsilon_{rel}}$ intensity vs. latitude and frequency for disturbed conditions).

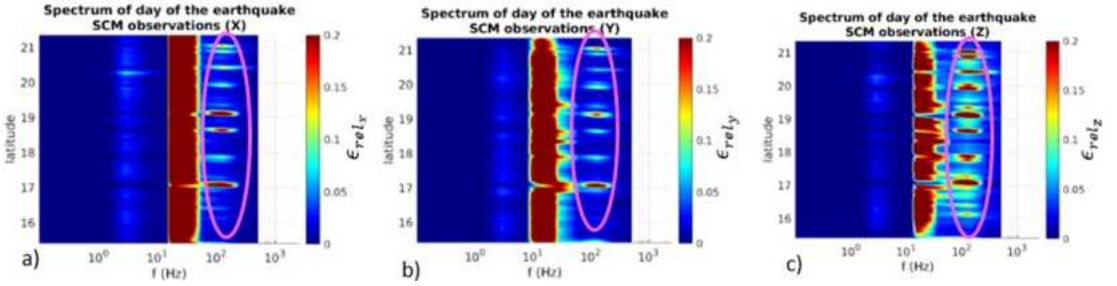

Figure 3.9: CSES-01/SCM observations on August 14, 2021, six hours before the event, when the satellite flew over the EE. In addition to the second Schumann resonance, another signal appears with more evidence in the z component.

visible, the background spectra include the ≈2 Hz signature due to satellite motion into the geomagnetic field, the Schumann resonance at ≈15 Hz, and the plasmaspheric hiss at ≈1 kHz.

Both figures A.1 and A.2 retain ionospheric signals at ≈2 Hz, ≈15 Hz and ≈1 kHz. Yet, a higher level of noise can be recovered in figure A.2 with respect to the seismic event in the first test, and high activity at very low frequency (< 1 Hz). This is caused by dominant external (solar) forcing, as highlighted by the algorithm classifying the day as stormy (figure A.4).

The same considerations hold for magnetic field observations (not shown). In general, nothing significant emerges from the comparison between average background spectra and observations closely prior to EQ.

Case event: July and August 2020 - Vanuatu (Melanesia)

The ionospheric background has been calculated over a cell centered on the point [15° S, 168° E], corresponding to the island country of Vanuatu in Melanesia. We selected this region because it is frequently interested by strong seismic activity. In this case, since the satellite guarantees a good coverage over this region, we opted for a 3° × 3° cell. Figures A.5, A.6 and A.7 show respectively the background for all the ionospheric conditions for x, y and z components of EFD-ELF observations. Each figure is made up of nine panels, one for every background condition considered in table 3.1.

As mentioned, the region is affected by intense seismic activity and dozens of earthquakes with $M_W > 5$ were registered during the period of CSES-01 data availability. In particular, the two strongest earthquakes that occurred in this region in the considered period were registered on July 31, 2019 and on August 05, 2020; both with a magnitude of $M_W = 6.4$. The closest available observations to these events are orbit 084190 on August 10, 2019 and orbit 138150 on July 30, 2020, respectively. They are both diurnal orbits occurring during disturbed conditions, so the appropriate background to be considered is the disturbed diurnal, represented in panels f) of figures A.5, A.6 and A.7.

The EFD-ELF spectra of these two orbits are shown in figures A.8 (August 10, 2019) and A.9 (July 30, 2020). In both, a signal at ≈ 400 ± 120 Hz is detected, on X and Z components in the former and on all the components in the latter. In this frequency band, the diurnal disturbed backgrounds of all components show no activity at all.

Case event: November 2022 - Marche (Italy)

The same approach was applied on a 3° × 3° cell (the satellite coverage is good) centered over central Italy, on the Adriatic coast ([44 ° N, 13 ° E]). This region has been affected by several earthquakes with $M_W > 3.5$ during late 2022 and early 2023, with the strongest earthquake occurred on November 9, 2022, and having $M_W = 5.6$.

Figures A.10, A.11 and A.12 show the 9 different EFD-ELF backgrounds obtained for x, y and z components respectively.

Figure A.13 shows the one to one comparison between observations of November 21, 2022 (orbit 266510, the closest to the strongest earthquake) and the appropriate background, which is disturbed diurnal. Here, left panels show the observations of orbit 266510 and the right panels the background for diurnal disturbed orbits (from top to bottom x, y and z components).

From this comparison, an intense signal at ≈ 80 Hz appears on the X component, without any counterpart on the background.

3.1.4 A robust definition of an anomalous signal

The procedure described in section 3.1, allowed to identify signals emerging from the background. In order to give a robust characterization of these signals, we analyzed the probability distribution function (PDF) of ϵ_{rel} at the detected frequency. Specifically, we compared the ϵ_{rel} PDF with and without the observations closest (in time) to the earthquake. Such procedure allows to distinguish between rare and anomalous events.

A "rare" event, while falling within the tail of the distribution (and thus defined as rare), is still considered to follow the distribution of events usually observed. Consequently, the inclusion of a rare event in the calculation of the observed distribution would not materially alter the shape of the distribution.

In contrast, an "anomalous" event is one that deviates from the distribution of events usually observed. Measurements derived from anomalous events would distort the shape of the observed distribution. This is the case exemplified in figure 3.10, which displays the ϵ_{rel} PDF at the frequency identified in the case event of Marche (80 $\pm$ 30 Hz). Panel a) shows the PDF representative of the usual conditions, which does not include the closest observations to the earthquake. In the PDF shown in panel b), these observations have been included. As highlighted by the magenta ellipse, the measurements obtained from the orbit closest to the earthquake change the shape of the observed distribution, and thus they do not belong to that original distribution. So, the identified signal could be defined as anomalous with respect to the background.

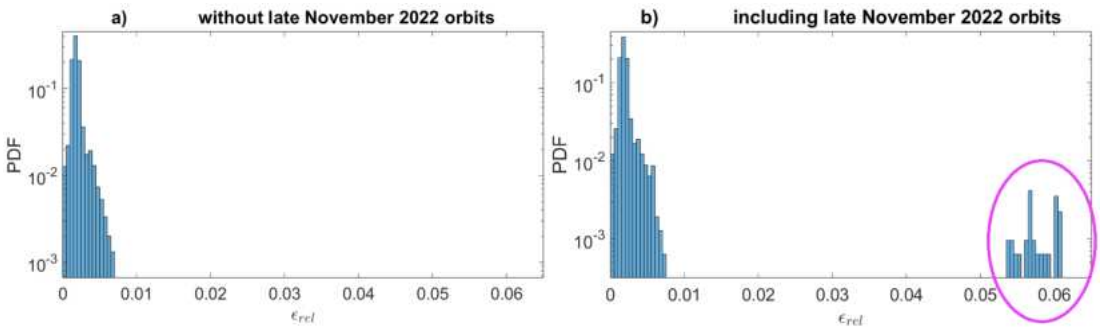

Figure 3.10: ϵ_{rel} PDF: a) Without closest observations to the earthquake; b) including closest observations to the earthquake. The magenta ellipse highlights the high ϵ_{rel} value appearing only in the left panel.

3.1.5 Ionospheric background and EM anomalies: discussion

We developed a procedure to evaluate the ionospheric background relying on the FIF technique, which represents an optimum tool for non-linear and non-stationary signal analysis (Ghobadi et al. [105], Cicone and Pellegrino [59]). Such procedure permits to take into account

the impact of the solar driver and the diurnal variation on background determination, by considering the nine different ionospheric conditions showed in table 3.1. In addition, the analysis has been optimized with respect to other works (e.g. Bertello et al. [25], Piersanti et al. [217]) by examining the effects of the cell size, which allows to maximize the number of observations suitable for analysis on the region of interest and by considering a logarithmic scale for the frequencies.

Our procedure is able to correctly identify the characteristic frequencies of well known signals in the ionosphere. In the analyzed electric field background spectra the following signatures appear:

- ≈ 2 Hz: due to the $\mathbf{v} \times \mathbf{B}$
- ≈ 8 and ≈ 15 Hz: first and second Schumann ionospheric resonances
- ≈ 1 kHz: signature of the plasmaspheric hiss.

The magnetic field background spectra only shows the signature of second Schumann resonance, since the SCM-ULF quality factor is high only in the range $10 - 200$ Hz (see Cao et al. [42]).

The application of the procedure over different geographic locations allowed to assess the geographical dependence of these signals. The $\mathbf{v} \times \mathbf{B}$ emerging from Marche (Italy, figures A.10, A.11 and A.12) and Crete (Greece, figure A.1) exhibits a similar behaviour, as expected from close and middle latitude regions. In fact, the signal appears with higher intensity in the X component, with less intensity in the Y component and it is very faint in Z. On the Marche region it appears with high intensity on the nocturnal background spectra. We attributed this behaviour to the presence of others very intense signals appearing on the diurnal spectra. On Haiti (figures 3.3 and 3.4), instead, the signal has an opposite behaviour, showing higher intensity on the Y and Z component. On Vanuatu (figures A.5, A.6 and A.7) this signal is not clearly seen regardless of the ionospheric conditions. We attributed such characteristics to the presence of other very intense signals (especially in the diurnal backgrounds). In addition, the equatorial ionosphere is characterized by peculiar phenomena, such as the equatorial ionization anomaly (see e.g. Abdu [1]), whose effects may hinder the identification of this signal.

As visible from figures 3.3 and 3.4 [Haiti], A.1 [Crete], A.5, A.6 and A.7 [Vanutatu], A.10, A.11 and A.12 [Marche], the signatures of the Schumann resonances exhibit spatial and temporal variations accordingly to what is reported in Volland [275], which links the variability of the Schumann resonances to the corresponding variability in the totality of the global lightning source function. Such signatures may appear on all components with variable intensity, depending on the intensity of other signals (in particular the plasmaspheric hiss, which is often dominant and may overwhelm the signature of the Schumann resonance on the spectra).

As from figures 3.3 and 3.4 [Haiti], A.1 [Crete], A.5, A.6 and A.7 [Vanutatu], A.10, A.11 and A.12 [Marche], the signature of the plasmaspheric hiss is very intense on the Y component and it appears with less intensity on the other components in all the analyzed regions (with the exception of Haiti, where it is more intense on X). Such behaviour confirms that the signal properties remain essentially constant throughout the plasmasphere (Thorne et al. [258]). The intensity of this signal is much higher in diurnal spectra (see e.g. figures A.6), confirming

that hiss intensity is stronger on the day side (Thorne et al. [258], Taylor and Gurnett [256], Meredith et al. [185], Bortnik, Thorne, and Meredith [34]).

The developed procedure also allowed to investigate the dependence of these signals from the ionospheric level of perturbation induced by the solar activity. As can be seen from figures 3.3 and 3.4 [Haiti], A.5, A.6 and A.7 [Vanutatu], A.10, A.11 and A.12 [Marche], these signals generally occur, as expected, with higher intensity during disturbed conditions. Indeed, the amount of energy coming from the Sun and transferred to the ionosphere is greater during disturbed conditions (see e.g. Kamide and Baumjohann [142]). The observed behaviour has the sole exception for the Schumann resonances on Vanuatu (figures A.5, A.6 and A.7), that are slightly stronger on quiet spectra. We attribute this behaviour to the fact that the plasmaspheric hiss is very intense during disturbed conditions, overwhelming other signals.

It is important to underline that particular attention must be directed at those signals exhibiting intermittent occurrence, such as anthropogenic ones. Such signals may not appear in the background, since they could be switched on only for limited time windows. This could lead to a misinterpretation of them as natural and anomalous. An example of these signals are the ones generated by VLF transmitter, such as the NWC transmitter in Australia, which operates at a 19.8 kHz frequency (see e.g. Němec, Pekař, and Parrot [201]). Figure 3.11 shows the power spectral density of the EFD-VLF signal filtered at 19.8 kHz (X, Y, Z components and their sum from top to bottom) during a CSES-01 passage over Australia. When the satellites is close to the transmitter (the yellow rectangle highlights the region within 10° with respect to NWC position), the PSD increases, indicating that the transmitter is switched on. Therefore, a complete knowledge of electromagnetic ionospheric environment is needed to correctly interpret these signals and be able to detect possible anomalies.

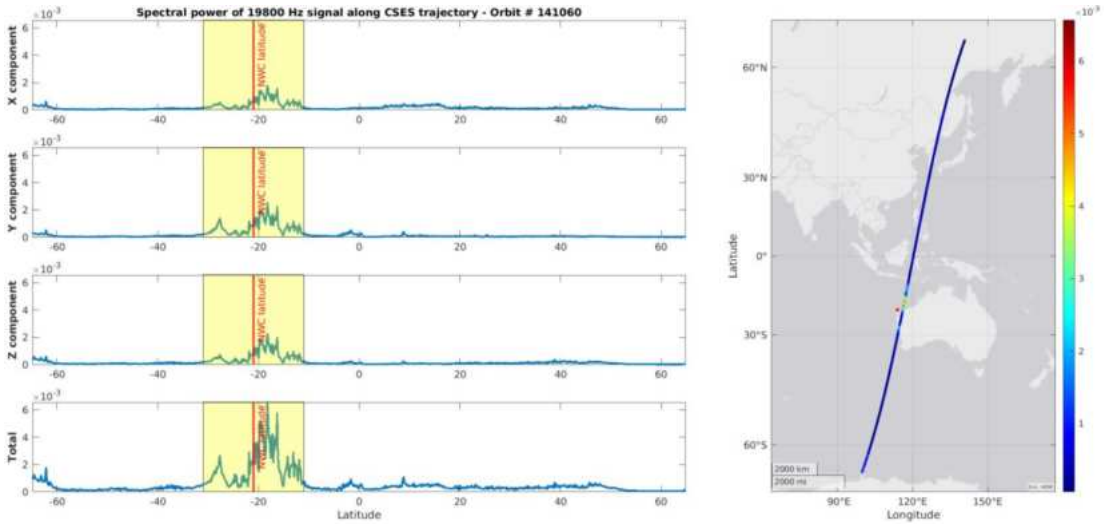

Figure 3.11: Power spectral density of the EFD-VLF signal filtered at 19.8 kHz (X, Y, Z components and their sum from top to bottom). The yellow rectangle highlights the region within 10° with respect to NWC transmitter position. On the right panel, CSES-01 trajectory with PSD in the color scale.

With the exception of the the three mentioned signals ($\mathbf{v} \times \mathbf{B}$, Schumann resonances and plasmasperic hiss), the background spectra never shows any other clear signature. This means that any eventual signal detected in the range from $\approx$ 50 and $\approx$ 800 Hz is worthy of consideration for detailed analysis to determine whether it is a possible signal related to the seismic activity. Indeed, Zong, Tao, and Shen [306] showed that electromagnetic emissions associated with seismic activity were mainly found in the range from $\approx$ 50 to $\approx$ 300 Hz. Within this context, the detected signals emerging from the background ($\approx$ 250 Hz over Haiti, $\approx$ 420 Hz over Vanuatu and $\approx$ 80 Hz over Italy) appear to be linked with seismic activity. As a confirmation of this, such signals are well fitted by the MILC model (section 1.3.3), exemplifying litho-iono-magnetospheric coupling during seismic events. Notably, the MILC model accurately predicted the occurrence of these signals during the co-seismic phase. These case studies expand the range of experimental evidence supporting the MILC model, which has previously been validated for its ability to accurately predict co-seismic electromagnetic signals (Piersanti et al. [217], D'Angelo et al. [72]) that induce changes in magnetospheric field line resonance eigenfrequency.

As emerging from the proposed analysis, our methodology leads to a reliable disentanglement of EQ-induced effects from ionospheric variations due to the solar forcing, latitudinal and diurnal/nocturnal dependencies. In fact, our analysis is repeated 9 different times corresponding to the nine different backgrounds (see table 3.1).

In addition, the investigation of the ϵ_{rel} PDF under the considered conditions, allows the analysis to be independent of geomagnetic conditions. This means that by applying our procedure it is possible to overcome the difficulty in detecting signals possibly correlated to seismic activity during stormy conditions (such as the Crete event described in Recchiuti et al. [225]).

To our knowledge, the proposed procedure represents the first methodology to compute electric and magnetic field background of the ionosphere. Even if such procedure requires a remarkable amount of computational time, it proved to be very efficient in determining the ionospheric background under different conditions. The procedure, on one hand, allows detecting known features related to the ionospheric variability in a selected portion of the globe, on the other hand, it allows detecting signals which are not explained by the typical ionospheric variations, such as those that could be related to seismic activity.

Anomalies definition

To date, some authors relied on the visual comparison between the background and observations in the proximity of the earthquake for possible anomaly detection. This approach allowed to identify some interesting signals possibly correlated to the seismic activity:

- a $\approx$ 333 Hz signal over L'Aquila, Italy (Bertello et al. [25]);
- a $\approx$ 180 Hz over Bayan, Indonesia (Piersanti et al. [217]);
- a $\approx$ 250 Hz over Haiti (Recchiuti et al. [225]).

In addition, authors also analyzed such signals to rule out other known sources as their possible cause (such as solar or atmospheric activity). However, an approach based only on

the visual comparison between the background and the observations in the proximity of the earthquake does not allow for a statistically robust definition of an anomaly with respect to the background and it can fail in case of analysis on days characterized by geomagnetic storms, as was shown for the Crete event (see e.g. section 3.1.3 and Recchiuti et al. [225]).

Within this framework, we developed an analysis tool able to identify an anomalous signal with respect to the background in a statistically robust way. The proposed technique is based on the study of the ϵ_{rel} (see chapter 2.3.2) probability distribution function. Specifically, we compared the ϵ_{rel} PDF obtained by excluding the temporally closest observations to the seismic activity and the one obtained considering all the observations used for the background calculation. This is shown in figure 3.10, which reports ϵ_{rel} excluding the closest (in time) observations to the earthquake (left) and including the closest (in time) observatiosn to the earthquake (right). As highlighted by the magenta ellipse on the right panel, very high ϵ_{rel} values appear when closest (in time) observations are included. Such values are one order of magnitude greater than the background values, appearing also very far from their distribution. Such multimodal behavior of ϵ_{rel} PDF suggests that the electric signal of the observations closest (in time) to the earthquake may have a different physical origin, which could be possibly related to the earthquake via an ionosphere-atmosphere-lithosphere coupling mechanism.

3.2 Short-time signals

The methodology described in section 3.1 proved to be very efficient in detecting EM signals characterized by medium-long term trend. However, as described in chapter 1, the ionosphere is a very complex environment and it is also affected by very short-time signals which endure for a second or less, like the whistlers waves (see section 1.4 and Walker [277]).

The analysis of these types of signals requires a completely different approach. In fact, due to their short duration, they affect a very short portion of the satellite's orbit. In addition, as stated in Barbarino and Cicone [18], when a signal contains mono-components that have rapid varying instantaneous frequencies like chirps or whistlers, it becomes particularly hard for most techniques to properly factor out these components.

To date, most of the techniques used to automatically detect whistler waves are based on image recognition, due to the peculiar shape as a chirped falling tone structure of these signals (e.g. Lichtenberger et al. [167]). However, such technique requires explicit knowledge of the signal structure. In addition, these machine learning based approaches tend to obscure the physical interpretability of the results. For these reasons, we developed a new technique, which is totally based on physical quantities, as described in the following section.

3.2.1 Automatic detection of whistler waves: a physics-based method

a The EFD and SCM onboard CSES-01 satellite can collect information that cannot be accessed through a simple visual inspection of the EM spectra, due to the high sampling frequency. This could be clarified by the example showed in figures 3.12 and 3.13, which respectively show electric and magnetic field spectrograms recorded along orbit 141060 on August 18, 2020. These

spectrograms are obtained with a Fast Fourier Transform (FFT) in time windows of approximately 0.4 seconds, corresponding to 4096 points for SCM and 2048 for EFD.

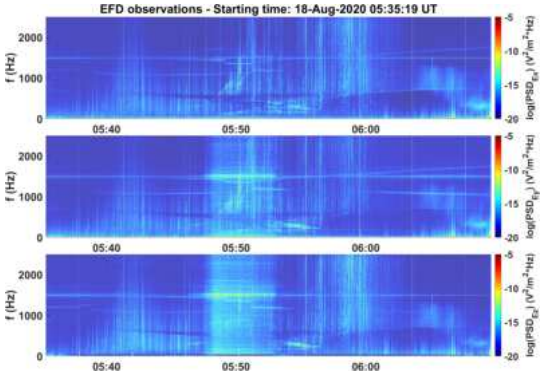

(a) EFD spectrograms of the whole orbit. X, Y and Z component from top to bottom.

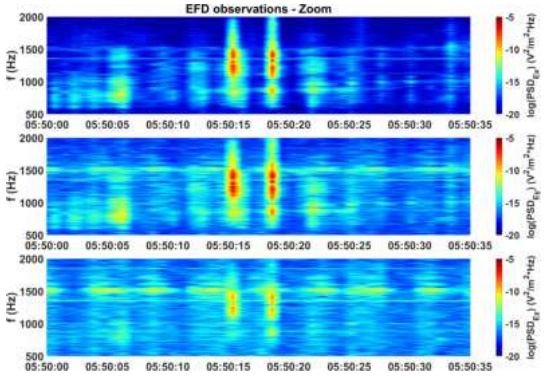

(b) Zoom in a time interval of $\approx 35\ s$, with the two evident signals appearing.

Figure 3.12: Electric field spectra of the CSES observation in the ELF band on August 18, 2020. From top to bottom: X, Y and Z component respectively.

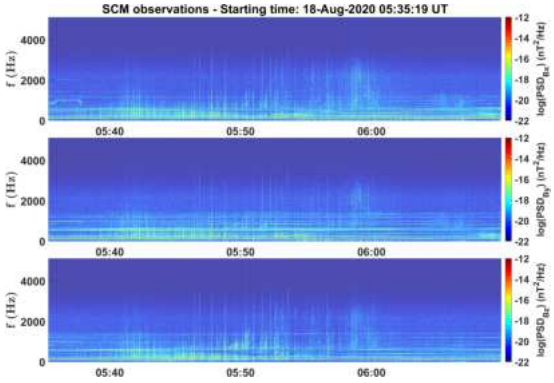

(a) SCM spectrograms of the whole orbit. X, Y and Z component from top to bottom.

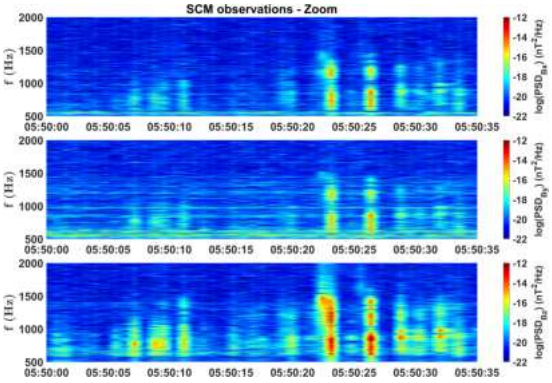

(b) Zoom in a time interval of $\approx 35\ s$ with the two evident signals appearing.

Figure 3.13: Same as figure 3.12, but for the magnetic field.

Figure 3.12a shows the electric field spectra of X, Y and Z component as recorded along 141060 CSES-01 orbit in the ELF band on August 18, 2020. Panel 3.12b, show the same observations in which the electric field components are magnified in a time window of $\approx 35\ s$. As visible, the zoom shows two signals appearing at $\approx$ 05:50:15 UT and $\approx$ 05:50:18 UT, both characterized by a frequency spanning from $\approx$ 500 to $\approx$ 1500 Hz. Such signals emerge in all the components, even if it is faint in Z. The same considerations hold for the magnetic field too, as can be seen in figure 3.13, which reports the SCM observations for the same orbit. The only difference is that the signals are more pronounced in the Z component and they are faint on the other two.

The absence of signals in the spectra performed on the whole orbit can be attributed to the limited pixel resolution of the image in relation to the sampling frequency of the signal. As shown in the recent work by Svenningsson et al. [251], the median duration of whistler waves ranges between 0.13 s and 0.17 s. Consequently, the temporal windows employed for both EFD and SCM PSD calculations (0.4 s) represent an optimal time interval for detecting these events. Within these windows, the presence of a whistler is expected to manifest as an enhanced PSD across a broad frequency range, consistent with the characteristic rapid descending tone of whistler waves Storey [250]. To highlight the expected enhancement of PSD across a broad frequency range, we introduce a novel physical quantity termed the integrated PSD (IPSD), which is defined as follows:

$$IPSD_i = \sum_{j=eb}^{j_{MAX}} PSD_i \; f_j \tag{3.1}$$

where $i = x, y, z$ represents the electric or magnetic field component and j the frequency bin. To focus on fluctuations of this quantity, frequencies constituting the baseline are excluded from the summation. Consequently, the summation extends from the minimum frequency bin exceeding the baseline (eb) to the maximum value ($j_{MAX} \sim 800$ for SCM and $j_{MAX} \sim 1024$ for EFD). The baseline is determined by summing frequencies that retain at least 90 % of the total PSD. This step is necessary when analyzing EFD data, which include low frequencies. Indeed, the lowest frequency bins of EFD-ELF data encompass characteristic frequencies of Schumann Resonances (SR, $\sim 6 - 30Hz$, Sentman [238] and the first Power Line Harmonic Radiation (PLHR, $50 - 60$ Hz, Karslı and Dondurur [145]). These signatures have been experimentally detected in EFD data (SR detection described in Recchiuti et al. [225]; PLHR in Zhao et al. [303] and Ma et al. [174]). If not excluded, the high PSD of these signatures could significantly compromise the effectiveness of the technique. Consequently, for SCM-ELF $eb = j_{MIN} = 1$, while for EFD-ELF we typically obtain $eb \sim 30$.

As an example of the technique, right panels of figure 3.14 shows the IPSD (red lines) related to the spectra of SCM observation along orbit 141060. Here, at $\approx$ 05:50 UT (in correspondence to the signals identified in the magnified version of the spectra, see figure 3.13b) a very large spike appears on the IPSD plot. The same happens for electric field observations (see figure A.14 in appendix A).

The IPSD is the starting point for the development of a new algorithm able to automatically detect whistler waves events. This procedure is based on the detection of peaks (which we relate to the presence of whistlers) in the IPSD using a thresholding algorithm. Specifically, if such a peak exceeds the average value by a fixed threshold, it is selected as an event. By the visual inspection analysis performed on thousands of orbits, we fixed this threshold at 150 times the average, in order avoid false positives. In this way, all the found events are whistler-like waves. This criterion is applied on the total IPSD, namely the sum of the IPSD for X, Y and Z components.

Since, as visible by comparing figures 3.14 and A.14, the electric field spectrograms (and, consequently, the IPSD plots) are noisier than the magnetic field ones, we used the SCM data for such automatic detection. The high level of noise on the EFD observations is due to the

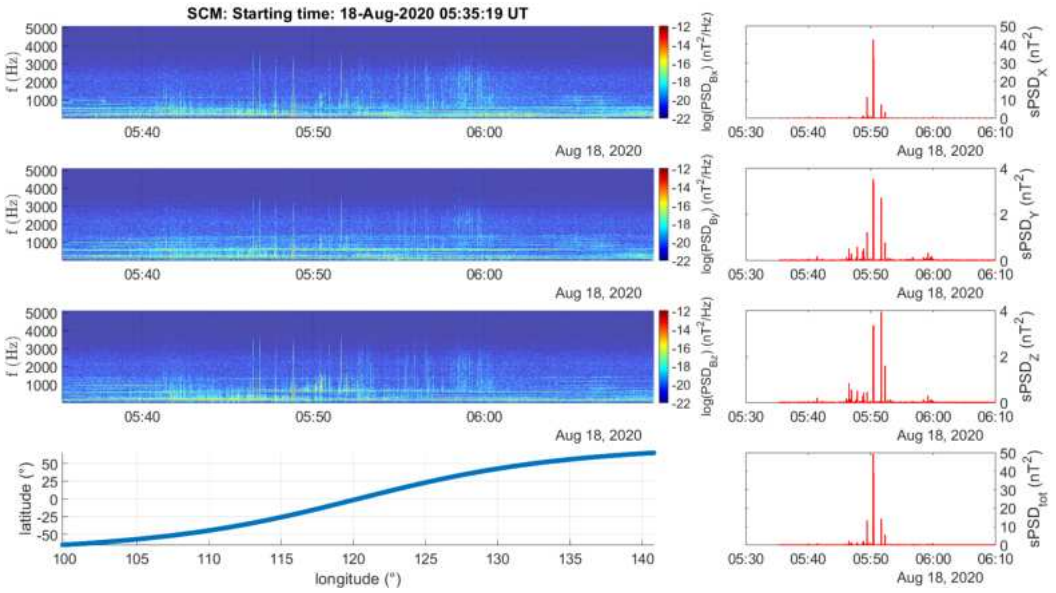

Figure 3.14: On the left, spectra of the magnetic field observations (X, Y and Z components from top to bottom and satellite's trajectory). On the right, IPSD (from top to bottom: X, Y, Z components and their sum). A very large spike appears at ≈ 5:50 UT.

mechanical friction induced by the vibration of the boom-B (greater in summer and during the daylight because of the higher photoionization, see Diego et al. [76] and reference therein.

Since whistler waves are mostly characterized by a frequency of few kHz (Walker [277]), we selected observations in the ELF band.

3.2.2 Statistical analysis of detected whistlers

We applied the methodology described in section 3.2.1 on 1175 days from January 01, 2019 to March 21, 2022 (data from April 2019 were not available at the time of analysis - last access on the database: February 08, 2024). This results in a dataset of 34847 orbits (≈ 10000 orbits per year on average), enabling a comprehensive statistical analysis of whistlers.

The analysis is restricted to a latitude band between $-40°$ and $40°$ geographic latitude, in order to exclude high latitude regions where effects induced by the solar forcing that may dominate whistler signatures are more frequent and significant (see chapter 1). Table 3.3 gives an overview of the results of the statistical analysis. Since CSES-01 is the first satellite able to measure the three components of electric and magnetic field simultaneously in the top-side ionosphere, to our knowledge, this is the first analysis that covers such a long period and amount of whistlers recorded in that region. In fact, usually, these investigations are developed through data given by geomagnetic stations at ground (see e.g Lichtenberger et al. [167]).

Table 3.3 summarizes the results of statistical analysis, showing that the selection algorithm identifies ≈ 0.7 events per orbit (i.e. ≈ 20 events per day). The related histogram, shown in figure 3.15 (in which the heights of the bars are normalized to 1), reveals that ≈ 60 % of the

Days	Orbits	Selected events	Events per orbit	Variance
1175	34847	24136	0.6926	1.0906

Table 3.3: Summary of the results of the selection of the events in the time interval from 01/01/2019 to 21/03/2022.

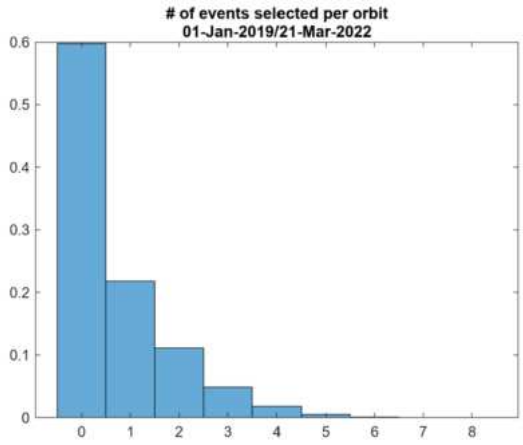

Figure 3.15: Percentage of the number of selected events per orbit.

orbits have no events. This percentage exponentially decreases with the increase of selected events and varies only moderately by analyzing diurnal and nocturnal orbits separately (figure 3.16).

To investigate if the variation of the solar activity has an impact on the occurrence of such events we analyzed separately the distributions of the number of whistlers per orbit emerging during quiet, disturbed and stormy days. The days are classified as quiet, disturbed or stormy accordingly to data and thresholds described in chapter 2. The results of this analysis are shown in figure 3.17.

The three panels of figure 3.17 show a very similar distribution, which is also similar to the one considering all days (figure 3.15). No significant dependence of whistler occurrence by variation in the geomagnetic conditions emerges from this investigation.

Figure 3.18 shows the geographical distribution of the detected whistlers, in which panel 3.18a considers all orbits, panel 3.18b only diurnal orbits and panel 3.18c only nocturnal ones.

The comparison between figures 3.18b and 3.18c reveals that, with minor differences, the same geographical trend is observed between nocturnal and diurnal observations. The occurring frequency is slightly higher in the northern hemisphere with respect to the southern; in fact, $\approx$ 55 % of the events were found above the equator.

Figure 3.18 clearly shows that the geographical distribution of the events is not uniform. There are regions (i.e. central America, Madagascar, southeast Asia...) characterized by a very high concentration of events and other regions (i.e. saharian Africa, Brazil, Arabian peninsula) characterized by few events and by large portions of these regions with no events at all. In order to quantify the geographical variations, we divided the earth's surface into cell with longitudinal size equal to 10° and latitudinal size equal to 5° and verified that the number of events per cell goes from 0 up to almost 200. Specifically, the cell identified by longitude

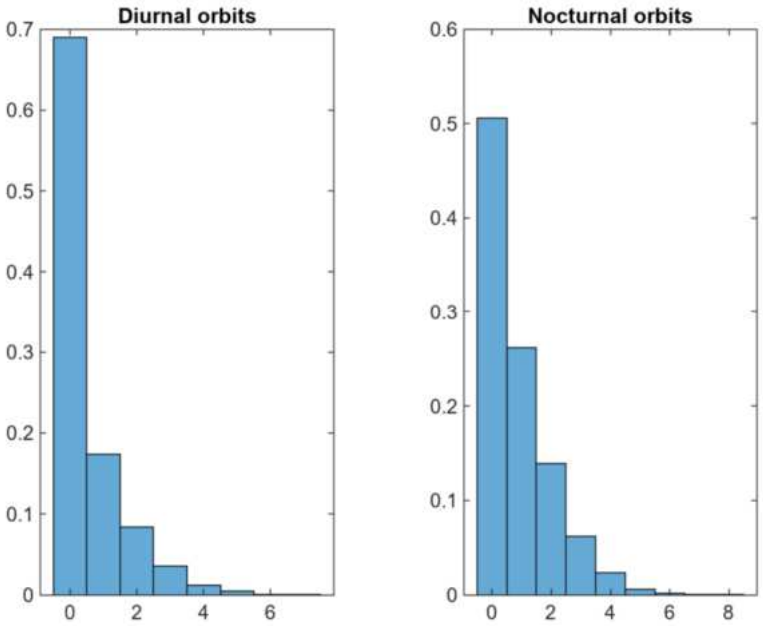

Figure 3.16: Percentage of the number of selected events for diurnal (left) and nocturnal (right) orbit.

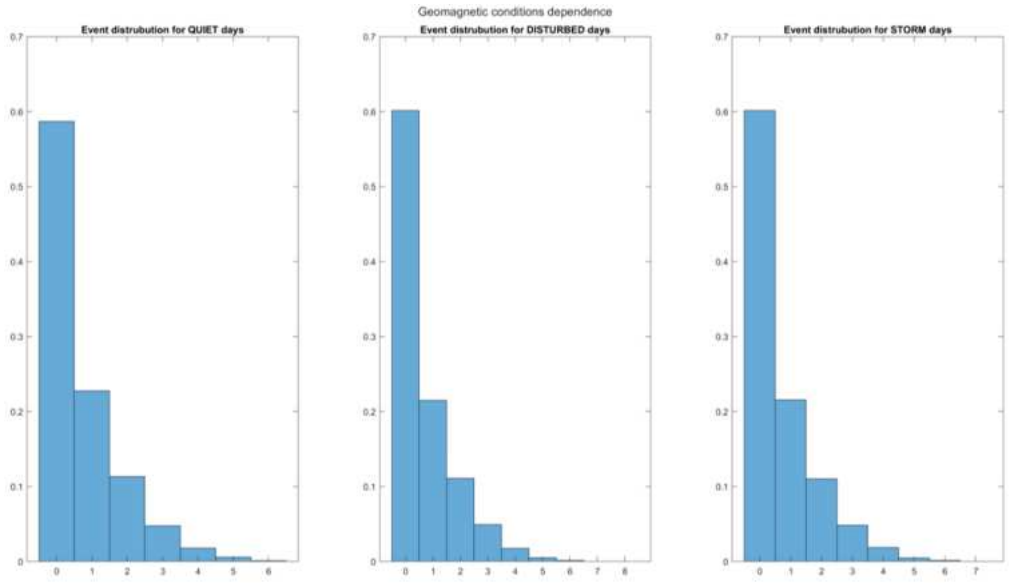

Figure 3.17: Distribution of events per orbit during quiet (left panel), disturbed (central panel) and storm (right panel) days.

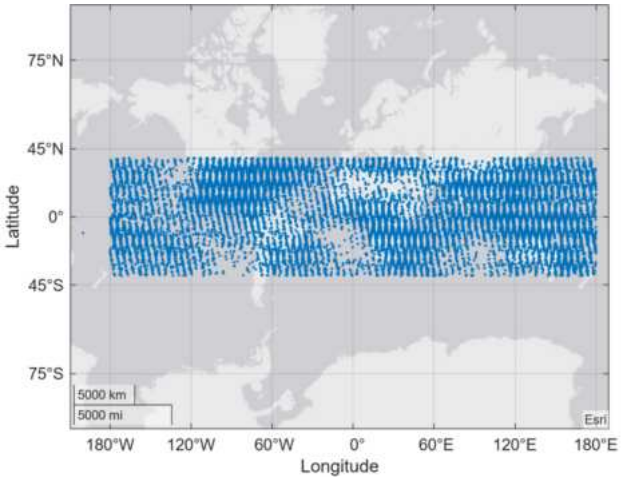

(a) All orbits.

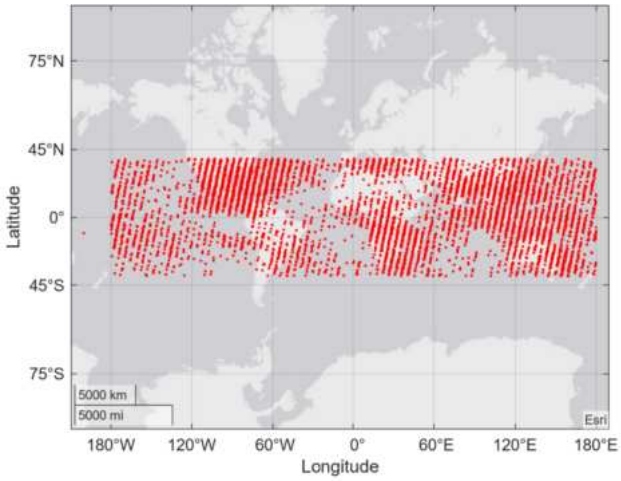

(b) Diurnal orbits.

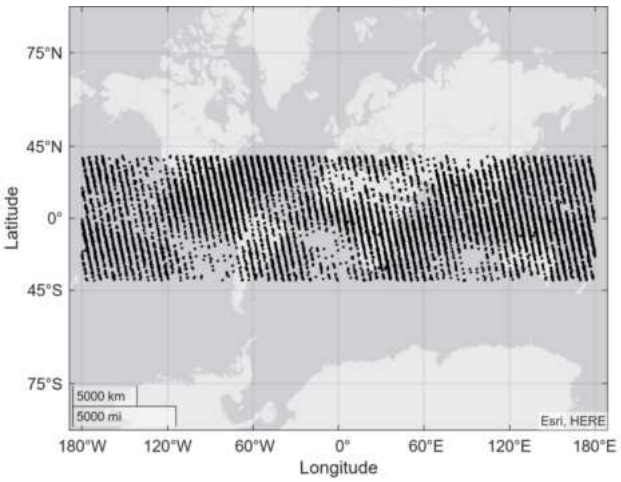

(c) Nocturnal orbits.

Figure 3.18: Geographical distribution of the events.

$-20°$ < LON < $-10°$ and latitude $-15°$ < LAT < $-10°$ (corresponding to the Atlantic ocean far from both the south American and African coasts) contains 0 events, with the adjacent cells containing 12 events or less. On the contrary, the cell identified by longitude $-90°$ < LON < $-80°$ and latitude $25°$ < LAT < $30°$ (corresponding to the Gulf of Mexico) contains 185 events, with the adjacent cells containing always more than 100 events.

We also investigated the monthly distribution of the events, which is shown in figure 3.19. The distribution is normalized by the number of orbits in each months, since not all the months have the same number of days.

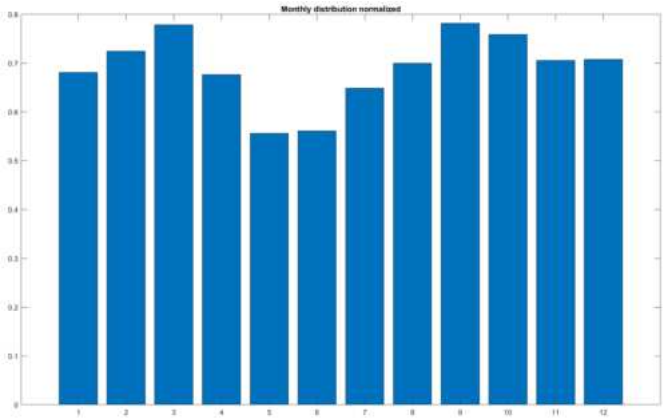

(a) Both the hemispheres.

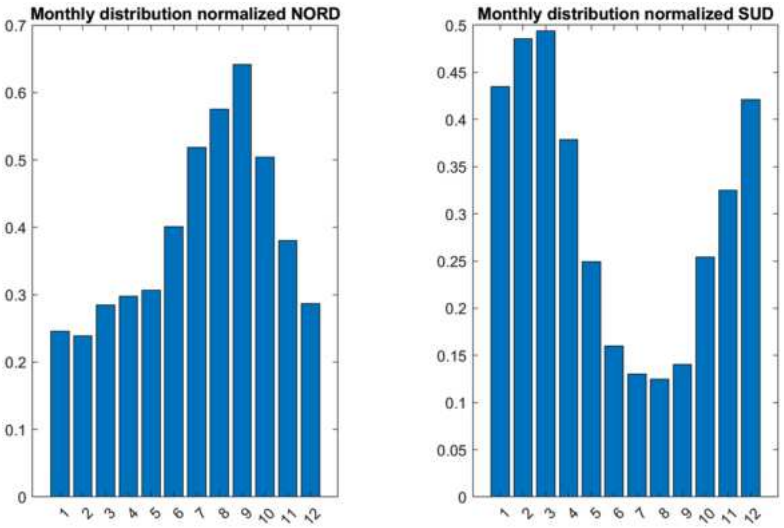

(b) Northern (left) and southern (right) hemisphere.

Figure 3.19: Monthly distribution of the events.

Figure 3.19a show the distribution for all the observations, while the two panels of figure 3.19b show separately the distribution for northern (left) and southern (right) hemisphere. While the monthly dependence is very faint considering all the observations, an evident sea-

sonal dependence appears when the distribution is split in northern and southern hemisphere. In both hemispheres the distribution exhibits a peak at the end of the local summer (August and September in the northern hemisphere, February and March in the southern hemisphere).

All the identified events constitute a large database, resulting very useful to quick verify if a specific phenomena can induce such events. For example, it is known that volcanic eruptions are associated to various EM phenomena, the most significant one is the strong electric field generated by volcanic ash clouds (Lane, James, and Gilbert [160]). As a consequence, during eruptions, lightning discharges occur (Johnston [137], Cimarelli and Genareau [62]). Hence, it is possible to detect whistler waves associated to volcanic eruptions. Indeed, investigating the geographical distribution of the detected whistlers on 14 and 15 January 2022, we identified 3 events associated to the Tonga-Hunga Ha'apai volcano eruptions. In such days, the volcano produced several large eruptions causing a 20 km ash clouds in the atmosphere (see e.g. Yuen et al. [301]). Figure 3.20 shows the location of the whistlers (the red star indicates the location of the volcano).

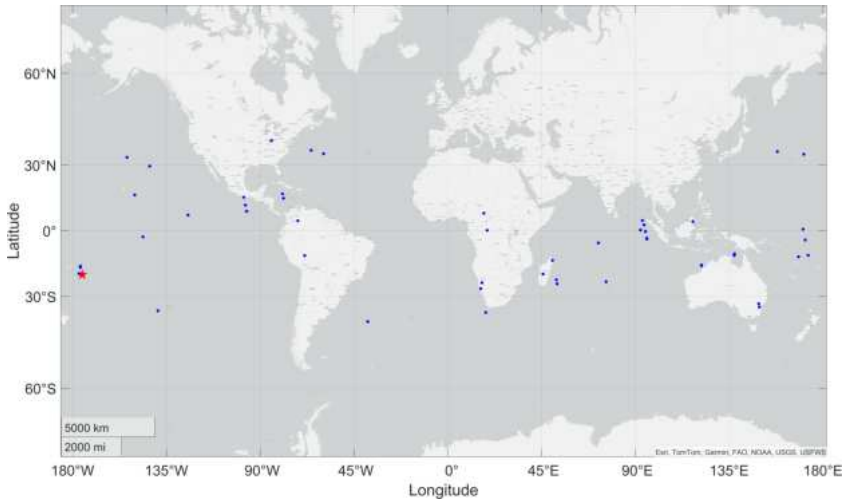

Figure 3.20: Events identified by the selection algorithm on 14 and 15 of January 2022 (blue points). The red star indicates the location of the Hunga Volcano.

3.2.3 Characterization of EM waves

The automatic detection of whistlers described in section 3.2.1 relied only on the analysis of the spectrograms, allowing for a characterization in terms of spatial and temporal occurrence of such events. However, the sole analysis of the spectrograms is not able to accurately determine all the physical characteristics of the detected signal, such as duration, amplitude, frequency, polarization, direction of propagation (Priestley [219]). To this end, we conducted an in-depth analysis of waveforms, developing two novel methodologies for the identification of these characteristics. Although the initial focus was on the newly built whistler wave database, these methodologies exhibit broader applicability and can be employed for characterizing general electromagnetic wave phenomena, beyond whistlers.

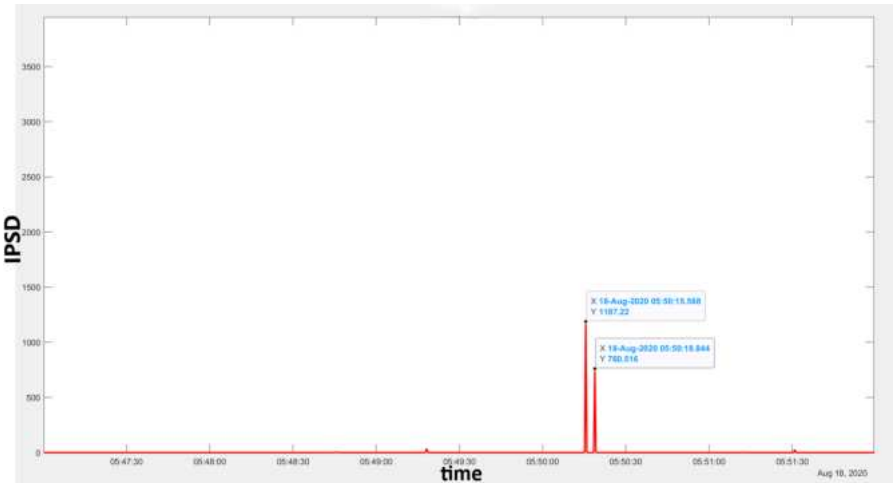

Figure 3.21: IPSD for the X component in a time interval of ≈ 5 min around 5:50 UT. Two peaks are distinguishable.

Case 1

The proposed methodology is based on the following steps:

1. removing the mechanical noise affecting EFD observations. The task is here accomplished through Iterative Filtering technique (IF, Cicone [55]), thanks to its good performance in decomposing non stationary and non linear signals (see chapter 2 for further details);

2. performing a high-resolution spectrogram on a short time window centered on the time of the IPSD peak;

3. realigning, through a cross covariance analysis (see chapter 2), the electric and magnetic field signals. This procedure is necessary since the two signals are not synchronized due to the different hardware and software implementations between EFD and SCM (see Zhima et al. [305], Yang et al. [297]);

4. performing a principal component analysis (see chapter 2) on the electric and magnetic field separately.

Here we show the application of this methodology on CSES-01 data recorded on August 18, 2020, along orbit 141060.

Figure 3.21 shows the IPSD plot for the X component of the electric field after the application of the IF technique, in a time interval of ≈ 5 min around 05:50 UT. By comparison with figure A.14 (IPSD plot, upper panel), the good performance of IF for noise removal can be appreciated. Two very sharp peaks appear, in perfect agreement with the two very energetic band showed in the magnified spectra reported in figure 3.12b, upper panel.

The high-resolution IPSD plot shown in figure 3.21 allows to determine the exact time of the peak, useful to analyze the waveform in a short time window around the peak. We investigated both the peaks, but only the results related to the first one are reported, since the same considerations hold for the second one.

Figure 3.22 shows the three components of the electric (left panel) and magnetic field (right panel), in a short time window around the first IPSD peak (X, Y and Z from top to bottom). As it visible on both panels, the IPSD peak is the consequence of oscillating structures enduring for less than 0.5 seconds.

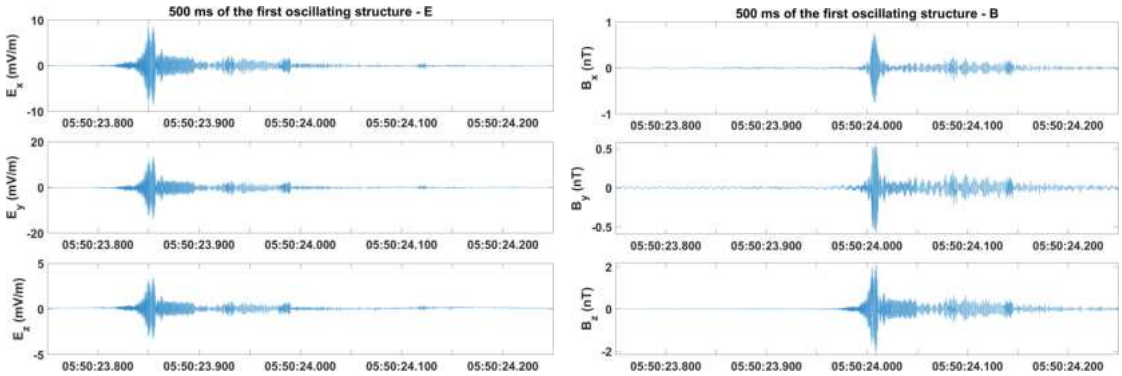

(a) Electric field around the first IPSD spike.

(b) Magnetic field around the first IPSD spike.

Figure 3.22: The three components of electric field and magnetic field in a 500 ms time window around the first IPSD spike.

In order to identify the frequency of these oscillating structures, we performed the spectrograms of both magnetic and electric field observations in a narrow time window of 400 ms (including the main oscillations and the subsequent decreasing phase). These spectrograms are shown in the upper panels of figure 3.23 (X, Y and Z component from left to right; the color scale indicating the PSD), while lower panels show the waveform in the same time window. Electric and magnetic field results are shown in panels 3.23a and 3.23b respectively. The two fields show very similar results. Differences in y-axis between two fields are due to the different sampling frequency between EFD (5 kHz) and SCM (10.24 kHz). For all components the signal has an initial frequency of $\approx$ 2 kHz and rapidly go down, in a typical chirped shape, to $\approx$ 0.5 kHz in $\approx$ 150-200 ms. Correspondingly, the fluctuations of the waveform show a very fast increase up to the maximum amplitude enduring $\approx$ 150-200 ms.

The spectrograms in figure 3.23 exhibit the typical chirped structure of the whistler waves. However, as can be seen in the lower panels of figure 3.23 and also by comparing figures 3.22a 3.22b, the two oscillating structures on electric and magnetic field are asynchronous. For this reason, we realigned the signals with the cross covariance technique (chapter 2), whose results are shown in figure 3.24. Here, we report in the 9 panels the cross covariance as a function of the time shift between the two signals component by component. For all the combinations, we obtained that the electric field is anticipated by $\approx$ 155 ms, in agreement with Zhima et al. [305] and Yang et al. [297]. We used such value to realign the electric and magnetic field signals. The result of this realignment is shown in figure 3.25, where the magnetic field (blue) is multiplied

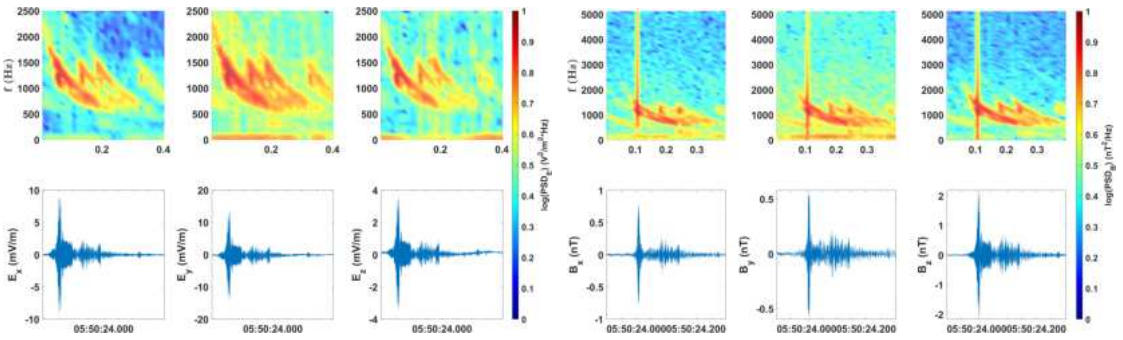

(a) Electric field. (b) Magnetic field.

Figure 3.23: Analysis around the first peak in the PSD. Upper panels: spectrograms. Lower panels: waveform. From left to right: X, Y and Z component.

by a factor of 4 just to make it comparable with electric field (red). In figure, the x-axis is in milliseconds (the entire length of the time window is 150 ms), while the y-axis is in mV/m for electric field and in nT for magnetic field. As can be easily seen, the two signals are now perfectly aligned. In addition, the major oscillations can be observed on the X and Y component of the electric field and the Z component of the magnetic field. Such components also exhibit the same waveform shape. Therefore, the realigned signal exhibits the characteristics of an electromagnetic wave.

To test such hypothesis, we performed a principal component analysis (PCA, see chapter 2) on the electric and magnetic field separately. The three principal components just obtained constitute a new orthogonal basis for the space of the data and hereafter they will be denoted as PC1E, PC2E and PC3E for the electric field and PC1B, PC2B and PC3B for magnetic field. Figure 3.26 shows from top to bottom PC1B, PC2B and PC3B with a black dashed line. In addition, each panel also shows X, Y and Z component of the magnetic field in green, blue and red respectively. As it visible in the top panel, PC1B basically coincides with Z. Central panel shows how PC2B have the same behaviour of both Y and Z components, while PC3B (bottom panel) is practically constant.

A further confirmation comes from figure 3.27, showing the explained variance, which is a measure of how much the total variance in the original data is explained by each principal component. In figure, the blue bars represent the percentage of the total variance explained by each principal component (PC1B, PC2B and PC3B from left to right respectively), while the red circles represent the cumulative explained variance. As in panel a), PC1B explains $\approx$ 90 % of the total variance, while the sum of PC1B and PC2B explains basically the 100 % of the variance (the third principal component is negligible). Such behaviour confirms that the magnetic field oscillates mainly only along one direction, corresponding to PC1B in the PCA reference frame, which is close to the Z direction in the original reference frame. Regarding the electric field (panel b), PC1E (left bar) explains basically all the variance, since PC2E and PC3E are negligible.

Figure 3.28 shows in black the original reference versors (X with solid line, Y with dashed line, Z with dashed dotted line), in blue PC1B (solid line), PC2B (dashed line), PC3B (dashed dotted line), finally in red PC1E (solid line), PC2E (dashed line), PC3E (dashed dotted line). The

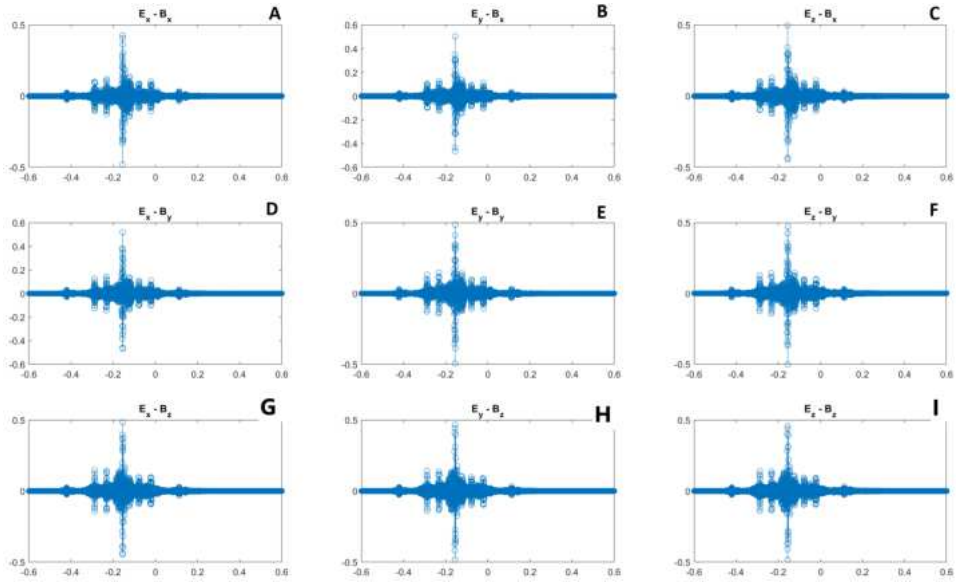

Figure 3.24: Cross covariance between electric and magnetic field observations. Each panel reports the cross covariance component by component and the time that maximizes the cross covariance. Specifically, with the indication of the time of the maximum value. A: E_x-B_y, B:E_y-B_x, C:E_z-B_x, D:E_x-B_y, E:E_y-B_y, F:E_z-B_y, G:E_x-B_z, H:E_y-B_z, I:E_z-B_z.

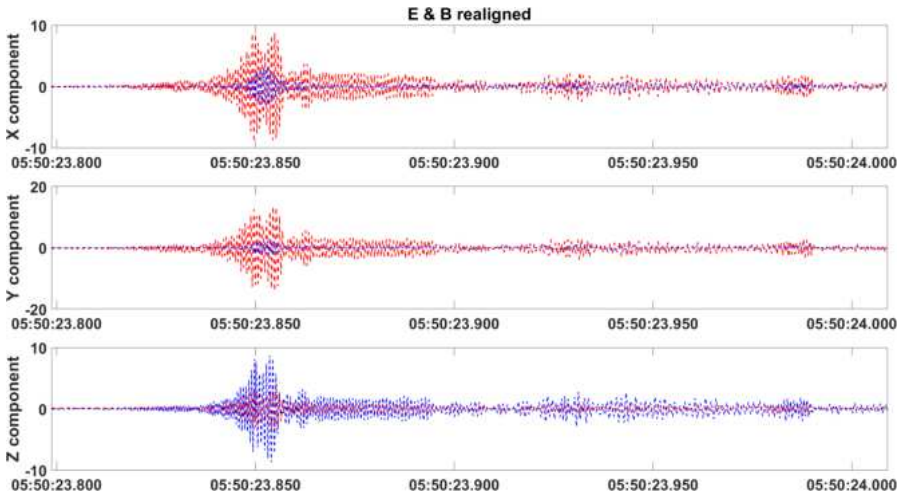

Figure 3.25: The three components of electric (red) and magnetic (blue) field for the first oscillating structure. The two signals were aligned using the time delay that maximizes the cross covariance between E_y and B_z.

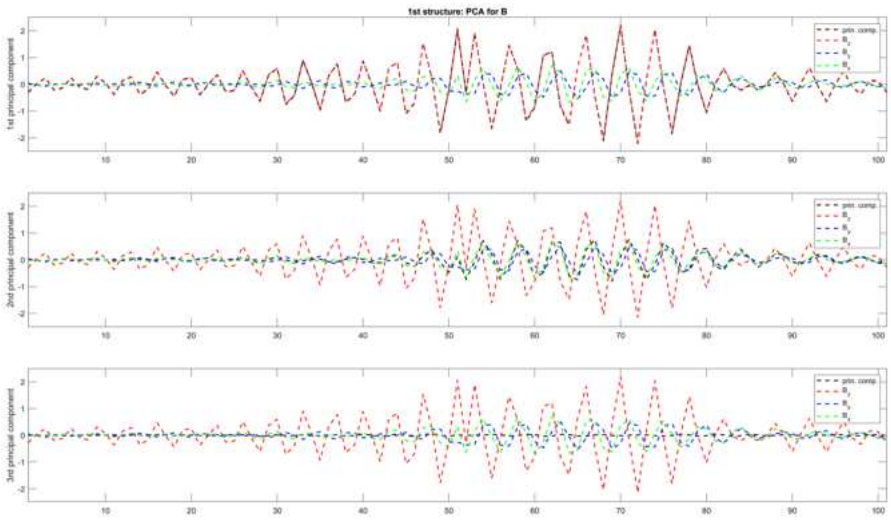

Figure 3.26: The three components in both the original reference frame and the PCA reference frame. The X, Y and Z components are plotted in all panels in green, blue and red respectively. PC1, PC2 and PC3 are plotted in a black dashed line in the top, central and bottom panel respectively.

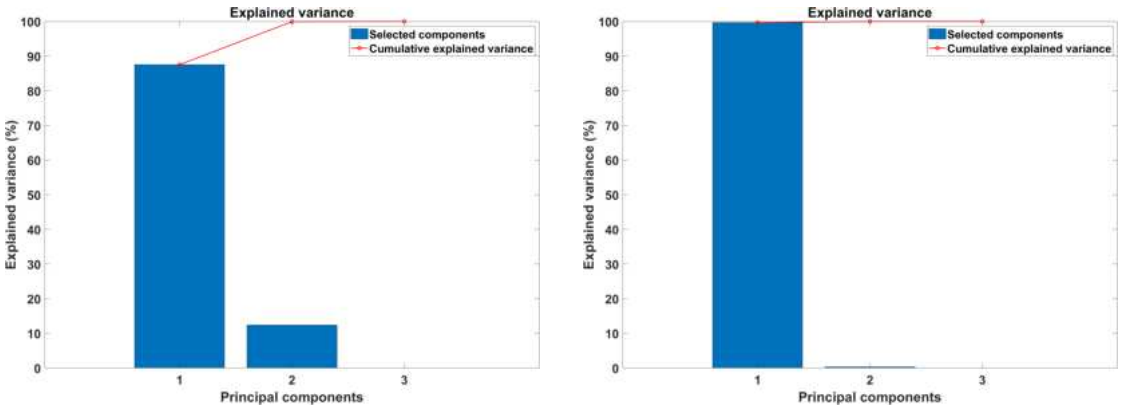

(a) Magnetic field.

(b) Electric field.

Figure 3.27: Percentage of the total variance explained by each PCA component: PC1 (left), PC2 (central), and PC3 (right). The red circles show the cumulative value.

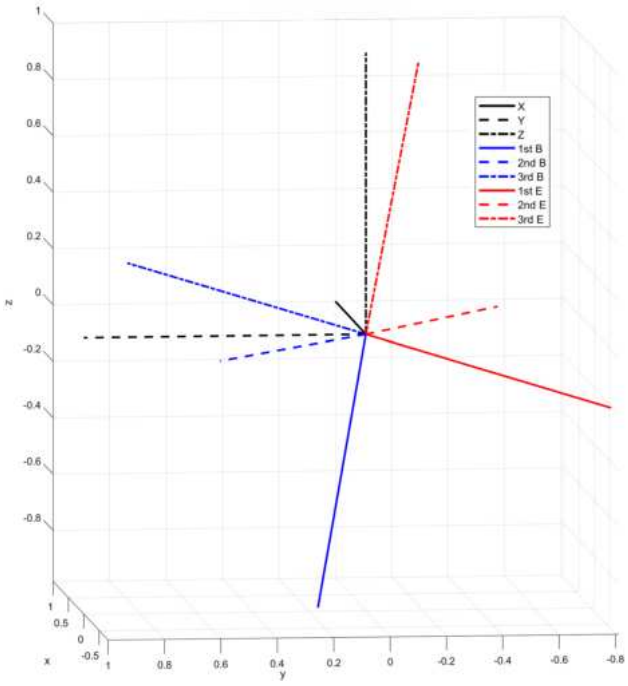

Figure 3.28: Base vectors for the three reference frames. Original reference frame in black (X with solid line, Y with dashed line, Z with dashed dotted line). PCA reference frame for magnetic field in blue and electric field in red (PC1 with solid line, PC2 with dashed line, PC3 with dashed dotted line).

figure shows that PCA reference frame versors for both electric and magnetic field identify a unique reference frame. Indeed, PC1B is orthogonal to PC1E, which coincides with PC3B. PC2B and PC2E identifies the same direction. As expected, this signal exhibits the characteristics of an electromagnetic wave, in which the electric field oscillates along PC1E (which is along the XY plane with a slight tilt along Z) perpendicularly to PC1B. This signal hence appears as a linearly polarized electromagnetic wave.

Case 2

A second approach, developed to determine the physical characteristics of circular polarized whistlers, is based on the following step:

1. determining the oscillation plane of the magnetic field. Since the signal is a circular polarized electromagnetic wave, the electric field oscillations must lie on the same plane;

2. neglecting the electric field observations whose distance from the oscillation plane exceeds a fixed threshold. After a visual inspection of several events, we defined such threshold at 0.2 * D_M, where D_M is the maximum distance of electric field oscillations from the plane;

3. filling the missing part of the signal through piecewise cubic Hermite interpolating polynomia (Chand and Viswanathan [46]);

4. applying an high-pass filter to remove the possible noise introduced by the interpolation. The cut-off frequency has been fixed to 50 Hz after a visual inspection of several events;

5. projecting the electric field observations on the oscillation plane;

6. realigning the signal as in the case 1, described in section 3.2.3.

Here we show the application of this methodology on CSES-01 data recorded on August 14, 2022, along the orbit 219160, during the eruption of the Tonga volcano.

Figures 3.29 and 3.30 show, from top to bottom, the spectrograms and IPSD plots of X, Y and Z component of magnetic and electric field observations in the ELF band, respectively. As visible by comparing figures, the electric field spectrograms appear noisier than the magnetic field ones. Due to the high level of noise, on the electric field observations it is impossible to identify the selected events, highlighted in both figures by black dashed vertical lines.

Since such events show the same characteristics, hereafter, we will show results only for the first one.

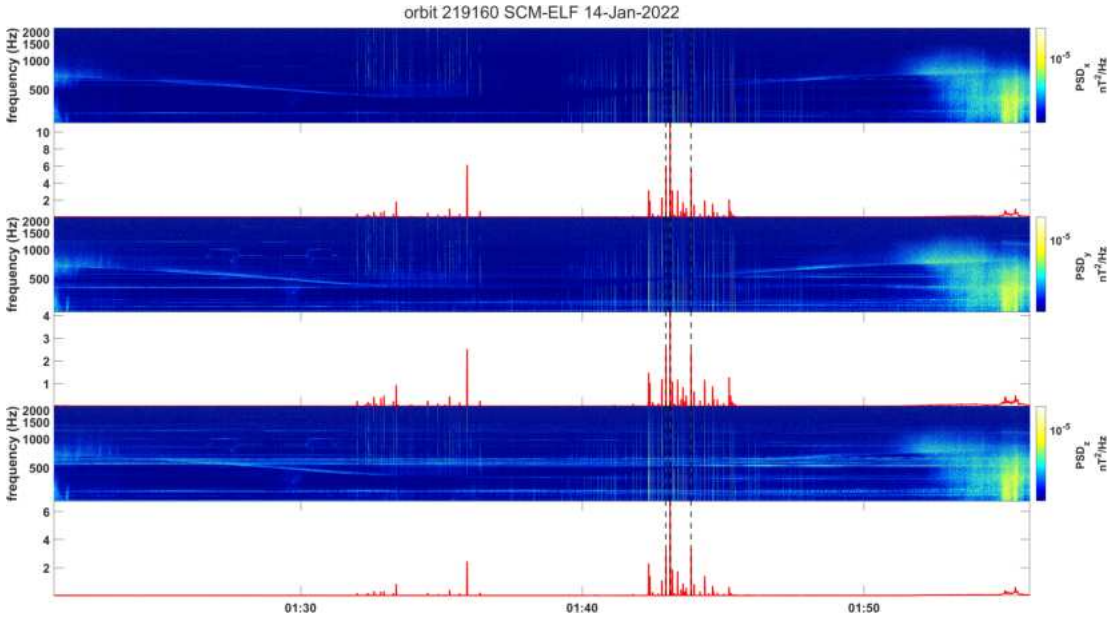

Figure 3.29: Spectrograms and IPSD plots, SCM-ELF observations (X, Y and Z component from top to bottom). The black dashed vertical lines highlight selected events.

Figure 3.31 and 3.32 show the waveforms (left panels) and spectrograms (right panels) in a time window of 1 s around the selected peak (corresponding to $\approx$ 01:42:57.850 UT, highlighted in both figures by the magenta dashed vertical line) for magnetic and electric field observations, respectively. In both figures, X, Y and Z components are from top to bottom.

As from figure 3.31, the magnetic field waveforms (left panels) show an oscillating structure with falling tone frequency on all the three components. Correspondingly, the spectrograms (right panels) exhibit the typical chirped structure, confirming that the detected signal is a whistler.

The electric field observations, instead, shown in figure 3.32, are affected by a high level of noise, which exhibits a higher PSD appearing roughly at the same frequency of the chirped

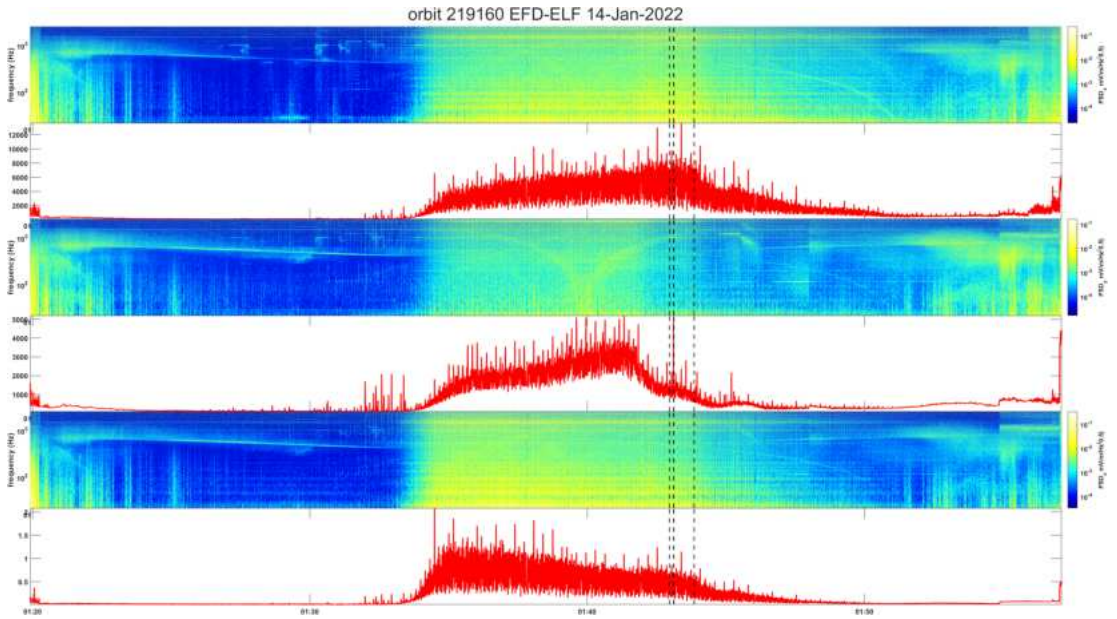

Figure 3.30: Spectrograms and IPSD plots, EFD-ELF observations (X, Y and Z component from top to bottom). The black dashed vertical lines highlight selected events.

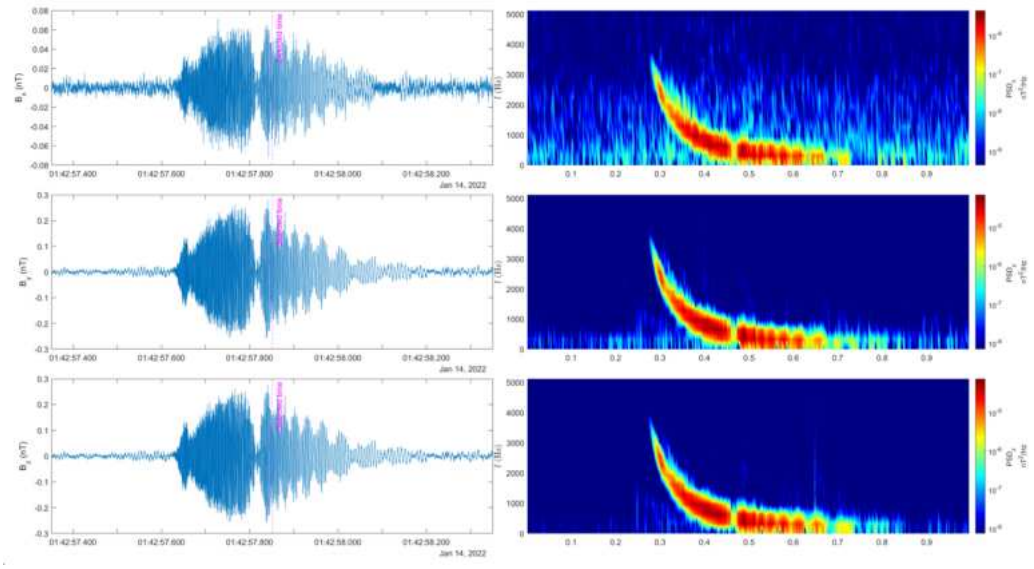

Figure 3.31: Waveforms (left panels) and spectrograms (right panels) in a time window of 1 s around ≈ 01:42:57.850 UT (highlighted by magenta dashed vertical line). X, Y and Z magnetic field components in the ELF band are from top to bottom.

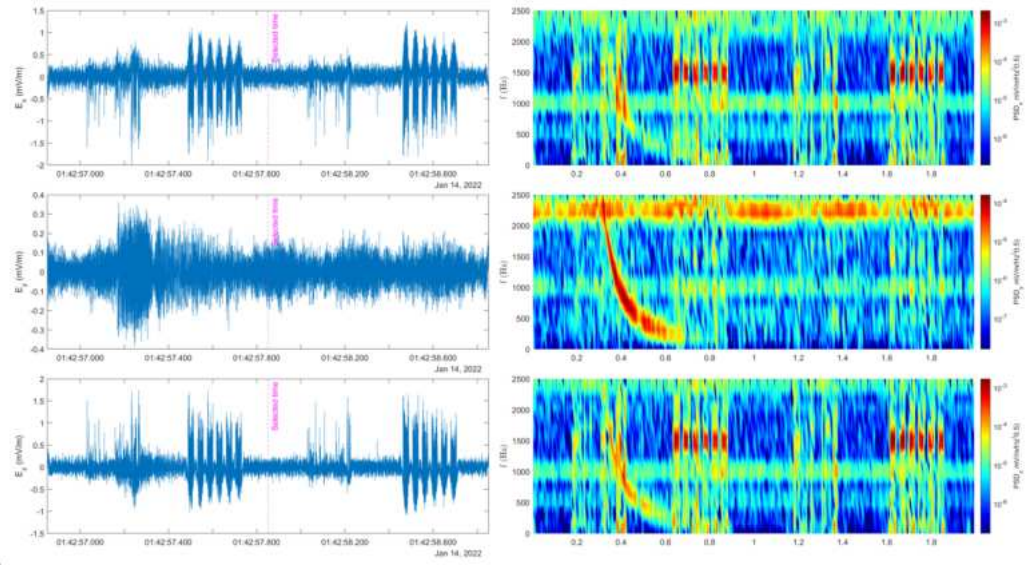

Figure 3.32: Waveforms (left panels) and spectrograms (right panels) in a time window of 1 s around ≈ 01:42:57.850 UT (highlighted by magenta dashed vertical line). X, Y and Z electric field components in the ELF band are from top to bottom.

signal. Specifically, the noise is characterized by beats appearing at ≈ 01:42:57.500 UT and ≈ 01:42:58.600, clearly visible both in the waveform as huge peaks and in the spectrograms as red bands at ≈ 1.5 kHz. They are more pronounced in the X and Z components. In addition, two continuous bands at ≈ 1 kHz and ≈ 2.2 kHz appear on all the three components. As explained in section 3.1.3, the 1 kHz signal corresponds to the plasmaspheric hiss; the ≈ 2.2 kHz signal could be the second harmonics of the same signal. Due to the noise, the typical chirped shape of the spectrogram is hidden in the X and Z components, remaining well visible only on Y. In addition, because of the noise, the 3D behaviour of the electric field oscillations strongly differs from the magnetic field one, as showed in figure 3.33b, winch show the 3D perspective view of the magnetic (left panel) and electric (right panel) signal. As from the right panel, the main electric field oscillations appear to occur along the X direction, in contrast to the magnetic field, where they occur approximately on the YZ plane.

The peculiar behaviour of the electric field is confirmed by the PCA. The percentage of the total variance explained by each PCA component is shown in figure 3.34, for magnetic and electric field in the right and left panel respectively. As from the right panel, PC1E explains more than 90 % of the variance, suggesting the linear polarization, approximately along the X axis. However, keeping in mind that the mechanical noise affecting the EFD is more pronounced on the X component, it is easy to understand that this behaviour is an artefact induced by the noise. In fact, even if PC2E and PC3E explains only the ≈ 10 % of the variance, they have comparable intensity, suggesting a residual circular polarization, which would be in agreement with the magnetic field behaviour. The latter (left panel) is characterized by two principal components, each explaining ≈ 50 % of the variance, confirming its circular polarization.

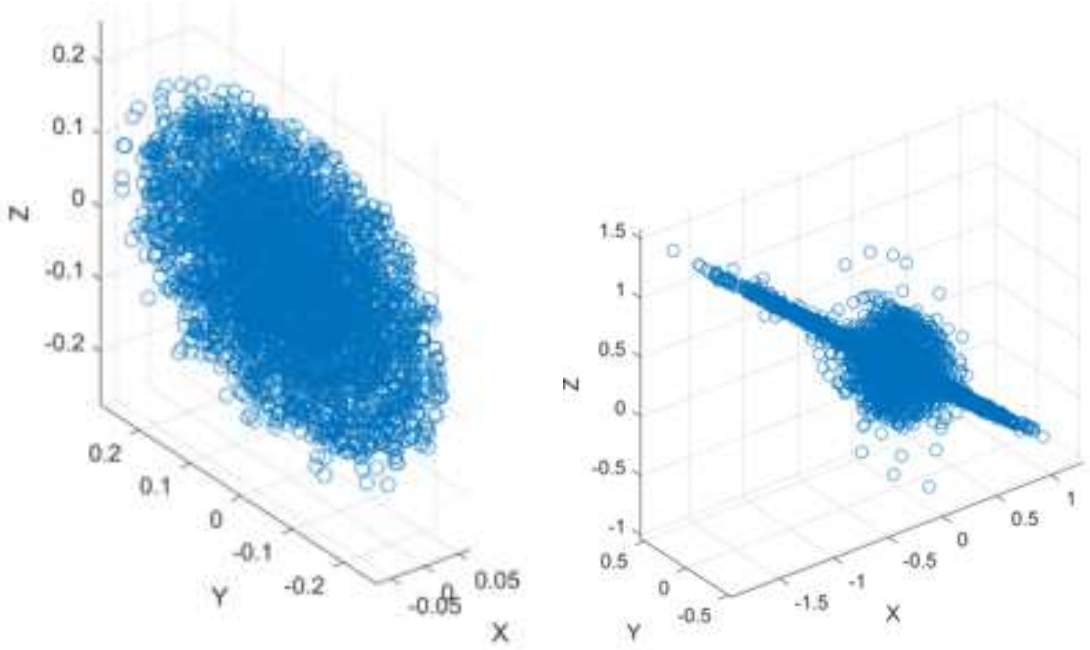

(a) (b)

Figure 3.33: 3D perspective view of magnetic (left) and electric (right) field oscillations.

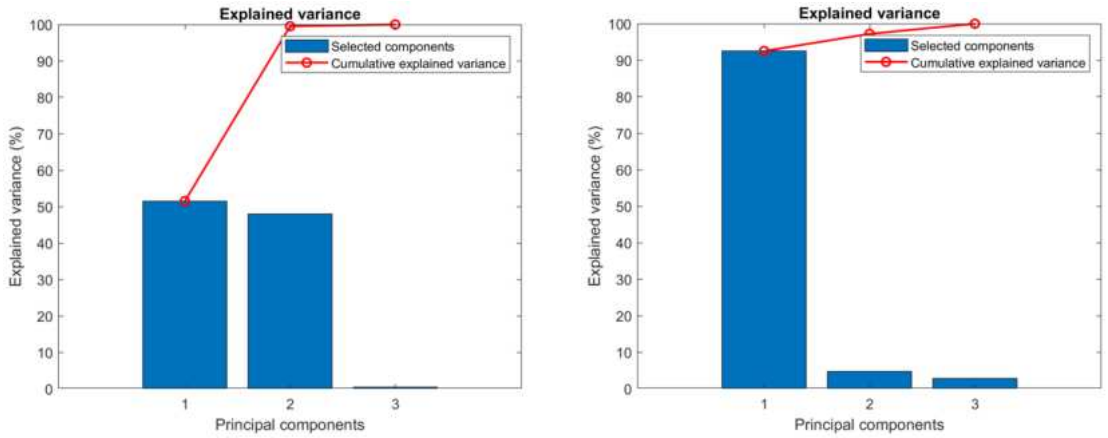

(a) Magnetic field. (b) Electric field.

Figure 3.34: Percentage of the total variance explained by each PCA component for the first event: PC1 (left), PC2 (central), and PC3 (right). The red circles show the cumulative value.

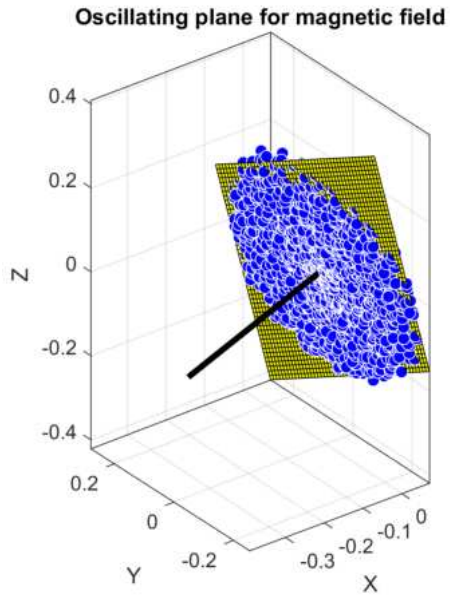

Figure 3.35: Oscillating plane for the magnetic field and perpendicular direction to the plane indicated by the black segment.

In order to determine the physical characteristics of the chirped signal (and eventually link it to its source), we need to remove the noise affecting electric field observations. To this scope, we assume that the signal is an electromagnetic wave. Under such assumption, the electric field oscillations should lie on the same plane of the magnetic field ones. Therefore, we used the magnetic field observations to determine the oscillation plane, since as shown in figure 3.33a its oscillations lie on a plane. The equation of such plane is obtained by fitting a polynomial surface of degree one to the magnetic field observations. The results of such procedure are shown in figure 3.35, where the oscillation plane is represented by the yellow surface, the direction of propagation by the black line and the magnetic field observations by the blue dots.

Therefore, we followed the steps (2-5) described above to clean the electric field observations from the noise, as sketched in figure 3.36. The figure shows the application of the procedure for the X component, but the same was done also for the Z one (not shown). We did not apply the procedure to the Y component, since, as shown in figure 3.32, it is less affected by noise with respect to X and Z. In the figure, the electric field observations are shown by blue dots, the neglected observations by red crosses and the oscillation plane by the yellow surface.

Figure 3.37 shows the effects of the various steps (2-5 from top to bottom) of the procedure on both waveform (left panels) and spectrogram (right panels) of the EFD observations (X component). Figure 3.38 shows the waveforms (left) and spectrograms (right) for all the three components of the cleaned signal.

As can be seen by comparing figure 3.32 and 3.38, the procedure performs very well in cleaning up the signal. In fact, in the cleaned spectrograms (right panels of figure 3.38, the chirped structure of the signal become clearly visible. In addition, the effects of the beats affecting the X and Z components are completely removed both from spectrograms and waveforms.

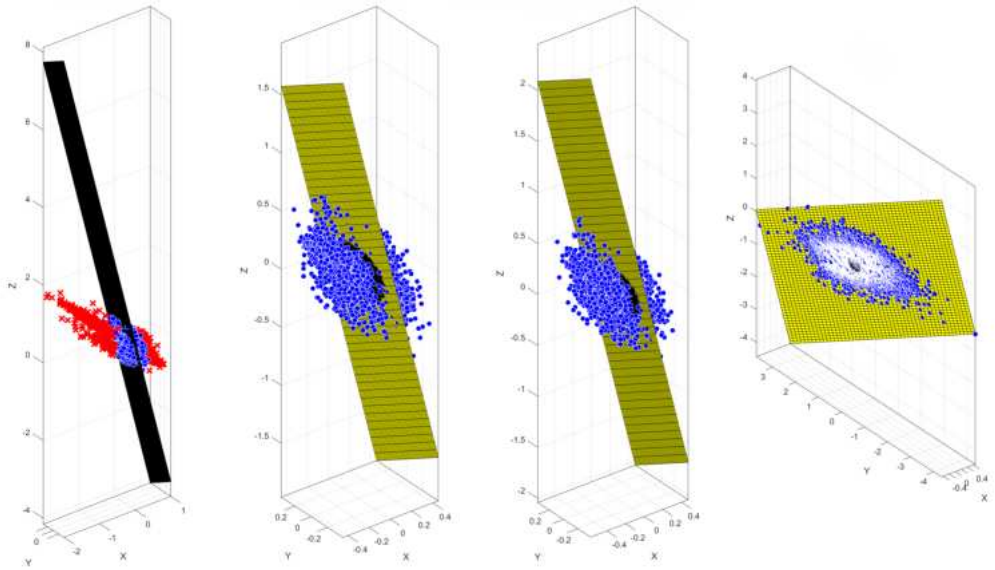

Figure 3.36: From left to right, sketch of the procedure steps used to remove the noise on EFD observations (X component): 2 - neglecting electric field observations whose distance from the oscillation plane exceeds the threshold, 3 - filling the missing part of the signal though interpolation, 4 - applying a high-pass filter, 5 - 5 projecting onto the oscillation plane.

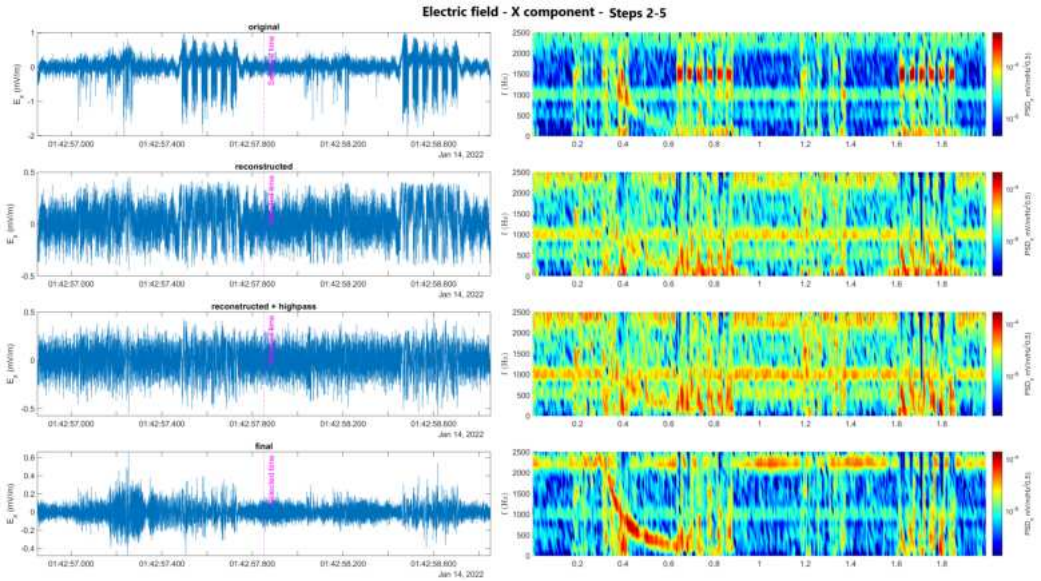

Figure 3.37: Waveforms (left) and spectrograms (right) for the X component of the electric field after the application of steps 2-5 from top to bottom.

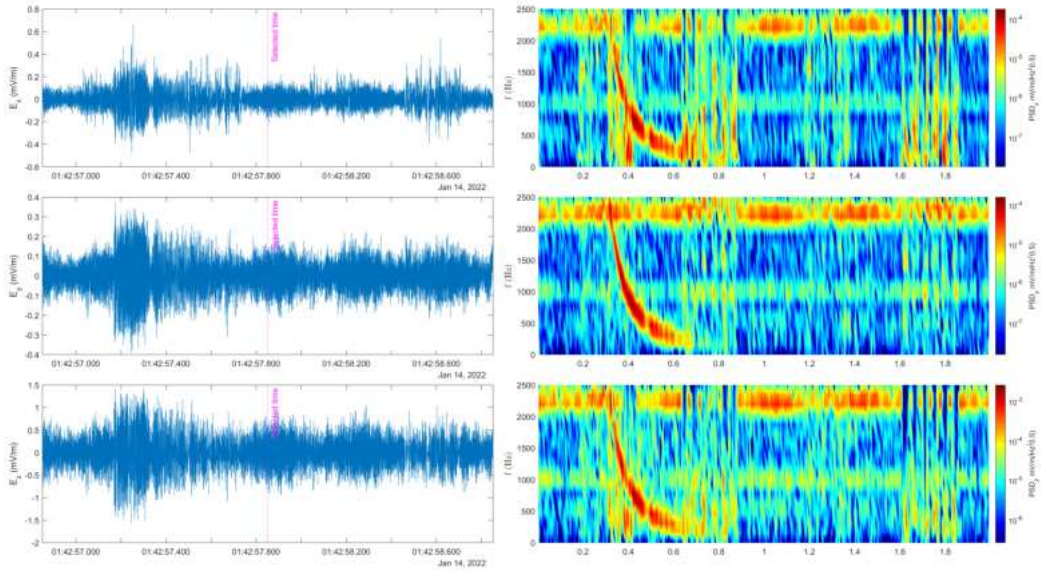

Figure 3.38: Waveforms (left) and spectrograms (right) for the cleaned signal (X, Y and Z components from top to bottom).

Once the signal is cleaned, the same joint electric and magnetic field analysis described in case 1 can be applied.

3.2.4 Ionospheric short-time signals: discussion

To detect short-duration signals, we conducted a joint analysis of spectrograms and IPSD. In several cases, the latter show significant spikes, enabling the immediate identification of the timing of potentially interesting signals. Relying on these plots, we developed an algorithm able to detect whistler waves in the ionosphere. This algorithm allowed to build a large database of events, specifically $\approx$ 24000 detected whistlers in $\approx$ 3 years of data. Compared to other works (e.g. Tarcsai, Szemeredy, and Hegymegi [255], that found 985 whistlers in four years and a half recorded at Tihany, Hungary) the dataset is orders of magnitude bigger. Therefore, the detection algorithm presented here represents a very fast and efficient way to detect whistlers in the top-side ionosphere on a large time-scale.

Such large number of events allowed us to perform a statistical analysis to study possible patterns in the occurrence of this kind of events, whose results are summarized as follows:

- $\approx 60\%$ of the orbits have no events, $\approx 20\%$ of the orbits have one event, $\approx 10\%$ of the orbits have two events and so on, with the number of events per orbits exponentially decreasing;

- this behaviour shows no geomagnetic conditions dependence at all, demonstrating that these events are not induced by external forcing;

- there is a remarkable geographical dependence, in fact, there are regions with a high density of events (e.g. southeast Asia, central America) and regions with few or no events at all (e.g. Sahara Desert);
- there is a clear seasonal dependence, in fact, a higher concentration of events is observed at the end of the local summer.

Such behaviour suggests that a significant portion of these events are attributable to neutral atmospheric processes. Notably, the spatial distribution of these events closely resembles the global lightning distribution recorded by the World Wide Lightning Location Network (WWLLN) and the National Lightning Detection Network (NLDN), as illustrated in Collier et al. [63] and Bitzer [32]. Moreover, the seasonal distribution of these events aligns with the findings reported in Dowdy and Kuleshov [77] and in Holle, Cummins, and Brooks [120]. In the first, the authors observed an increase in lightning activity from November to April in Australia. Similarly, in the second, authors identified a similar trend in summer months in North America. Consequently, our extensive database of events serves as a valuable resource for the rapid identification of lightning-related phenomena. As demonstrated in Section 3.2.3, our selection algorithm effectively detected volcanic-induced lightning events.

In order to determine the characteristics of the whistler waves, we developed two different tools for the joint analysis of electric and magnetic field. In both tools, SCM data are the starting point, since they are cleaner. In fact, EFD data exhibit high level of noise in the low-latitude phase of the orbit, especially on the X and Z component. The two tools differ in the way they clean up the electric field data. In fact, tool 1 relies on Iterative Filtering (see section 3.2.3), while tool 2 on the physical properties of the EM wave (see section 3.2.3). The latter is faster (in terms of computational time) and has a better interpretability, since it relies only on physical considerations. In addition, for the same reason, it is not affected by mathematical artifacts due to the signal decomposition technique. However, it requires the identification of the oscillation plane from SCM observations. Specifically, it is suitable only for waves exhibiting circular (or elliptic) polarization, but not for linearly polarized waves. On the contrary, tool 1 can be applied to every signal, even if it requires longer computational time. In any case, as shown in sections 3.2.3 and 3.2.3, they both perform exceptionally well in the noise removal, allowing to detect the typical chirped structure of the whistler waves.

Through the study of the three components of both electric and magnetic field and a PCA, we were able to identify the direction of the main oscillations for both electric and magnetic field confirming their perpendicular oscillations and therefore obtaining, as expected, the characteristics of an electromagnetic wave. This confirms the validity of the procedure used to characterize the oscillation and propagation direction of the signal.

To summarize, our analysis tool is able to:

- identify the chirped signal from the IPSD plot on SCM data;
- finding its counterpart on EFD data after cleaning it with pre-processing tools;
- study the waveforms of the three components of both electric and magnetic field, that appear as an oscillatory structure;

- determine the frequency of the oscillatory structures with the spectrograms, that reveal falling tone chirps;
- determine amplitude and duration of the signal;
- determine the orientation of the signal in the 3D space;
- determine the direction of main oscillations (this step allows us also to verify that these signal are electromagnetic waves);
- determine the characteristics of the detcted electromagnetic waves (polarization, propagation direction...).

In particular, the exact determination of the propagation direction is an important feature to investigate the source of such signals, since we are able to determine if the signal is propagating upward, downward or along the magnetic field line.

Chapter 4

Numerical simulations of wave-particle interactions in ionospheric plasmas

In addition to electromagnetic anomalies, increases in particle flux, referred to as particle bursts (PBs), have been reported in association with large seismic events (see e.g. Anagnostopoulos, Vassiliadis, and Pulinets [12], Battiston and Vitale [20]). Indeed, numerous studies over the past decades have suggested a concurrent occurrence of energetic particle flux variations and ELF-VLF electromagnetic activity in correspondence to (or even before) large earthquakes (Pulinets and Boyarchuk [220], Sgrigna et al. [239], Aleksandrin et al. [5], Anagnostopoulos et al. [11], Fidani, Battiston, and Burger [83], Sidiropoulos, Anagnostopoulos, and Rigas [242]).

Previous studies have demonstrated that particle precipitation events can be induced through the interaction of plasma with electromagnetic waves. For instance, Imhof et al. [132], Imhof et al. [133] reported on the precipitation of energetic electrons from the radiation belts due to controlled injection of VLF radio waves from the ground. In particular, whistlers are the main source of particles precipitation via the whistler electron precipitation (WEP) mechanism (Dungey [78], Rodger, Clilverd, and McCormick [228]) due to the resonant interaction between circularly polarized VLF waves propagating along the geomagnetic field lines and trapped electrons. The interaction results in electrons deflection in the loss cone and their consequent precipitation.

However, to date, the underlying mechanisms connecting seismic-related electromagnetic processes to satellite-detected particle precipitation events remain elusive. In addition, a comprehensive analytical model capable of explaining observed EM perturbations and PBs is still missing. The lack of detailed investigation into these processes introduces uncertainty regarding the expected time delay between the two phenomena. This poses challenges for repeatability and confirmation of reported findings across different studies, even when employing identical methodologies or analyzing the same parameters (Picozza, Conti, and Sotgiu [213]). Consequently, the temporal distribution of claimed seismo-related phenomena exhibits significant variability (Picozza, Conti, and Sotgiu [213]).

To assess these issues, numerical simulations were conducted to model wave-particle inter-

actions in a plasma environment replicating ionospheric conditions. Specifically, the evolution of the ion velocity distribution function (VDF) was examined to determine the potential formation of fast ion beams, which could lead to particle precipitation.

The following sections provide the theoretical basis for the description of wave-particle interactions. For a comprehensive exploration of plasma physics, waves in plasmas and wave-particle interactions, interested readers are referred to Gendrin [101], Goldston [107], Chiuderi and Velli [54], Stix [249], Tsurutani and Lakhina [262], Koch [153].

4.1 The need for a kinetic modelling of the ions

The appropriate approach for plasma description hinges on the characteristic length scale (Colonna and D'Angola [64]). The spectrum of plasma treatment ranges from the microscopic, exact description given by the Klimontovich equation (Klimontovich [152]) combined with the Maxwell equations, to the macroscopic fluid description provided by magnetohydrodynamics (MHD, see e.g. Cowling [67], Roberts [227], Moreau [191], Wang et al. [283]). The MHD approach, treats the plasma as a single, ionized fluid, which is inadequate for investigating WPIs and thus unsuitable for our investigation. On the other side, while the Klimontovich equation provides a complete picture of plasma behaviour, its computational demands for large-scale systems are prohibitive. A good compromise between accuracy and tractability is given by the the statistical approach of kinetic theory (Brambilla [36], Swanson [253]), which offers an intermediate description between the two approaches, bridging the gap between microscopic and macroscopic scales.

The standard kinetic theory involves the introduction of the phase space distribution function f_α^D for each plasma specie α, given by:

$$f_\alpha^D(\vec{x}, \vec{v}, t) = \frac{dN_\alpha}{dx^3 dv^3} \tag{4.1}$$

where $\vec{x}$ and $\vec{v}$ are respectively the position and the velocity of the (large) number of N particles composing the plasma. This quantity represents the probability of finding a particle in the infinitesimal element of the six dimensional phase space $dxdydz\ dv_x dv_y dv_z$ around the point ($\vec{x}$,$\vec{v}$) at time t.

Instead of the particle number N_α, it is often used number density $n_\alpha = dN_\alpha/dx^3$ and consequently the velocity distribution function (VDF) is introduced, defined as:

$$f_\alpha(\vec{x}, \vec{v}, t) = \frac{dn_\alpha}{dv^3} \tag{4.2}$$

From now on, we will drop the subscript α.

4.1.1 From the Boltzmann to the Vlasov equation

As detailed in many plasma physics textbooks (e.g. Treumann and Baumjohann [259], Stix [249], Bittencourt [31]), it is possible to show that, under general conditions, the single-particle distribution function f satisfies the Boltzmann (or kinetic) equation:

$$\left[\frac{\partial}{\partial t} + \vec{v}\cdot\frac{\partial}{\partial \vec{x}} + \frac{q}{m}\left(\vec{E}(\vec{x},t) + \vec{v}\times\vec{B}(\vec{x},t)\right)\cdot\frac{\partial}{\partial \vec{v}}\right] f(\vec{x},\vec{v},t) = C\frac{\partial f}{\partial t}\bigg|_C \tag{4.3}$$

where the term in the right side represents inter-particle collisions (usual expressions for this term are the Krook (Bhatnagar, Gross, and Krook [26]) or Fokker-Plank (Belli and Candy [22]) collision models).

However, ideal plasmas are referred to as collisionless, as they are dominated by collective interactions rather than collisions. When this condition is valid, electrostatic interactions prevail over the processes of ordinary gas kinetics. For these kind of plasma the collisional term can be neglected and the right side of the kinetic Boltzmann equation vanishes. Thus, the so called Vlasov equation (Vlasov [274]) is obtained:

$$\left[\frac{\partial}{\partial t} + \vec{v}\cdot\frac{\partial}{\partial \vec{x}} + \frac{q}{m}\left(\vec{E}(\vec{x},t) + \vec{v}\times\vec{B}(\vec{x},t)\right)\cdot\frac{\partial}{\partial \vec{v}}\right] f(\vec{x},\vec{v},t) = 0 \tag{4.4}$$

4.1.2 Macroscopic quantities: moments of the VDF

The macroscopic quantities described by fluid models can be obtained by integrating equation 4.2 in the velocity space with an appropriate weight (see e.g. Treumann and Baumjohann [259]). In particular, the sources of Maxwell equations (i.e. the charge density $\rho(\vec{x},t)$ and current density $\vec{J}(\vec{x},t)$) can be obtained from the moments of order 0 and 1 of the VDF:

$$\rho(\vec{x},t) = q\int dv^3 f(\vec{x},\vec{v},t) \tag{4.5}$$

$$\vec{J}(\vec{x},t) = q\int dv^3 \vec{v} f(\vec{x},\vec{v},t) \tag{4.6}$$

The Vlasov and Maxwell equations, with ρ and J as functions of the VDF, form a complete set of non-linear integro-differential equations in the variables $\vec{E}$, $\vec{B}$ and f. Consequently, variations in the electric or magnetic field directly influence the motion of charged particles within the plasma, leading to alterations in their VDF. Conversely, changes in the VDF can also induce modifications in the electric or magnetic fields. Indeed, the main goal of this study is to examine the evolution of the VDF in response to plasma perturbations driven by WPIs.

4.2 Wave-particle interactions

WPIs constitute the core of this investigation. Such processes involve the exchange of energy and momentum between electromagnetic waves and particles, resulting in modifications of particles velocity distribution. One of the most prominent example of WPI is the Landau damping (Mouhot and Villani [193], Misra and Brodin [189]), which is shown in figure 4.2. When an electromagnetic wave interacts with particles in a plasma, it accelerates particles moving at slightly lower velocities than its phase velocity, v_{ph}, and slows down the faster ones. Consequently, wave loses energy from the former interaction and gains energy from the

latter (Tsurutani and Lakhina [262]). Since the particles in an equilibrium plasma follow the Maxwellian distribution ($f(v_x) = \frac{1}{\sqrt{2\pi v_{th}^2}} \exp\left(\frac{-v_x^2}{2v_{th}^2}\right)$, Belmont et al. [23], see figure 4.1), there are always more particles with lower velocity (in the absolute value sense; see figure 4.1). In the Maxwell distribution, v_{th} is the thermal velocity, i.e. the typical velocity of the thermal motion of particles that make up a gas. Therefore, the number of particles getting accelerated is always higher than the number of particles slowed down and the total electromagnetic energy of the wave is decreasing. This results in a "flattening" of the distribution function around the wave phase velocity.

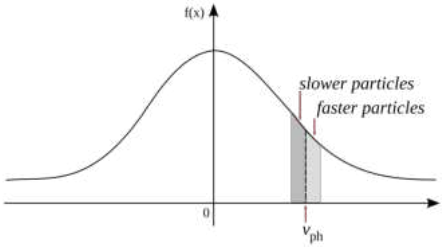

Figure 4.1: Maxwellian distribution: where the slope of the distribution function is negative, the number of particles with $v < v_{ph}$ is greater than the number of particles with $v > v_{ph}$.

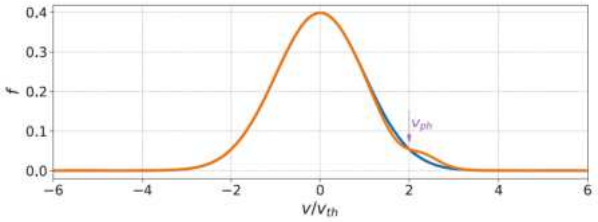

Figure 4.2: Landau damping: a wave with phase velocity $v_{ph} = 2v_{th}$ is interacting with an equilibrium particle distribution (blue). The interaction results in the "flattening" of the distribution around v_{ph} (orange). From: Cagas [38].

The previous example illustrates the particle-scale nature of WPIs. However, even waves at fluid scales can indirectly interacts with the plasma. Specifically, EM waves may interact with one another through wave-wave interaction (WWI) processes, resulting in the generation of waves at ion (or electron) scales.

4.2.1 The parametric instability as a driver for WPIs

WWIs are fundamental processes in space plasma physics. They involve the exchange of energy and momentum between different electromagnetic waves, significantly influencing the propagation and characteristics of waves (Vladimirov and Popel [273], Nazarenko, Newell, and Zakharov [200]). In particular, these processes may be responsible for the generation of new waves at ion scale, that can be susceptible to wave-particle interactions. Indeed, at the heart of WWIs lies the concept of nonlinearity, which asserts that the behavior of a system cannot be fully described by the superposition of its individual components (Nayfeh and Balachandran [199]). When electromagnetic waves interact with each other, the nonlinear properties of the medium can lead to complex interactions that result in new wave modes, energy transfer, and wave phenomena that are not present in the absence of interactions (Zaslavski [302]). In this way, waves at fluid scale can interact and generate (through WWIs) waves at ion scale, interacting with the plasma. This is the case of parametric instabilities (see Hollweg [121] and reference therein), which are a class of wave-wave interactions characterized by the decay

of Alfvén waves of finite-amplitude. These are nonlinear processes where the coupling between a mother (or pump) wave and a compressive acoustic-like perturbation (and other electromagnetic fluctuations) leads to different parametric instabilities, depending on the plasma characteristics. The most known of these parametric instabilities is the so-called parametric decay instability (see e.g. Goldstein [106]). This process is characterized by the excitation of a compressive wave having a larger wave vector k_s than the mode k_M of the mother wave. The interaction leads to an energy transfer from the pump wave to the acoustic wave, which grows in amplitude, and to another reflected Alfvén wave (daughter wave) with $k_r < k_M$. This three-wave process satisfies the condition: $k_r = k_s - k_M$ so that the reflected wave is always backward propagating.

4.3 Numerical simulations of wave-particle interactions in the ionosphere

For our purposes, modelling the plasma particles VDF is necessary to investigate potential modifications resulting from the interaction of the plasma with EM waves. However, as we aim to simulate a very low beta plasma, our simulations poses a significant computational challenge, since an elevated spatial resolution is needed. In this context, full particle-in-cell (PIC) simulations represent the most comprehensive numerical tool for simulating the plasma dynamics down to electron spatial and temporal scales (see e.g. Svidzinski et al. [252], Saito, Gary, and Narita [235], Chang, Peter Gary, and Wang [47], Camporeale and Burgess [40], Gary, Chang, and Wang [100], Wan et al. [282], Karimabadi et al. [144], Wan et al. [281], Wan et al. [280]). However, they employ limited accuracy (in terms of spatial resolution, small number of particles, small ion-to-electron mass ratio...) due to computational limitations (Franci et al. [86]). Since for our investigation a high resolution and a large number of particles are needed, and we do not need to model the dynamics of individual electrons, we opted for a HPIC (hybrid particle in-cell) code (Verscharen et al. [272], Vasquez and Markovskii [268], Vasquez, Markovskii, and Chandran [269], Ozak, Ofman, and Viñas [204], Parashar et al. [207], Parashar and Matthaeus [206]). A hybrid model differentiates the treatment of various plasma components by representing part of the plasma as particles and the rest as a fluid (see Winske [293] for a review). In particular, for our purposes, it is sufficient to model the ions VDF explicitly, while the electrons can be treated as a fluid.

Hybrid simulations lie between MHD and full-PIC simulations. Given that the ionosphere is a multi-species plasma, we have opted for CAMELIA (Current Advance Method Et cycLIc leApfrog) among hybrid codes. This choice is motivated by CAMELIA's advantage of enabling the straightforward treatment of multiple ion species (Matthews [183]). Furthermore, in recent years, the code has produced significant outcomes that are highly consistent with experimental findings (Franci et al. [88], Franci et al. [90], Franci et al. [86]).

In the following paragraph we provide a brief description of the code. A comprehensive documentation can be found on the CAMELIA website:

http://terezka.asu.cas.cz/helinger/camelia.html.

4.3.1 The hybrid code CAMELIA

The CAMELIA code treats ions as macro-particles, statistically-representative portions of the distribution function in the phase space, while electrons are described as a massless, charge neutralizing fluid (Franci et al. [86]). In the model, the dynamic of the plasma is governed by the following Vlasov-fluid equations (Matthews [183]):

$$\frac{d\mathbf{x}_i}{dt} = \mathbf{v}_i \tag{4.7}$$

$$\frac{d\mathbf{v}_i}{dt} = \frac{q_i}{m_i}\left(\mathbf{E} + \mathbf{v}_i \times \mathbf{B}\right) \tag{4.8}$$

$$\frac{\partial \mathbf{B}}{\partial t} = -\nabla \times \mathbf{E} \tag{4.9}$$

$$\nabla \times \mathbf{B} = \mu_0 \mathbf{J} \tag{4.10}$$

$$n_e m_e \frac{d\mathbf{u}_e}{dt} = -n_e e\mathbf{E} + \mathbf{J}_e \times \mathbf{B} - \nabla p_e \tag{4.11}$$

$$p_e = n_e k_B T_e \tag{4.12}$$

where $\mathbf{x}_i$, $\mathbf{v}_i$, q_i and m_i are ion position, velocity, charge and mass respectively; $\mathbf{E}$ and $\mathbf{B}$ the electric and magnetic field; μ_0 the magnetic permeability, $\mathbf{J}$ the current density; n_e, m_e, u_e and e the electron number density, mass, fluid velocity, and charge respectively; $\mathbf{J}_e = -n_e e U_e$ is the electron current density, p_e is the electron fluid pressure, k_B is the Boltzmann constant and T_e the electron temperature.

The subscript i may denote individual particles belonging to an ion species with particle mass m_i and charge q_i. Alternatively, it may refer to collective quantities evaluated for species i, such as n_i and $\mathbf{J}_i$ which are defined using other related quantities as follows:

$$n_i = \int f_i(\mathbf{x}_i, \mathbf{v}_i)\, d^3\mathbf{v}_i \tag{4.13}$$

$$(nu)_i = \int \mathbf{v}_i f_i(\mathbf{x}_i, \mathbf{v}_i)\, d^3\mathbf{v}_i \tag{4.14}$$

$$\mathbf{u}_i = \frac{(n\mathbf{u})_i}{n_i} \tag{4.15}$$

$$q_c = \sum_i n_i q_i \tag{4.16}$$

$$q_m = \sum_i n_i m_i \tag{4.17}$$

$$\mathbf{J}_i = q_i n_i \mathbf{u}_i \tag{4.18}$$

$$\mathbf{J}_I = \sum_i \mathbf{J}_i \tag{4.19}$$

$$\mathbf{J} = \mathbf{J}_i + \mathbf{J}_e \tag{4.20}$$

where $f_i(\mathbf{x}_i, \mathbf{v}_i)$ is the species distribution function; n_i, $(n\mathbf{u})_i$, $\mathbf{u}_i$, the species particle number density, "velocity density" and fluid velocity respectively. Q_c and Q_m are the are the charge density and mass respectively; $\mathbf{J}_i$ is the species current density and $\mathbf{J}_I$ the ionic current density.

The assumption that electrons are a massless, charge-neutralizing fluid implies that:

$$m_e = 0 \tag{4.21}$$

$$n_e e = Q_c \tag{4.22}$$

Equation 4.11, using equations 4.10 and 4.20, can be rearranged to obtain an expression for the electric field:

$$E = -\frac{\mathbf{J}_i \times \mathbf{B}}{Q_c} + \frac{(\nabla \times \mathbf{B}) \times \mathbf{B}}{\mu_0 Q_c} - \frac{\nabla p_e}{Q_c} \tag{4.23}$$

so that $E = E(Q_c, J_i, B, T_e)$ is a state function. Substituting 4.23 into 4.9 gives:

$$\frac{\partial B}{\partial t} = \nabla \times \frac{\mathbf{J}_i \times \mathbf{B}}{Q_c} - \nabla \times \frac{(\nabla \times \mathbf{B} \times \mathbf{B})}{\mu_0 Q_c} \tag{4.24}$$

The first term describe induction and the second dispersion. Therefore, the electron pressure in equation 4.12 does not influence magnetic field evolution.

The code is based on the Current Advance Method and Cyclic Leapfrog (CAM-CL) scheme by Matthews (for a complete description, see Matthews [183]). In essence, the leapfrog scheme for particle advance is the midpoint method (Bowers, Dror, and Shaw [35]) applied to equation 4.8 along with a time-centred integration of equation 4.7. A time-step Δt is introduced, and quantities relative to t_0 are evaluated at different time levels t_k as follows:

$$x(t_k) = x(t_0 + k\Delta t) \tag{4.25}$$

In the end, the differential equations are rewritten as difference equations:

$$x^{1/2} = x^{-1/2} + \Delta t v^0 \tag{4.26}$$

$$v^1 = v^0 + \Delta t \frac{q}{m}(E^{1/2}(x^{1/2}) + v^{1/2} \times B^{1/2}(x^{1/2})) \tag{4.27}$$

where we have denoted quantities at different time levels with superscript ($x(t_k) \equiv t^k$).

4.3.2 Wave-particle interactions: numerical setup

In the code, the characteristic spatial unit is represented by the ion inertial length d_i, which is the scale at which ions decouple from electrons and the magnetic field becomes frozen into the electron fluid rather than the bulk plasma. It is defined as: $d_i = c/\omega_i$, where $\omega_i = (4\pi n_i q_i^2/m_i\epsilon_0)^{1/2}$ is the plasma frequency of the ion species i (i.e. the oscillation frequency of ion species i), n_i, q_i and m_i are respectively the number density, charge and mass of the ion species i and ϵ_0 is the permittivity of free space. Units of time are expressed in terms of

the inverse ion cyclotron frequency Ω_i^{-1}, which is defined as $\Omega_i = (4\pi n q_i^2/m_i)^{1/2}$ and represents the angular frequency of the circular motion of an ion i in the plane perpendicular to the magnetic field B_0. The amplitude B of the perturbing wave is expressed in unit of the ambient magnetic field $B_0 \equiv 1$. The velocities are expressed in unit of the Alfvén velocity $v_A = B_0/(4\pi n_i m_i)^{1/2}$, which is the speed of waves resulting from ions oscillations in response to the restoring force provided by an effective tension on the magnetic field lines (see Iwai et al. [135], Cramer [68], Chen and Zonca [51]).

Here we summarize the numerical setup of our modelling:

- **1D domain**: due to the high computational demands of our simulations, we choose to employ a one-dimensional domain that coincides with the x direction. It is important to note, however, that vector quantities (such as the magnetic field and ion velocity) are fully resolved in all three components (x, y, z) at every point within this 1D domain.

- Δx: we guarantee a spatial resolution Δx of the order of $5 \cdot 10^{-2} d_i$, in agreement with other works employing the same hybrid code (e.g. Matteini et al. [182], Franci et al. [89]). The spatial resolution is defined as $\Delta x = L_{box}/N_x$, where L_{box} is the length of the 1D domain (expressed in unity of d_i) and N_x is the number of cells of the domain.

- **ppc**: the number of particle per cell. We always employ a $ppc = 10^4$ or greater to prevent non-physical effects such as numerical heating (Markidis and Lapenta [179], Horkỳ, Miloch, and Delong [126], Alves, Mori, and Fiuza [10]). This number is of the same order of magnitude or even greater with respect to other works in literature employing the same hybrid code (Matteini et al. [182], Franci et al. [89], Franci et al. [87]).

- **Perturbing wave**: we perturb the plasma with different small-amplitude Alfvén waves (Alfvén and Lindblad [7]) directed along the ambient magnetic field B_0 (i.e. in the positive direction of the x-axis). The wave has amplitude B, wave-number W_0 and wave vector $k_M = k_0 W_0$, where $k_0 = 2\pi/L_{box}$ is the minimum wave vector distinguishable with our setup. Wave vectors are expressed in terms of d_i^{-1}. Henceforth, the wave perturbing the plasma will be denoted as the "mother" or "pump" wave. Polarization of the wave can be right (+) or left (-). We investigated also the effects of changing the wave polarization in the evolution of ion VDF.

- **Plasma beta**: the plasma beta is the ratio of the plasma pressure ($p_{i,e} = n_{i,e} k_B T_{i,e}$ to the magnetic pressure ($p_{mag} = B^2/2\mu_0$). This value is an input parameter in the code both for ions species i (β_i) and electrons e (β_e).

We have selected values that allow for a very good description of the particle distribution function with low numerical noise (Matteini et al. [182]). Therefore, the configuration permits the investigation of both wave-particle and wave-wave interactions, also accounting for deviations of the ion VDF from Maxwell-Boltzmann equilibrium due to non-linear coupling between particle and waves.

4.4 Simulation results

4.4.1 Testing the apparatus

To validate our numerical framework, we initially replicate the findings presented in Matteini et al. [182] before gradually transitioning to our target conditions. In their study, the authors employed numerical simulations within a hybrid regime to investigate the evolution of Alfvén waves under modulational and decay instabilities, incorporating the effects of ion kinetics. Their results indicated that ion dynamics significantly influence instability growth and saturation, notably with the observation of proton acceleration parallel to the magnetic field. Specifically their run B examined the impact of a right-handed Alfvén wave with $B/B_0 = 5 \cdot 10^{-2}$ impacting on a single species plasma with $\beta_i = 0.01$ and $\beta_e = 0.1$, finding a parametric decay and, as a consequence, a ballistic velocity beam aligned with the ambient magnetic field. Nevertheless, in replicating these results, we opted for a wave vector k_M closer to the ion kinetic scale, aligning with our objectives. Furthermore, we investigated the impact of the variation of k_M on the evolution of the VDF by employing boxes of different lengths in run A, B and C, whose input parameters are shown in table 4.1.

run	β_e	β_i	B/B_0	W_0	Pol.	$L_{box}(d_i)$	$k_0(d_i^{-1})$	$k_M(d_i^{-1})$	ppc
A	$1 \cdot 10^{-2}$	$5 \cdot 10^{-2}$	$5 \cdot 10^{-2}$	20	+	121.6	0.05	1.03	10^4
B	$1 \cdot 10^{-2}$	$5 \cdot 10^{-2}$	$5 \cdot 10^{-2}$	20	+	60.8	0.1	2.07	10^4
C	$1 \cdot 10^{-2}$	$5 \cdot 10^{-2}$	$5 \cdot 10^{-2}$	20	+	243.2	0.025	0.52	10^4

Table 4.1: Run A, B and C parameters.

Run A

Figure 4.3 (left panel) shows the temporal evolution of kinetic energy E_K (black dashed line), magnetic energy E_M (blue line) and the total energy E_T (green line) during the simulation. This plot serves as a verification of energy conservation, confirming that the numerical setup is correct. As energy conservation is consistently observed in our simulations, this analysis will be omitted from run B onward.

Figure 4.3 (right panel) reports the trend of $E_K/E_{K,0}$, $E_M/E_{M,0}$ and $E_T/E_{T,0}$ with $E_{K,0}$, $E_{M,0}$ and $E_{T,0}$ being the kinetic, magnetic and total energy at time $t = 0$ respectively. This plot illustrates the conservation of total energy while energy is transferred from the magnetic field to the ion kinetic energy. This transfer initiates at $t \approx 100$ and continues until $t \approx 300$ where the E_K reaches a plateau and remains approximately constant. During the initial phase ($t \leq 50$), the plot exhibits numerical noise due to the spatial grid discretization. This is a common artefact of PIC simulations (Matteini et al. [182]). However, through the choice of a high number of ppc, the noise level was maintained at a low level of approximately 10^{-3}.

To verify the occurrence of a parametric decay (as in Matteini et al. [182]) and to study the dynamics of the system it is useful to introduce the energy E^+ and E^-, associated with the backward (daughter) and forward (mother) Alfvén propagation and defined by: $E^{\pm} = (B \pm v)^2$ (both B and v are in Alfvén units, with B expressed in terms of B_0 and v in terms of v_A,

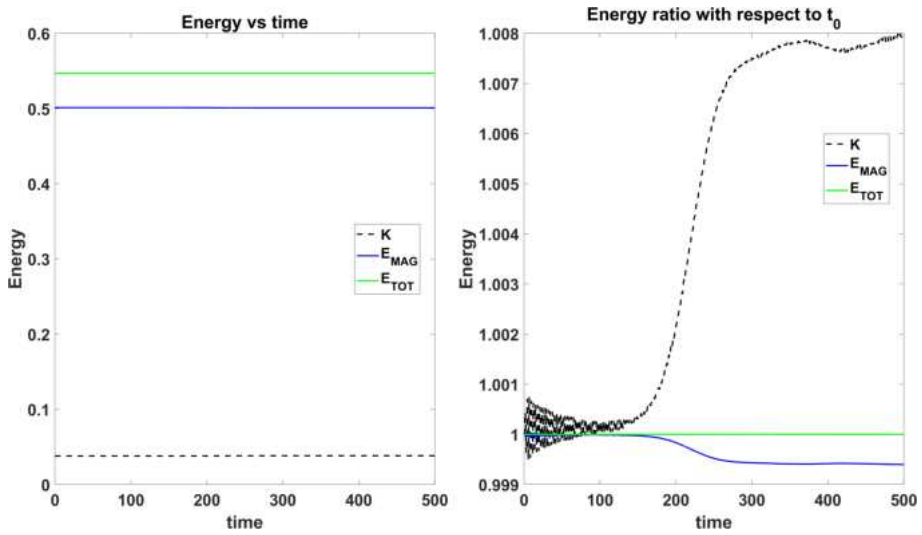

Figure 4.3: Left panel: E_K (black dashed line), E_M (blue line) and E_T (green line). Right panel: $E_K/E_{K,0}$, $E_M/E_{M,0}$ and $E_T/E_{T,0}$.

Matteini et al. [182]). In addition, the evolution of the cross helicity $\sigma = (E^+ - E^-)/(E^+ + E^-)$ is examined as a measure of the prevailing mode (Matteini et al. [182]).

Figure 4.4a shows the temporal evolution of $E^+/E^-(0)$ (red line) and $E^-/E^-(0)$ (blue line), which exhibit an opposite behaviour increasing (decreasing) in time and having the same value at t approximately between 200 and 250. At the same time, the cross helicity, whose temporal evolution is shown in figure 4.4b, is equal to zero, meaning that backward and forward waves have the same energy. This behaviour is consistent with findings reported in Matteini et al. [182], confirming the occurrence of parametric decay.

The outcome of this parametric decay can be elucidated by examining the wave spectrum at different times (figures 4.5a, 4.5b and 4.5c). The figures show the power spectra of the y component of the magnetic field (blue) and density (black) at $t = 0$, $t = 190$ and $t = 480$ respectively. To facilitate a clearer visualization of temporal evolution, the plot for times $t > 0$ also includes the corresponding values at $t = 0$ as thinner dashed lines of the same color. The mother wave perturbing the system has wave number $W_0 = 20$, which corresponds to the magnetic energy peak at $k = 1.03$ in the blue line in figure 4.5a (as highlighted by the blue thin vertical line). At time $t = 0$ no other signatures are present in the spectra. The decay generates a higher frequency compressive acoustic-like wave, as described in Matteini et al. [182]. This wave appears as a peak on the density (black line) at $k_s \approx 2$ in figures 4.5b and 4.5c (evidenced by the vertical black line). Simultaneously, a lower frequency backward Alfvén wave arises, corresponding to the second peak in the magnetic field fluctuations at $k \approx 0.9$ in figure 4.5b (vertical dashed blue line). As the time progresses, this second peak surpasses the first one, as can be seen in figure 4.5c. These observations align with the resonant condition for wave numbers in parametric decay: $k_r = k_M - k_s$.

A comparative analysis of figures 4.5b and 4.5c reveals that, subsequent to the linear growth phase of the acoustic mode (which persists until approximately $t \simeq 190$), the instability enters

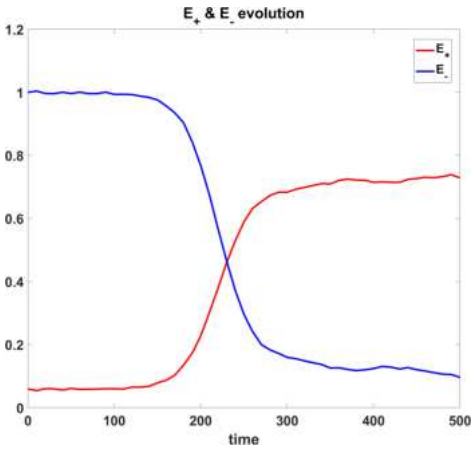

(a) Temporal evolution of $E^+/E^-(0)$ (red line) and $E^-/E^-(0)$ (blue line)

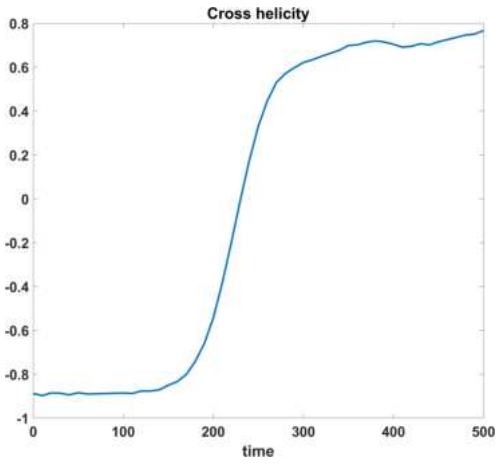

(b) temporal evolution of cross helicity.

Figure 4.4: E^+, E^- and cross helicity for run A

a saturation phase, marked by a cessation in the density peak's growth. Nevertheless, nonlinear wave interactions continue to occur during this post-saturation regime (Matteini et al. [182]). This is well illustrated in ion VDF plots presented in figure 4.6 for times $t = 0, 200, 250, 460$. The VDFs are depicted in the plane defined by the parallel ($\|$) and perpendicular ($\perp$) direction with respect to the ambient magnetic field (directed along x), with velocities normalized to the Alfvén velocity (v_A) such that the x-axis indicates $v_\|/v_A$ and y-axis $v_\perp/v_A$. To enhance the visualization of temporal evolution, the VDF at $t = 0$ is overlaid as thinner gray contours for comparison. At $t = 200$ (figure 4.6b), when the peak on the density is approximately at its maximum, the VDF begins to deviate from its initial state and undergo rapid evolution, as evidenced from figures 4.6c and 4.6d, representing the ion VDF at $t = 250$ and $t = 460$ respectively.

As previously mentioned, a saturation phase commences around $t \approx 300$, attributed to particle trapping, a well-established mechanism for suppressing wave growth in collisionless plasmas (Matteini et al. [182]). Within this kinetic regime, this process yields two significant consequences: firstly, wave-wave interactions and parametric decay are modified relative to fluid-based predictions due to kinetic effects (Inhester [134], Vasquez [266], Araneda [14], Nariyuki and Hada [197, 196] and Araneda, Marsch, and Vinas [15]); secondly, trapping and associated wave-particle interactions stemming from the saturation phase can substantially influence ion dynamics. A direct consequence of trapping is the acceleration of particles that resonate with the wave, leading to the formation of a faster ion population.

This phenomenon is clearly visible looking at a perpendicular cut of the ion VDF. To this end, we define a parallel VDF obtained with a perpendicular cut as $\hat{f}(v_\|) \equiv f(v_\|, v_{\perp=0})$ and a perpendicular VDF obtained with a parallel cut as $\hat{f}(v_\perp) \equiv f(v_\| = 0, v_\perp)$. Figure 4.7 shows $\hat{f}(v_\|)$ at various times. Here, the gray line represents the initial distribution ($t = 0$), while the colored curves correspond to $t = 200$ (4.7a) and $t = 460$ (4.7b). At $t = 200$, the distribution

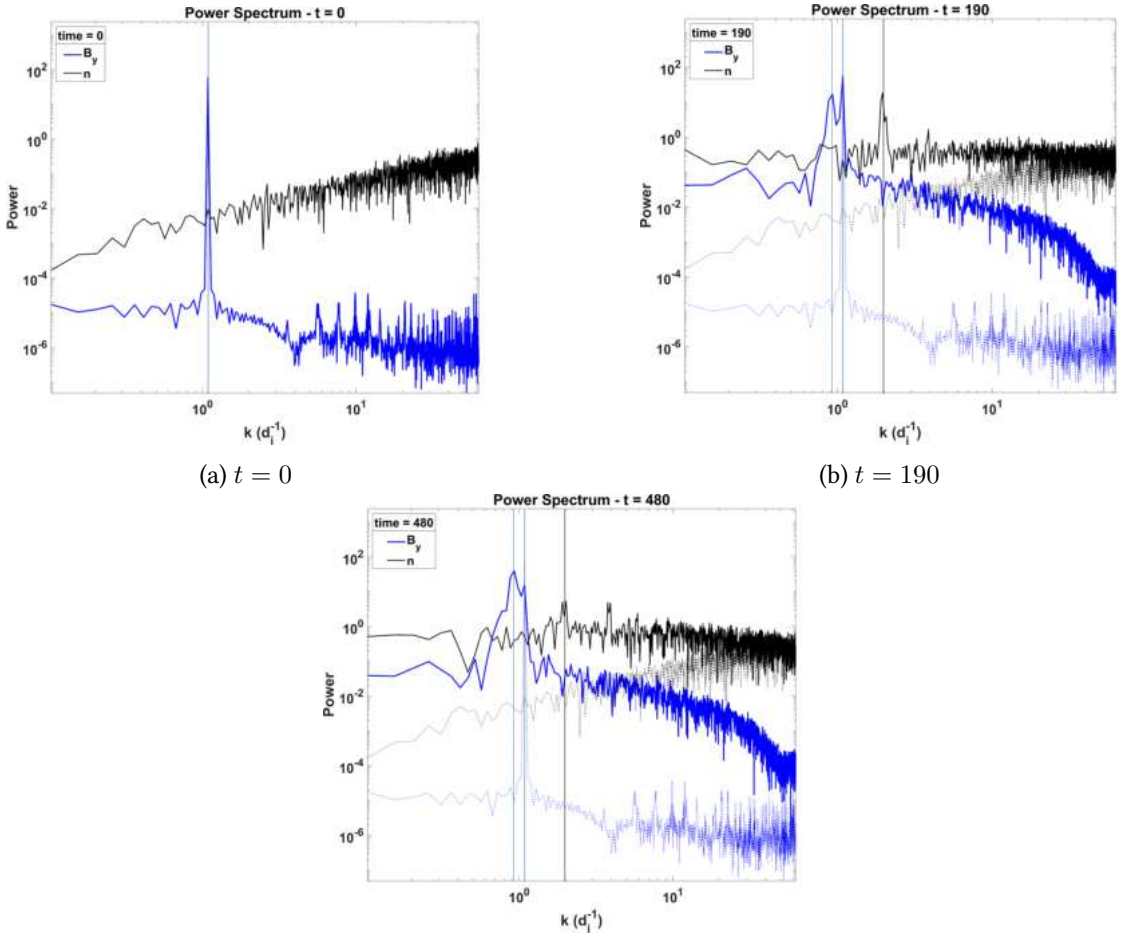

(a) $t = 0$

(b) $t = 190$

(c) $t = 480$

Figure 4.5: Power spectrum of the y component of the magnetic field (blue) and ion density (black). Values at $t = 0$ are overlaid as thinner dashed lines of the same color. Vertical lines highlight significant peaks.

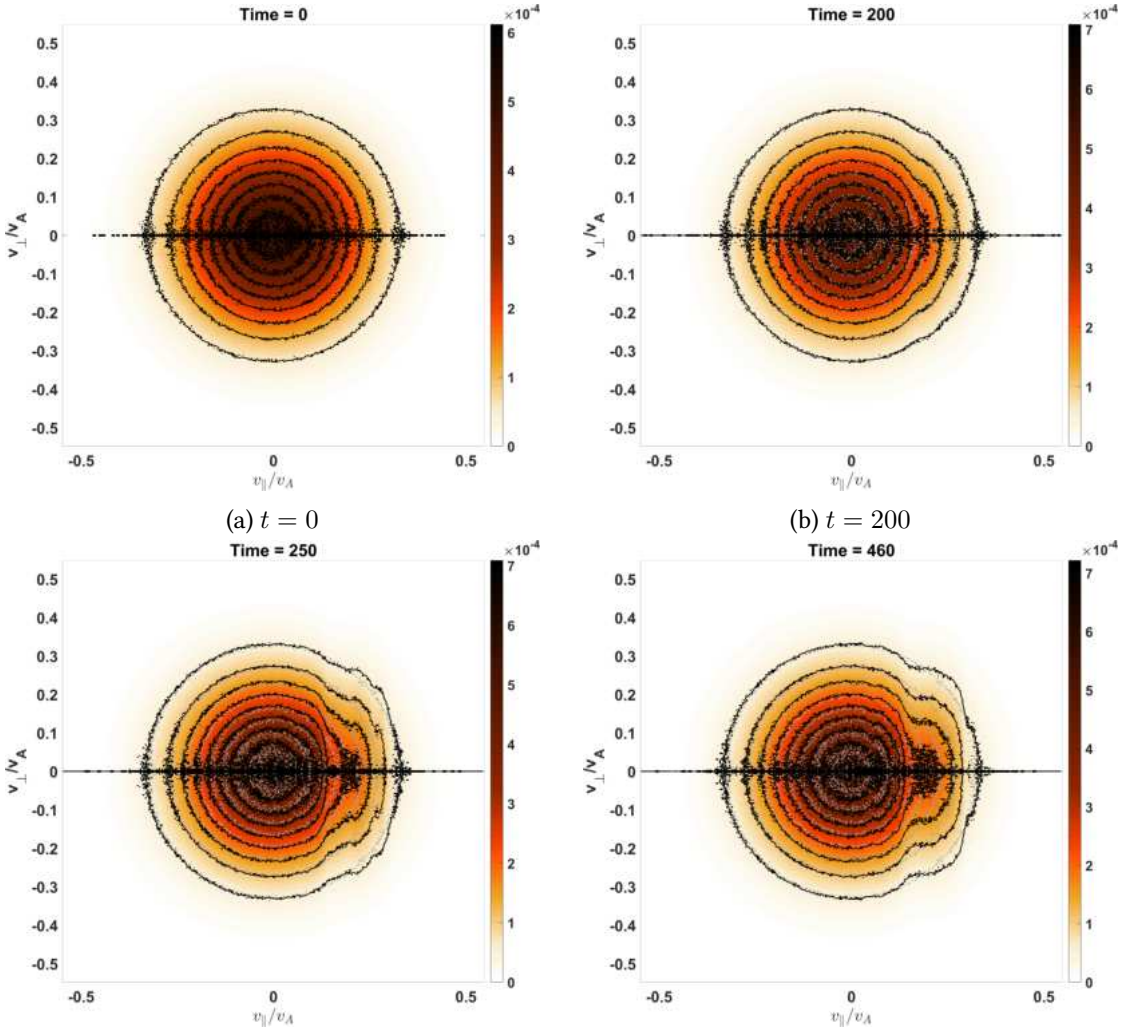

(a) $t = 0$

(b) $t = 200$

(c) $t = 250$

(d) $t = 460$

Figure 4.6: Ion VDF at various times. Grey lines represents the initial configuration.

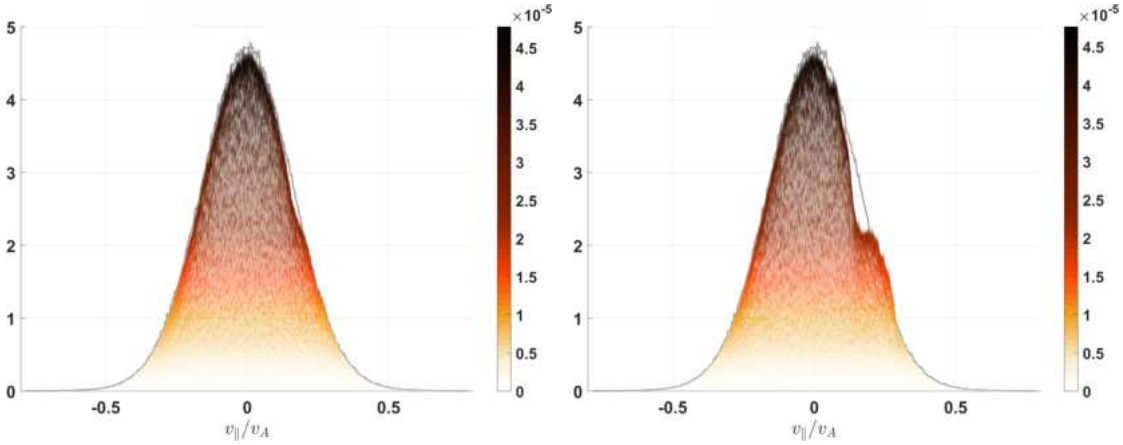

(a) $t = 200$ (b) $t = 460$

Figure 4.7: Ion parallel velocity distribution. Grey lines represents the initial configuration.

exhibits subtle deviations from its initial state. Subsequently, since the excited monochromatic acoustic wave starts to lose its coherence, the trapped particles that are no more confined by the electric potential start to fill in the phase space, producing a ballistic velocity beam aligned with the ambient magnetic field (Matteini et al. [182]). This process results in the emergence of a secondary peak at $v_\parallel/v_A \approx 0.25$, as observed in figure 4.7b.

Run B

For the second run (B), the simulation box length is halved compared to run A, while the mother wave wavenumber, W_0, is maintained at 20, resulting in a doubled wave vector: $k_M = 2.07$. All other parameters remain constant. Since the instability growth rate depends on the mother wave properties, a faster parametric decay is expected, given the halved box length, which reduces the transit time of the wave.

As depicted in figure 4.8, which illustrates the temporal evolution of $E_K/E_{K,0}$, $E_M/E_{M,0}$, and $E_T/E_{T,0}$, a first decrease in magnetic energy accompanied by a corresponding increase in ion kinetic energy is observed at $t \approx 80$. This confirms the faster decay. Notably, a second decay phase emerges at $t \approx 140$.

This behaviour is corroborated by the evolution of E^+ and E^-, as well as by the cross helicity, as depicted in Figure 4.9. The cross helicity intersects zero, signifying equal energy in backward and forward propagating perturbations, twice: at $t \approx 80$ and $t \approx 140$ (figure 4.9b). Correspondingly, E^+ and E^- exhibit equal values and interchange dominance at the same times (figure 4.9a).

Consequently, a double decay process occurs, as substantiated by the wave spectrum evolution illustrated in figure 4.10. At $t = 0$ (figure 4.10a), the spectrum exhibits solely the mother wave peak at $k = 2.07$. Subsequently, a rapid decay process generates a higher frequency compressive wave ($k_s \approx 4$). A density peak (black line) becomes evident at $t = 50$ (figure 4.10a), accompanied by a backward Alfvén wave manifested as a small peak in the blue line at

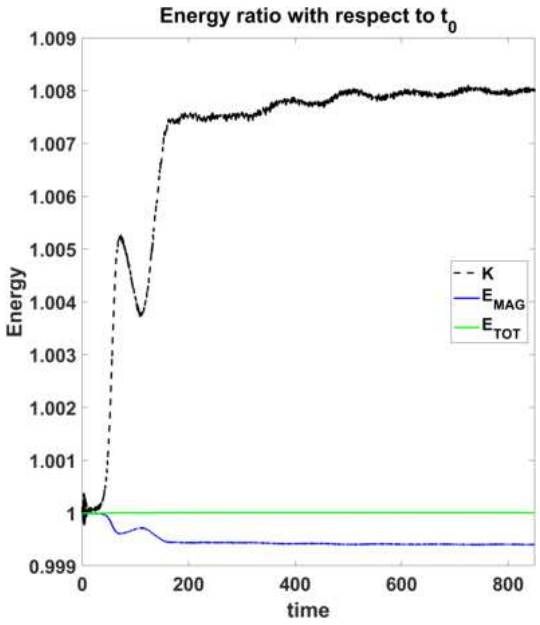

Figure 4.8: $E_K/E_{K,0}$, $E_M/E_{M,0}$ and $E_T/E_{T,0}$ vs time for run B.

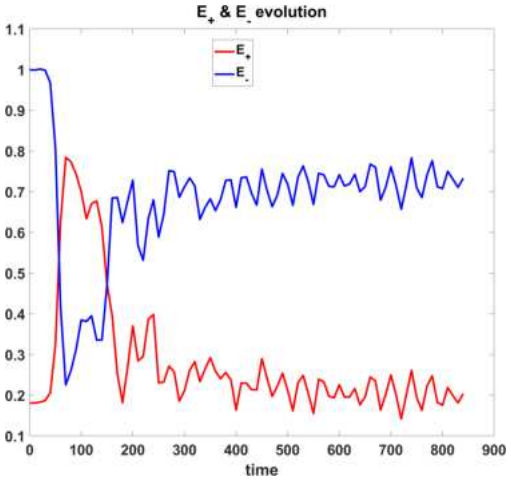

(a) E^+ and E^-

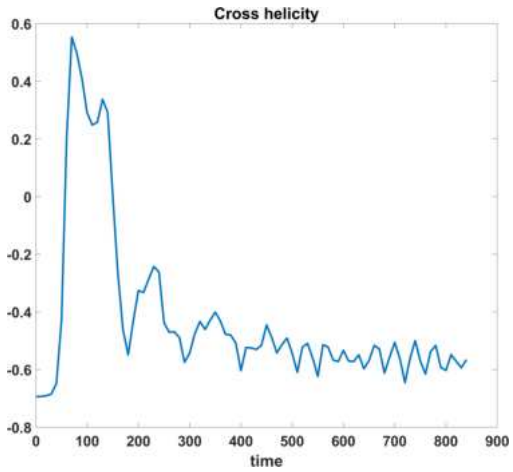

(b) cross helicity

Figure 4.9: Overview of run B.

$k \approx 1.9$ (figure 4.10b). The amplitude of this backward daughter wave peak rapidly escalates, surpassing the original mother wave peak at $t = 80$ (figure 4.10c). The rapid evolution leads to a secondary density peak emerging at $k \approx 3.8$ by $t = 100$ (figure 4.10d). This peak rapidly grows, surpassing the first density peak at $t = 140$ (figure 4.10e). Concurrently, a third peak in the magnetic field develops at at even lower k ($k \approx 1.8$, vertical blue dashed-dotted line), representing a granddaughter wave. This wave quickly becomes the dominant peak, as illustrated in figure 4.10f, showing the spectrum at $t = 200$.

The occurrence of a double decay is substantiated by the generation of both daughter and granddaughter waves. The impact on the ion VDF is visualized in figures 4.11 and 4.12, presenting snapshots of ion VDF and $\hat{f}(v_\parallel)$ at $t = 80$ and $t = 200$, respectively. The former exhibits similarities to run A, with the formation of faster ion populations, corresponding to peaks at $v_\parallel/v_A \approx 0.1$ and $v_\parallel/v_A \approx 0.25$. Subsequently, after the second decay and the emergence of the granddaughter wave, the VDF exhibits a symmetric shape, and ion beams appear also at $v_\parallel/v_A \approx -0.1$ and $v_\parallel/v_A \approx -0.25$.

Run C

For run C, the simulation box length is doubled relative to run A, while the mother wave wavenumber remains constant, resulting in a halved mother wave vector: $k_M(d_i^{-1}) = 0.52$. All other parameters are identical to run A. Consequently, the wave transit time is doubled, suggesting a slower evolution. Furthermore, kinetic effects are expected to be less pronounced due to the simulation being closer to the MHD regime.

The slower evolution is confirmed by figure 4.13, showing the temporal evolution of $E_K/E_{K,0}$, $E_M/E_{M,0}$, $E_T/E_{T,0}$ (4.13a), E^+ and E_- (4.13b), and the cross helicity (4.13c). As expected, the parametric decay occurs at later times in the simulation compared to previous cases. The energy exchange between magnetic and kinetic components takes place at $t \approx 750$ (figure 4.13a). Concurrently, E^+ and E^- attain equal values (figure 4.13b), while the cross helicity is equal to zero (Figure 4.13c), indicating equivalent energy in forward and backward propagating perturbations.

The simulation results closely resemble those of run A, with the sole distinction being a slower evolutionary process. This is corroborated by the evolution of wave spectrum and VDF, as depicted in figure 4.14. In this case, the density peak emerges only after $t = 430$, coinciding with the rise of the daughter wave at a lower wavenumber ($k \approx 0.4$, figure 4.14a). At the same time, the VDF remains virtually unchanged compared to the initial state (figure 4.14c). The density peak grows gradually, and the secondary magnetic field peak, corresponding to the daughter wave, attains equivalence with the original peak at $t = 750$ (figure 4.14b), accompanied by the emergence of a faster ion population at $v_\parallel/v_A \approx 0.2$ (figure 4.14d).

These simulations have served to validate our numerical setup, yielding results consistent with those presented in Matteini et al. [182]. Furthermore, by varying the wave vector of the mother wave, we have explored its impact on the parametric decay rate and its subsequent effects on the ion VDF. As expected, a faster evolution is obtained with the smaller box. Consequently, following simulations will employ the small simulation box to maximize kinetic effects and obtain a rapid evolution. While these initial simulations provide valuable insights into the fundamental physics of parametric instabilities, they are not representative of

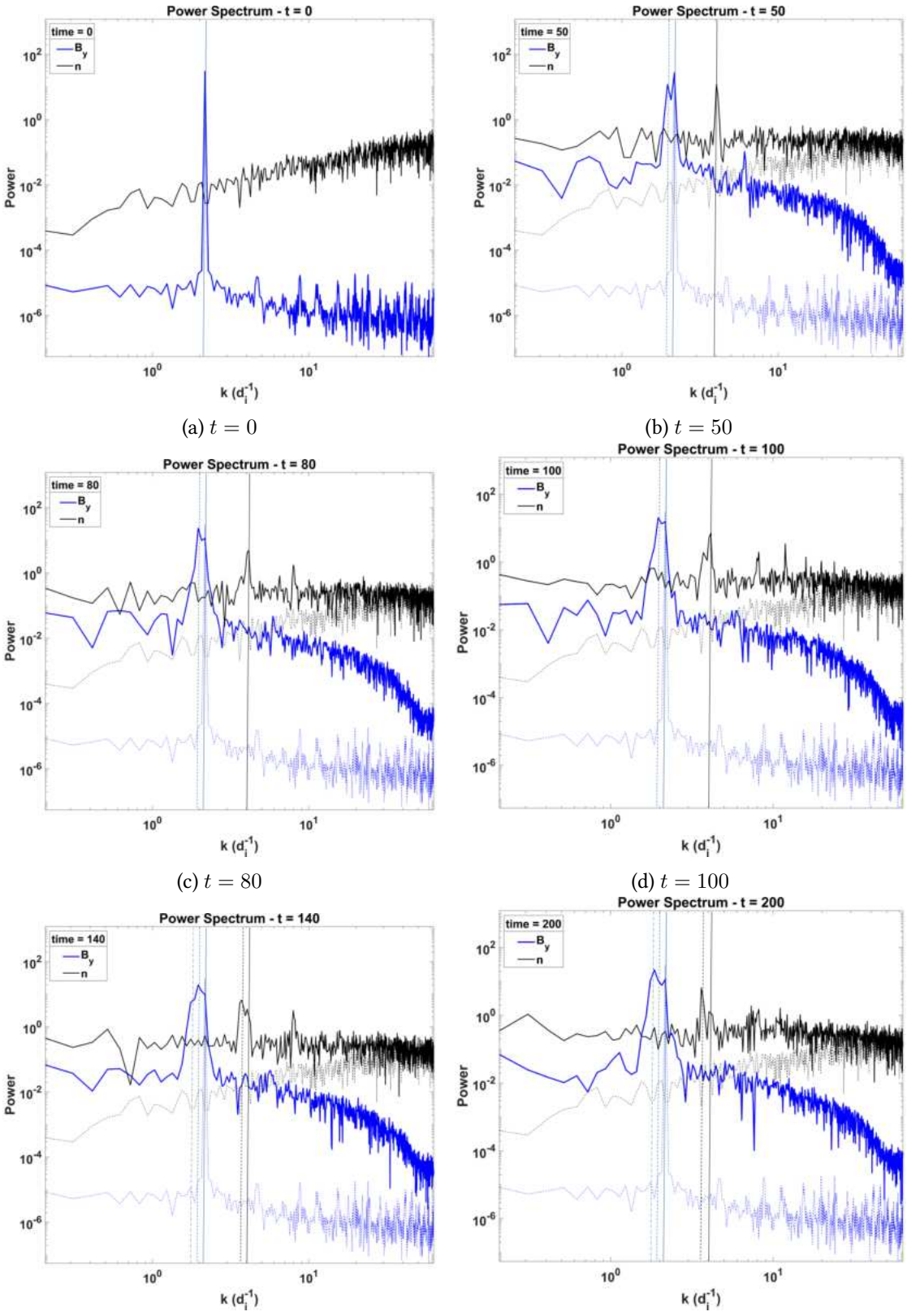

(a) $t = 0$ (b) $t = 50$

(c) $t = 80$ (d) $t = 100$

(e) $t = 140$ (f) $t = 200$

Figure 4.10: Power spectrum of the y component of the magnetic field (blue) and density (black) at various time. Values at $t = 0$ are overlaid as thinner dashed lines of the same color. Vertical lines highlight significant peaks.

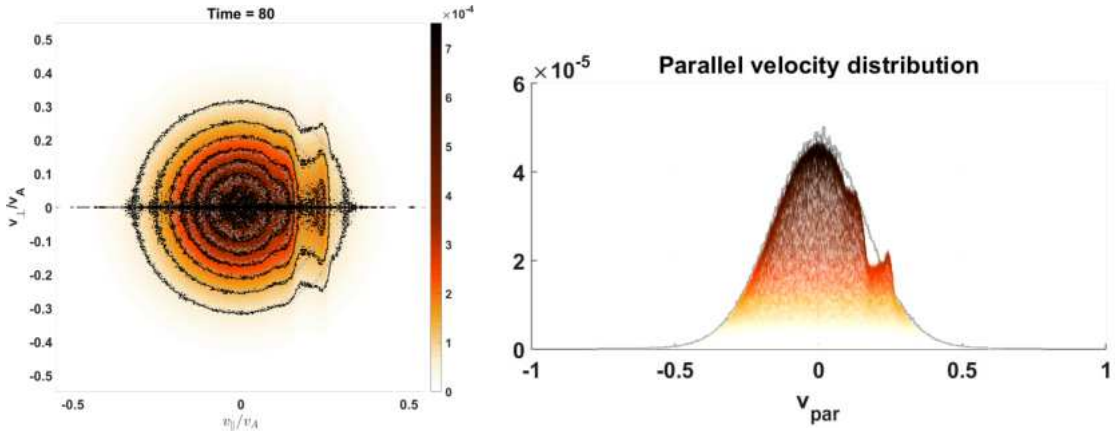

(a) VDF in the $v_{\parallel} - v_{\perp}$ plane (b) $\hat{f}(v_{\parallel})$

Figure 4.11: Ion VDF for run B a $t = 80$.

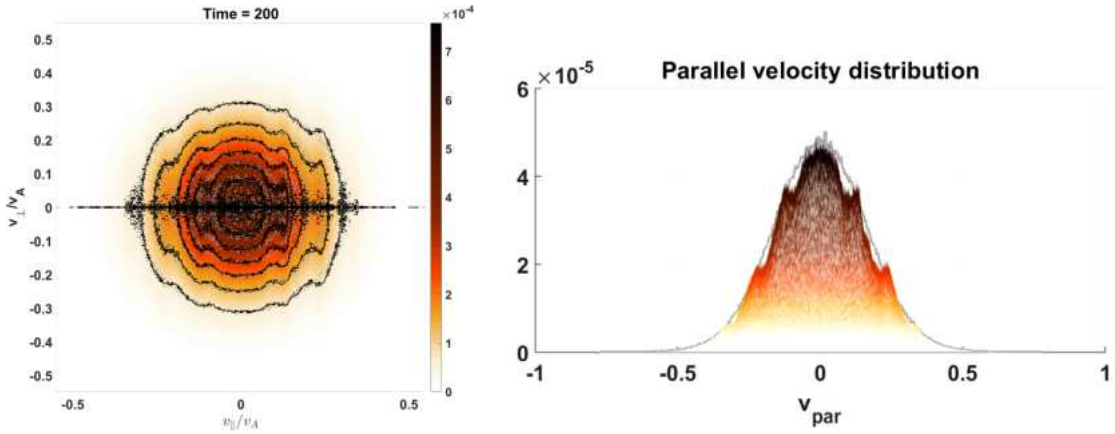

(a) VDF in the $v_{\parallel} - v_{\perp}$ plane (b) $\hat{f}(v_{\parallel})$

Figure 4.12: Ion VDF for run B a $t = 200$.

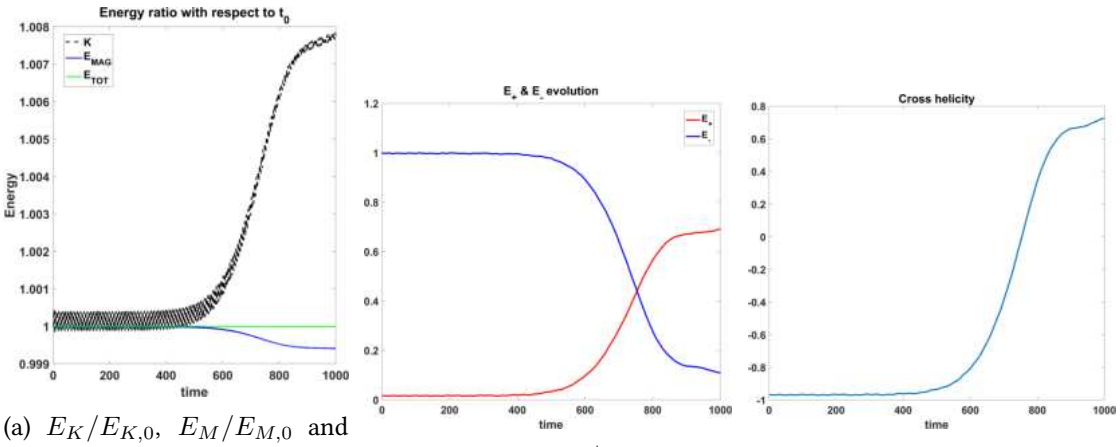

(a) $E_K/E_{K,0}$, $E_M/E_{M,0}$ and $E_T/E_{T,0}$.

(b) Evolution of E^+ and E^-.

(c) Cross helicity vs time

Figure 4.13: Overview of run C.

actual ionospheric conditions. Thus, in following simulations, we will modify the parameters to obtain simulations that model the ionosphere in a more realistic manner.

4.4.2 Towards a more realistic ionospheric environment: lower beta values

The ultimate objective of this study is to model a realistic ionospheric environment at the CSES-01 satellite altitude of approximately 507 km. To achieve this, ionospheric parameters were derived from the International Reference Ionosphere (IRI) model (Bilitza [27]). IRI is an internationally recognized empirical model, sponsored by the Committee on Space Research (COSPAR) and the International Union of Radio Science (URSI), designed to represent the global ionosphere based on a comprehensive dataset. For specified location, time, and date, IRI provides monthly averaged values of electron density, electron temperature, ion temperature, and ion composition across the ionospheric altitude range.

As input parameters for the IRI model, we selected equatorial latitudes, an early morning time, and the year 2021 (a period of low solar activity, being far from the solar maximum) to represent typical ionospheric conditions at 500 km altitude. Based on the IRI model output, table 4.2 was generated, serving as a reference for our ionospheric conditions. The table lists the particle species (s), their percentage composition in the plasma ($\%_s$), temperature (T_s), density (n_s), cyclotron frequency ($\Omega_{g,s}$), Alfvén speed ($v_{A,s}$), plasma beta (β_s), plasma frequency (ω_s) and inertial length (d_s). We include only electrons, protons, and O^+, as these are the primary species composing the plasma at this altitude. Indeed, as visible from table 4.2, H^+ and O^+ constitutes over 98% of the ion composition of the ionosphere.

As evident from table 4.2, a realistic ionospheric simulation necessitates a lower plasma beta compared to previous simulations. Consequently, for following simulations, whose parameters are listed in table 4.3, the beta value was reduced by one order of magnitude (run D) and two orders of magnitude (run E) for both ions and electrons. Additionally, the effects of increasing the ppc count were explored in run E2. Other parameters remain identical with those in run B.

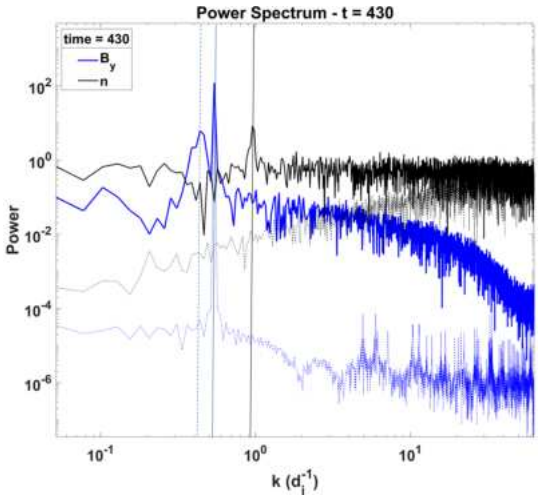

(a) wave spectrum at $t = 430$

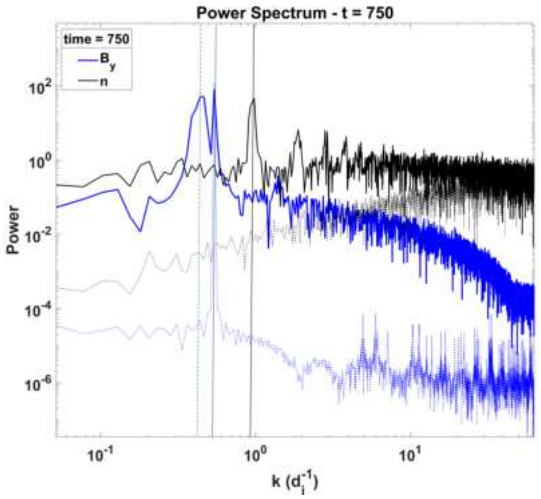

(b) wave spectrum at $t = 750$

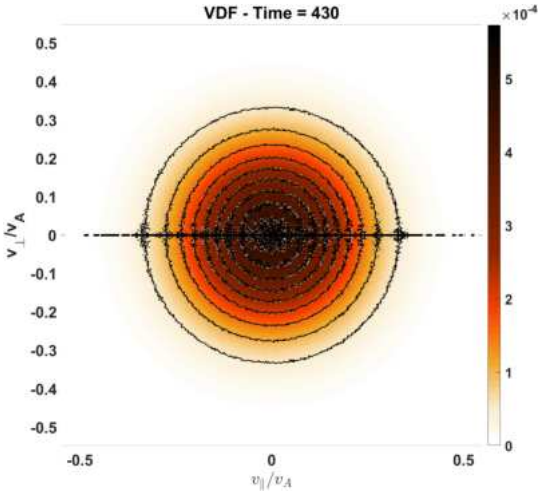

(c) VDF at $t = 430$

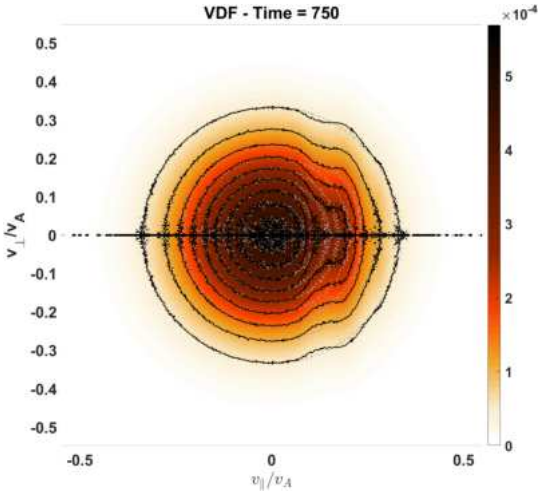

(d) VDF at $t = 750$

Figure 4.14: Wave spectrum and VDF for run C.

s	$\%_s$	T_s (K)	$n_s(m^{-3})$	$\Omega_{g,s}$ (Hz)	$v_{A,s}(m/s)$	β_s	ω_s (Hz)	d_s (m)
e	-	$1.4 \cdot 10^3$	$2.3 \cdot 10^{11}$	$8.4 \cdot 10^5$	$5.8 \cdot 10^7$	$1.3 \cdot 10^{-5}$	$4.3 \cdot 10^6$	11.1
H^+	4.2	$1.1 \cdot 10^3$	$9.7 \cdot 10^9$	457	$6.6 \cdot 10^6$	$4.2 \cdot 10^{-7}$	$2.1 \cdot 10^4$	$2.3 \cdot 10^3$
O^+	93.9	$1.1 \cdot 10^3$	$2.2 \cdot 10^{11}$	29	$3.5 \cdot 10^5$	$9.4 \cdot 10^{-6}$	$2.4 \cdot 10^4$	$2.0 \cdot 10^3$

Table 4.2: Ionospheric parameters.

run	β_e	β_i	B/B_0	W_0	Pol.	$L_{box}(d_i)$	$k_0(d_i^{-1})$	$k_M(d_i^{-1})$	ppc
D	$1 \cdot 10^{-3}$	$1 \cdot 10^{-3}$	$5 \cdot 10^{-2}$	20	+	60.8	0.1	2.07	10^4
E	$1 \cdot 10^{-4}$	$1 \cdot 10^{-4}$	$5 \cdot 10^{-2}$	20	+	60.8	0.1	2.07	10^4
E2	$1 \cdot 10^{-4}$	$1 \cdot 10^{-4}$	$5 \cdot 10^{-2}$	20	+	60.8	0.1	2.07	$8 \cdot 10^4$

Table 4.3: Run D, E and E2 parameters.

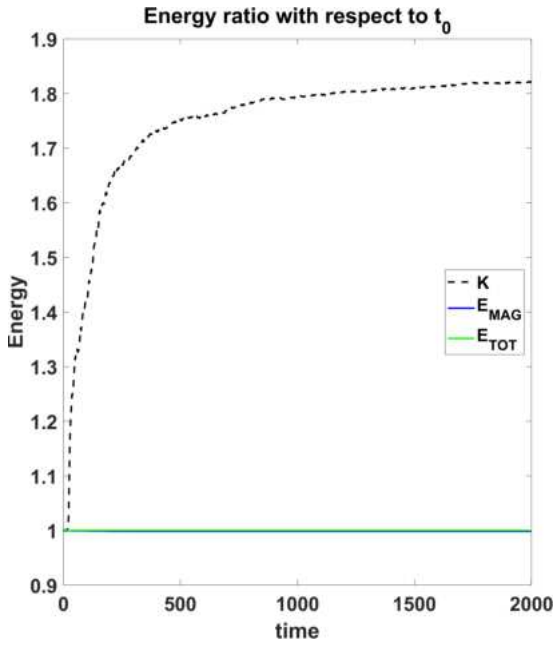

Figure 4.15: $E_K/E_{K,0}$, $E_M/E_{M,0}$ and $E_T/E_{T,0}$ for run D. Saturation occurs at $t \approx 300$.

Run D

Figure 4.15, illustrating the temporal evolution of $E_K/E_{K,0}$, $E_M/E_{M,0}$, and $E_T/E_{T,0}$ for run D, reveals a rapid transfer of energy from the magnetic field to ion kinetic energy, occurring at approximately $t = 20$, followed by saturation at $t \approx 300$.

This rapid evolution is corroborated by the behaviour of E^+ and E^-, as well as the cross helicity, as depicted in figure 4.16. As expected, the cross helicity reaches zero concurrently with the energy transfer from magnetic field to ions (at $t \approx 20$). At this stage, E^+ and E^- attain equal values, indicating balanced forward and backward propagating wave energies. However, in this case, the cross helicity exhibits multiple zero crossings throughout the simulation, accompanied by corresponding changes in the dominance of E^+ and E^-.

A more complex behaviour with respect to previous simulations is also exhibited by the wave spectrum, as shown in figure 4.17. At $t = 20$ a peak on the density has already grown at $k \approx 4$ (figure 4.17a) but no secondary peaks are observed in the magnetic field, suggesting a deviation from a pure parametric decay. The density spectrum evolves rapidly, with several density peaks, corresponding to subsequent harmonics of main peak, appearing at $t = 30$,

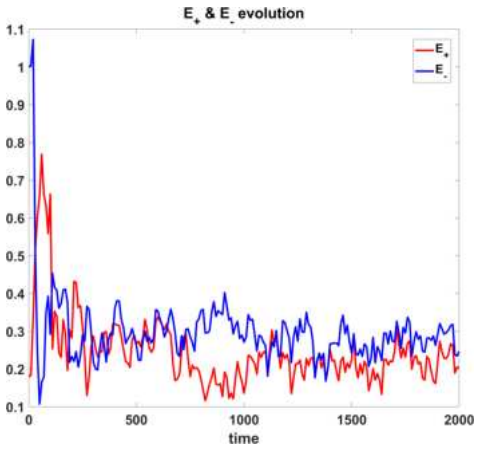

(a) E^+ and E^-

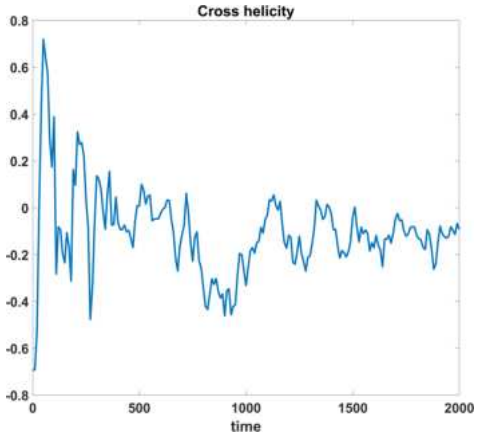

(b) cross helicity

Figure 4.16: Evolution of E^+, E^- and cross helicity for run D.

characterized by $k \approx 8$, $k \approx 12$, $k \approx 16$. Correspondingly, two secondary peaks, one at a lower frequency and the other at a higher frequency with respect to mother wave, emerge in the magnetic field spectrum (figure 4.17b), as well as harmonics at $k \approx 6, 10, 14 \ldots$. At $t = 40$, the first three harmonics on the density are still present, but they exhibit peaks broadened on a quite large range of k values. Concurrently, the peak corresponding to the mother wave disappears, and the two other peaks at lower and higher frequencies also broaden (figure 4.17c). The peaks decrease and vanish fast; at $t = 200$ (figure 4.17d) no major peaks is present, neither on the magnetic field nor on the density, with the exception of a large structure on the magnetic field in a large range from $k \approx 1$ to $k \approx 2$. At greater k values, both magnetic field and density spectra exhibit a power-law behaviour, with magnetic field decreasing more rapidly than the density.

To assess the effect of this peculiar behavior, which differs from previous simulations, on the plasma ions, we studied the evolution of the ion VDF. The results are presented in figure 4.18.

At $t = 20$, even if a peak on the density is already present, there is no daughter wave visible on the magnetic field (figure 4.17a) and the VDF exhibits no deviation with respect $t = 0$. At $t = 30$ and $t = 40$, two additional peaks emerge in the magnetic field spectrum flanking the mother wave peak, at lower and higher k values (figures 4.17b and 4.17c). As a consequence, the VDF results symmetrically modified in both sides of parallel direction, with ion populations generated in both positive and negative parallel velocity domains (figure 4.18b). Subsequently, the density and magnetic field peaks diminish and vanish before $t = 200$ (figure 4.17d). However, velocity beams aligned with the ambient magnetic field persist. Indeed, the VDF at $t = 200$ (figure 4.18c) reveals populations of even faster ions in both sides of parallel direction, although with reduced symmetry. The VDF evolution then exhibits oscillatory behaviour, with the oval shape in the $v_\parallel$-$v_\perp$ plane undergoing slight expansion and contraction, as evident from comparing figures 4.18c and 4.18d. This oscillation stabilizes at later times, with the VDF at $t = 1500$ (figure 4.18e) and $t = 2000$ (figure 4.18f) showing minimal differences.

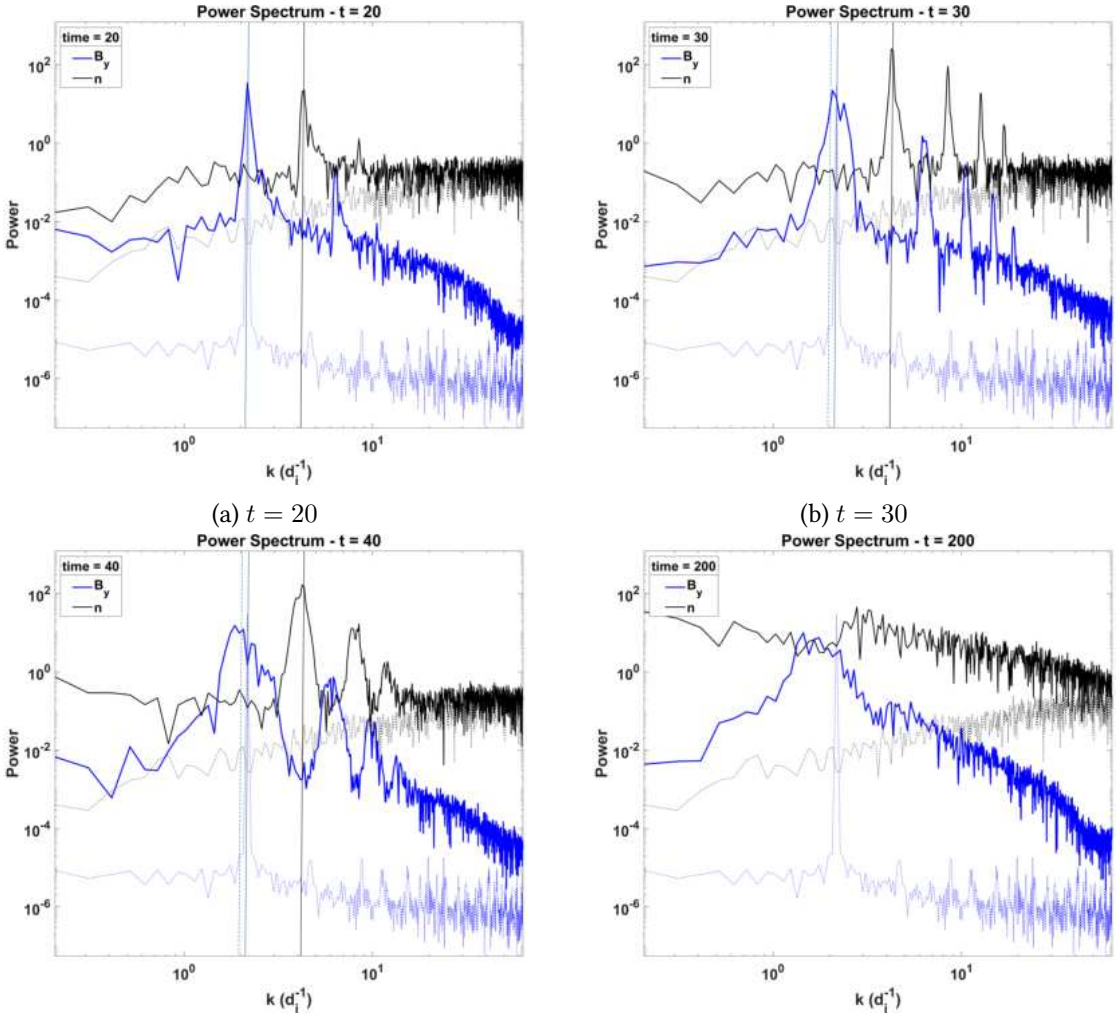

(a) $t = 20$ (b) $t = 30$

(c) $t = 40$ (d) $t = 200$

Figure 4.17: Power spectrum of the y component of the magnetic field (blue) and density (black) at various time for run D. Vertical lines highlight significant peaks.

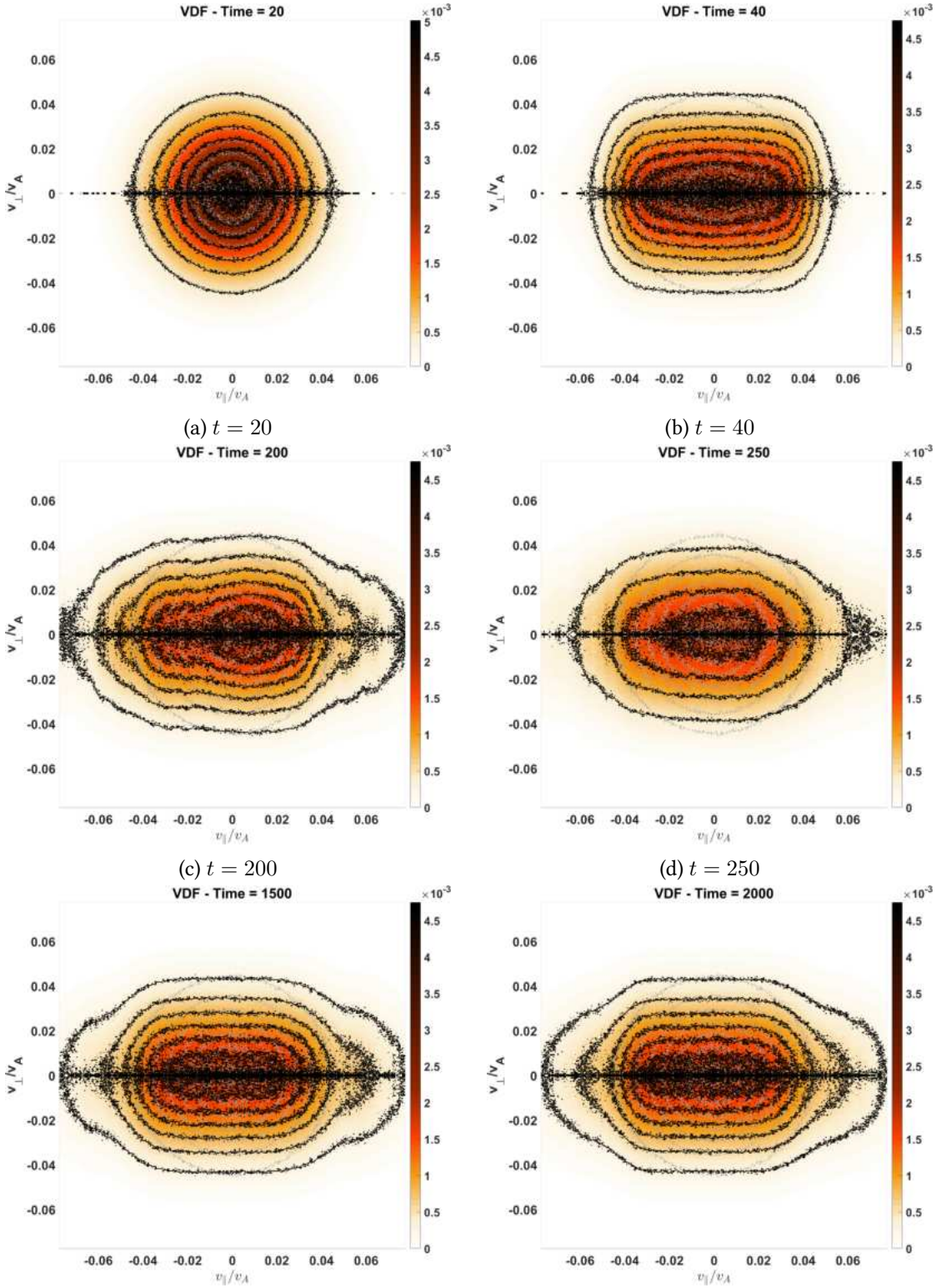

(a) $t = 20$ (b) $t = 40$

(c) $t = 200$ (d) $t = 250$

(e) $t = 1500$ (f) $t = 2000$

Figure 4.18: VDF at various times for run D.

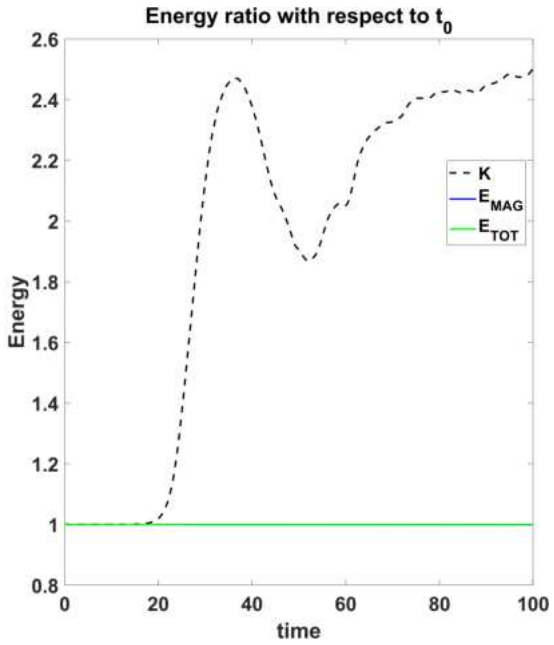

Figure 4.19: $E_K/E_{K,0}$, $E_M/E_{M,0}$ and $E_T/E_{T,0}$ for run E.

This peculiar behaviour, characterized by a significant portion of the plasma populating the distribution tails, is not entirely unexpected. In lower beta plasmas, the ion VDF is confined to a narrow region around $v_\parallel = v_\perp = 0$ (in fact, extrema of the plots are at $v_\parallel/v_A \approx 0.6$ for runs A, B, and C, and at $v_\parallel/v_A \approx 0.06$ for run D, as illustrated in figures 4.6 and 4.18). Consequently, the same perturbing wave has a larger impact on the ion velocity distribution and the plasma reacts faster.

Run E

With a plasma beta even lowered of one order of magnitude further as in run E (see table 4.3), we expect an even larger impact at very fast times. Therefore, run E runs only to $t = 100$. Indeed, as shown in figure 4.19, illustrating the evolution of $E_K/E_{K,0}$, $E_M/E_{M,0}$ and $E_T/E_{T,0}$, there is transferred energy from the magnetic field to the ions already at $t \approx 20$.

Cross helicity and E^+ and E^- (not shown) exhibit behaviour analogous to run D. Cross helicity intersect the zero at the same time as the energy transfer ($t \approx 20$) and multiple times thereafter, accompanied by corresponding changes in the dominance of E^+ and E^-.

Figure 4.20 presents snapshots of the most significant stages in the wave spectrum evolution. At $t = 20$ (Figure 4.20a), a density peak emerges at $k \approx 4$, while the magnetic field peak at $k = 2.07$, corresponding to the mother wave, remains unaffected. However, a secondary harmonic begins to develop in the magnetic field at $k \approx 6.5$. By $t = 30$ (figure 4.20b), the density spectrum exhibits multiple peaks, appearing as harmonics of the peak at $k \approx 4$. While no secondary peak at lower k corresponding to a daughter wave is observed in the magnetic field, the mother wave peak diminishes and broadens. Notably, the magnetic field spectrum

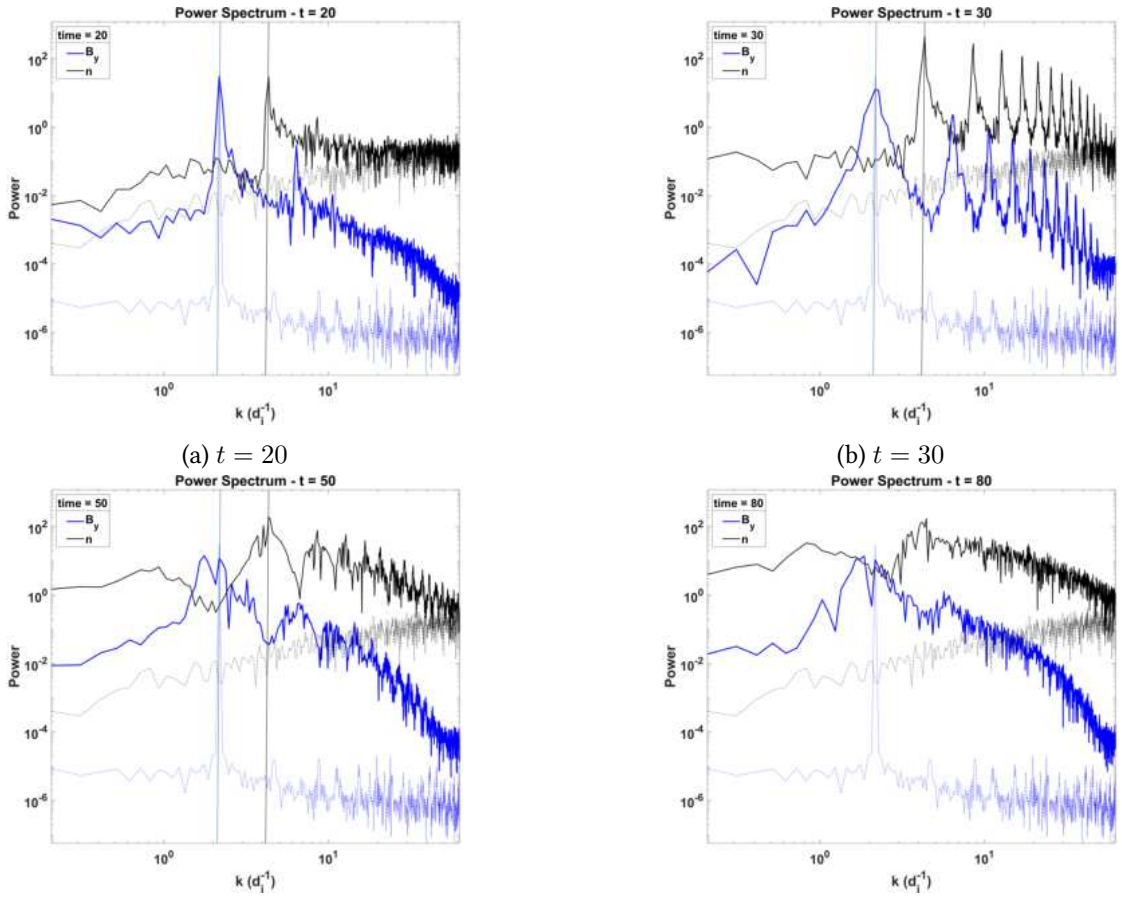

(a) $t = 20$ (b) $t = 30$

(c) $t = 50$ (d) $t = 80$

Figure 4.20: Power spectrum of the y component of the magnetic field (blue) and density (black) at various time for run E. Vertical lines highlight significant peaks.

at higher k values displays a similar pattern to the density, with multiple evenly spaced peaks intermediate to the density peaks. Both density and magnetic field peaks exhibit rapid growth and decay, with reduced amplitude and broadening by $t = 50$ (figure 4.20c) and complete disappearance by $t = 80$ (figure 4.20d). Similarly to run D, a power law behaviour is observed on both magnetic field and density spectra.

Figure 4.21 presents snapshots of the most significant stages of the ion VDF evolution. At $t = 20$, when the peak in the density has already developed, there is no evident change in the magnetic field spectrum (figure 4.20a), and the VDF remains unaltered compared to the initial state (figure 4.21a). Then, at $t = 30$, the VDF begins to expand on both sides of the parallel direction (figure 4.21b), with the plasma filling the tails of the distribution. The broadening continues, and at $t = 40$ (figure 4.21c), the VDF is completely different from the initial time (indicated by the light gray points) and populations of much faster ions appear in the parallel plane. This phase is actually oscillatory; the VDF broadens and shrinks in the parallel direction

(see figure 4.21d, showing the VDF at $t = 50$). After this oscillatory phase, the VDF undergoes further broadening on both sides of the parallel direction, eventually stabilizing as shown in the VDFs at $t = 80$ and $t = 100$ (figures 4.21e and 4.21f), respectively.

The filling of the distribution tails can be better appreciated by analyzing the evolution of the ions parallel velocity distribution, which is shown in figure 4.22. At $t = 30$ (figure 4.22b), both tails of the distribution exhibit growth. This effect is intensified at $t = 40$ (figure 4.22c), with ions populating previously unoccupied regions of the distribution tails. Nevertheless, the distribution remains centred around $v_{\parallel}/v_A = 0$, although the peak height diminishes rapidly. By $t = 50$ (figure 4.22d), the peak height is reduced by half compared to $t = 0$, and a minor peak appear at $v_{\parallel}/v_A \approx 0.003$, corresponding to a fast ion beam. By $t = 80$, there is basically no peak, with the plasma occupying the entire phase space (Figure 4.22e).

Run E2

To ascertain that the peculiar outcomes observed in run E were not attributable to numerical artifacts, an additional simulation was performed with a heightened particle-per-cell count ($ppc = 8 \cdot 10^4$ instead of 10^4). Indeed, collisions constitute a critical aspect of numerical simulations. In CAMELIA hybrid code, collisions are not modelled explicitly but numerical noise can act like a collision operator. By increasing the *ppc*, eventual numerical noise is mitigated.

The results (not shown) closely resemble those of run E, validating the accuracy of the original findings. Therefore, under these conditions, the impact of the Alfvén wave can induce effects leading to a significant deviation of the ion VDF, culminating in the filling of the tails of the distribution and the generation of high-speed ion beams.

4.4.3 Perturbing wave with a smaller amplitude

The identification of fast field aligned ion beams generated by the interaction of an Alfvén wave with the plasma constitutes the key finding of this study. However, despite the very low beta values simulated in run E, the previous simulations do not accurately represent ionospheric conditions due to the unrealistic perturbation amplitude ($B/B_0 = 5 \cdot 10^{-2}$). In fact, the geomagnetic field has an order of magnitude of 10^4 nT (Campbell [39]), rendering such perturbations of the order of hundreds of nT and thus improbable (Le et al. [163]). To address this, the amplitude of the perturbing wave was reduced by a factor of 10 in the following simulation (run F, see Table 4.4), providing a more realistic representation of the ionospheric environment. Other parameters were maintained identical to run E.

run	β_e	β_i	B/B_0	W_0	Pol.	$L_{box}(d_i)$	$k_0(d_i^{-1})$	$k_M(d_i^{-1})$	ppc
F	$1 \cdot 10^{-4}$	$1 \cdot 10^{-4}$	$5 \cdot 10^{-3}$	20	+	60.8	0.1	2.07	$8 \cdot 10^4$

Table 4.4: Characteristics of run F.

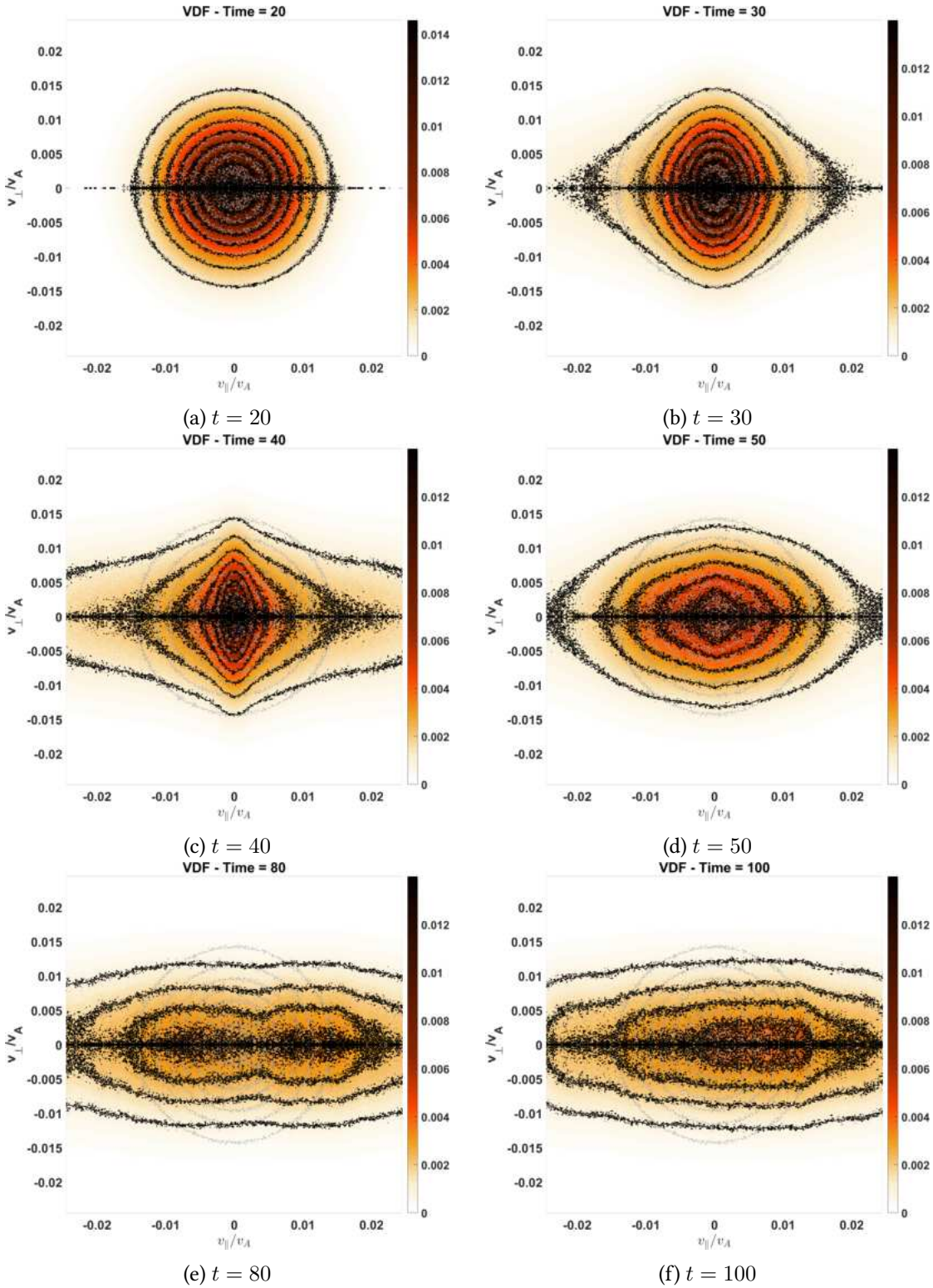

(a) $t = 20$ (b) $t = 30$

(c) $t = 40$ (d) $t = 50$

(e) $t = 80$ (f) $t = 100$

Figure 4.21: Ion VDF for run E.

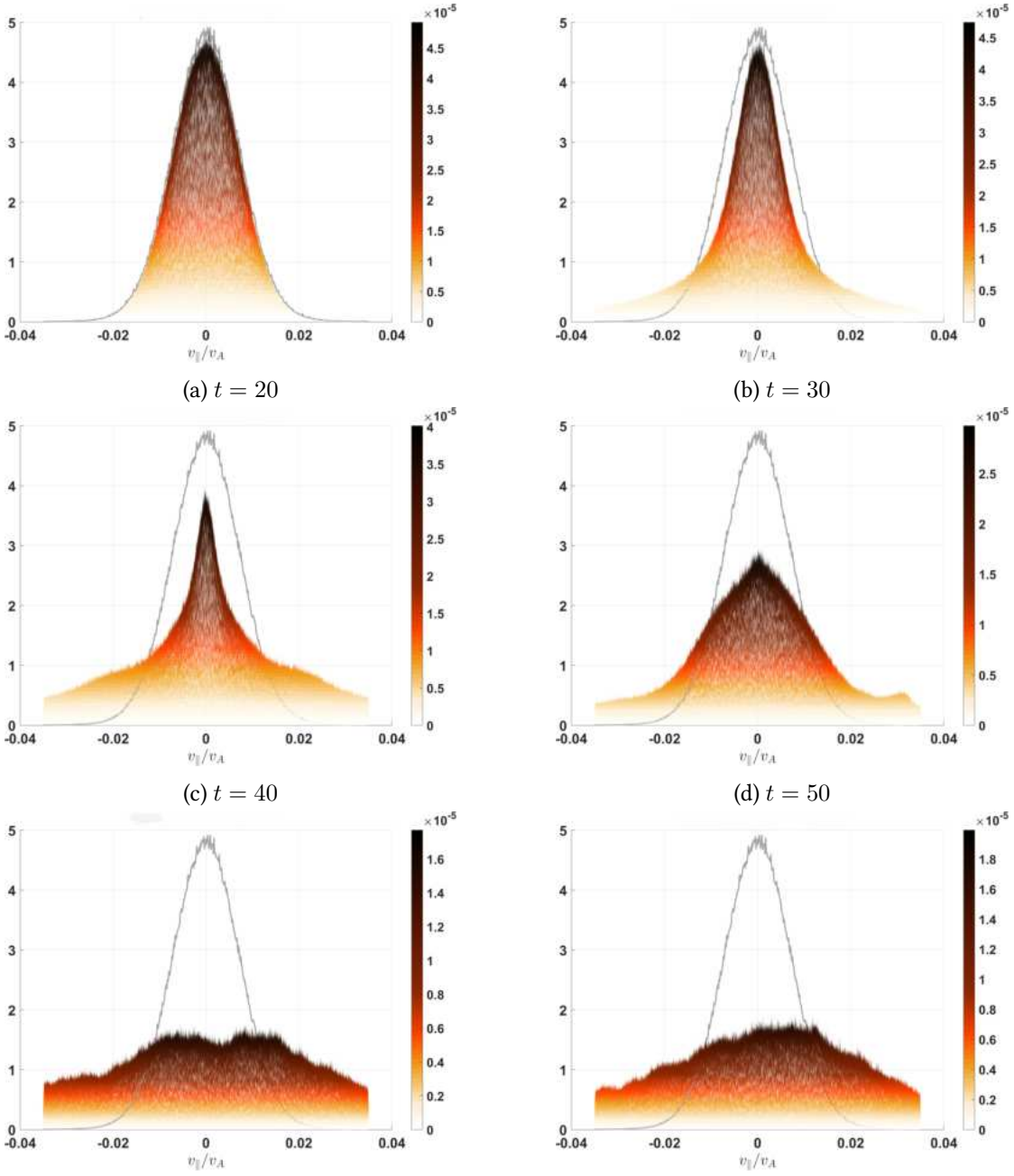

(a) $t = 20$

(b) $t = 30$

(c) $t = 40$

(d) $t = 50$

(e) $t = 80$

(f) $t = 100$

Figure 4.22: Ion parallel velocity distribution for run E.

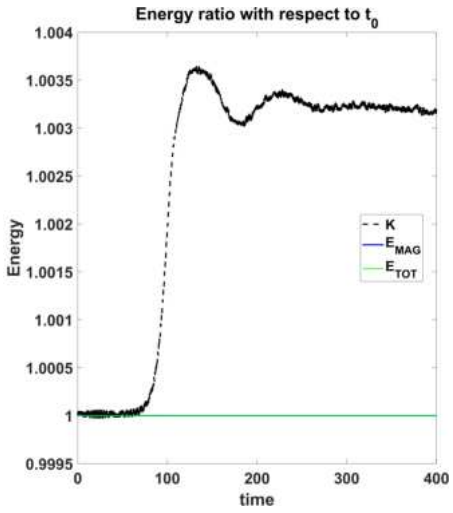

(a) $E_K/E_{K,0}$, $E_M/E_{M,0}$ and $E_T/E_{T,0}$

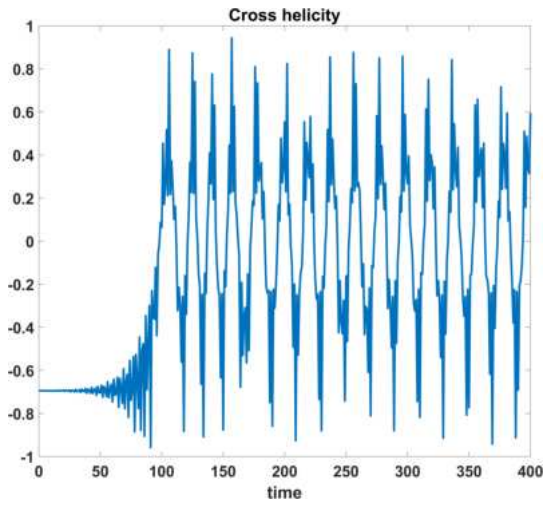

(b) Cross helicity

Figure 4.23: Overview of run F.

Run F

Figure 4.23a illustrates the temporal evolution of $E_K/E_{K,0}$, $E_M/E_{M,0}$, and $E_T/E_{T,0}$. In this case, the energy transfer from the magnetic field to ion kinetic energy occurs at a later time ($t \approx 90$) compared to run E ($t \approx 20$). Correspondingly, the cross helicity (figure 4.23b) exhibits an initial increase before intersecting zero multiple times at approximately 15-time intervals.

Figure 4.24 presents two key snapshots of the wave spectrum evolution. At $t = 60$, a density peak emerges at $k \approx 4$, which subsequently grows to a maximum at $t = 120$. Concurrently, second harmonics develop in both the density (at $k \approx 8$) and magnetic field (at $k \approx 6$). This wave spectrum configuration exhibits only a small oscillatory behaviour for an extended period (the simulation ends at $t = 400$). In this case, no clear appearance of a daughter wave can be detected.

With a reduced amplitude perturbing wave, the deviation of the ion VDF from its initial configuration is less pronounced and occurs at a slower pace. At $t = 200$, the ion VDF remains virtually identical to its initial state, exhibiting only small oscillatory deviations from its original configuration (see figure 4.25a). Only by $t = 400$, subtle changes become apparent. Indeed, figure 4.26b reveals a decreased height and broadened shape of the central distribution peak around $v_\parallel/v_A = 0$, accompanied by the emergence of two (slightly visible) symmetric populations of faster ions at $v_\parallel/v_A \approx 0.01$.

Consequently, with a plasma beta of approximately 10^{-4} and a reduced wave amplitude, a distinct density spectrum peak is still present, though it appears with a significant time delay compared to previous simulations. A clear parametric decay, characterized by the emergence of a daughter wave in the magnetic field, is not observed, and the resulting effects on the ion VDF are both subtle and delayed.

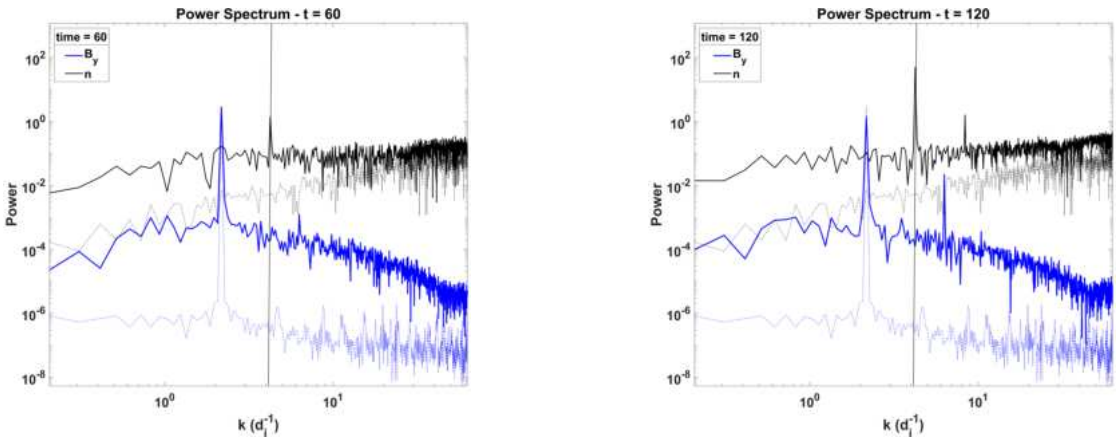

(a) $t = 60$ (b) $t = 120$

Figure 4.24: Power spectrum of the y component of the magnetic field (blue) and density (black) at various time for run F. Vertical lines highlight significant peaks.

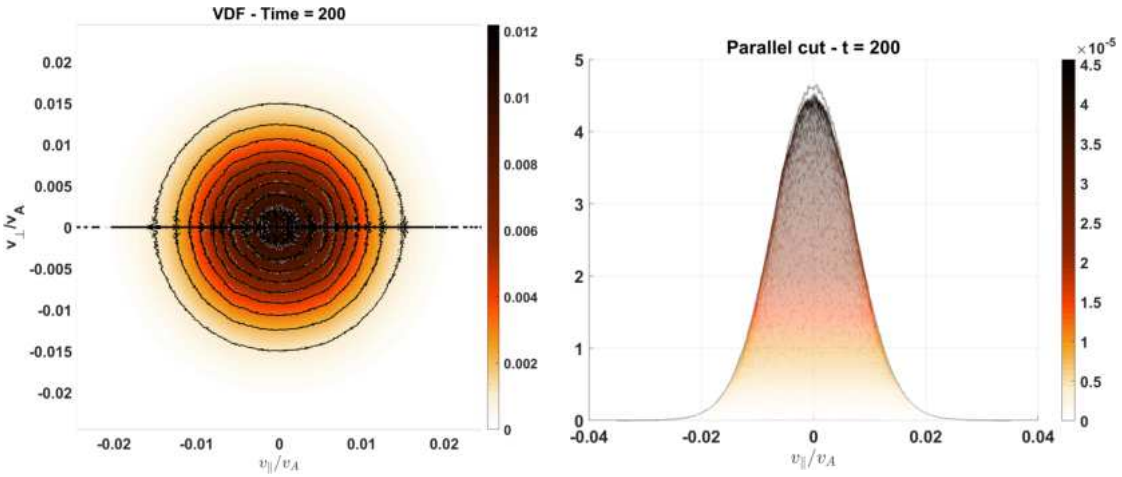

(a) VDF in the $v_{\parallel} - v_{\perp}$ plane (b) $\hat{f}(v_{\parallel})$

Figure 4.25: Ion VDF for run F a $t = 200$.

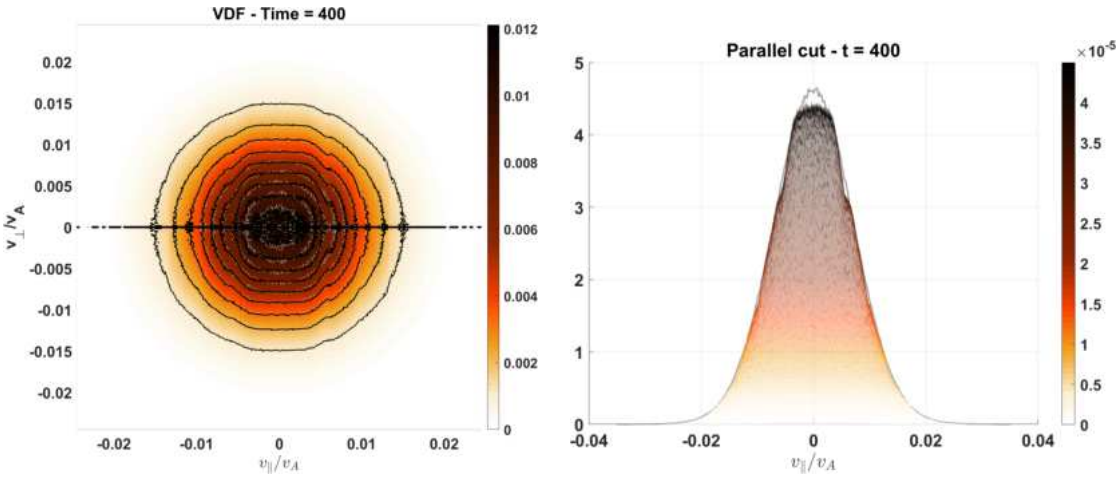

(a) 2-D velocity distribution in the $v_{\parallel} - v_{\perp}$ plane (b) parallel velocity distribution

Figure 4.26: Ions velocity distribution function for run F a $t = 400$.

4.4.4 Spectrum of waves

The presence of a perfectly monochromatic wave is not a common situation in the ionosphere. Indeed, as discussed in chapter 3, the ionosphere is characterized by a complex electromagnetic environment, with the presence of several signatures at different frequencies and waves with rapidly varying frequencies such as whistlers. For this reason, for the subsequent runs, we consider a spectrum of waves perturbing the plasma, rather than a monochromatic wave, with the aim of modelling a more realistic situation in the ionosphere. Furthermore, we investigate the effects of inverting the wave polarization. Therefore, for run G, we consider the same parameters as run F, but in this case, we perturb the plasma with a spectrum of Alfvén waves with wave numbers from $W_{min} = 19$ to $W_{max} = 21$, corresponding to wave vectors from $k_{min} = 1.96\ d_i^{-1}$ to $k_{max} = 2.17\ d_i^{-1}$. Moreover, since we have verified that a $10^4 ppc$ are sufficient to avoid numerical artifacts, we return to that number of particles per cell to reduce the computational time. Subsequent run (H) has the same parameters as run G but with the wave spectrum polarization reversed (left-handed instead of right-handed), as shown in table 4.5.

run	β_e	β_i	B/B_0	Pol.	$L_{box}(d_i)$	$k_{min}(d_i^{-1})$	$k_{max}(d_i^{-1})$	ppc
G	$1 \cdot 10^{-4}$	$1 \cdot 10^{-4}$	$5 \cdot 10^{-3}$	+	60.8	1.96	2.17	$1 \cdot 10^4$
H	$1 \cdot 10^{-4}$	$1 \cdot 10^{-4}$	$5 \cdot 10^{-3}$	-	60.8	1.96	2.17	$1 \cdot 10^4$

Table 4.5: Run G and H parameters.

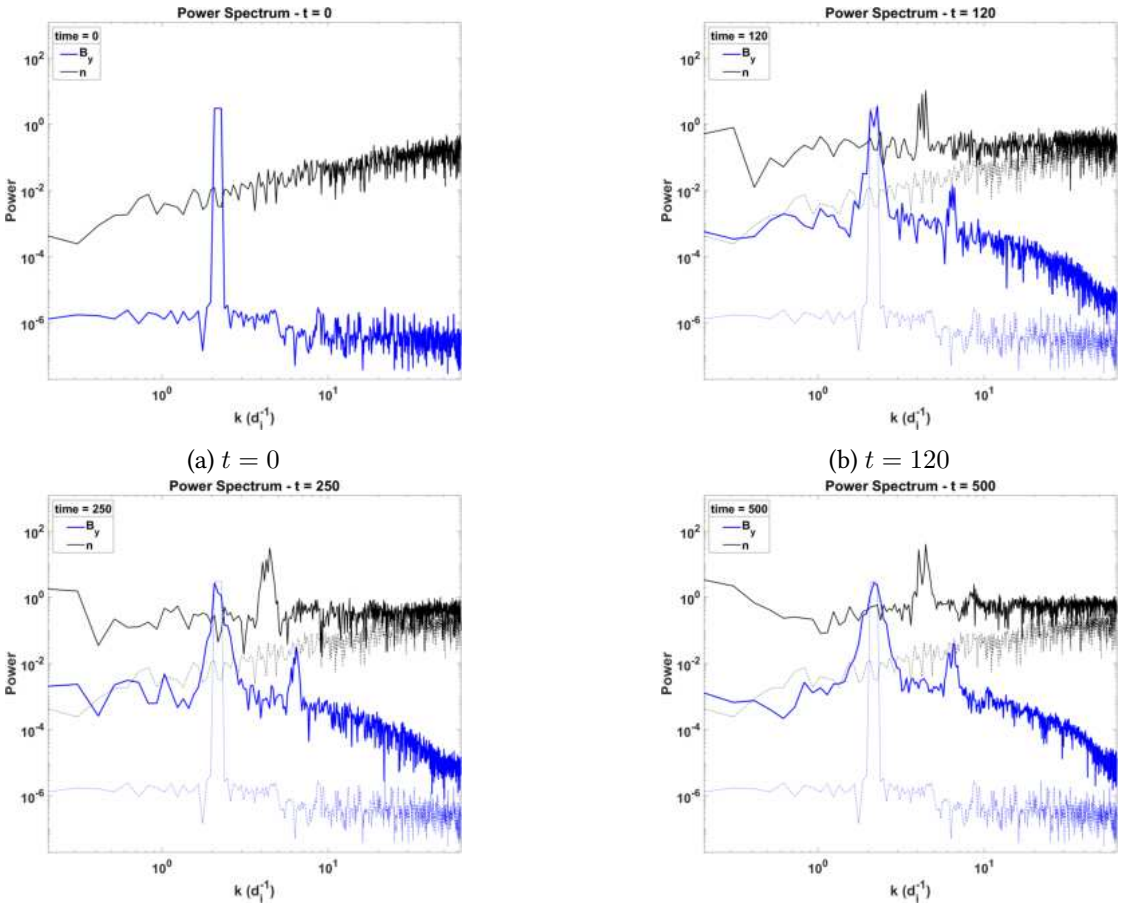

(a) $t = 0$

(b) $t = 120$

(c) $t = 250$

(d) $t = 500$

Figure 4.27: Power spectrum of the y component of the magnetic field (blue) and density (black) at various time for run G.

Run G

Figure 4.27 presents key snapshots of the wave spectrum for run G. At $t = 0$ (figure 4.27a), the wave spectrum exhibits a solitary, broad and pronounced peak in the magnetic field, corresponding to the mother Alfvén waves. At $t = 120$, a spectrum of compressive modes on the density arises, identifiable as three closely spaced peaks on the black line from $k \approx 4$ to $k \approx 5$ in figure 4.27b. Correspondingly, a second harmonics in the magnetic field appears at k values from approximately 6 to 7. These structures undergo minor oscillations as time progresses and persist for extended periods (at least until $t = 500$ when the simulation ends, see figures 4.27c and 4.27d). As in run F, there is no clear appearance of a daughter Alfvén wave nor the clear occurrence of a parametric decay.

The parallel and perpendicular ion velocity distribution functions at the final simulation time ($t = 500$) are shown in figure 4.28. The VDF evolution is similar to that described for run

F, with a slow and minor departure from the initial configuration. Nevertheless, the impact of perturbing the plasma with a wave spectrum, rather than a monochromatic wave, while subtle, is non-negligible. Specifically, the VDF exhibits a slightly more pronounced deviation from its initial state compared to run F, characterized by a more substantial reduction in the distribution peak centred around $v_{\parallel}/v_A = 0$ and its more evident broadening.

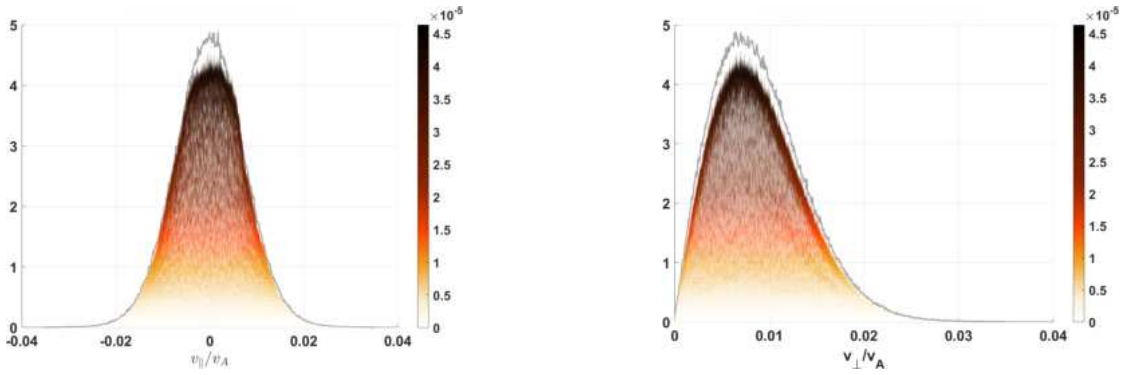

(a) $\hat{f}(v_{\parallel})$ (b) $\hat{f}(v_{\perp})$

Figure 4.28: Parallel and perpendicular velocity distribution at $t = 500$ for run G.

Run H

Figure 4.29 presents four representative snapshots of the power spectrum evolution. At $t = 60$ (figure 4.29a), the system exhibits a configuration analogous to that observed in run G at $t = 120$, characterized by the emergence of a multi-peak in the density spectrum within the wave-vector range $k \approx 4$ to $k \approx 5$. This indicates a more rapid evolution compared to the previous case. Unlike run G, where this configuration undergoes only minor oscillations with increasing time, here the density peak rapidly amplifies and successive harmonics develop at $t = 90$ (figure 4.29b) in both the magnetic field ($k \approx 6 - 8$ and $k \approx 10 - 12$) and density ($k \approx 8 - 10$ and $k \approx 12 - 14$). These structures continue to intensify, with a fourth harmonic appearing in the magnetic field at $t = 150$ (figure 4.29c). At later times, they broaden and gradually diminish, as illustrated in figure 4.29d, representing the wave spectrum at $t = 400$. As in run G, no clear evidence of parametric decay or the generation of a daughter Alfvén wave is observed.

The faster and more complex evolution of the system due to the reversed polarization is confirmed by the VDF (figure 4.30) and the parallel velocity distribution (figure 4.31). At time $t = 150$, the VDF in the $v_{\parallel} - v_{\perp}$ plane exhibits a widening in the parallel direction (figure 4.30a) relative to the initial state. Consequently, the central peak of the parallel velocity distribution broadens and decreases in amplitude (figure 4.31a). This scenario bears resemblance to observations in run G at $t = 500$. However, in the present case, subsequent simulation stages reveal the emergence of ion beams at $v_{\parallel}/v_A \approx 0.01$ and $v_{\parallel}/v_A \approx 0.017$, as shown in figures 4.30b and 4.31b.

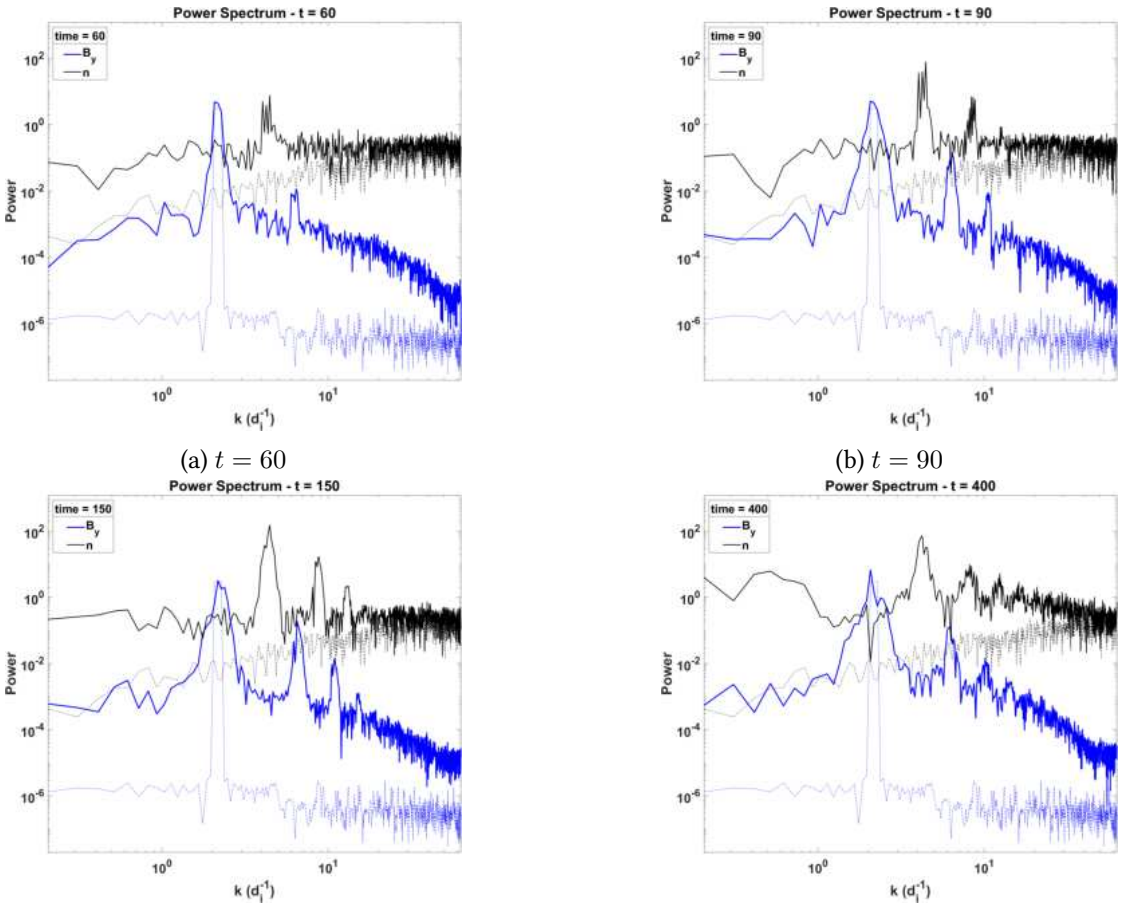

(a) $t = 60$ (b) $t = 90$

(c) $t = 150$ (d) $t = 400$

Figure 4.29: Power spectrum of the y component of the magnetic field (blue) and density (black) at various time for run H.

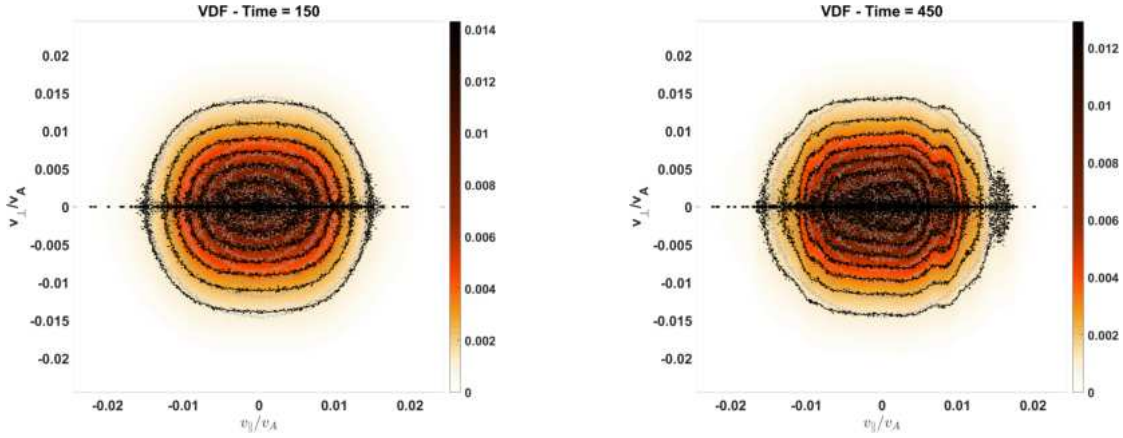

(a) $t = 150$ (b) $t = 450$

Figure 4.30: VDF in the $v_{\parallel} - v_{\perp}$ plane for run H.

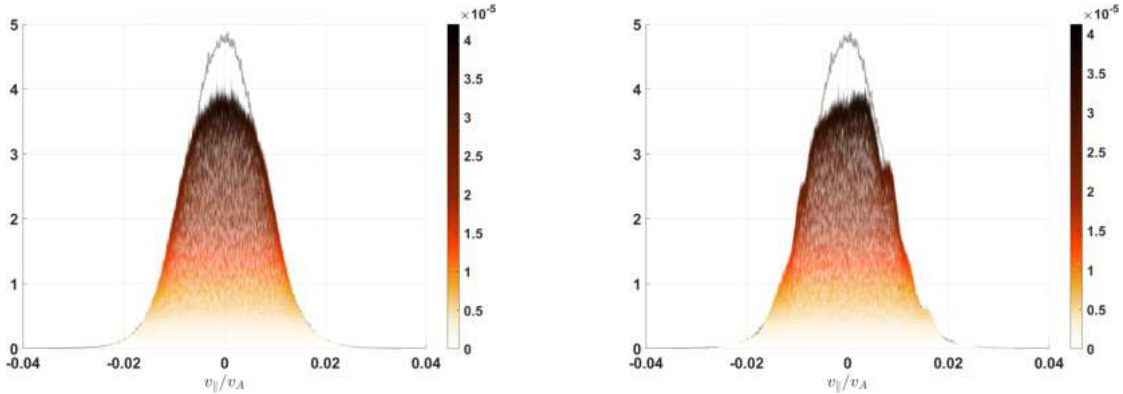

(a) $t = 150$ (b) $t = 450$

Figure 4.31: Ion parallel velocity distributions for run H.

4.4.5 Realistic ionospheric composition

As shown in table 4.2, at CSES-01 altitude (500 km), the plasma is composed primarily of O^+ ions ($\approx 94\%$). However, among other minor ion populations, there is also a non-negligible concentration ($\approx 4.2\%$) of H^+ ions. To more accurately simulate ionospheric conditions, subsequent simulations considered a two-species plasma composed of heavier ions (95% number density) and 16 times lighter ions (5% number density). Therefore, run I replicates run H but with a two-species plasma. Additionally, in subsequent simulations, to model a realistic WPI in the ionospheric environment, the plasma beta was further reduced to match values from the IRI model (run J), and subsequently, an even smaller amplitude spectrum of perturbing waves was considered (run K). For all these runs, whose parameters are shown in table 4.6, the spectrum of perturbing waves has wavenumbers from $W_{min} = 19$ to $W_{max} = 21$ and left-handed polarization. In table 4.6, we indicate the beta value of all the plasma components: electrons (β_e), oxygen ions (β_O), and hydrogen ions (β_H). Hereafter, with d_i we denote the inertial length of the more abundant species (O^+).

run	B/B_0	β_e	β_O	β_H	$L_{box}(d_i)$	n_O	n_H	ppc
I	$5 \cdot 10^{-3}$	$1 \cdot 10^{-4}$	$1 \cdot 10^{-4}$	$5 \cdot 10^{-6}$	60.8	0.95	0.05	$1 \cdot 10^4$
J	$5 \cdot 10^{-3}$	$1 \cdot 10^{-5}$	$1 \cdot 10^{-5}$	$5 \cdot 10^{-7}$	60.8	0.95	0.05	$1 \cdot 10^4$
J2	$5 \cdot 10^{-3}$	$1 \cdot 10^{-5}$	$1 \cdot 10^{-5}$	$5 \cdot 10^{-7}$	60.8	0.95	0.05	$5 \cdot 10^5$
K	$2 \cdot 10^{-3}$	$1 \cdot 10^{-5}$	$1 \cdot 10^{-5}$	$5 \cdot 10^{-7}$	60.8	0.95	0.05	$1 \cdot 10^4$

Table 4.6: Run I, J, J2 and K parameters.

Run I

This run replicates run H but with a two-species plasma. The time evolution of the wave spectrum is reported in figure 4.32. Here, two density spectra are presented: the O^+ spectrum is indicated in black and the H^+ spectrum in gray. At $t = 60$, a triple peak emerges in both the O^+ and H^+ densities (figure 4.32b) at $k \approx 4$. Simultaneously, the second harmonic appears in the magnetic field at $k \approx 6 - 7$. At later times, subsequent harmonics appear in both densities (black and gray lines) and the magnetic field (figure 4.32c, $t = 100$). These structures reach their maximum in number and intensity at approximately $t = 270$ (figure 4.32d) before slowly decreasing (figure 4.32e, $t = 550$). At $t = 1000$ (figure 4.32f), only a broad peak corresponding to the first harmonic persists in both the densities and the magnetic field. As in the previous run, there is no clear evidence of a daughter Alfvén wave.

Figure 4.33 shows key moments in the evolution of the VDF for both ion species (O^+ on the left panels and H^+ on the right panels). As in the previous run, no variation in the VDF is observed immediately after the rise of the density peak. In fact, at $t = 100$ (figure 4.33a), the VDF is essentially identical to its initial state. The first effects on the VDF become apparent in figure 4.33b, representing the VDF at $t = 230$, with particles moving towards the distribution tails and the formation of distinct ion velocity beams (particularly for H^+ ions). These ion beams persist for a long time with some oscillations, as evidenced by figures 4.33c and 4.33d, depicting the VDFs at $t = 530$, and $t = 1000$, respectively.

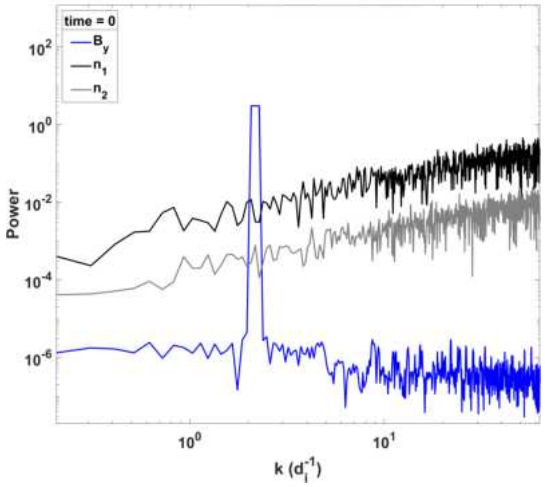

(a) $t = 0$

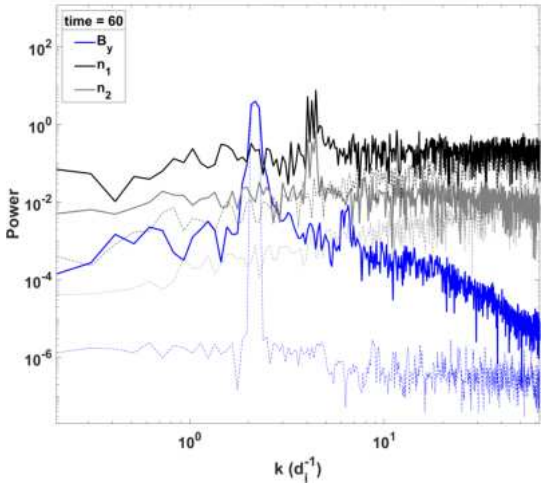

(b) $t = 60$

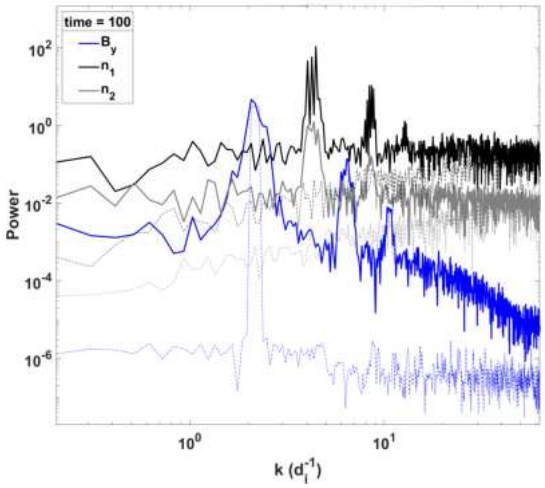

(c) $t = 100$

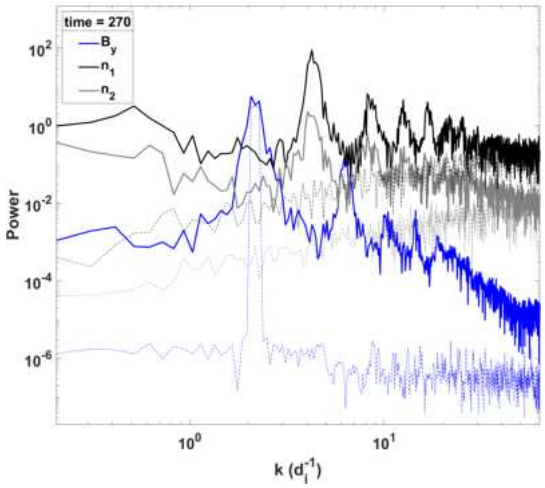

(d) $t = 270$

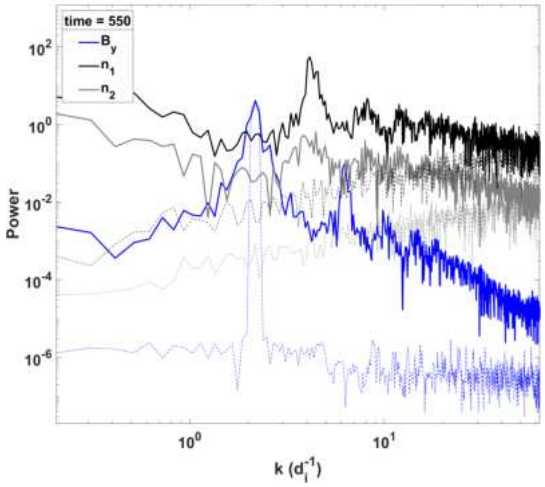

(e) $t = 550$

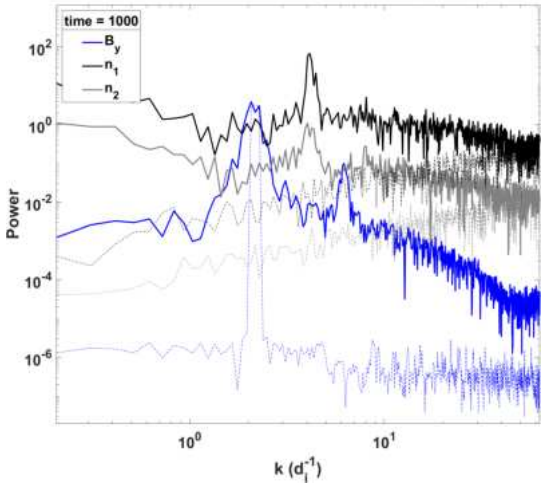

(f) $t = 1000$

Figure 4.32: Run I: power spectrum of the y component of the magnetic field (blue), O^+ density (black) and H^+ density (grey) at various time. Dashed lines indicate values at time 0, while solid lines at time t.

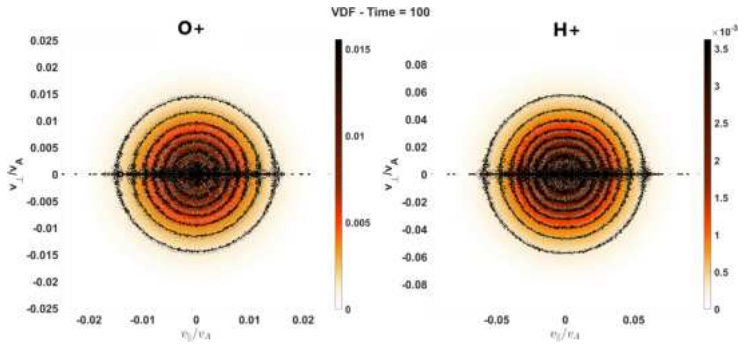

(a) $t = 100$

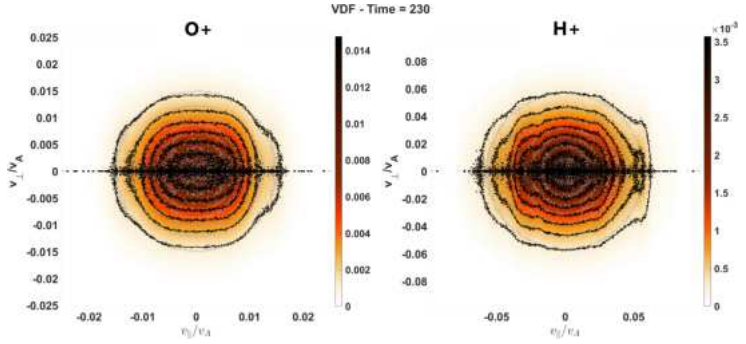

(b) $t = 230$

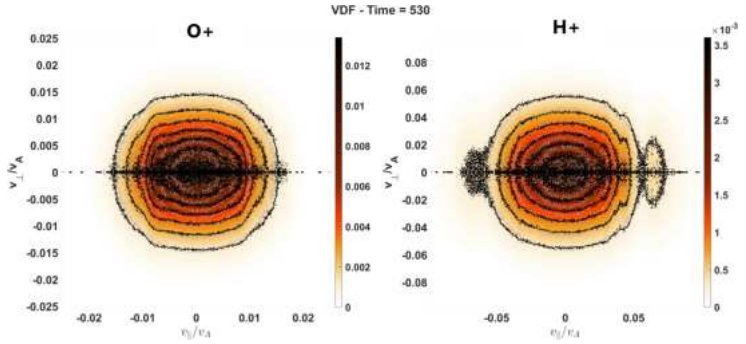

(c) $t = 530$

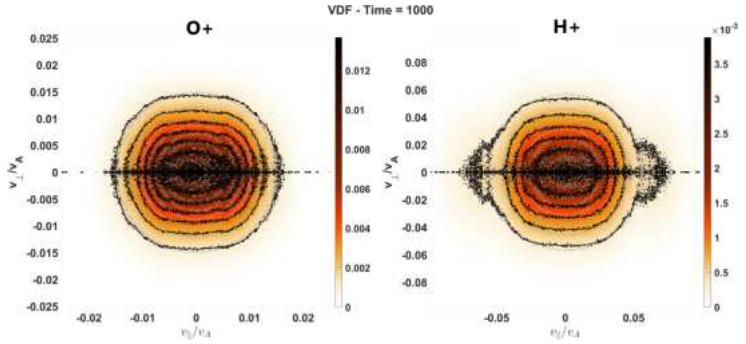

(d) $t = 1000$

Figure 4.33: VDFs in the $v_{\parallel}$-$v_{\perp}$ plane at various times for run I. O^+ ions on the left and H^+ ions on the right of each panel.

The effects on the VDF and the emergence of fast ion beams are better appreciable when observing the evolution of the parallel velocity distribution, shown in figure 4.34 at times $t = 230$, $t = 300$, $t = 500$, and $t = 1000$. For O^+ ions (upper panels), the effect is similar to that seen in previous simulations: the distribution spreads on both sides of the parallel direction, and the peak centred around 0 is lowered. Compared to the initial time, there are fewer particles with $v_\parallel/v_A \approx 0$ and more particles in both tails of the distribution. The evolution of the parallel velocity distribution of H^+ ions is more strongly affected by interactions with the Alfvén wave spectrum with respecto to O^+ ions, although the deviation from its original configuration begins at the same time. For H^+, at $t = 230$ and $t = 300$, two distinct ion beams can be detected at approximately $v_\parallel/v_A = \pm 0.03$ and $v_\parallel/v_A = \pm 0.06$. At later simulation times ($t = 500$), a larger portion of the plasma fills the distribution tails, and only the beam at $v_\parallel/v_A = \pm 0.06$ remains apparent. This effect persists at longer times, with the tails even increasing at $t = 1000$ (figure 4.34d).

Run J

In this run, we further reduced the plasma beta, adopting realistic ionospheric values for all plasma components. As shown in table 4.6, the beta values are very close to those provided by the IRI model and shown in table 4.2. Other parameters remain unchanged compared to run I.

Key snapshots of the wave spectrum evolution are shown in figure 4.35. Similarly to run I, a triple peak in the density is visible at $t = 70$ at $k \approx 4$ (figure 4.35a). However, in this case, a rapid growth of successive harmonics occurs in both ion densities (O^+, black line; H^+, gray line) and the magnetic field (blue line), as evidenced in figures 4.35b, 4.35c, and 4.35d, depicting the wave spectrum at $t = 90$, $t = 120$, and $t = 140$, respectively. Subsequently, these structures broaden and decrease (figure 4.35e, $t = 200$) until they essentially vanish (figure 4.35f, $t = 1000$). In this figure, the power law behaviour of the three spectra can be appreciated, with the density spectra of the two ion species exhibiting a smaller slope than the magnetic field spectrum.

Figure 4.36 shows the evolution of the ion VDFs. For both ion species, the VDF completely broaden along both sides of the parallel direction, with a more rapid effect on H^+ ions (right panels).

The filling of the distribution tails is better illustrated in figure 4.37, depicting the evolution of ion parallel velocity distributions at $t = 140$, $t = 200$, and $t = 1000$. Here, we can observe the rapid depletion of the central region (centred around 0) and the filling of both distribution tails by both ion populations. The figure highlights the different rates at which this process occurs for the two plasma components. In fact, at $t = 140$ and $t = 200$ (figures 4.37a and 4.37b, respectively), a narrow central peak is still present in the O^+ ions (upper panels), while the H^+ distribution (lower panels) is already flattened.

Run J2

To ensure that the behaviour observed on run J is not induced by numerical noise, we replicated the run with an increased number *ppc* (from 10^4 to $5 \cdot 10^5$). The obtained results are identical to run J, confirming the accuracy of the original findings.

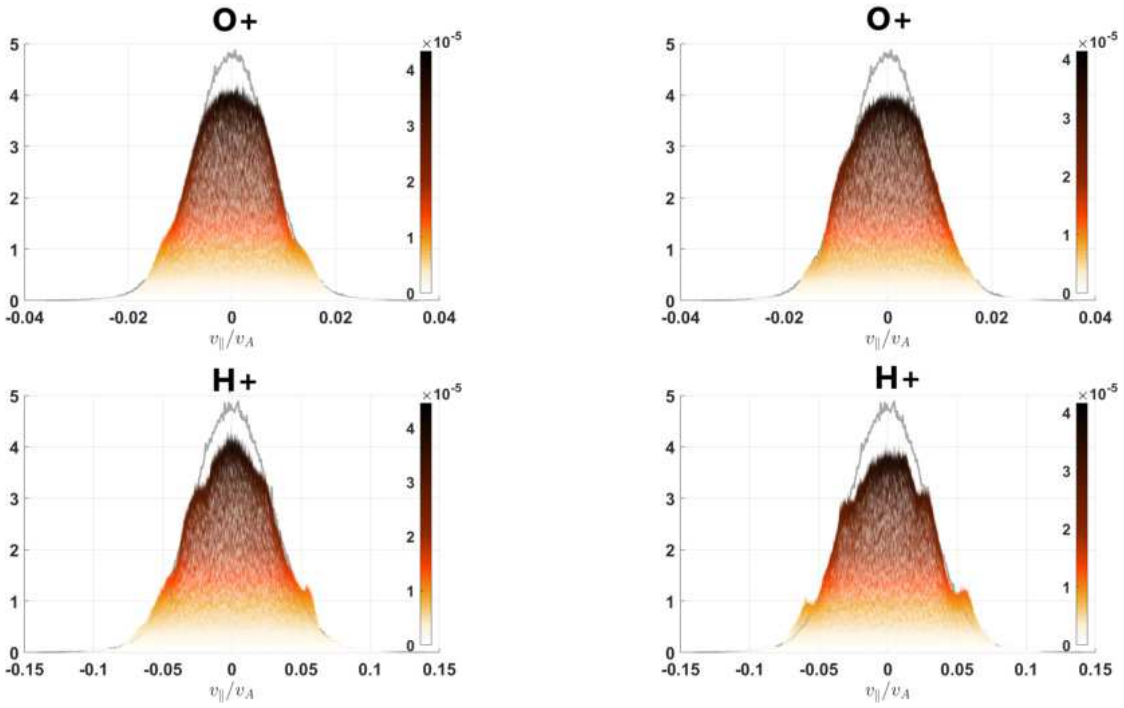

(a) $t = 230$

(b) $t = 300$

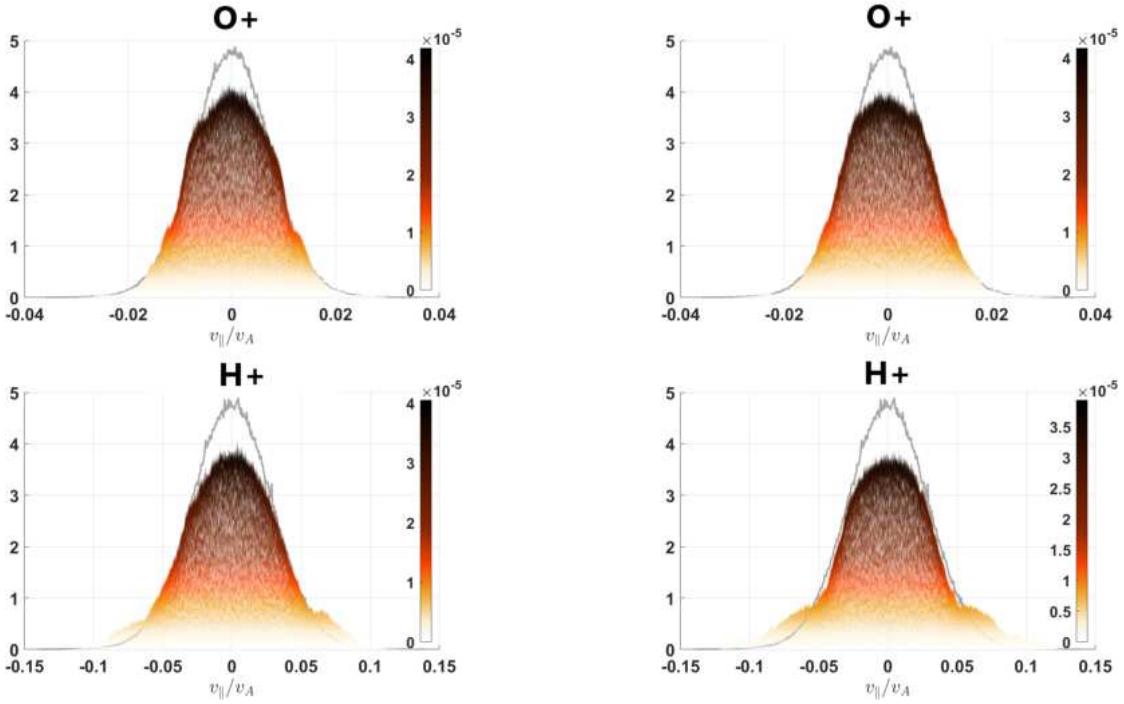

(c) $t = 500$

(d) $t = 1000$

Figure 4.34: Ions parallel velocity distribution for run I. O^+ ions and H^+ ions in the upper and lower panels respectively.

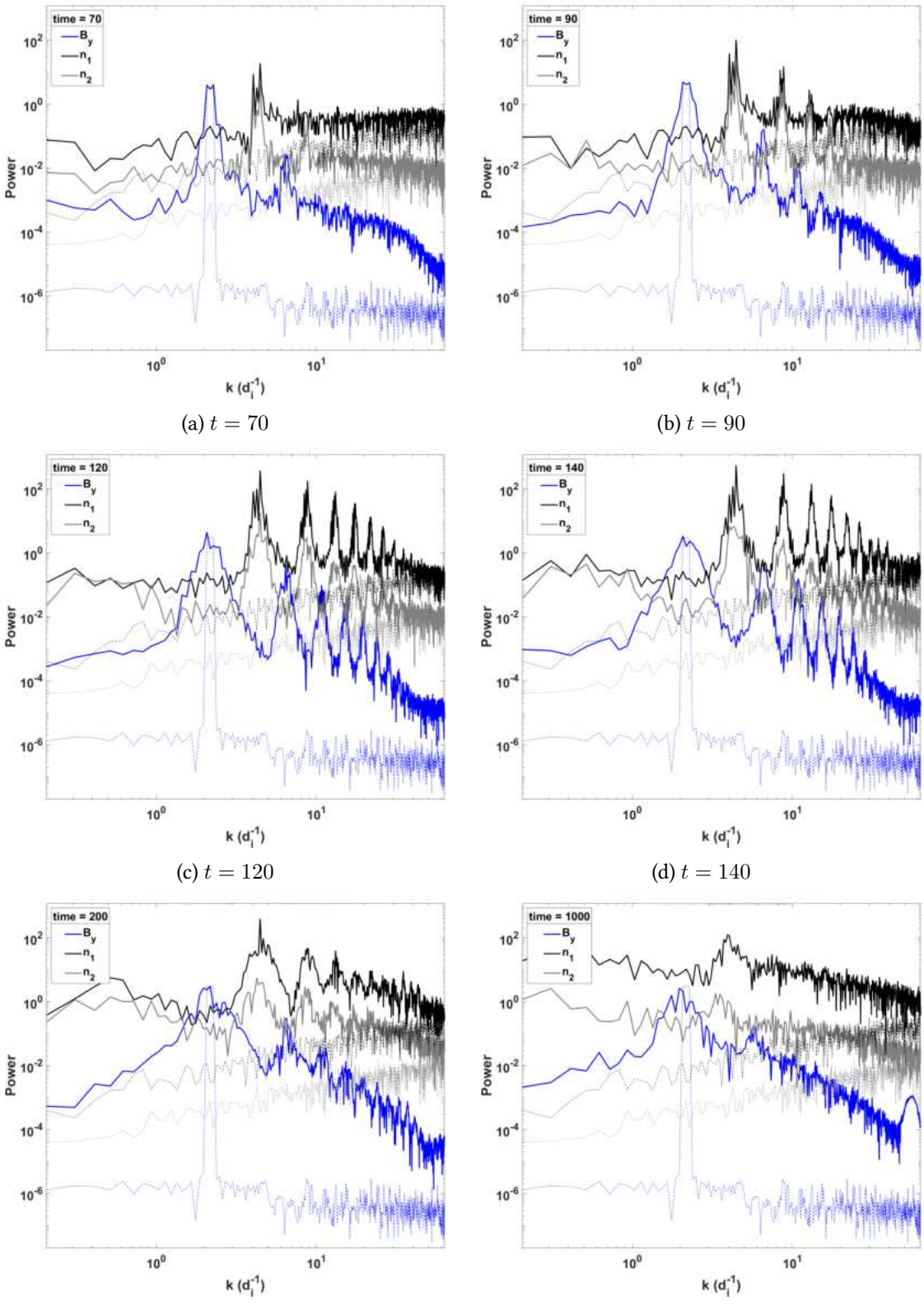

(a) $t = 70$ (b) $t = 90$

(c) $t = 120$ (d) $t = 140$

(e) $t = 200$ (f) $t = 1000$

Figure 4.35: Run J: power spectrum of the y component of the magnetic field (blue), O^+ density (black) and H^+ density (grey) at various time. Dashed lines indicate values at time 0, while solid lines at time t.

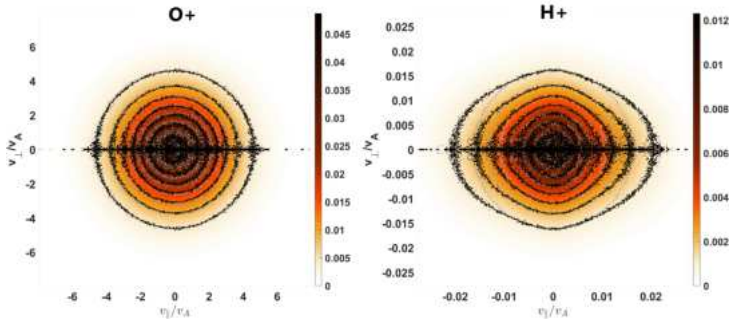

(a) $t = 90$

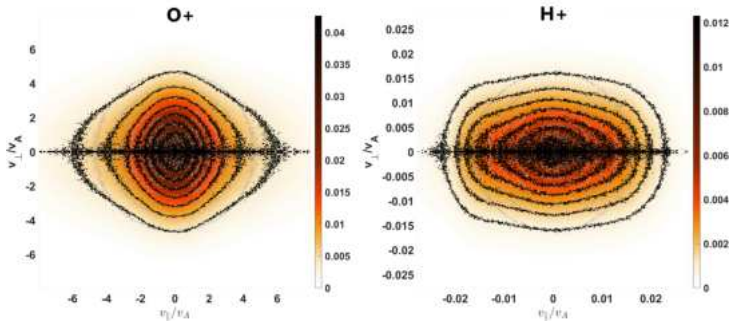

(b) $t = 120$

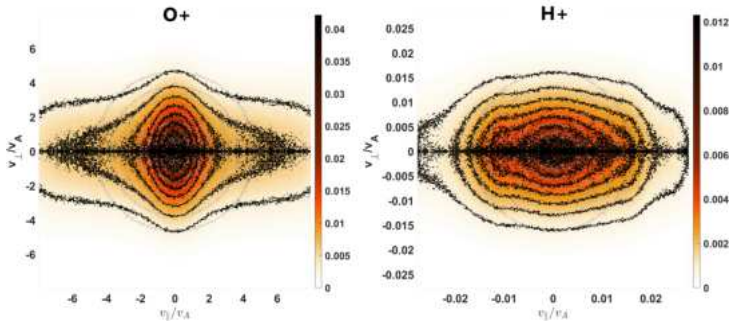

(c) $t = 140$

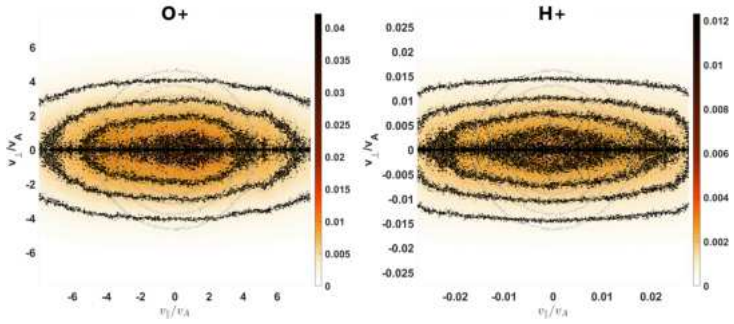

(d) $t = 1000$

Figure 4.36: Ion VDF in the $v_{\parallel}$-$v_{\perp}$ plane at various time for run J. O^+ on the left and H^+ on the right of each panel.

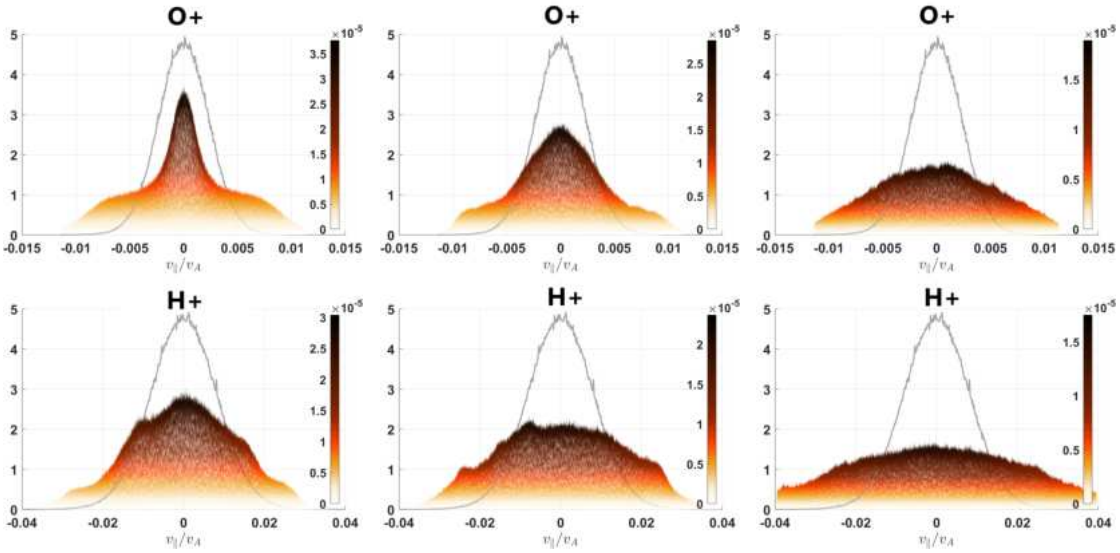

(a) $t = 140$ (b) $t = 200$ (c) $t = 1000$

Figure 4.37: Ion parallel velocity distribution for run J. O^+ and H^+ in the upper and lower panels respectively.

Run K

Run J models a realistic ionospheric environment, both in terms of plasma compositions and plasma beta. To simulate also a realistic amplitude of the perturbing waves, in run K we replicate run J but with a B/B_0 of the mother waves lowered to $2 \cdot 10^{-3}$.

Figure 4.38 shows the key moments of the temporal evolution of the wave spectrum. The behaviour is similar to run J, but the evolution occur at slower pace. In fact, the peak on both ion densities (O^+, black line and H^+, grey line) at $k \approx 4$ becomes appreciable only at $t = 100$ (figure 4.38a). Then, subsequent harmonics starts to grow (figure 4.38b, $t = 230$) and reach their maximum amplitude approximately at $t = 500$ (figure 4.38c). All the structures decrease slowly (see figure 4.38d, depicting the wave spectrum at $t = 1300$), confirming the slower evolution.

Figure 4.39 shows the evolution of both ion parallel velocity distributions. At $t = 300$, the peak centred around zero is lowered and flattened for both plasma species (figure 4.39a). Subsequently, the center of the distribution begins to empty out, and two symmetric peaks appear on both sides of the parallel direction, at $v_\parallel/v_A \approx \pm 0.005$ for O^+ ions and $v_\parallel/v_A \approx \pm 0.01$ for H^+ ions (see figure 4.39b, corresponding to $t = 370$). At later times, the behaviour of the two ion populations slightly diverges: for O^+, we observe a symmetric distribution with respect to zero, but with a lower central peak and larger tails compared to the initial time. The situation for H^+ is more complex, as peaks on both sides of the parallel direction rapidly rise, corresponding to the generation of new populations of faster ion beams (figure 4.39c, $t = 790$, corresponding to approximately 10 seconds). These peaks undergo minor oscillations at longer times, as depicted by figure 4.39d, showing the parallel velocity distribution at $t = 1300$.

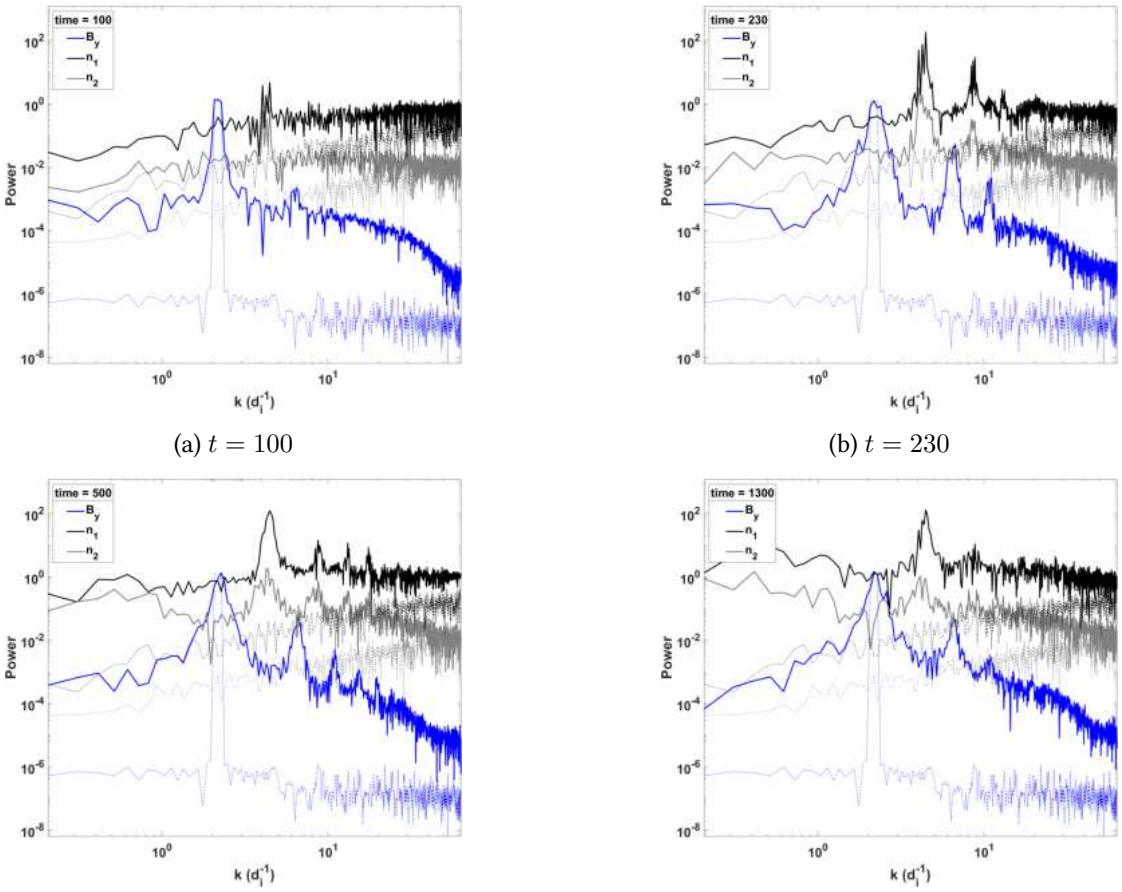

(a) $t = 100$ (b) $t = 230$

(c) $t = 500$ (d) $t = 1300$

Figure 4.38: Run K: power spectrum of the y component of the magnetic field (blue), O^+ density (black) and H^+ density (grey) at various time. Dashed lines indicate values at time 0, while solid lines at time t.

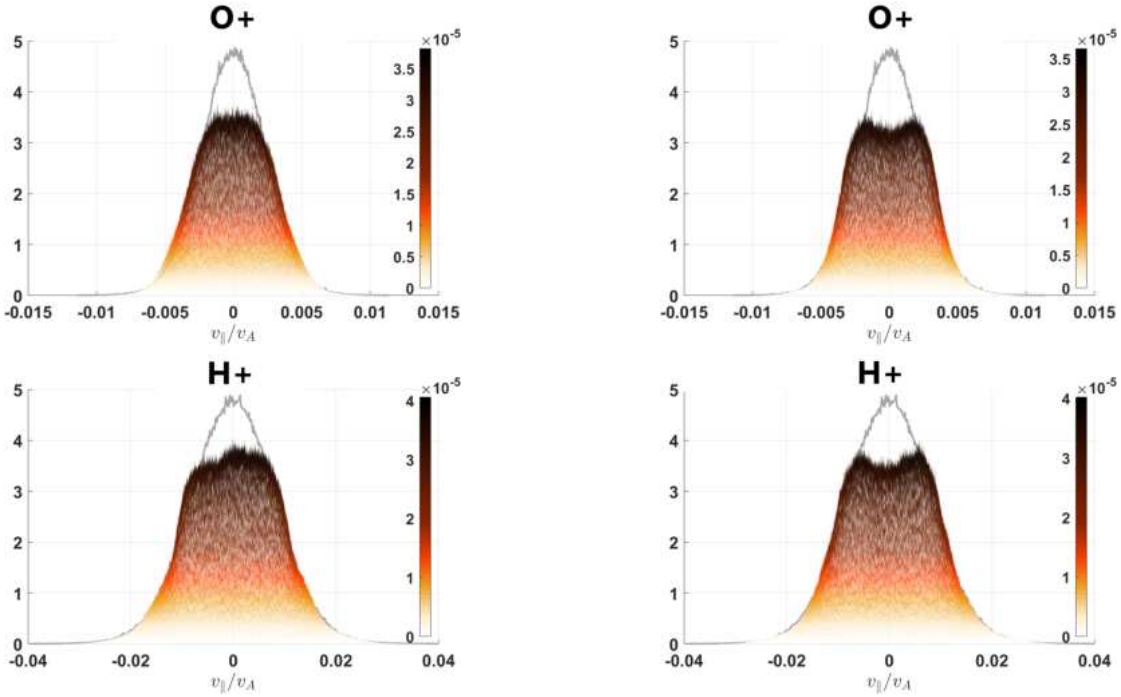

(a) $t = 300$

(b) $t = 370$

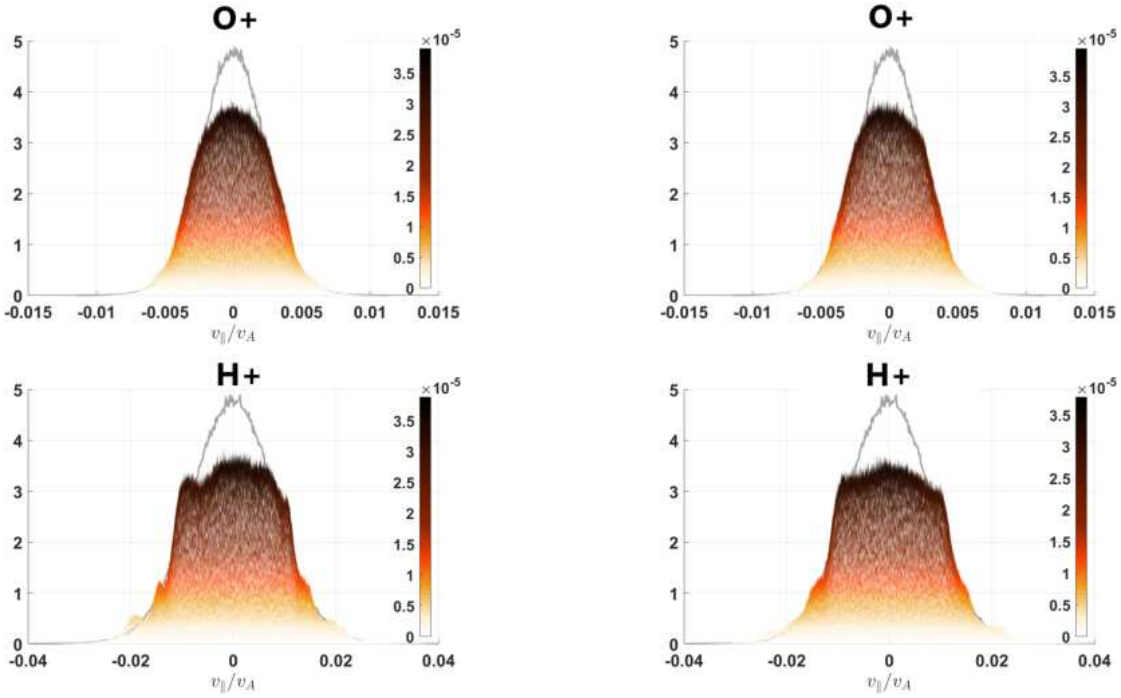

(c) $t = 790$

(d) $t = 1300$

Figure 4.39: Ion parallel velocity distribution for run K. O^+ and H^+ in the upper and lower panels respectively.

4.5 Modeling WPI in ionospheric environment: discussion

To investigate the potential mechanisms responsible for the concurrent occurrence of EM anomalies and PBs, we performed hybrid simulations of low-beta plasma perturbed by Alfvén waves, with a particular focus on the evolution of the ion VDF. The obtained results are summarized in table 4.7.

To conduct realistic simulations, three key aspects were considered. Firstly, a very low-beta plasma was modelled. As shown in table 4.2, ionospheric components exhibit plasma beta of the order of 10^{-5} for electrons and O^+ ions, and 10^{-7} for H^+ ions. Runs J and K model plasmas with these beta values. Notably, to the best of our knowledge, this is the first successful simulation of such a low-beta plasma using a hybrid code. For comparison, previous studies adopted $\beta_i = \beta_e = 0.01$ (Franci et al. [89]), $\beta_i = 0.01$ and $\beta_e = 0.1$ (Matteini et al. [182]), $\beta_i = 0.005$ (Fu et al. [93]), $\beta_i = 0.01$ (Gao et al. [99]).

Secondly, a realistic ionospheric composition at 500 km was incorporated, modelling a plasma composed of 95% heavier O^+ ions and 5% lighter H^+ ions. In all simulations with the double-species plasma (runs I, J, K), a faster and more pronounced modification of the H^+ VDF from its initial state was observed. This is attributed to the combination of lower mass and significantly lower beta of H^+ compared to O^+. Indeed, in lower-beta plasmas, the ion VDF is confined to a narrower region around $v_\parallel = v_\perp = 0$ (e.g., the VDF extrema are at $v_\parallel/v_A \approx 0.6$ for runs A, B, and C, and at $v_\parallel/v_A \approx 0.06$ for run D, as illustrated in figures 4.6 and 4.18). Consequently, the same perturbing wave exerts a larger impact on the lower beta ion VDF.

Thirdly, the plasma was perturbed by a realistic wave. Given the ubiquitous Earth's magnetic field of approximately 10^4 nT, realistic ionospheric perturbations constitute only a small fraction of the ambient field. Furthermore, as detailed in chapter 3, the ionosphere is filled with various signatures at different frequencies, including rapidly varying waves like whistlers. Therefore, run K employed a spectrum of perturbing waves with an amplitude of $B/B_0 = 2 \cdot 10^3$, a realistic value for ionospheric magnetic perturbations (see, e.g., Le et al. [163]). As shown in figure 4.39, even such a small perturbing wave spectrum can induce fast ion beams.

To validate our numerical setup, initial simulations replicated the configuration described in Matteini et al. [182], successfully reproducing their observed parametric decay with the emergence of a density mode at approximately double the mother wave number (k_M) and a daughter wave at lower k_r. These findings align with the parametric decay resonant condition: $k_r = k_M - k_s$. Concurrently, a population of accelerated ions formed.

Subsequent simulations systematically varied parameters to investigate their impact:

- **Wave number (k_M)**: Runs A, B, and C are characterized by identical parameters, except for the wavenumber of the mother wave k_M. Reducing k_M (Run C), attenuated kinetic effects due the proximity to the MHD regime. A parametric decay similar to run A is observed, with the same evolution of the VDF but at a slower pace. Conversely, increasing k_M (Run B) accelerated VDF evolution. Notably, Run B exhibited a double decay, with the appearance of a daughter and a granddaughter wave and the corresponding the generation of ion beams on both sides of the VDF. This effect is described in Tsurutani [261], and granddaughter waves have been found in several works (e.g., Kojima et al. [154] and Umeda, Saito, and Nariyuki [265]).

Run	Summary	Results
A	Test of the setup	Single parametric decay at $t \approx 200$, with the rising of a daughter wave at lower k. Correspondingly, modification of the positive side of the parallel velocity distribution with the generation of populations of faster ions.
B	Double k_M with respect to run A	Double decay, faster evolution. First decay $\rightarrow$ daughter wave at lower k $\rightarrow$ fast ion beams (positive side). Second decay $\rightarrow$ granddaughter wave at even lower $k \rightarrow$ ion beams (negative side).
C	Halved k_M w.r.t. run A	Single decay, same as run A but slower evolution.
D	Reduced beta w.r.t. run B	Single decay, even faster evolution w.r.t. run B. Generation of a daughter wave at lower k. Rapid generation and destruction of several harmonics in density and magnetic field. Widening of the VDF in both side of the parallel direction.
E	Reduced beta w.r.t. run D	Same behaviour of run D, but with an even faster evolution, more harmonics on the wave spectrum and VDF completely spread out along the parallel direction.
F	Reduced B/B_0 w.r.t. run E	Density peak at $t = 60$ and second harmonics at $t = 120$ on the spectrum. No daughter wave. Minor modification of the VDF, with the central peak slightly lower and barely visible beams on both side of the parallel direction at $t \geq 400$.
G	Spectrum of Alfvén waves	Rising of a triple peak at $t = 120$ and correspondingly the second harmonic on the magnetic field. Effects on the VDF slightly increased.
H	Reverse polarization w.r.t run G	Faster evolution w.r.t. G. Appearance of several harmonics. Remarkable evolution of the VDF, with generation of fast ion beams at $t > 400$.
I	As run H but with two species plasma	Same behaviour of run H for the O^+ ions. Generation of fast proton beams in both sides and filling of the tails of the H^+ VDF.
J	Lower beta w.r.t. run I (reaching realistic values)	Similar situation as run E with the fast appearance of several harmonics on the spectrum and a VDF completely spread out along both sides of the parallel direction.
K	As run J but with lowered B/B_0	Several harmonics in both the density and the magnetic field rise and decrease with a slow evolution. Remarkable deviation of both species VDF from its original configuration. For H^+, lot of the plasma in the tails of the VDF and generation of fast ion beams at $t \geq 700$.

Table 4.7: Summary of simulation results.

- **Plasma beta**: Very low-beta plasma simulations (runs D-K) displayed deviations from standard parametric decay behaviour. The ion VDF evolves later than the density peak, maintaining approximate symmetry around $v_{\parallel}/v_A = 0$. Additionally, especially from runs F to K, no clear daughter wave is observed. This effect can be explained by referring to the resonant condition: $k_r = k_s - k_M$. When $\beta \ll 1$, then $k_r \simeq k_M$, and thus no daughter wave can be distinguished from the original pump wave. However, the first harmonic in the density always arises at approximately $2k_M$, regardless of the clear occurrence of parametric decay. Finally, at low beta values, the ion VDF typically exhibits a decrease and spread of the peak centred at $v_{\parallel}/v_A = 0$, which becomes a plateau (runs D, F, G, H, I, K).

- **Combined beta and amplitude**: As mentioned before, the same perturbation is more effective on a lower beta plasma. In fact, comparing simulations with the same parameters (in particular same perturbing wave) but lower beta values (run E with respect to run D; run J with respect to run I), we observe the fast rise of several harmonics in both the density and magnetic field spectrum accompanied by rapid VDF broadening. In these cases, the plasma completely fills both tails of the distribution. This behaviour suggests intense electric fields driven by high-pressure gradients, shooting particles in both directions. The effect vanishes with reduced wave amplitude (run F with respect to run E). Moreover, the mother wave magnetic field peak disappears as the VDF flattens.

- **Initial wave spectrum**: In addition to representing a more realistic situation in the electromagnetic environment, compared to monochromatic waves, a wave spectrum induces more pronounced VDF modifications. Potential mechanisms explaining this phenomenon include ponderomotive effects driving the plasma towards the static approximation ($n \propto B^2$), as described by Spangler and Sheerin [247] and Spangler [246]. In addition, the breakdown of this approximation due to B^2 modulation (Machida, Spangler, and Goertz [175] and Nariyuki and Hada [198]) and modulational instability of wave packets (Machida, Spangler, and Goertz [175], Vasquez [267], Velli et al. [270], and Buti et al. [37]) may also contribute. Finally, Nariyuki and Hada [196] explained how an alternative way for the mother wave energy dissipation can be provided by the modulational instability driven by incoherent modes.

- **Wave polarization**: Inverting the polarization from right-handed to left-handed (from run H to G) leads to a faster and more pronounced evolution of the ion VDF. This is explained by the fact that left-handed polarized waves have the same sense of rotation as the cyclotron motion of positively charged particles (Verscharen, Klein, and Maruca [271]).

All of these findings should be considered as preliminary results, and further investigation is needed. In fact, we focused on the observations of fast ion beams due to WPI interactions induced by a small amplitude wave impacting an ionospheric plasma, and a full investigation of all the plasma physics effects resulting from the simulations is beyond the scope of this thesis. Nevertheless, the results are fully satisfactory in terms of linking EM waves and PBs in a ionospheric environment. In fact, the findings identify two primary scenarios:

1. **High-amplitude waves (**$B/B_0 \geq 5 \times 10^{-3}$**)**: Rapid and complete VDF spreading for both ion species.

2. **Low-amplitude waves (**$B/B_0 \leq 2 \times 10^{-3}$**)**: Slower and less pronounced VDF changes, primarily affecting lighter ions with the formation of fast ion beams after approximately $t = 300$.

While scenario 1 represents extreme conditions associated with severe space weather events, scenario 2 is more common due to the frequent occurrence of such perturbations (Le et al. [163]). The generated ion beams, with velocities of the order of magnitude of 10^3 m/s, possess the potential to induce particle precipitation, establishing a possible link between EM anomalies and PBs. Furthermore, the highly realistic simulation (run K) has demonstrated a notable finding. Ion VDF evolution is relatively slow, exhibiting significant changes with respect its initial configuration only after $t \geq 300$ time units, corresponding to approximately 10.5 seconds. This outcome suggests caution when attributing concurrent observations of EM anomalies and PBs to a common origin. A quantitative estimation of the expected time delay is crucial before drawing definitive conclusions.

Conclusions

The potential correlation between ionospheric anomalies and seismic activity is a contentious topic within the scientific community. Despite numerous claims of seismo-related ionospheric anomalies (Molchanov and Hayakawa [190], Pulinets and Boyarchuk [220], Hayakawa [114], Pulinets et al. [221], Yao et al. [299]), several critical factors can influence the reliability of such analyses. This thesis addresses and overcomes key limitations of previous investigations, representing a significant advancement in the detection of ionospheric anomalies associated with seismic activity.

Accurate anomaly identification necessitates a precise definition of the background state. Only deviations from this background can be considered potential anomalies. Furthermore, since the spectrum of ionospheric variations extends across a large frequency range, it is crucial to consider both short duration (< 1 second) and medium-long duration (> 1 second) signals.

The methodology outlined in chapter 3 of this thesis and in Recchiuti et al. [225] represents the first robust characterization of the ionospheric EM environment at approximately 500 km altitude for medium-long duration signals. It presents several major strengths and key advancements compared to previous studies. First, such methodology has been validated through the accurate identification of known ionospheric signatures over different geographical regions. Furthermore, given the strong dependence of the ionospheric environment on solar activity, the proposed background calculation methodology incorporates solar activity data and diurnal ionospheric variability. The identified signatures exhibit variations consistent with existing literature, validating the method's effectiveness under all ionospheric conditions.

Developed in MATLAB but adaptable to other programming languages, the method is fully automated, facilitating global application. With approximately 300 core-hours of computation time per cell (considering approximately 4 years of data in the ELF band), the ionospheric background can be calculated for electric and magnetic fields on a $3^\circ \times 3^\circ$ grid covering the entire Earth. Minor modifications enable its application to other physical quantities measured by the CSES-01 satellite, such as particle flux.

To ensure an accurate characterization, the background procedure includes only observations geographically proximate to the seismic region under investigation, excluding potentially unrelated local anomalies. Additionally, a preliminary study of satellite orbits optimized the geographical cell size, and a logarithmic frequency grid was employed for optimal representation of frequencies in the range of interest (approximately 100-300 Hz; Zong, Tao, and Shen [306]).

A primary outcome of this research is the identification of distinctive signatures emerg-

ing from the background in proximity of seismic activity. These signatures were discerned through comparison of background and observations in the proximity of the earthquake. The investigation encompassed a wide range of seismic events, geographic locations, and geomagnetic conditions, confirming the versatility of the proposed technique and its effectiveness in all scenarios.

However, while the identified signatures exhibit distinctive characteristics, their definitive classification as anomalies would be misleading, due to the lack of statistical robustness. This is one of the most critical aspects in the literature, hindering the reproducibility of certain results, as highlighted by e.g. Picozza, Conti, and Sotgiu [213]. Indeed, previous studies in this field often relied on subjective visual inspection (e.g. Bertello et al. [25]) for anomaly detection. This approach is influenced by the choice of parameters, such as color scales, and is inherently susceptible to human bias. Additionally, some research has employed a simplistic method based on a fixed number of standard deviations without considering diurnal or geomagnetic variations (e.g. De Santis et al. [74]). However, such analyses often neglect the investigation of the underlying distribution function of the data, which may differ from the normal distribution. Standard deviation is a reliable metric for describing dispersion only in normally distributed data and, for non-normally distributed variables, alternative dispersion indicators are preferable (Madadizadeh, Asar, and Hosseini [176]). Misinterpreting standard deviation as if calculated from normally distributed data can lead to erroneous conclusions when dealing with non-normal distributions. To overcome these limitations, we propose a novel definition of anomaly. Our approach is based on the analysis of the ϵ_{rel} distribution at the identified frequency. Only if this distribution is significantly altered by observations in the proximity of the earthquake can the corresponding signature be classified as a seismic-related anomaly. This contribution represents a significant advancement in the field, representing the first statistically robust definition of anomaly. According to this definition, an anomaly has been identified for the Marche earthquake. Specifically, the ϵ_{rel} distribution exhibits a bimodal form when the nearest observations to the earthquake are incorporated, suggesting a different origin for the signal detected in the proximity of the earthquake. Adopting this definition in future analyses will significantly enhance the reliability and reproducibility of research in this area.

In addition, this thesis presents the first accurate characterization of short-duration ionospheric EM signatures in this field. A novel algorithm for whistler identification is introduced, offering distinct advantages over methods commonly employed in the literature. Indeed, unlike conventional techniques based on image recognition, the proposed algorithm relies solely on physical quantities. This approach has a twofold advantage: first, it enhances interpretability, basing event selection criteria on signal energy content. Second, it significantly improves computational efficiency, facilitating the classification of large number of events and a comprehensive statistical analysis.

Taking advantage of the high sampling frequency of CSES-01 instruments, the proposed analysis tools enable the generation of high-resolution whistler spectrograms. This capability facilitates a more precise determination of whistler characteristics, such as dispersion, compared to previous studies. Moreover, these tools, applicable to general EM waves beyond whistlers, accurately identify wave properties including amplitude, polarization, propagation

direction etc. Given the invaluable role of whistlers in mapping and monitoring the ionosphere and magnetosphere (Park, Carpenter, and Wiggin [208], Helliwell [116], Sazhin [236], Ferencz [82]) and their potential as precursors to natural hazards (see Wang et al. [288] and reference therein), the developed tools and the newly constructed whistler database represent a significant milestone for future investigations.

Finally, this thesis establishes, for the first time in the field, causal link between EM anomalies and PBs. Indeed, while several studies have reported coincidences or temporal associations between ionospheric anomalies (particularly EM anomalies and PBs) and strong earthquakes, they have often lacked a clear explanation of the underlying connection and the expected time delay between the two phenomena.

The presented simulations, modelling and investigating wave-particle interactions in an ionospheric plasma perturbed by a low-amplitude wave, represent (to the best of our knowledge) the first successful model of a plasma with ionospheric characteristics using a hybrid code. Specifically, our simulations are conducted in an ultra-low beta plasma regime (orders of magnitude lower than those considered in previous space plasma simulations) and model a multi-species plasma resembling real ionospheric composition at 500 km. This allowed us to investigate a parameter space that has not been previously explored, enabling the study of the effects of these conditions on wave-particle interaction processes.

The simulations demonstrate that, under realistic conditions, even a small (compared to usual ionospheric disturbances) amplitude wave can induce the generation of fast ion beams with velocities of approximately 10^3 m/s. Consequently, electromagnetic perturbations akin to those observed in the ionosphere (chapter 3) possess the potential to trigger particle precipitation detectable by ionospheric satellites. These simulations reveal a previously unidentified link between the two phenomena, addressing a significant gap in the field. Moreover, the results suggest that significant particle flux variations are more likely to be observed for H^+ ions than O^+ ions due to the more pronounced deviation of their VDF from the initial state. Crucially, the simulations provide the first estimate of the time delay between wave impact and ion beam generation. Considering the time difference between the impact of the waves and the generation of fast ion beams observed in the more realistic simulation (run K), this thesis shows how the underlying mechanism connecting EM anomalies and PBs is not instantaneous, with a characteristic delay of the order of magnitude 10 seconds. This finding emphasizes the importance of exercising caution when attributing simultaneous EM anomaly and PB events to a common origin. Rigorous analyses of ionospheric anomalies associated with seismic phenomena must account for this temporal offset.

The established connection between EM anomalies and PBs paves the way for a novel, more rigorous multi-instrumental approach to detecting seismo-related ionospheric anomalies, which could represent a significant breakthrough in the field.

By addressing and overcoming the major challenges in this area, this thesis represents a significant advancement in improving our of knowledge of lithosphere-ionosphere-magnetosphere coupling. Further development and application of presented techniques to a large dataset of events could provide the key to unlocking the complex interplay between the ionosphere and seismic processes.

Future directions

The research presented in this doctoral thesis lays the groundwork for several future studies, some of which are already underway.

The global ionospheric background and its variations

As previously outlined, the ionospheric background calculation procedure is fully automated and applicable to any global region. The background calculation algorithm is currently operational on the IAPS-INAF server, with the goal of determining the global background level. This will enable investigations into regional variations of the ionospheric background, including latitudinal, longitudinal, and hemispheric dependencies. Additionally, the seasonal variation of the global background level and its solar cycle dependence can be explored. With CSES-01 data collection ongoing since 2018, a sufficient dataset is now available for such analyses.

Moreover, the ionospheric background can be calculated using other instruments aboard the CSES-01 satellite by adapting the procedure developed for the electromagnetic background.

Application to a large dataset

Upon establishing the global background level, the developed anomaly detection procedure can be applied to a comprehensive earthquake dataset. This will enable the identification of anomalous signal occurrences, their spatial distribution, and temporal characteristics, including frequency and duration. A comprehensive interdisciplinary investigation correlating anomalous signal properties with earthquake parameters (magnitude, depth, etc.) has the potential to significantly advance the field, elucidating the connection between seismic activity and the ionosphere. Furthermore, extending the analysis of ϵ_{rel} distribution function to the pre-seismic period may lead to the identification of precursory anomalies, a crucial step towards earthquake forecasting.

Investigation of the characteristics of the anomalies

Since the identified EM anomalies exhibit the characteristics of EM waves, the whistler analysis procedures outlined in section 3.2 can be adapted to comprehensively characterize these signals. In particular, a statistical analysis of propagation direction based on a large dataset is

crucial for elucidating the origin of these EM anomalies. Upward propagation would suggest a terrestrial source, meaning that they are injected from below. Otherwise the most probable explanation is the the excitation of a new ionospheric mode triggered by seismic activity, resonating at the observed frequency.

In this investigation, a rotation of both electric and magnetic field components in the mean-filed aligned (MFA) coordinate system can be useful to determine the direction of propagation with respect to the ambient geomagnetic field.

Classification of EM chirps via CNN

Spectrograms (0.6-second time intervals) generated for all whistlers detected using the algorithm presented in section 3.2 consistently revealed the characteristic falling tone chirp associated with whistler mode propagation. However, these spectrograms exhibited diverse features. As illustrated in figures 4.40, 4.41, and 4.42, while all examples display the falling tone chirp, variations in chirp definition, duration, and frequency content are evident. The presence of multiple chirps and lower-frequency bands in some cases suggests distinct source mechanisms. In collaboration with ESA-ESRIN, we are currently developing a machine learning-based classification system to attribute each signal to its corresponding source. Known sources of whistler waves include "standard" lightning, transient luminous events (TLEs), and lightning induced by volcanic activity.

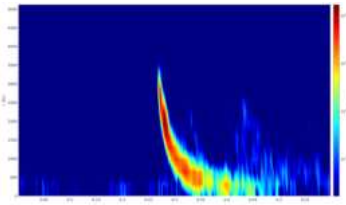

Figure 4.40: Example of a very definite and very brief falling tone chirp.

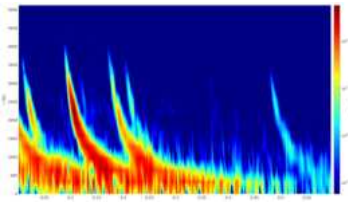

Figure 4.41: Example of a signal made by various chirps and a lower frequency band.

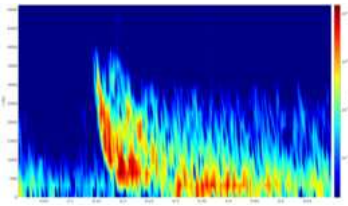

Figure 4.42: Example of a broadened chirp with a lower frequency band.

A multidisciplinary approach, incorporating the analysis of lightning maps, could further enhance this investigation.

Extended whistler analysis

In this study, whistler analysis was confined to latitudes between -40° to 40°. To expand our understanding of whistler occurrence near the polar cap, where ionospheric conditions are significantly influenced by solar activity, future investigations should extend the analysis to higher latitudes (up to $\pm 65°$, the operational limit of CSES-01 instruments). Furthermore, the upcoming launch of CSES-02 in December 2024, equipped with continuously operating instruments, will enable further exploration of whistler characteristics within the polar cap.

Ionospheric electron density deduced from whistler

The whistler database can be leveraged to determine and investigate ionospheric electron density profiles, as extensively documented in the literature (Carpenter [45], Liemohn and Scarf [168], Angerami and Carpenter [13], Allcock [9], Carpenter and Anderson [44]).

Improving the WPI numerical simulations

In a plasma, charged particle trajectories are known to follow magnetic field lines (e.g. Rossi and Olbert [230]). Consequently, the 1D simulations presented in this thesis accurately represent particle motion along one-dimensional field lines. However, there are various mechanisms through which this constraint can be violated (see Minnie et al. [188] and reference therein). Moreover, recent studies have explored hybrid simulations in 2D and 3D, investigating both agreements and discrepancies between these two approaches (e.g. Franci et al. [91]), confirming the importance of dimensionality in these simulations.

Consequently, even though the computational requirements may be challenging to meet, numerical simulations of WPI in the ionosphere can be enhanced by incorporating 2D or 3D domains and electron VDF analysis using full-PIC code or test particle simulations (Trotta et al. [260] and reference therein).

Comparison between simulations and observations

The simulations presented in this thesis represent a preliminary step toward direct comparisons between numerical model results and observational data. This approach is commonly employed in solar wind and magnetospheric physics to evaluate the effectiveness of theories and models in describing and predicting observed phenomena. While CSES-01 observations do not include particle velocity distribution functions (VDFs), the satellite carries instruments capable of measuring both electromagnetic fields (HPM, SCM, EFD) and plasma characteristics (LAP, PAP, HEPP, HEPD). This enables similar comparisons at the same observational point and time.

To enhance simulation accuracy, actual electromagnetic waves measured by SCM and EFD, characterized using the techniques described in chapter 3, can be input into the simulations. The expected effects of these detected signals on the plasma can then be simulated. Signals exhibiting rapid frequency variations, such as whistlers, are anticipated to have a more significant impact on the plasma distribution compared to those with constant or slowly varying frequencies, as shown in Khachatryan et al. [149]. The simulated modifications to plasma characteristics for various waves can be compared with actual observations.

Appendix A

Characterization of the ionosphere: extra figures

This appendix contains figures regarding the characterization of the ionosphere that, for the reader's convenience, have been extrapolated from the main body of the thesis.

A.1 Inospheric backgrounds

A.1.1 Crete

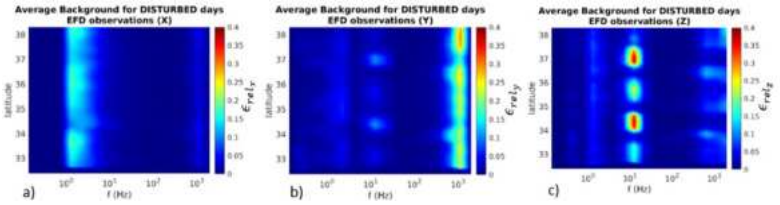

Figure A.1: Average environmental background for disturbed conditions over the 6°x6° considered (EFD). Ionospheric signals already detected for the Haitian case event can be found again.

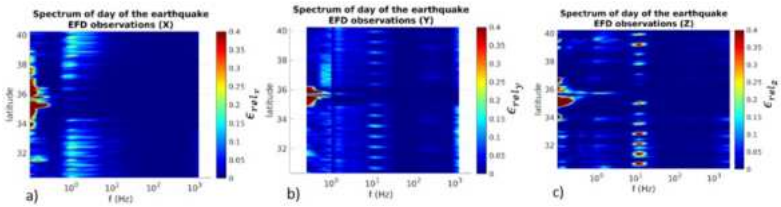

Figure A.2: CSES-01/EFD spectra for Sept 27, 2021, seventeen hours before the event, on the same 6° × 6° LAT-LON cell. In this case, no clear signal emerges from the background.

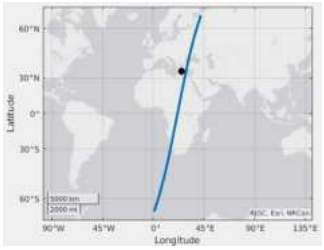

Figure A.3: CSES-01 orbit (blue line) flying over the EE, 17 hours before the earthquake. The black point represents the EE.

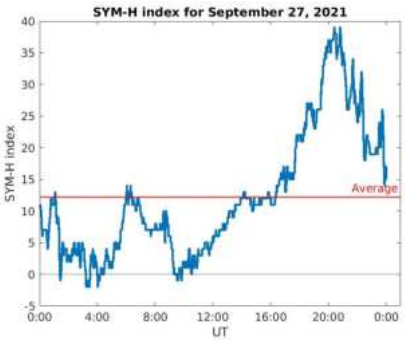

Figure A.4: SYM-H index for Sept 27, 2021. This day is classified as stormy.

A.1.2 Vanuatu

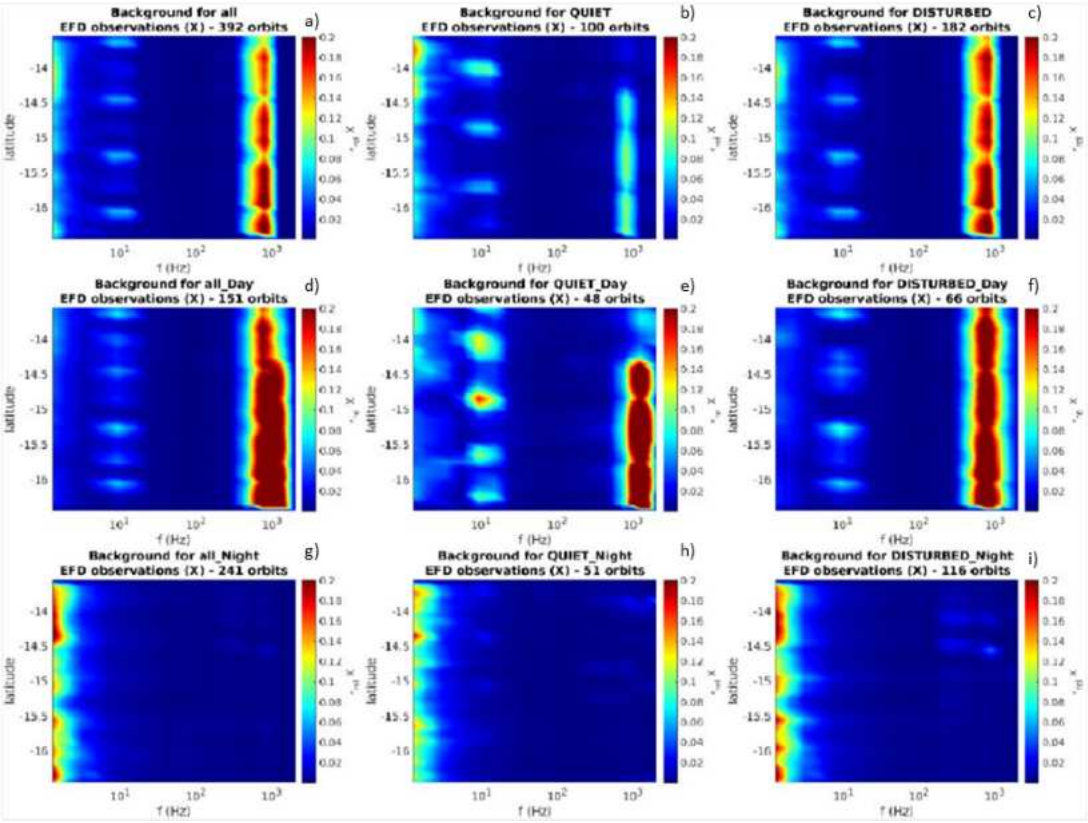

Figure A.5: The nine different background for the region of Vanuatu (X component). a) ALL; b) QUIET; c) DISTURBED; d) DIURNAL; e) QUIET DIURNAL; f) DISTURBED DIURNAL; g) NOCTURNAL; h) QUIET NOCTURNAL; i) DISTURBED NOCTURNAL. Apart from nocturnal spectra, two evident signals emerge from these spectra, the ≈ 8 Hz, which is the 1_{st} Schumann ionospheric resonance, and the ≈ 1 kHz, which is the signature of the plasmaspheric hiss.

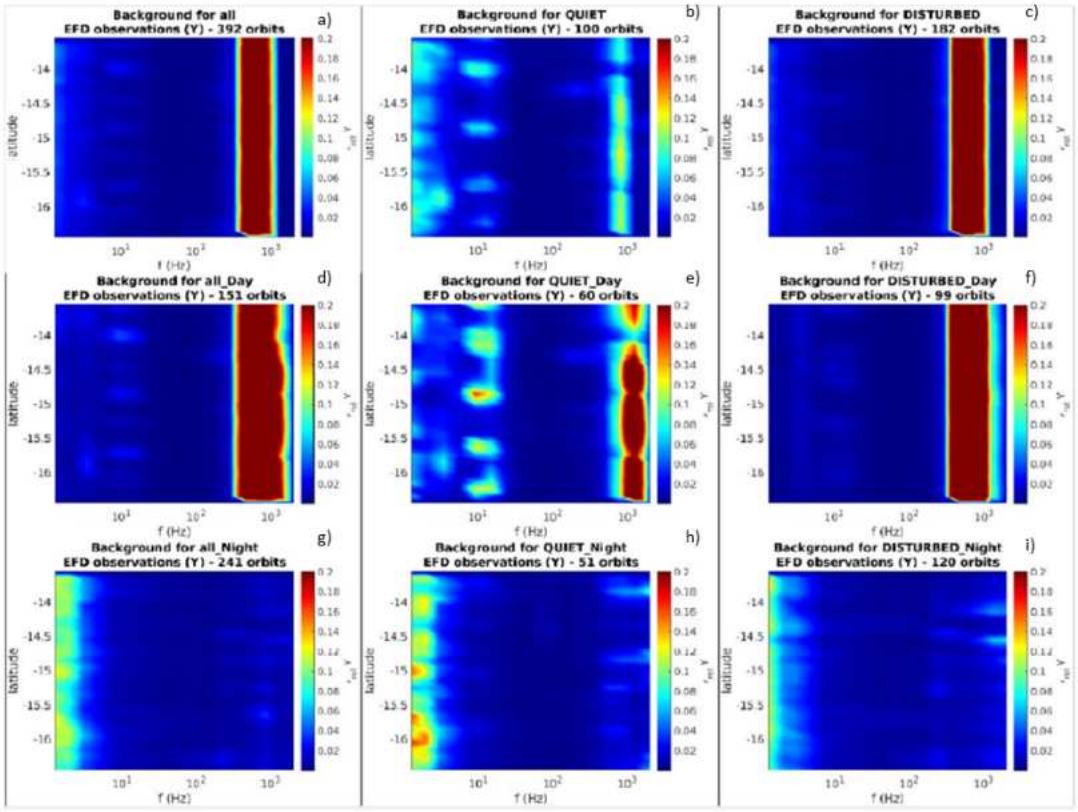

Figure A.6: The nine different background for the region of Vanuatu Island (Y component). a) ALL; b) QUIET; c) DISTURBED; d) DIURNAL; e) QUIET DIURNAL; f) DISTURBED DIURNAL; g) NOCTURNAL; h) QUIET NOCTURNAL; i) DISTURBED NOCTURNAL. The signature of plasmaspheric hiss is evident in the diurnal observations but it is faint in the nocturnal ones.

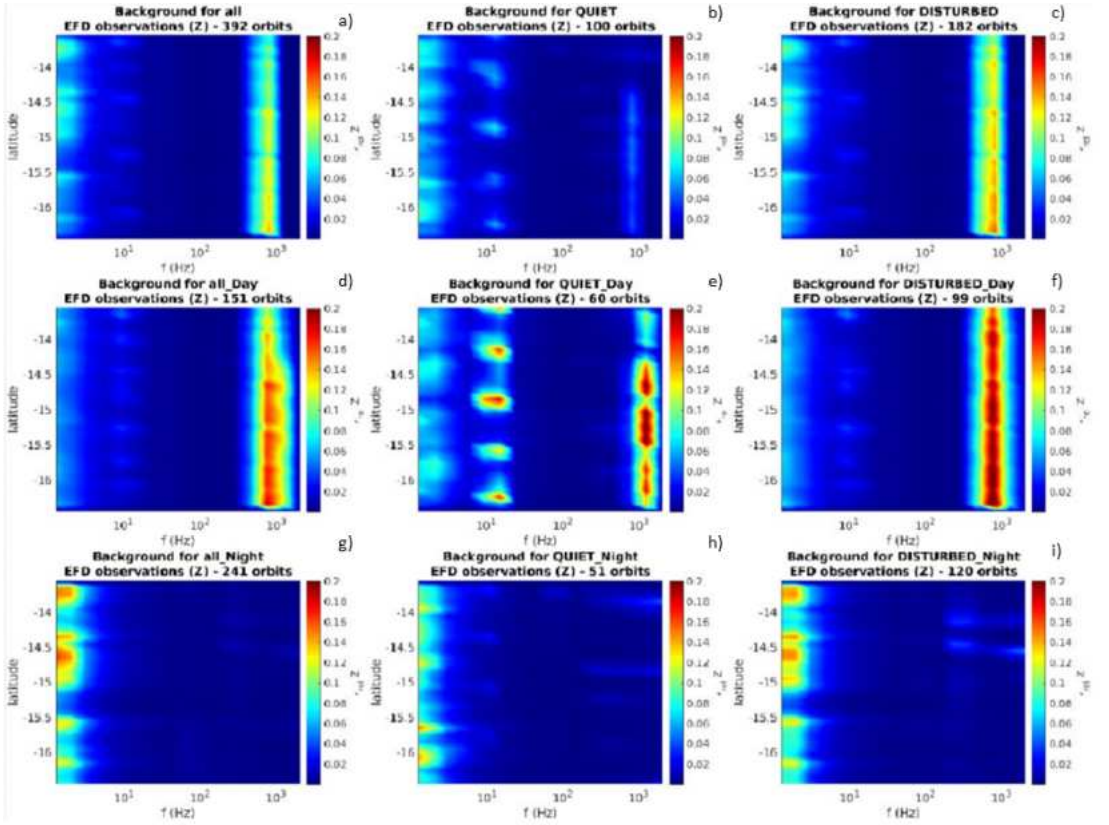

Figure A.7: The nine different background for the region of Vanuatu Island (Z component). a) ALL; b) QUIET; c) DISTURBED; d) DIURNAL; e) QUIET DIURNAL; f) DISTURBED DIURNAL; g) NOCTURNAL; h) QUIET NOCTURNAL; i) DISTURBED NOCTURNAL. Again, the signature of the plasmaspheric hiss shows a very different behaviour between nocturnal and diurnal observations.

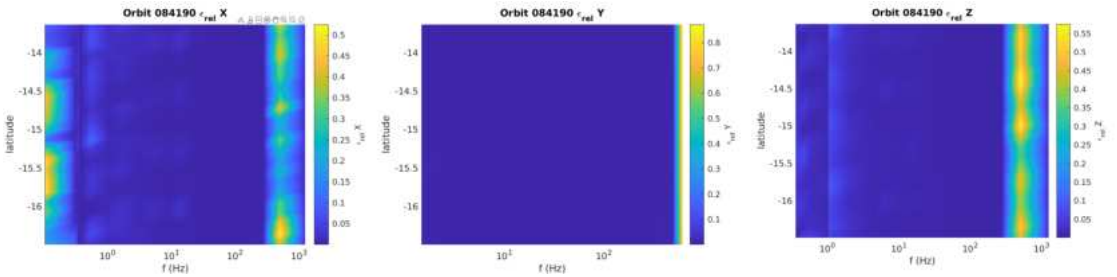

Figure A.8: CSES-01/EFD spectra for orbit 084190 (August 10, 2019) just after days of strong seismic activity, on the same 3° × 3° LAT-LON cell. A clear ≈ 400 ± 120 Hz signal is detected on X and Z components.

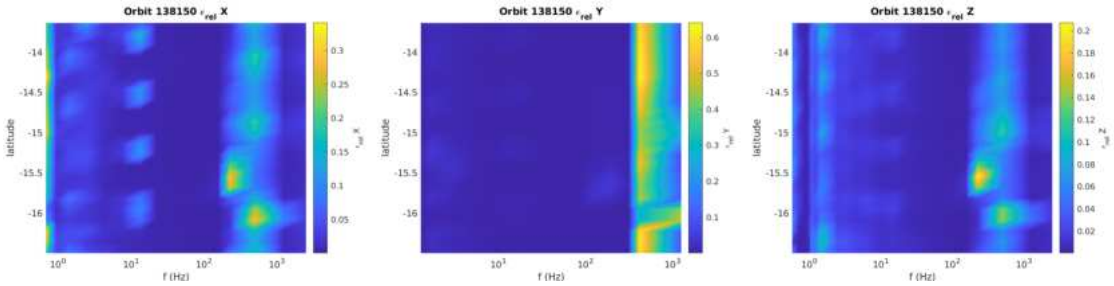

Figure A.9: CSES-01/EFD spectra for orbit 084190 (July 30, 2020) just before a strong earthquake occurred on August 5, 2020, on the same $3° \times 3°$ LAT-LON cell. A clear $\approx 400 \pm 120$ Hz signal emerges again from the background, this time on all the components.

A.1.3 Italy (Marche)

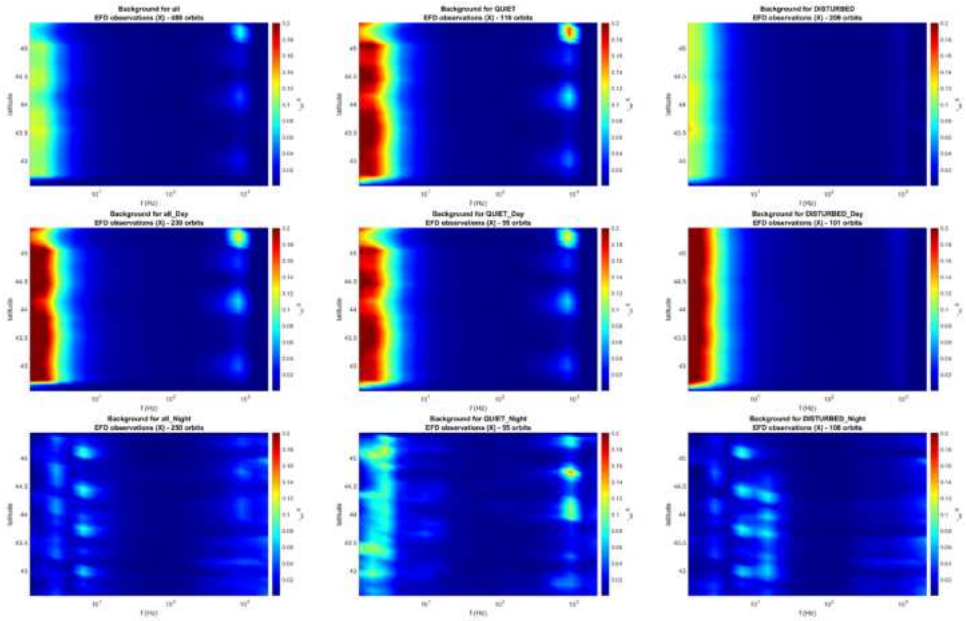

Figure A.10: The nine different background for the italian region of Marche (X component). From top to bottom: all the observations, only diurnal observations and only the nocturnal ones. From left to right: all geomagnetic conditions, only quiet days and only disturbed days. Diurnal spectra reveal only the $\approx$ 1 kHz signal, which is the signature of the plasmaspheric hiss. It is not intense in this case, but slightly clearer during quiet conditions. The large very intense band at very low frequencies probably hide the presence of the other signals. In fact, the 2 Hz signature of the satellite's motion into a magnetic field and the Schumann resonances (8 and 15 Hz) are visible only during nocturnal observations (lower panels, with higher intensity during disturbed conditions).

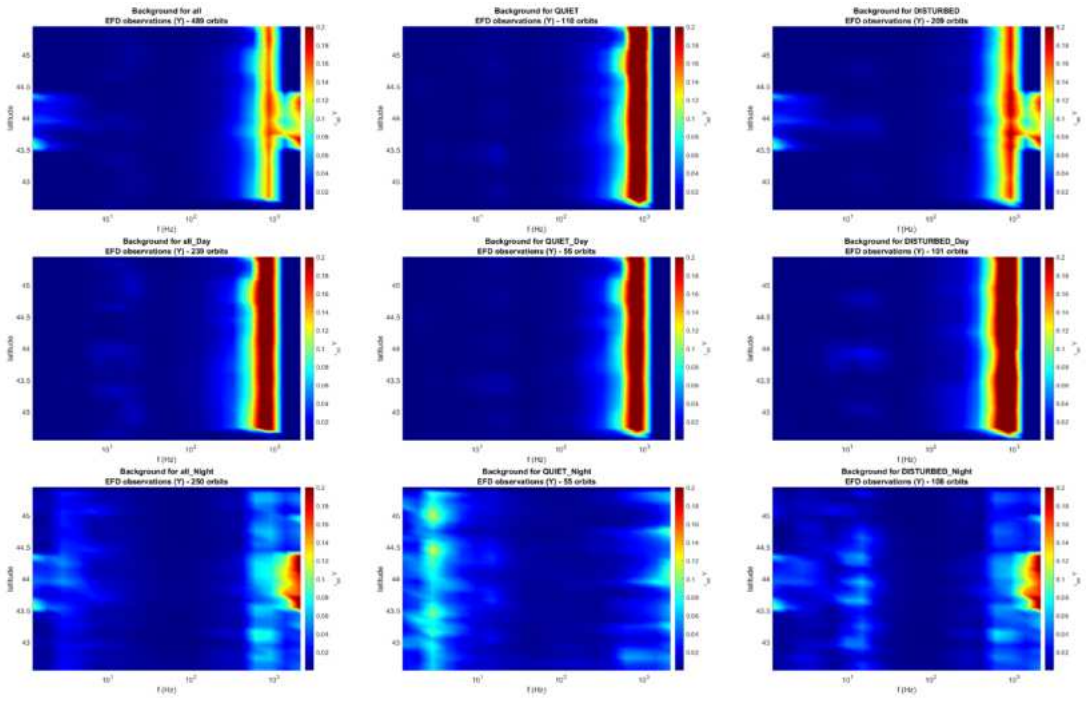

Figure A.11: The nine different background for the italian region of Marche (Y component). From top to bottom: all the observations, only diurnal observations and only the nocturnal ones. From left to right: all geomagnetic conditions, only quiet days and only disturbed days. Diurnal and nocturnal spectra are very different; in the former, the signature of the plasmaspheric hiss (1 kHz) can be observed clearly, in the latter, this signal is faint but the 2 Hz (especially during quiet conditions) and the 8 and 15 Hz (especially during disturbed conditions) become visible.

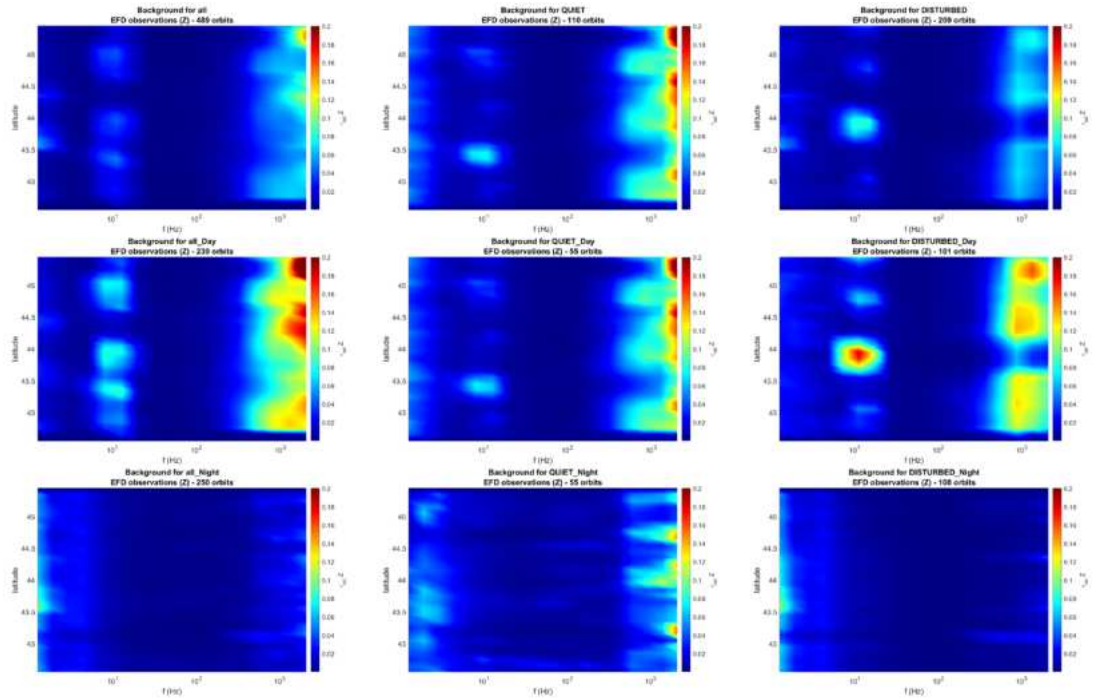

Figure A.12: The nine different background for the italian region of Marche (Z component). From top to bottom: all the observations, only diurnal observations and only the nocturnal ones. From left to right: all geomagnetic conditions, only quiet days and only disturbed days. Diurnal observations clearly show the presence of the Schumann resonances and the plasmaspheric hiss. Nocturnal spectra are quiet clean.

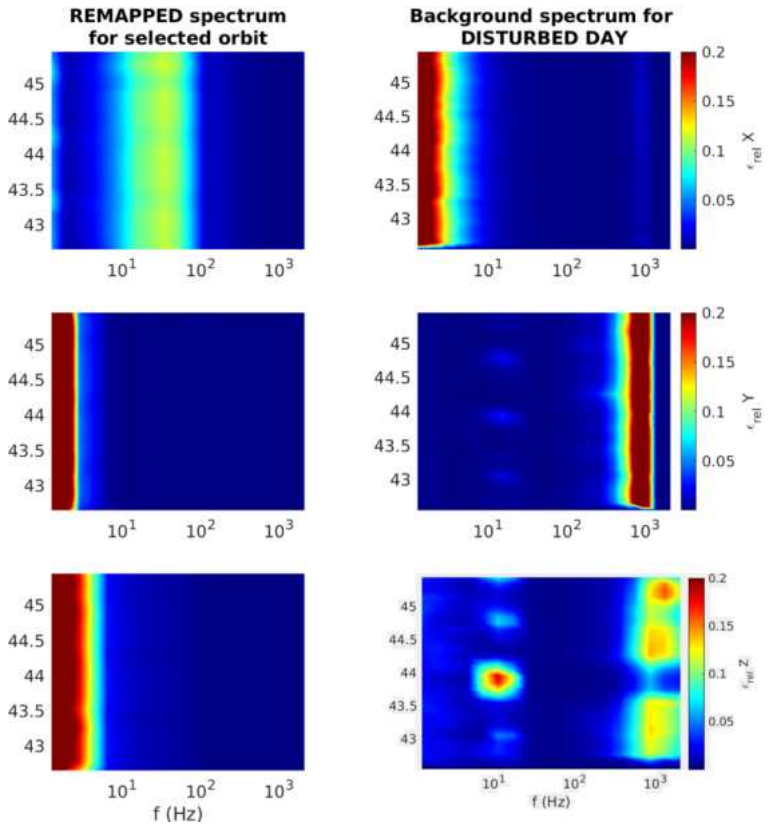

Figure A.13: Left panels: spectra for orbit 266510. Right panels: background for diurnal disturbed orbits. X, Y and Z components from top to bottom, respectively. An intense signal at ≈ 80 Hz appears on the X component.

A.2 Short time signals

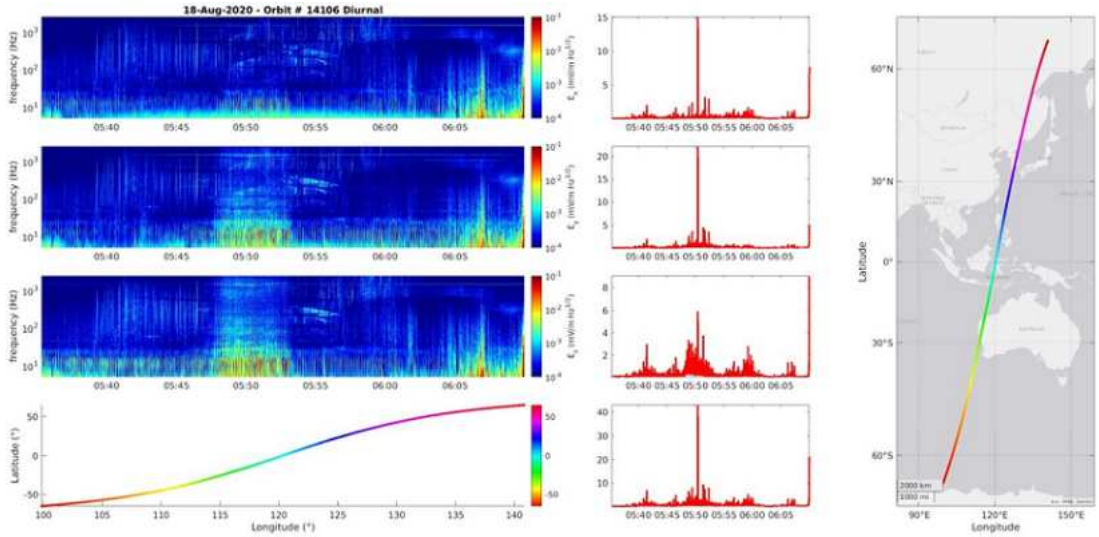

Figure A.14: On the left, spectra of the electric field observations (X, Y and Z components from top to bottom and trajectory of the orbit). On the central panels, plot of the integrated PSD (from top to bottom: X, Y, Z components and their sum). On the right, trajectory of the orbits on the geographical map. On the integrated PSD plot a very large spike is present at $\approx$ 5:50 UT.

Bibliography

[1] Mangalathayil Ali Abdu. "Equatorial ionosphere–thermosphere system: Electrodynamics and irregularities". In: *Advances in Space Research* 35.5 (2005), pp. 771–787.

[2] Timothée Achilli. *Statistical study of the Earth's magnetopause boundary layer particle populations*. 2015.

[3] S I Akasofu and Sydney Chapman. "Solar-terrestrial physics." In: (1972).

[4] Tommaso Alberti et al. "Identification of the different magnetic field contributions during a geomagnetic storm in magnetospheric and ground observations". In: *Annales Geophysicae*. Vol. 34. 11. Copernicus GmbH. 2016, pp. 1069–1084.

[5] S Yu Aleksandrin et al. "High-energy charged particle bursts in the near-Earth space as earthquake precursors". In: *Annales Geophysicae*. Vol. 21. 2. Copernicus Publications Göttingen, Germany. 2003, pp. 597–602.

[6] Hannes Alfvén. "On the existence of electromagnetic-hydrodynamic waves". In: *Arkiv for matematik, astronomi och fysik* 29 (1943), pp. 1–7.

[7] Hannes Alfvén and B Lindblad. "Granulation, magneto-hydrodynamic waves, and the heating of the solar corona". In: *Monthly Notices of the Royal Astronomical Society* 107.2 (1947), pp. 211–219.

[8] Patrick Alken et al. "International geomagnetic reference field: the thirteenth generation". In: *Earth, Planets and Space* 73 (2021), pp. 1–25.

[9] G McK Allcock. "The electron density distribution in the outer ionosphere derived from whistler data". In: *Journal of Atmospheric and Terrestrial Physics* 14.3-4 (1959), pp. 185–199.

[10] E Paulo Alves, Warren B Mori, and Frederico Fiuza. "Numerical heating in particle-in-cell simulations with Monte Carlo binary collisions". In: *Physical Review E* 103.1 (2021), p. 013306.

[11] G Anagnostopoulos et al. "Temporal evolution of energetic electron precipitation as a promising tool for earthquake prediction research: Analysis of IDP/DEMETER observations". In: *9th International Conference of the Hellenic Astronomical Society*. Vol. 424. 2010, p. 67.

[12] Georgios C Anagnostopoulos, Efthymios Vassiliadis, and Sergey Pulinets. "Characteristics of flux-time profiles, temporal evolution, and spatial distribution of radiation-belt electron precipitation bursts in the upper ionosphere before great and giant earthquakes". In: *Annals of geophysics* 55.1 (2012).

[13] JJ Angerami and Don L Carpenter. "Whistler studies of the plasmapause in the magnetosphere: 2. Electron density and total tube electron content near the knee in magnetospheric ionization". In: *Journal of Geophysical Research* 71.3 (1966), pp. 711–725.

[14] JA Araneda. "Parametric instabilities of parallel-propagating Alfvén waves: kinetic effects in the MHD-model". In: *Physica Scripta* 1998.T75 (1998), p. 164.

[15] Jaime A Araneda, Eckart Marsch, and Adolfo F Vinas. "Collisionless damping of parametrically unstable Alfvén waves". In: *Journal of Geophysical Research: Space Physics* 112.A4 (2007).

[16] Elvira Astafyeva. "Ionospheric detection of natural hazards". In: *Reviews of Geophysics* 57.4 (2019), pp. 1265–1288.

[17] Bhavik R Bakshi. "Multiscale analysis and modeling using wavelets". In: *Journal of chemometrics* 13.3-4 (1999), pp. 415–434.

[18] Giovanni Barbarino and Antonio Cicone. "Stabilization and variations to the adaptive local iterative filtering algorithm: The fast resampled iterative filtering method". In: *Numerische Mathematik* (2024), pp. 1–39.

[19] Roberto Basile et al. "Migration responses to earthquakes: evidence from Italy". In: *Italian Economic Journal* 10.1 (2024), pp. 269–291.

[20] Roberto Battiston and Vincenzo Vitale. "First evidence for correlations between electron fluxes measured by NOAA-POES satellites and large seismic events". In: *Nuclear Physics B-Proceedings Supplements* 243 (2013), pp. 249–257.

[21] Wolfgang Baumjohann and Rudolf A Treumann. *Basic space plasma physics*. World Scientific, 2012.

[22] EA Belli and J Candy. "Full linearized Fokker–Planck collisions in neoclassical transport simulations". In: *Plasma physics and controlled fusion* 54.1 (2011), p. 015015.

[23] Gérard Belmont et al. *Introduction to plasma physics*. Elsevier, 2019.

[24] Julius S Bendat and Allan G Piersol. *Random data: analysis and measurement procedures*. John Wiley & Sons, 2011.

[25] Igor Bertello et al. "Electromagnetic field observations by the DEMETER satellite in connection with the 2009 L'Aquila earthquake". In: *Annales Geophysicae*. Vol. 36. 5. Copernicus GmbH. 2018, pp. 1483–1493.

[26] Prabhu Lal Bhatnagar, Eugene P Gross, and Max Krook. "A model for collision processes in gases. I. Small amplitude processes in charged and neutral one-component systems". In: *Physical review* 94.3 (1954), p. 511.

[27] D Bilitza. "35 years of International Reference Ionosphere–Karl Rawer's legacy". In: *Advances in Radio Science* 2 (2005), pp. 283–287.

[28] ST Bingham et al. "The outer radiation belt response to the storm time development of seed electrons and chorus wave activity during CME and CIR driven storms". In: *Journal of Geophysical Research: Space Physics* 123.12 (2018), pp. 10–139.

[29] Cheng Bingjun et al. "Performance of the engineering model of the CSES high precision magnetometer". In: *2015 IEEE SENSORS*. IEEE. 2015, pp. 1–4.

[30] Dieter Biskamp. "Magnetic reconnection". In: *Physics Reports* 237.4 (1994), pp. 179–247.

[31] José A Bittencourt. *Fundamentals of plasma physics*. Springer Science & Business Media, 2013.

[32] Phillip M Bitzer. "Global distribution and properties of continuing current in lightning". In: *Journal of Geophysical Research: Atmospheres* 122.2 (2017), pp. 1033–1041.

[33] Joseph E Borovsky. "What magnetospheric and ionospheric researchers should know about the solar wind". In: *Journal of Atmospheric and Solar-Terrestrial Physics* 204 (2020), p. 105271.

[34] Jacob Bortnik, Richard M Thorne, and Nigel P Meredith. "The unexpected origin of plasmaspheric hiss from discrete chorus emissions". In: *Nature* 452.7183 (2008), pp. 62–66.

[35] Kevin J Bowers, Ron O Dror, and David E Shaw. "The midpoint method for parallelization of particle simulations". In: *The Journal of chemical physics* 124.18 (2006).

[36] Marco Brambilla. *Kinetic theory of plasma waves: homogeneous plasmas*. 96. Oxford University Press, 1998.

[37] B Buti et al. "Hybrid simulations of collapse of Alfvénic wave packets". In: *Physics of Plasmas* 7.10 (2000), pp. 3998–4003.

[38] Petr Cagas. "Continuum kinetic simulations of plasma sheaths and instabilities". In: *arXiv preprint arXiv:1809.06368* (2018).

[39] Wallace Hall Campbell. *Introduction to geomagnetic fields*. Cambridge University Press, 2003.

[40] Enrico Camporeale and David Burgess. "The dissipation of solar wind turbulent fluctuations at electron scales". In: *The Astrophysical Journal* 730.2 (2011), p. 114.

[41] JinBin Cao et al. "In-flight observations of electromagnetic interferences emitted by satellite". In: *Science in China Series E: Technological Sciences* 52.7 (2009), pp. 2112–2118.

[42] JinBin Cao et al. "The electromagnetic wave experiment for CSES mission: Search coil magnetometer". In: *Science China Technological Sciences* 61 (2018), pp. 653–658.

[43] Vincenzo Carbone et al. "A mathematical model of lithosphere–atmosphere coupling for seismic events". In: *Scientific Reports* 11.1 (Apr. 2021), p. 8682. ISSN: 2045-2322. DOI: 10.1038/s41598-021-88125-7. URL: https://doi.org/10.1038/s41598-021-88125-7.

[44] DL Carpenter and RR Anderson. "An ISEE/whistler model of equatorial electron density in the magnetosphere". In: *Journal of Geophysical Research: Space Physics* 97.A2 (1992), pp. 1097–1108.

[45] Don L Carpenter. "Electron-density variations in the magnetosphere deduced from whistler data". In: *Journal of Geophysical Research* 67.9 (1962), pp. 3345–3360.

[46] AKB Chand and P Viswanathan. "Cubic Hermite and cubic spline fractal interpolation functions". In: *AIP conference Proceedings*. Vol. 1479. 1. American Institute of Physics. 2012, pp. 1467–1470.

[47] Ouliang Chang, S Peter Gary, and Joseph Wang. "Whistler turbulence forward cascade: Three-dimensional particle-in-cell simulations". In: *Geophysical research letters* 38.22 (2011).

[48] Sydney Chapman. "The morphology of geomagnetic storms and bays: A general review". In: *Vistas in Astronomy* 2 (1956), pp. 912–928.

[49] Baojia Chen et al. "Integrated early fault diagnosis method based on direct fast iterative filtering decomposition and effective weighted sparseness kurtosis to rolling bearings". In: *Mechanical Systems and Signal Processing* 171 (2022), p. 108897.

[50] Huaifei Chen et al. "Analysis of the cloud-to-ground lightning characteristics before and after installation of the coastal and inland wind farms in China". In: *Electric Power Systems Research* 190 (2021), p. 106835.

[51] Liu Chen and Fulvio Zonca. "Physics of Alfvén waves and energetic particles in burning plasmas". In: *Reviews of Modern Physics* 88.1 (2016), p. 015008.

[52] Wanfang Chen, Marc G Genton, and Ying Sun. "Space-time covariance structures and models". In: *Annual Review of Statistics and Its Application* 8 (2021), pp. 191–215.

[53] G Chisham et al. "Measuring the dayside reconnection rate during an interval of due northward interplanetary magnetic field". In: *Annales Geophysicae*. Vol. 22. 12. Copernicus Publications Göttingen, Germany. 2004, pp. 4243–4258.

[54] Claudio Chiuderi and Marco Velli. *Basics of plasma astrophysics*. Springer, 2015.

[55] Antonio Cicone. "Iterative filtering as a direct method for the decomposition of nonstationary signals". In: *Numerical Algorithms* 85.3 (2020), pp. 811–827.

[56] Antonio Cicone. "Nonstationary signal decomposition for dummies". In: *Advances in Mathematical Methods and High Performance Computing* (2019), pp. 69–82.

[57] Antonio Cicone and Pietro Dell'Acqua. "Study of boundary conditions in the iterative filtering method for the decomposition of nonstationary signals". In: *Journal of Computational and Applied Mathematics* 373 (2020), p. 112248.

[58] Antonio Cicone, Jingfang Liu, and Haomin Zhou. "Adaptive local iterative filtering for signal decomposition and instantaneous frequency analysis". In: *Applied and Computational Harmonic Analysis* 41.2 (2016), pp. 384–411.

[59] Antonio Cicone and Enza Pellegrino. "Multivariate Fast Iterative Filtering for the Decomposition of Nonstationary Signals". In: *IEEE Transactions on Signal Processing* 70 (2022), pp. 1521–1531. DOI: 10.1109/TSP.2022.3157482.

[60] Antonio Cicone and Haomin Zhou. "Multidimensional iterative filtering method for the decomposition of high–dimensional non–stationary signals". In: *Numerical Mathematics: Theory, Methods and Applications* 10.2 (2017), pp. 278–298.

[61] Antonio Cicone and Haomin Zhou. "Numerical analysis for iterative filtering with new efficient implementations based on FFT". In: *Numerische Mathematik* 147.1 (2021), pp. 1–28.

[62] Corrado Cimarelli and Kimberly Genareau. "A review of volcanic electrification of the atmosphere and volcanic lightning". In: *Journal of Volcanology and Geothermal Research* 422 (2022), p. 107449.

[63] Andrew B Collier et al. "Global lightning distribution and whistlers observed at Dunedin, New Zealand". In: *Annales Geophysicae*. Vol. 28. 2. Copernicus GmbH. 2010, pp. 499–513.

[64] Gianpiero Colonna and Antonio D'Angola. *Plasma Modeling: Methods and Applications*. IOP Publishing, 2022.

[65] Catherine Constable. "Earth's electromagnetic environment". In: *Surveys in Geophysics* 37.1 (2016), pp. 27–45.

[66] Catherine G Constable and Steven C Constable. "Satellite magnetic field measurements: applications in studying the deep earth". In: *The state of the planet: Frontiers and challenges in geophysics* 150 (2004), pp. 147–159.

[67] Thomas George Cowling. "Magnetohydrodynamics". In: (1976).

[68] Neil F Cramer. *The physics of Alfvén waves*. John Wiley & Sons, 2011.

[69] NU Crooker. "Reverse convection". In: *Journal of Geophysical Research: Space Physics* 97.A12 (1992), pp. 19363–19372.

[70] J Crouchley. "A study of whistling atmospherics. V. Dispersion". In: *Australian Journal of Physics* 17.1 (1964), pp. 88–105.

[71] Steven A Cummer et al. "Quantification of the troposphere-to-ionosphere charge transfer in a gigantic jet". In: *Nature Geoscience* 2.9 (2009), pp. 617–620.

[72] Giulia D'Angelo et al. "Haiti Earthquake (Mw 7.2): Magnetospheric–Ionospheric–Lithospheric Coupling during and after the Main Shock on 14 August 2021". In: *Remote Sensing* 14.21 (2022). ISSN: 2072-4292. DOI: 10.3390/rs14215340. URL: https://www.mdpi.com/2072-4292/14/21/5340.

[73] Kenneth Davies and Donald M Baker. "Ionospheric effects observed around the time of the Alaskan earthquake of March 28, 1964". In: *Journal of Geophysical Research* 70.9 (1965), pp. 2251–2253.

[74] Angelo De Santis et al. "Potential earthquake precursory pattern from space: The 2015 Nepal event as seen by magnetic Swarm satellites". In: *Earth and planetary science letters* 461 (2017), pp. 119–126.

[75] Cristian De Santis et al. “The High Energy Particle Detector (HEPD-02) for the second China Seismo-Electromagnetic Satellite (CSES-02)”. In: *POS PROCEEDINGS OF SCIENCE* 395 (2022).

[76] Piero Diego et al. “The Electric Field Detector on Board the China Seismo Electromagnetic Satellite—In-Orbit Results and Validation”. In: *Instruments* 5.1 (2021). ISSN: 2410-390X. DOI: 10.3390/instruments5010001. URL: https://www.mdpi.com/2410-390X/5/1/1.

[77] Andrew J Dowdy and Yuriy Kuleshov. “Climatology of lightning activity in Australia: spatial and seasonal variability”. In: *Australian Meteorological and Oceanographic Journal* 64.2 (2014), pp. 103–108.

[78] JW Dungey. “Loss of Van Allen electrons due to whistlers”. In: *Planetary and Space Science* 11.6 (1963), pp. 591–595.

[79] Thomas L Eckersley. “Musical atmospherics”. In: *Nature* 135.3403 (1935), pp. 104–105.

[80] Barbara J Falkowski et al. “Two sources of dayside intense, quasi-coherent plasmaspheric hiss: A new mechanism for the slot region?” In: *Journal of Geophysical Research: Space Physics* 122.2 (2017), pp. 1643–1657.

[81] JA Fedder and JG Lyon. “The solar wind-magnetosphere-ionosphere current-voltage relationship”. In: *Geophysical Research Letters* 14.8 (1987), pp. 880–883.

[82] Csaba Ferencz. *Whistler phenomena: short impulse propagation*. Vol. 262. Springer Science & Business Media, 2001.

[83] Cristiano Fidani, Roberto Battiston, and William J Burger. “A study of the correlation between earthquakes and NOAA satellite energetic particle bursts”. In: *Remote Sensing* 2.9 (2010), pp. 2170–2184.

[84] C. C. Finlay et al. “International Geomagnetic Reference Field: the eleventh generation”. In: *Geophysical Journal International* 183.3 (Dec. 2010), pp. 1216–1230. ISSN: 0956-540X. DOI: 10.1111/j.1365-246X.2010.04804.x. eprint: https://academic.oup.com/gji/article-pdf/183/3/1216/1785065/183-3-1216.pdf. URL: https://doi.org/10.1111/j.1365-246X.2010.04804.x.

[85] Patrick Flandrin. *Time-frequency/time-scale analysis*. Academic press, 1998.

[86] L Franci et al. “Three-dimensional simulations of solar wind turbulence with the hybrid code CAMELIA”. In: *Journal of Physics: Conference Series*. Vol. 1031. 1. IOP Publishing. 2018, p. 012002.

[87] Luca Franci et al. “Anisotropic electron heating in turbulence-driven magnetic reconnection in the near-sun solar wind”. In: *The Astrophysical Journal* 936.1 (2022), p. 27.

[88] Luca Franci et al. “High-resolution hybrid simulations of kinetic plasma turbulence at proton scales”. In: *The Astrophysical Journal* 812.1 (2015), p. 21.

[89] Luca Franci et al. “Plasma beta dependence of the ion-scale spectral break of solar wind turbulence: high-resolution 2D hybrid simulations”. In: *The Astrophysical Journal* 833.1 (2016), p. 91.

[90] Luca Franci et al. “Solar wind turbulence from MHD to sub-ion scales: high-resolution hybrid simulations”. In: *The Astrophysical Journal Letters* 804.2 (2015), p. L39.

[91] Luca Franci et al. “Solar wind turbulent cascade from MHD to sub-ion scales: large-size 3D hybrid particle-in-cell simulations”. In: *The Astrophysical Journal* 853.1 (2018), p. 26.

[92] HU Frey et al. “Continuous magnetic reconnection at Earth’s magnetopause”. In: *Nature* 426.6966 (2003), pp. 533–537.

[93] Xiangrong Fu et al. “Heating of Heavy Ions in Low-beta Compressible Turbulence”. In: *The Astrophysical Journal* 890.2 (2020), p. 161.

[94] Martin Füllekrug. “Schumann resonances in magnetic field components”. In: *Journal of Atmospheric and Terrestrial Physics* 57.5 (1995), pp. 479–484.

[95] Martin Füllekrug and Michael J Rycroft. “The contribution of sprites to the global atmospheric electric circuit”. In: *Earth, planets and space* 58.9 (2006), pp. 1193–1196.

[96] Janis Galejs. “Schumann resonances”. In: *Radio Sci. J. Res. NBS D* 69 (1965), pp. 1043–1056.

[97] Rajesh Ganesan, Tapas K Das, and Vivekanand Venkataraman. “Wavelet-based multiscale statistical process monitoring: A literature review”. In: *IIE transactions* 36.9 (2004), pp. 787–806.

[98] N Yu Ganushkina, MW Liemohn, and Stepan Dubyagin. “Current systems in the Earth’s magnetosphere”. In: *Reviews of Geophysics* 56.2 (2018), pp. 309–332.

[99] Xinliang Gao et al. “Parametric instability of a monochromatic Alfven wave: Perpendicular decay in low beta plasma”. In: *Physics of Plasmas* 20.7 (2013).

[100] S Peter Gary, Ouliang Chang, and Joseph Wang. “Forward cascade of whistler turbulence: three-dimensional particle-in-cell simulations”. In: *The Astrophysical Journal* 755.2 (2012), p. 142.

[101] R Gendrin. “Waves and wave-particle interactions in the magnetosphere: A review”. In: *Space Science Reviews* 18.2 (1975), pp. 145–200.

[102] Naum Gershenzon and Gust Bambakidis. “Modeling of seismo-electromagnetic phenomena”. In: *Russian Journal of Earth Sciences* 3.4 (2001), pp. 247–275.

[103] Naum I Gershenzon, Mikhail B Gokhberg, and SL Yunga. “On the electromagnetic field of an earthquake focus”. In: *Physics of the earth and planetary interiors* 77.1-2 (1993), pp. 13–19.

[104] Hossein Ghobadi et al. “Disentangling ionospheric refraction and diffraction effects in GNSS raw phase through fast iterative filtering technique”. In: *GPS Solutions* 24.3 (2020), p. 85.

[105] Hossein Ghobadi et al. “Disentangling ionospheric refraction and diffraction effects in GNSS raw phase through fast iterative filtering technique”. In: *GPS Solutions* 24 (June 2020). DOI: 10.1007/s10291-020-01001-1.

[106] Melvyn L Goldstein. "An instability of finite amplitude circularly polarized Alfvén waves". In: *Astrophysical Journal, Part 1, vol. 219, Jan. 15, 1978, p. 700-704.* 219 (1978), pp. 700–704.

[107] Robert J Goldston. *Introduction to plasma physics*. CRC Press, 2020.

[108] WD Gonzalez et al. "What is a geomagnetic storm?" In: *Journal of Geophysical Research: Space Physics* 99.A4 (1994), pp. 5771–5792.

[109] Virginia Gray. *Principal component analysis: methods, applications and technology*. Nova Science Publishers, 2017.

[110] Michael Greenacre et al. "Principal component analysis". In: *Nature Reviews Methods Primers* 2.1 (2022), p. 100.

[111] Donald A Gurnett and Amitava Bhattacharjee. *Introduction to plasma physics: With space, laboratory and astrophysical applications*. Cambridge University Press, 2017.

[112] John Keith Hargreaves. *The solar-terrestrial environment: an introduction to geospace-the science of the terrestrial upper atmosphere, ionosphere, and magnetosphere*. Cambridge university press, 1992.

[113] M Hayakawa et al. "Recent findings on VLF/ELF sferics". In: *Journal of Atmospheric and Terrestrial Physics* 57.5 (1995), pp. 467–477.

[114] Masashi Hayakawa. *Earthquake prediction with radio techniques*. John Wiley & Sons, 2015.

[115] Kosuke Heki. "Ionospheric disturbances related to earthquakes". In: *Ionosphere Dynamics and Applications* (2021), pp. 511–526.

[116] Robert A Helliwell. *Whistlers and related ionospheric phenomena*. Courier Corporation, 2014.

[117] LU Hengxin et al. "Typical event observation of the tri-band beacon onboard the CSES (ZH-1) satellite". In: *CHINESE JOURNAL OF RADIO SCIENCE* 37.3 (2022), pp. 426–433.

[118] M Hesse and PA Cassak. "Magnetic reconnection in the space sciences: Past, present, and future". In: *Journal of Geophysical Research: Space Physics* 125.2 (2020), e2018JA025935.

[119] Colin O Hines. "Internal atmospheric gravity waves at ionospheric heights". In: *Canadian Journal of Physics* 38.11 (1960), pp. 1441–1481.

[120] Ronald L Holle, Kenneth L Cummins, and William A Brooks. "Seasonal, monthly, and weekly distributions of NLDN and GLD360 cloud-to-ground lightning". In: *Monthly Weather Review* 144.8 (2016), pp. 2855–2870.

[121] Joseph V Hollweg. "Beat, modulational, and decay instabilities of a circularly polarized Alfven wave". In: *Journal of Geophysical Research: Space Physics* 99.A12 (1994), pp. 23431–23447.

[122] RH Holzworth et al. "Electrical measurements in the atmosphere and the ionosphere over an active thunderstorm: 2. Direct current electric fields and conductivity". In: *Journal of Geophysical Research: Space Physics* 90.A10 (1985), pp. 9824–9830.

[123] Edward W Hones. "The earth's magnetotail". In: *Scientific American* 254.3 (1986), pp. 40–47.

[124] EW Hones Jr et al. "Structure of the magnetotail at 220 RE and its response to geomagnetic activity". In: *Geophysical research letters* 11.1 (1984), pp. 5–7.

[125] Yoshimori Honkura, Hideyuki Satoh, and Naoto Ujihara. "Seismic dynamo effects associated with the M7. 1 earthquake of 26 May 2003 off Miyagi Prefecture and the M6. 4 earthquake of 26 July 2003 in northern Miyagi Prefecture, NE Japan". In: *Earth, planets and space* 56 (2004), pp. 109–114.

[126] Miroslav Horkỳ, Wojciech Jacek Miloch, and Vojtěch Adalbert Delong. "Numerical heating of electrons in particle-in-cell simulations of fully magnetized plasmas". In: *Physical Review E* 95.4 (2017), p. 043302.

[127] W Horton et al. "The solar-wind driven magnetosphere–ionosphere as a complex dynamical system". In: *Physics of Plasmas* 6.11 (1999), pp. 4178–4184.

[128] Chao Huang, Lihua Yang, and Yang Wang. "Convergence of a convolution-filtering-based algorithm for empirical mode decomposition". In: *Advances in Adaptive Data Analysis* 1.04 (2009), pp. 561–571.

[129] JianPing Huang et al. "The Electric Field Detector (EFD) onboard the ZH-1 satellite and first observational results". In: *Earth and Planetary Physics* 2.6 (2018), pp. 469–478.

[130] Norden E Huang et al. "The empirical mode decomposition and the Hilbert spectrum for nonlinear and non-stationary time series analysis". In: *Proceedings of the Royal Society of London. Series A: mathematical, physical and engineering sciences* 454.1971 (1998), pp. 903–995.

[131] Robert D Hunsucker and John Keith Hargreaves. *The high-latitude ionosphere and its effects on radio propagation*. Cambridge University Press, 2007.

[132] WL Imhof et al. "Direct observation of radiation belt electrons precipitated by the controlled injection of VLF signals from a ground-based transmitter". In: *Geophysical Research Letters* 10.4 (1983), pp. 361–364.

[133] WL Imhof et al. "The modulated precipitation of radiation belt electrons by controlled signals from VLF transmitters". In: *Geophysical research letters* 10.8 (1983), pp. 615–618.

[134] B Inhester. "A drift-kinetic treatment of the parametric decay of large-amplitude Alfvén waves". In: *Journal of Geophysical Research: Space Physics* 95.A7 (1990), pp. 10525–10539.

[135] K Iwai et al. "Pressure change accompanying Alfvén waves in a liquid metal". In: *Magnetohydrodynamics* 39.3 (2003), pp. 245–250.

[136] Toshihiko Iyemori. "Storm-time magnetospheric currents inferred from mid-latitude geomagnetic field variations". In: *Journal of geomagnetism and geoelectricity* 42.11 (1990), pp. 1249–1265.

[137] MJS Johnston. "Review of electric and magnetic fields accompanying seismic and volcanic activity". In: *Surveys in geophysics* 18 (1997), pp. 441–476.

[138] Ian T Jolliffe. *Principal component analysis for special types of data*. Springer, 2002.

[139] Ian T Jolliffe and Jorge Cadima. "Principal component analysis: a review and recent developments". In: *Philosophical transactions of the royal society A: Mathematical, Physical and Engineering Sciences* 374.2065 (2016), p. 20150202.

[140] Adolph S Jursa et al. *Handbook of geophysics and the space environment*. Vol. 1. Air Force Geophysics Laboratory, Air Force Systems Command, United States ..., 1985.

[141] Yohsuke Kamide and Abraham Chian. *Handbook of the solar-terrestrial environment*. Springer, 2007.

[142] Yōsuke Kamide and Wolfgang Baumjohann. *Magnetosphere-ionosphere coupling*. Vol. 23. Springer Science & Business Media, 2012.

[143] Hiroshi Kamiyama. "The electron density distribution in the lower ionosphere produced through impact ionization by precipitating electrons and through photoionization by the associated bremsstrahlung X-rays". In: *Journal of geomagnetism and geoelectricity* 19.1 (1967), pp. 27–47.

[144] H Karimabadi et al. "Coherent structures, intermittent turbulence, and dissipation in high-temperature plasmas". In: *Physics of Plasmas* 20.1 (2013).

[145] Hakan Karslı and Derman Dondurur. "A mean-based filter to remove power line harmonic noise from seismic reflection data". In: *Journal of applied geophysics* 153 (2018), pp. 90–99.

[146] Justin C Kasper et al. "Solar wind helium abundance as a function of speed and heliographic latitude: variation through a solar cycle". In: *The Astrophysical Journal* 660.1 (2007), p. 901.

[147] MC Kelley et al. "Electrical measurements in the atmosphere and the ionosphere over an active thunderstorm: 1. Campaign overview and initial ionospheric results". In: *Journal of Geophysical Research: Space Physics* 90.A10 (1985), pp. 9815–9823.

[148] Michael C Kelley. *The Earth's ionosphere: Plasma physics and electrodynamics*. Academic press, 2009.

[149] AG Khachatryan et al. "Effect of frequency variation on electromagnetic pulse interaction with charges and plasma". In: *Physics of plasmas* 12.6 (2005).

[150] ATSUSHI KImpara. "Some characteristics of the dispersion of whistlers". In: *Proc. Res. Inst. Atmospherics, Nagoya Univ* 9 (1962), pp. 5–17.

[151] Margaret Galland Kivelson and Christopher T Russell. *Introduction to space physics*. Cambridge university press, 1995.

[152] Iu I Klimontovich. "Kinetic theory of nonideal gas and nonideal plasma". In: *Moscow Izdatel Nauka* (1975).

[153] R Koch. "Wave–particle interactions in plasmas". In: *Plasma physics and controlled fusion* 48.12B (2006), B329.

[154] H Kojima et al. "Nonlinear evolution of high frequency R-mode waves excited by water group ions near comets: Computer experiments". In: *Geophysical research letters* 16.1 (1989), pp. 9–12.

[155] Xiangyu Kong, Changhua Hu, and Zhansheng Duan. *Principal component analysis networks and algorithms*. Springer, 2017.

[156] S Koshevaya et al. "Spectrum of the seismic-electromagnetic and acoustic waves caused by seismic and volcano activity". In: *Natural Hazards and Earth System Sciences* 5.2 (2005), pp. 203–209.

[157] Paul R Krehbiel et al. "Upward electrical discharges from thunderstorms". In: *Nature Geoscience* 1.4 (2008), pp. 233–237.

[158] Dominique Lagoutte et al. "The DEMETER science mission centre". In: *Planetary and Space Science* 54.5 (2006), pp. 428–440.

[159] Gurbax S Lakhina and Bruce T Tsurutani. "Geomagnetic storms: historical perspective to modern view". In: *Geoscience Letters* 3.1 (2016), pp. 1–11.

[160] SJ Lane, MR James, and JS Gilbert. "Electrostatic phenomena in volcanic eruptions". In: *Journal of Physics: Conference Series*. Vol. 301. 1. IOP Publishing. 2011, p. 012004.

[161] Roberto Lanza and Antonio Meloni. *The Earth's Magnetic Field*. Springer, 2006.

[162] Jan Larsen. "Correlation functions and power spectra". In: *Section for Cognitive Systems, Informatics and Mathematical Modelling* (2009).

[163] Guan Le et al. "C/NOFS measurements of magnetic perturbations in the low-latitude ionosphere during magnetic storms". In: *Journal of Geophysical Research: Space Physics* 116.A12 (2011).

[164] RP Lepping, D Berdichevsky, and CC Wu. "Sun-Earth electrodynamics: The solar wind connection". In: *Research Signpost* 37.661 (2003), p. 2.

[165] W Li et al. "New chorus wave properties near the equator from Van Allen Probes wave observations". In: *Geophysical Research Letters* 43.10 (2016), pp. 4725–4735.

[166] XQ Li et al. "The high-energy particle package onboard CSES". In: *Radiation Detection Technology and Methods* 3 (2019), pp. 1–11.

[167] J Lichtenberger et al. "Automatic whistler detector and analyzer system: Automatic whistler detector". In: *Journal of Geophysical Research: Space Physics* 113.A12 (2008).

[168] Harold B Liemohn and FL Scarf. "Whistler determination of electron energy and density distributions in the magnetosphere". In: *Journal of Geophysical Research* 69.5 (1964), pp. 883–904.

[169] Luan Lin, Yang Wang, and Haomin Zhou. "Iterative filtering as an alternative algorithm for empirical mode decomposition". In: *Advances in Adaptive Data Analysis* 1.04 (2009), pp. 543–560.

[170] Chao Liu et al. "The technology of space plasma in-situ measurement on the China Seismo-Electromagnetic Satellite". In: *Science China Technological Sciences* 62 (2019), pp. 829–838.

[171] NF Loureiro and DA Uzdensky. "Magnetic reconnection: from the Sweet–Parker model to stochastic plasmoid chains". In: *Plasma Physics and Controlled Fusion* 58.1 (2015), p. 014021.

[172] John G Lyon. "The solar wind-magnetosphere-ionosphere system". In: *Science* 288.5473 (2000), pp. 1987–1991.

[173] John G Lyon. "The solar wind-magnetosphere-ionosphere system". In: *Science* 288.5473 (2000), pp. 1987–1991.

[174] ZhenHui Ma et al. "Study of factors influencing the occurrence rate of 60 Hz power line radiation in the topside ionosphere: A systematic survey using the CSES satellite". In: *Science China Technological Sciences* (2024), pp. 1–14.

[175] S Machida, SR Spangler, and CK Goertz. "Simulation of amplitude-modulated circularly polarized Alfvén waves for beta less than one". In: *Journal of Geophysical Research: Space Physics* 92.A7 (1987), pp. 7413–7422.

[176] Farzan Madadizadeh, Mohamad Ezati Asar, and Mostafa Hosseini. "Common statistical mistakes in descriptive statistics reports of normal and non-normal variables in biomedical sciences research". In: *Iranian journal of public health* 44.11 (2015), pp. 1557–1558.

[177] David M Malaspina et al. "Variation in plasmaspheric hiss wave power with plasma density". In: *Geophysical Research Letters* 45.18 (2018), pp. 9417–9426.

[178] Stéphane Mallat. *A wavelet tour of signal processing*. Elsevier, 1999.

[179] Stefano Markidis and Giovanni Lapenta. "The energy conserving particle-in-cell method". In: *Journal of Computational Physics* 230.18 (2011), pp. 7037–7052.

[180] M Matsushima et al. "Seismoelectromagnetic effect associated with the Izmit earthquake and its aftershocks". In: *Bulletin of the Seismological Society of America* 92.1 (2002), pp. 350–360.

[181] Masaki Matsushima et al. "Circularly polarized electric fields associated with seismic waves generated by blasting". In: *Geophysical Journal International* 194.1 (2013), pp. 200–211.

[182] Lorenzo Matteini et al. "Kinetics of parametric instabilities of Alfvén waves: Evolution of ion distribution functions". In: *Journal of Geophysical Research: Space Physics* 115.A9 (2010).

[183] Alan P Matthews. "Current advance method and cyclic leapfrog for 2D multispecies hybrid plasma simulations". In: *Journal of Computational Physics* 112.1 (1994), pp. 102–116.

[184] Michel Menvielle et al. "Geomagnetic indices". In: *Geomagnetic observations and models*. Springer, 2010, pp. 183–228.

[185] Nigel P Meredith et al. "Substorm dependence of plasmaspheric hiss". In: *Journal of Geophysical Research: Space Physics* 109.A6 (2004).

[186] SE Milan et al. "Space-and ground-based investigations of solar wind–magnetosphere–ionosphere coupling". In: *Advances in Space Research* 38.8 (2006), pp. 1671–1677.

[187] Stephen Eric Milan et al. "Overview of solar wind–magnetosphere–ionosphere–atmosphere coupling and the generation of magnetospheric currents". In: *Space Science Reviews* 206 (2017), pp. 547–573.

[188] J Minnie et al. "When do particles follow field lines?" In: *Journal of Geophysical Research: Space Physics* 114.A1 (2009).

[189] Amar P Misra and Gert Brodin. "Wave-particle interactions in quantum plasmas". In: *Reviews of Modern Plasma Physics* 6.1 (2022), p. 5.

[190] OA Molchanov and M Hayakawa. "Subionospheric VLF signal perturbations possibly related to earthquakes". In: *Journal of Geophysical Research: Space Physics* 103.A8 (1998), pp. 17489–17504.

[191] René J Moreau. *Magnetohydrodynamics*. Vol. 3. Springer Science & Business Media, 2013.

[192] Daniele Mortari, Matthew P Wilkins, and Christian Bruccoleri. "On sun-synchronous orbits and associated constellations". In: *Paper of the 6-th Dynamics and Control of Systems and Structures in Space Conference, Riomaggiore, Italy*. 2004, p. 43.

[193] Clement Mouhot and Cedric Villani. "On landau damping". In: (2011).

[194] Aung Myat et al. "A hybrid model based on multivariate fast iterative filtering and long short-term memory for ultra-short-term cooling load prediction". In: *Energy and Buildings* 307 (2024), p. 113977.

[195] Ganesh R Naik. *Advances in principal component analysis: research and development*. Springer, 2017.

[196] Yasuhiro Nariyuki and Tohru Hada. "Consequences of finite ion temperature effects on parametric instabilities of circularly polarized Alfvén waves". In: *Journal of Geophysical Research: Space Physics* 112.A10 (2007).

[197] Yasuhiro Nariyuki and Tohru Hada. "Kinetically modified parametric instabilities of circularly polarized Alfvén waves: Ion kinetic effects". In: *Physics of plasmas* 13.12 (2006).

[198] Yasuhiro Nariyuki and Tohru Hada. "Remarks on nonlinear relation among phases and frequencies in modulational instabilities of parallel propagating Alfvén waves". In: *Nonlinear Processes in Geophysics* 13.4 (2006), pp. 425–441.

[199] AH Nayfeh and B Balachandran. "Applied Nonlinear Dynamics, Wiley Series in Nonlinear Science". In: (1995).

[200] SV Nazarenko, AC Newell, and VE Zakharov. "Communication through plasma sheaths via Raman (three-wave) scattering process". In: *Physics of Plasmas* 1.9 (1994), pp. 2827–2834.

[201] F Němec, J Pekař, and Michel Parrot. "NWC transmitter effects on the nightside upper ionosphere observed by a low-altitude satellite". In: *Journal of Geophysical Research: Space Physics* 125.12 (2020), e2020JA028660.

[202] Binbin Ni et al. "Unique banded structures of plasmaspheric hiss waves in the Earth's magnetosphere". In: *Journal of Geophysical Research: Space Physics* 128.3 (2023), e2023JA031325.

[203] MG Nicora et al. "Atmospheric Electrical Activity in central Argentina and its relationship with phenomena observed at the Auger Observatory". In: *Journal of Physics: Conference Series*. Vol. 2398. 1. IOP Publishing. 2022, p. 012005.

[204] N Ozak, L Ofman, and A-F Viñas. "Ion heating in inhomogeneous expanding solar wind plasma: The role of parallel and oblique ion-cyclotron waves". In: *The Astrophysical Journal* 799.1 (2015), p. 77.

[205] N.E. Papitashvili and J.H. King. "A Draft High Resolution OMNI Data Set". In: *AGU Spring Meeting Abstracts*. Vol. 2007. May 2006, SM33A-02, SM33A–02.

[206] Tulasi N Parashar and William H Matthaeus. "Propinquity of current and vortex structures: effects on collisionless plasma heating". In: *The Astrophysical Journal* 832.1 (2016), p. 57.

[207] Tulasi N Parashar et al. "Transition from kinetic to MHD behavior in a collisionless plasma". In: *The Astrophysical Journal* 811.2 (2015), p. 112.

[208] CG Park, DL Carpenter, and DB Wiggin. "Electron density in the plasmasphere: Whistler data on solar cycle, annual, and diurnal variations". In: *Journal of Geophysical Research: Space Physics* 83.A7 (1978), pp. 3137–3144.

[209] Kun Il Park, M Park, and James. *Fundamentals of probability and stochastic processes with applications to communications*. Springer, 2018.

[210] Eugene N Parker. "Dynamics of the interplanetary gas and magnetic fields." In: *Astrophysical Journal, vol. 128, p. 664* 128 (1958), p. 664.

[211] George K Parks. *Physics of space plasmas: an introduction*. CRC Press, 2019.

[212] P Picozza et al. "Scientific goals and in-orbit performance of the high-energy particle detector on board the CSES". In: *The Astrophysical Journal Supplement Series* 243.1 (2019), p. 16.

[213] Piergiorgio Picozza, Livio Conti, and Alessandro Sotgiu. "Looking for Earthquake Precursors From Space: A Critical Review". In: *Frontiers in Earth Science* 9 (2021). ISSN: 2296-6463. DOI: 10.3389/feart.2021.676775. URL: https://www.frontiersin.org/articles/10.3389/feart.2021.676775.

[214] Giovanni Piersanti et al. "An inquiry into the structure and dynamics of crude oil price using the fast iterative filtering algorithm". In: *Energy Economics* 92 (2020), p. 104952.

[215] M. Piersanti et al. "From the Sun to Earth: effects of the 25 August 2018 geomagnetic storm". In: *Annales Geophysicae* 38.3 (2020), pp. 703–724. DOI: 10.5194/angeo-38-703-2020. URL: https://angeo.copernicus.org/articles/38/703/2020/.

[216] Mirko Piersanti et al. "Adaptive local iterative filtering: A promising technique for the analysis of nonstationary signals". In: *Journal of Geophysical Research: Space Physics* 123.1 (2018), pp. 1031–1046.

[217] Mirko Piersanti et al. "Magnetospheric–ionospheric–lithospheric coupling model. 1: observations during the 5 August 2018 Bayan Earthquake". In: *Remote Sensing* 12.20 (2020), p. 3299.

[218] David I Pontin and Eric R Priest. "Magnetic reconnection: MHD theory and modelling". In: *Living Reviews in Solar Physics* 19.1 (2022), p. 1.

[219] Maurice Bertram Priestley. *Spectral analysis and time series*. Vol. 890. Academic press London, 1981.

[220] Sergey Pulinets and Kyrill Boyarchuk. *Ionospheric precursors of earthquakes*. Springer Science & Business Media, 2004.

[221] Sergey Pulinets et al. *Earthquake Precursors in the Atmosphere and Ionosphere*. Springer, 2022.

[222] Tuija Pulkkinen. "Space weather: Terrestrial perspective". In: *Living Reviews in Solar Physics* 4.1 (2007), p. 1.

[223] Vladimir A Rakov and Martin A Uman. *Lightning: physics and effects*. Cambridge university press, 2003.

[224] JA Ratcliffe and Thomas E Holzer. "An introduction to the ionosphere and magnetosphere". In: *American Journal of Physics* 41.5 (1973), pp. 761–762.

[225] D. Recchiuti et al. "Detection of electromagnetic anomalies over seismic regions during two strong (MW > 5) earthquakes". In: *Frontiers in Earth Science* 11 (2023). ISSN: 2296-6463. DOI: 10.3389/feart.2023.1152343. URL: https://www.frontiersin.org/articles/10.3389/feart.2023.1152343.

[226] N Sai Satwik Reddy et al. "A Fast Iterative Filtering Method for Efficient Denoising of Phonocardiogram Signals". In: *2023 3rd International Conference on Intelligent Technologies (CONIT)*. IEEE. 2023, pp. 1–6.

[227] Paul Harry Roberts. *An introduction to magnetohydrodynamics*. Vol. 6. Longmans London, 1967.

[228] Craig J Rodger, Mark A Clilverd, and Robert J McCormick. "Significance of lightning-generated whistlers to inner radiation belt electron lifetimes". In: *Journal of Geophysical Research: Space Physics* 108.A12 (2003).

[229] J. Rodríguez-Camacho et al. "Four Year Study of the Schumann Resonance Regular Variations Using the Sierra Nevada Station Ground-Based Magnetometers". In: *Journal of Geophysical Research: Atmospheres* 127.6 (2022). e2021JD036051 2021JD036051, e2021JD036051. DOI: https://doi.org/10.1029/2021JD036051. eprint: https://agupubs.onlinelibrary.wiley.com/doi/pdf/10.1029/2021JD036051. URL: https://agupubs.onlinelibrary.wiley.com/doi/abs/10.1029/2021JD036051.

[230] Bruno Rossi and Stanislaw Olbert. "Introduction to the physics of space." In: *Introduction to the physics of space* (1974).

[231] Harvey L Rowland. "Theories and simulations of elves, sprites and blue jets". In: *Journal of Atmospheric and Solar-Terrestrial Physics* 60.7-9 (1998), pp. 831–844.

[232] CT Russell. "The polar cusp". In: *Advances in Space Research* 25.7-8 (2000), pp. 1413–1424.

[233] Michael J Rycroft and R Giles Harrison. "Electromagnetic atmosphere-plasma coupling: the global atmospheric electric circuit". In: *Space Science Reviews* 168 (2012), pp. 363–384.

[234] Terence J Sabaka, Gauthier Hulot, and Nils Olsen. "Mathematical properties relevant to geomagnetic field modeling". In: *Handbook of geomathematics*. 2010.

[235] S Saito, S Peter Gary, and Y Narita. "Wavenumber spectrum of whistler turbulence: Particle-in-cell simulation". In: *Physics of Plasmas* 17.12 (2010).

[236] Sergeui Stepanovich Sazhin. *Whistler-mode waves in a hot plasma*. Cambridge University Press, 1993.

[237] Robert Schunk and Andrew Nagy. *Ionospheres: Physics, plasma physics, and chemistry*. Cambridge university press, 2009.

[238] Davis D Sentman. "Schumann resonances". In: *Handbook of Atmospheric Electrodynamics, Volume I*. CRC Press, 2017, pp. 267–295.

[239] V Sgrigna et al. "Correlations between earthquakes and anomalous particle bursts from SAMPEX/PET satellite observations". In: *Journal of atmospheric and solar-terrestrial physics* 67.15 (2005), pp. 1448–1462.

[240] Shivam Sharma, Aakash Shedsale, and Rishi Raj Sharma. "Multivariate Fast Iterative Filtering Based Automated System for Grasp Motor Imagery Identification Using EEG Signals". In: *International Journal of Human–Computer Interaction* (2023), pp. 1–9.

[241] XuHui Shen et al. "The state-of-the-art of the China Seismo-Electromagnetic Satellite mission". In: *Science China Technological Sciences* 61.5 (May 2018), pp. 634–642. ISSN: 1869-1900. DOI: 10.1007/s11431-018-9242-0. URL: https://doi.org/10.1007/s11431-018-9242-0.

[242] NF Sidiropoulos, G Anagnostopoulos, and V Rigas. "Comparative study on earthquake and ground based transmitter induced radiation belt electron precipitation at middle latitudes". In: *Natural Hazards and Earth System Sciences* 11.7 (2011), pp. 1901–1913.

[243] Devendraa Siingh et al. "The atmospheric global electric circuit: an overview". In: *Atmospheric Research* 84.2 (2007), pp. 91–110.

[244] Fernando Simões et al. "A review of low frequency electromagnetic wave phenomena related to tropospheric-ionospheric coupling mechanisms". In: *Space science reviews* 168 (2012), pp. 551–593.

[245] DK Singh, RP Singh, and AK Kamra. "The electrical environment of the Earth's atmosphere: A review". In: *Space Science Reviews* 113.3 (2004), pp. 375–408.

[246] Steven R Spangler. "Kinetic effects of Alfvén wave nonlinearity. I. Ponderomotive density fluctuations". In: *Physics of Fluids B: Plasma Physics* 1.8 (1989), pp. 1738–1746.

[247] Steven R Spangler and James P Sheerin. "Properties of Alfvén solitons in a finite-beta plasma". In: *Journal of plasma physics* 27.2 (1982), pp. 193–198.

[248] Elias M Stein and Rami Shakarchi. *Fourier analysis: an introduction*. Vol. 1. Princeton University Press, 2011.

[249] TH Stix. "Waves in Plasmas, American Inst". In: *Physics, New York* (1992).

[250] LRO Storey. "An investigation of whistling atmospherics". In: *Philosophical Transactions of the Royal Society of London. Series A, Mathematical and Physical Sciences* 246.908 (1953), pp. 113–141.

[251] Ida Svenningsson et al. "Whistler waves in the quasi-parallel and quasi-perpendicular magnetosheath". In: *Journal of Geophysical Research: Space Physics* 129.6 (2024), e2024JA032661.

[252] VA Svidzinski et al. "Particle in cell simulations of fast magnetosonic wave turbulence in the ion cyclotron frequency range". In: *Physics of Plasmas* 16.12 (2009).

[253] Donald Gary Swanson. *Plasma kinetic theory*. Crc Press, 2008.

[254] T Tanimoto and K Heki. "4.16-Interaction of Solid Earth, Atmosphere and Ionosphere". In: *Treatise on geophysics* (2015), pp. 421–443.

[255] Gy Tarcsai, P Szemeredy, and L Hegymegi. "Average electron density profiles in the plasmasphere between L= 1.4 and 3.2 deduced from whistlers". In: *Journal of atmospheric and terrestrial physics* 50.7 (1988), pp. 607–611.

[256] William WL Taylor and Donald A Gurnett. "Morphology of VLF emissions observed with the Injun 3 satellite". In: *Journal of Geophysical Research* 73.17 (1968), pp. 5615–5626.

[257] Paul Tenfjord and Nikolai Østgaard. "Energy transfer and flow in the solar wind-magnetosphere-ionosphere system: A new coupling function". In: *Journal of Geophysical Research: Space Physics* 118.9 (2013), pp. 5659–5672.

[258] Richard M Thorne et al. "Plasmaspheric hiss". In: *Journal of Geophysical Research* 78.10 (1973), pp. 1581–1596.

[259] Rudolf A Treumann and Wolfgang Baumjohann. *Advanced space plasma physics*. Vol. 30. Imperial College Press London, 1997.

[260] Domenico Trotta et al. "Fast acceleration of transrelativistic electrons in astrophysical turbulence". In: *The Astrophysical Journal* 894.2 (2020), p. 136.

[261] Bruce T Tsurutani. "A review of nonlinear low frequency (LF) wave observations in space plasmas: On the development of plasma turbulence". In: (1995).

[262] Bruce T Tsurutani and Gurbax S Lakhina. "Some basic concepts of wave-particle interactions in collisionless plasmas". In: *Reviews of Geophysics* 35.4 (1997), pp. 491–501.

[263] Bruce T Tsurutani et al. "Plasmaspheric hiss: Coherent and intense". In: *Journal of Geophysical Research: Space Physics* 123.12 (2018), pp. 10–009.

[264] Naoto Ujihara, Yoshimori Honkura, and Yasuo Ogawa. "Electric and magnetic field variations arising from the seismic dynamo effect for aftershocks of the M7. 1 earthquake of 26 May 2003 off Miyagi Prefecture, NE Japan". In: *Earth, planets and space* 56.2 (2004), pp. 115–123.

[265] Takayuki Umeda, Shinji Saito, and Yasuhiro Nariyuki. "Decay of nonlinear whistler mode waves: 1D versus 2D". In: *Physics of Plasmas* 25.7 (2018).

[266] Bernard J Vasquez. "Simulation study of the role of ion kinetics in low-frequency wave train evolution". In: *Journal of Geophysical Research: Space Physics* 100.A2 (1995), pp. 1779–1792.

[267] Bernard J Vasquez. "Strongly nonlinear evolution of low-frequency wave packets in a dispersive plasma". In: *Physics of Fluids B: Plasma Physics* 5.7 (1993), pp. 2021–2035.

[268] Bernard J Vasquez and Sergei A Markovskii. "Velocity power spectra from cross-field turbulence in the proton kinetic regime". In: *The Astrophysical Journal* 747.1 (2012), p. 19.

[269] Bernard J Vasquez, Sergei A Markovskii, and Benjamin DG Chandran. "Three-dimensional hybrid simulation study of anisotropic turbulence in the proton kinetic regime". In: *The Astrophysical Journal* 788.2 (2014), p. 178.

[270] M Velli et al. "Propagation and disruption of Alfvénic solitons in the expanding solar wind". In: *AIP Conference Proceedings*. Vol. 471. 1. AIP Publishing. 1999, pp. 445–448.

[271] Daniel Verscharen, Kristopher G Klein, and Bennett A Maruca. "The multi-scale nature of the solar wind". In: *Living Reviews in Solar Physics* 16.1 (2019), p. 5.

[272] Daniel Verscharen et al. "Kinetic cascade beyond magnetohydrodynamics of solar wind turbulence in two-dimensional hybrid simulations". In: *Physics of Plasmas* 19.2 (2012).

[273] SV Vladimirov and SI Popel. "Theory of modulational interactions in collisional plasmas". In: *Physica Scripta* 50.2 (1994), p. 161.

[274] A A Vlasov. "On vibration properties of electron gas". In: *Soviet Physics Uspekhi* 8 (1938), p. 291.

[275] Hans Volland. *Handbook of atmospheric electrodynamics*. Vol. 2. CRC Press, 1995.

[276] James R Wait. "Earth-ionosphere cavity resonances and the propagation of ELF radio waves". In: *Radio Sci* 69 (1965), p. 1057.

[277] ADM Walker. "The theory of whistler propagation". In: *Reviews of Geophysics* 14.4 (1976), pp. 629–638.

[278] John M Wallace and Peter V Hobbs. *Atmospheric science: an introductory survey*. Vol. 92. Elsevier, 2006.

[279] Andrew P Walsh et al. "Dawn–dusk asymmetries in the coupled solar wind–magnetosphere–ionosphere system: A review". In: *Annales Geophysicae*. Vol. 32. 7. Copernicus GmbH. 2014, pp. 705–737.

[280] M Wan et al. "Intermittency, coherent structures and dissipation in plasma turbulence". In: *Physics of Plasmas* 23.4 (2016).

[281] M Wan et al. "Intermittent dissipation and heating in 3D kinetic plasma turbulence". In: *Physical review letters* 114.17 (2015), p. 175002.

[282] M Wan et al. "Intermittent dissipation at kinetic scales in collisionless plasma turbulence". In: *Physical review letters* 109.19 (2012), p. 195001.

[283] Chi Wang et al. “Magnetohydrodynamics (MHD) numerical simulations on the interaction of the solar wind with the magnetosphere: A review”. In: *Science China Earth Sciences* 56 (2013), pp. 1141–1157.

[284] Xiuying Wang et al. “Validation of CSES RO measurements using ionosonde and ISR observations”. In: *Advances in Space Research* 66.10 (2020), pp. 2275–2288.

[285] Yang Wang, Guo-Wei Wei, and Siyang Yang. “Iterative filtering decomposition based on local spectral evolution kernel”. In: *Journal of scientific computing* 50 (2012), pp. 629–664.

[286] Yang Wang and Zhengfang Zhou. “On the convergence of iterative filtering empirical mode decomposition”. In: *Excursions in Harmonic Analysis, Volume 2: The February Fourier Talks at the Norbert Wiener Center* (2013), pp. 157–172.

[287] Yue Wang et al. “A novel interpretable model ensemble multivariate fast iterative filtering and temporal fusion transform for carbon price forecasting”. In: *Energy Science & Engineering* 11.3 (2023), pp. 1148–1179.

[288] Zijie Wang et al. “Lightning-generated Whistlers recognition for accurate disaster monitoring in China and its surrounding areas based on a homologous dual-feature information enhancement framework”. In: *Remote Sensing of Environment* 304 (2024), p. 114021.

[289] James A. Wanliss and Kristin M. Showalter. “High-resolution global storm index: Dst versus SYM-H”. In: *Journal of Geophysical Research: Space Physics* 111.A2 (2006). DOI: https://doi.org/10.1029/2005JA011034. eprint: https://agupubs.onlinelibrary.wiley.com/doi/pdf/10.1029/2005JA011034. URL: https://agupubs.onlinelibrary.wiley.com/doi/abs/10.1029/2005JA011034.

[290] Earle R Williams. “The global electrical circuit: A review”. In: *Atmospheric Research* 91.2-4 (2009), pp. 140–152.

[291] Charles Thomson Rees Wilson. “III. Investigations on lighting discharges and on the electric field of thunderstorms”. In: *Philosophical Transactions of the Royal Society of London. Series A, Containing Papers of a Mathematical or Physical Character* 221.582-593 (1921), pp. 73–115.

[292] CTR Wilson. “On the measurement of the earth-air current and on the origin of atmospheric electricity”. In: *Proc. Cambridge Philos. Soc.* Vol. 13. 6. 1906, pp. 363–382.

[293] D Winske. “Hybrid simulation codes with application to shocks and upstream waves”. In: *Space Science Reviews* 42.1 (1985), pp. 53–66.

[294] Alan G Wood et al. “Variability of ionospheric plasma: Results from the ESA swarm mission”. In: *Space Science Reviews* 218.6 (2022), p. 52.

[295] Ken’ichi Yamazaki. “Estimation of temporal variations in the magnetic field arising from the motional induction that accompanies seismic waves at a large distance from the epicentre”. In: *Geophysical Journal International* 190.3 (2012), pp. 1393–1403.

[296] Rui Yan et al. “Comparison of electron density and temperature from the CSES satellite with other space-borne and ground-based observations”. In: *Journal of Geophysical Research: Space Physics* 125.10 (2020), e2019JA027747.

[297] DeHe Yang et al. “Stability validation on the VLF waveform data of the China-Seismo-Electromagnetic Satellite”. In: *Science China Technological Sciences* 65.12 (2022), pp. 3069–3078.

[298] Yanyan Yang et al. “CSES high precision magnetometer data products and example study of an intense geomagnetic storm”. In: *Journal of Geophysical Research: Space Physics* 126.4 (2021), e2020JA028026.

[299] YB Yao et al. “Analysis of pre-earthquake ionospheric anomalies before the global M= 7.0+ earthquakes in 2010”. In: *Natural Hazards and Earth System Sciences* 12.3 (2012), pp. 575–585.

[300] Yury V Yasyukevich et al. “SIMuRG: System for ionosphere monitoring and research from GNSS”. In: *GPS solutions* 24 (2020), pp. 1–12.

[301] David A Yuen et al. “Under the surface: Pressure-induced planetary-scale waves, volcanic lightning, and gaseous clouds caused by the submarine eruption of Hunga Tonga-Hunga Ha’apai volcano”. In: *Earthquake Research Advances* 2.3 (2022), p. 100134.

[302] GM Zaslavski. “Nonlinear waves and their interaction”. In: *Soviet Physics Uspekhi* 16.6 (1974), p. 761.

[303] Shufan Zhao et al. “CSES Satellite Observations of 50 Hz Power Line Radiation Over Mainland China and Its Response to COVID-19”. In: *Journal of Geophysical Research: Space Physics* 127.9 (2022), e2022JA030693.

[304] ZEREN Zhima et al. “Current Status and Main Scientific Outcomes of the CSES Mission”. In: *Chinese Journal of Space Science* (2022).

[305] Zeren Zhima et al. “Cross-calibration on the electromagnetic field detection payloads of the China Seismo-Electromagnetic Satellite”. In: *Science China Technological Sciences* 65.6 (2022), pp. 1415–1426.

[306] Jiayi Zong, Dan Tao, and Xuhui Shen. “Possible ELF/VLF Electric Field Disturbances Detected by Satellite CSES before Major Earthquakes”. In: *Atmosphere* 13 (Aug. 2022), p. 1394. DOI: 10.3390/atmos13091394.

[307] Ellen G Zweibel and Masaaki Yamada. “Perspectives on magnetic reconnection”. In: *Proceedings of the Royal Society A: Mathematical, Physical and Engineering Sciences* 472.2196 (2016), p. 20160479.

List of Figures

List of Tables